

Generation, characterization, and infection of mature and heterogenous lung organoid models for viral drug screening

By

Alicia Reyes Valenzuela

Department of Biological and Biomedical Engineering

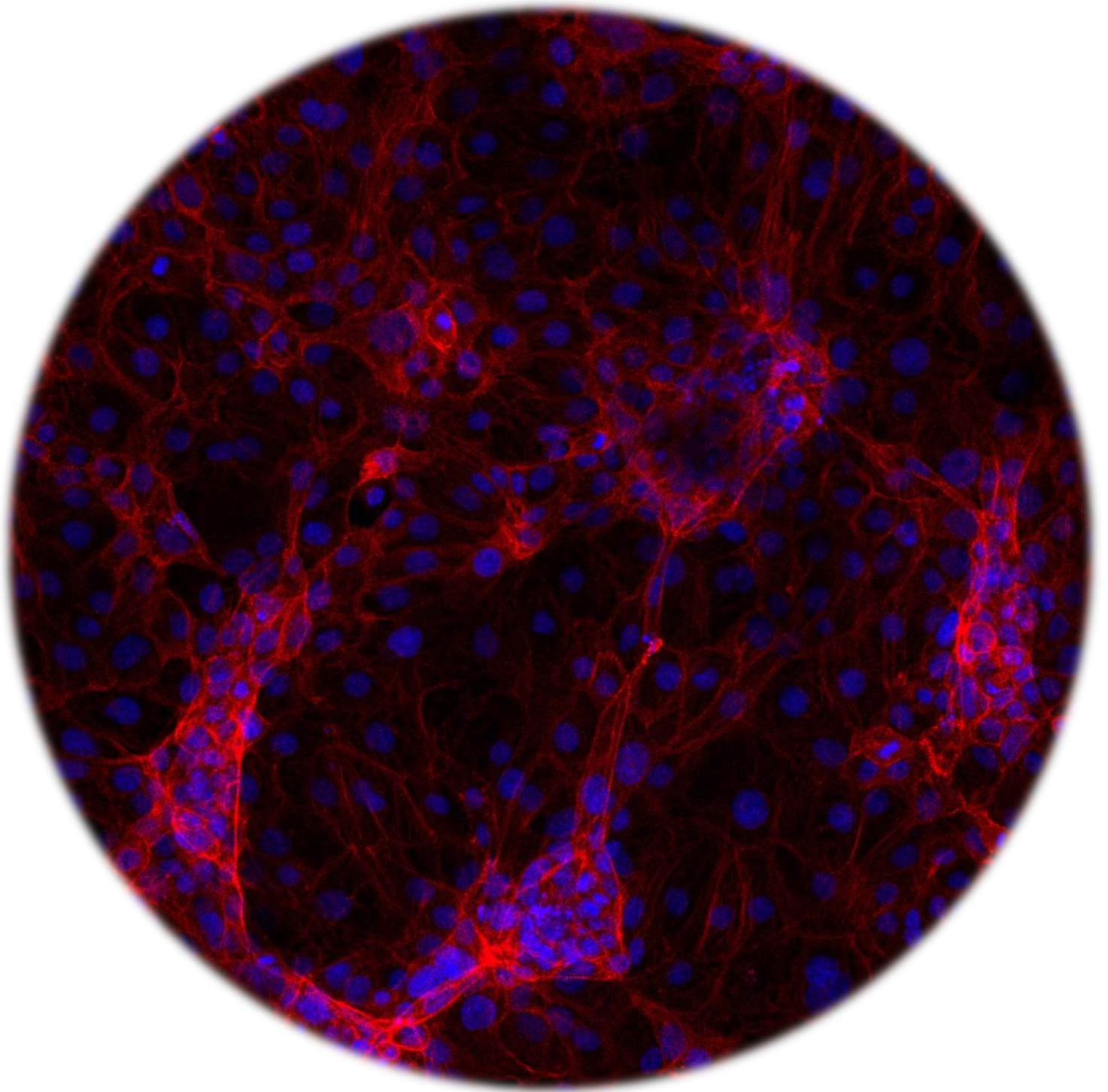
McGill University, Montréal



A thesis submitted to McGill University in partial fulfillment of the requirements of the degree of

Doctor of Philosophy

©ALICIA REYES VALENZUELA, 2024



*In loving memory of my beloved father Felipe de Jesus Reyes Pastrana who tragically lost his
life to the very virus that became part of my research subject.*

*This thesis is dedicated to you, Dad, because every step I took in this research was inspired by
your memory and the hope that someday, we can prevent others from experiencing the same loss
that our family endured.*

*Your legacy lives on in the pursuit of science, and I am forever grateful for the lessons you
taught me about resilience, determination, and the power of love.*

I miss you more than words can express.

*I also dedicate this work to all the animals whose lives have contributed to scientific progress. I
hope for a future where ethical alternatives continue to replace animal experimentation.*

Acknowledgements

Quiero expresar mi más sincera gratitud a mi familia, mi papá Felipe de Jesús Reyes Pastrana, mi mamá Nay Valenzuela, mi hermano Felipe Reyes Valenzuela y mi hermana Beatriz Reyes Valenzuela. Dejar mi hogar en México para perseguir mis sueños fue una de las decisiones más difíciles de mi vida. Aun así, siempre los sentí cerca, siempre sentí su apoyo y su amor. Gracias por siempre impulsarme y creer en mí, gracias por escucharme, darme fuerza en los días malos, y celebrar mis triunfos. No habría podido llegar hasta aquí sin todo su esfuerzo y sus sacrificios. Los amo.

When I started my PhD. I had a small, but very supportive and lovely family in Mexico, I was lucky enough to expand this family during my studies. Ironically, when I was living one of the worst moments of my life, I met the love of my life: Christophe Lachance-Brais, now my husband. Christophe, you are the sun of my life, my little angel. Thanks for showering me with love, thanks for being there for me in the good and bad moments, thanks for believing on my potential as a scientist. Your love makes me stronger.

Thanks to my new family, Stephane Brais, Caroline Lachance, and Nicolas Lachance-Brais. I haven't felt alone since all of you arrived at my life.

I would like to thank Prof. Mongeau. Thank you for your guidance and support throughout this journey. Thank you for believing in me and my crazy ideas. My Ph.D. project was completely new, and as such it was full of challenges and detours. Regardless of this, you always show me support. Thanks for showing me that giving up is not an option.

I would like to express my deepest gratitude to all professors and colleagues who become part of the project and take part of their time to guide me. Special thanks to Prof. Vidal, for their support and involvement in the project, thanks for your advice, feedback, and for making me part of your team. You are an inspiration as a woman scientist. Thanks Mark Turner, for be my very first mentor in the field of molecular biology, thanks for training me, and for sharing your protocols and insights about life and science. Thanks Lorne Taylor, from MUHC, for your constant guidance. Since the beginning we knew the proteomics analysis will be challenging, and yet you accepted the task. Thanks for your words of encouragement and appreciation towards my project and my “Funky” scientist persona, as you like to describe me.

Thanks to all lab members of Prof. Vidal: Nathan Makarian, Alice Hou, and Bennoit Charbonneau. Sharing part of my PhD with all of you was an enriching experience.

Thanks to all lab members of Prof. Mongeau: Guangyu Bao, Sareh Taheri, Sepideh Mohammed, Alda Profka, Rayane Ait Oubahou, Hossein Ravanbakhsh, Swen Groen, Sara Nejati, Maddy Liblong, Zixin He, and Bella Chen. Thanks for your friendship, insights, and company during this journey.

To my students Avigail Vikstrom, Priya Nagpal, Bernadette Ng, Charlotte Fouquet, and Lan Anh Huynh thanks for helping me in becoming a good mentor and be part of the organoid team. I appreciate all your efforts, hard work, and motivation on this journey.

I would like to appreciate my gratitude to CONACYT for funding the entire duration of my doctoral studies.

I would like to express my heartfelt gratitude to People for Ethical Treatment of Animals (PETA) for awarding and give visibility to my research. Their commitment to advocating for the ethical treatment of animals in scientific research is commendable and aligns with my own aspirations.

My work has always been driven by the hope that it can contribute to the reduction and replacement of animals in biomedical research. I firmly believe that as science advances, we have a moral obligation to explore alternative methods that do not involve the use of sentient beings.

Abstract

The lung is the primary target of many lethal respiratory viruses, causing significant global mortality. Lung organoid models are potentially helpful for studying emerging or re-emerging viral infections and fostering the development of novel in-vitro therapeutic strategies. But existing models have so far failed to accurately mimic the heterogeneity, cellular diversity and intricate tubular and branching structures of native lungs. Most current models include only cells markers from one single lung region, often primary cells harvested from invasive deep lung tissue biopsies. The present study was aimed at the creation of a heterogeneous lung organoid model from more readily accessible trachea/bronchi cells. Either primary or immortalized bronchial cells were combined with fibroblasts feeder cells in an alginate hydrogel coated with base membrane zone proteins. Fibroblasts were employed as the primary source of patterning molecules, including FGFs. This approach was inspired by the natural process of lung development, which involves interactions between epithelial progenitors and surrounding mesenchymal cells. The resulting organoid models, reaching maturity in only 21 days, offer a shorter fabrication timeline compared to other reported models, and they better mimic the diverse cellular and tubular morphology of the lung. Focused ion beam microscopy revealed structural heterogeneity within the organoids, as well as microvilli structures. Comprehensive characterizations were performed using transcriptomics and proteomics. The novel organoid models were found to exhibit upregulation in genes related to the respiratory system, tube development, and alveolar development. The organoid proteome showed notable improvements in comparison to the input cell lines, and higher similarity with the one from adult lung tissues. Notably, the functions associated with upregulated proteins in the organoid were specific to the lung development, alveolar type II cells, respiratory epithelium, oral mucosa, and response to stress. Primary-derived organoids (LOp) exhibit a closer resemblance in the regulation of proteins to that observed in adult lung tissue compared to organoids derived from immortalized cells (LOi). Despite this, LOi include several enriched

pathways specific to the lung, albeit to a lesser extent than their LOp counterparts. Notably, both LOp and LOi exhibit a degree of plasticity, irrespective of their cellular origin. It was found that both types of organoids express several genes to allow their infectivity with coronaviruses and influenza strains. In order to develop a rapid, cost-effective, and scalable infection model, organoids derived from immortalized cells were infected with SARS-CoV-2, influenza H1N1, and H3N2. Viral replication was found in the organoid lysate and supernatant. A similar protocol was used to create organoids derived from a female donor with asthma. This underscores the potential of organoids for future applications in personalized medicine. To enhance the scalability of the biofabrication process, we investigated organoid formation via bioprinting and cultivation within spinning bioreactors. The organoids described in this study show promise as an alternative model to animal studies for drug development and for targeting various lung pathologies.

Résumé

Le poumon est la cible de nombreux virus respiratoires mortels. Les modèles d'organoïdes pulmonaires sont potentiellement utiles pour étudier les infections virales émergentes ou réémergentes et favoriser le développement de nouvelles stratégies thérapeutiques in vitro. Mais les modèles existants ne peuvent reproduire fidèlement l'hétérogénéité et la diversité cellulaire, ainsi que les structures tubulaires et ramifiées des poumons. La plupart des modèles actuels ne contiennent que des marqueurs cellulaires d'une seule région pulmonaire, souvent des cellules primaires prélevées lors d'une biopsie de tissu pulmonaire. La présente étude visait à créer un modèle d'organoïde pulmonaire hétérogène à partir de cellules de la trachée ou des bronches, plus facilement accessibles que celles de poumons. Des cellules bronchiques, primaires ou immortalisées, ont été combinées avec de fibroblastes dans un hydrogel d'alginate recouvert de protéines de la zone de membrane de base. Les fibroblastes servent de source principale de facteurs de croissances, y compris les FGFs. Cette approche est inspirée par développement naturel des poumons, qui implique des interactions entre les progéniteurs épithéliaux et les cellules mésenchymateuses environnantes. Les protocoles existants requièrent souvent des facteurs exogènes ajoutés à la culture cellulaire. Les modèles d'organoïdes résultants atteignent la maturité qu'en seulement 21 jours, offrant aussi un temps de gestation plus court que les modèles existants. Les modèles imitent bien la morphologie cellulaire et tubulaire diversifiée du poumon. La microscopie par faisceau d'ions focalisé révèle l'hétérogénéité structurelle de ces organoïdes, ainsi que la présence de microvillosités. Une caractérisation complète de son protéome et transcriptomes a été réalisée. Ces

nouveaux organoïdes démontrent une surexpression de gènes liés au système respiratoire, au développement tubulaire et au développement alvéolaire. Quant au protéome des organoïdes, il offre des distinctions notables par rapport aux lignées cellulaires d'entrée, et une similitude plus élevée avec celle des tissus pulmonaires adultes. Notamment, les fonctions associées aux protéines surexprimées dans les organoïdes sont spécifiques au développement pulmonaire, aux cellules alvéolaires de type II, à l'épithélium respiratoire, à la muqueuse buccale et à la réponse au stress. Les organoïdes dérivés de cellules primaires (LOp) présentent une ressemblance plus étroite dans la régulation des protéines à celle observée dans le tissu pulmonaire adulte par rapport aux organoïdes dérivés de cellules immortalisées (LOi). Néanmoins, les LOi présentent plusieurs voies enrichies spécifiques au poumon, bien que dans une moindre mesure que leurs homologues LOp. Notamment, les LOp et les LOi retiennent un degré de plasticité, indépendamment de leur origine cellulaire. Il a été constaté que ces deux types d'organoïdes expriment plusieurs gènes permettant leur infection avec les coronavirus et la grippe. Dans le but de développer un modèle d'infection rapide, économique et évolutif, des organoïdes dérivés de cellules immortalisées ont été infectés avec le SARS-CoV-2, la grippe H1N1 et H3N2. La réplication virale a été détectée dans le lysat et le surnageant des organoïdes. De plus, un protocole similaire a été adapté pour fabriquer des organoïdes dérivés d'une donneuse asthmatique. Cela valorise les organoïdes pour applications futures en médecine personnalisée.

Contents

Acknowledgements	3
List of Tables	13
List of Figures.....	15
Contribution of original knowledge	31
Abbreviations	37
Chapter 1: Introduction.....	41
1.1 Introduction Outline	41
1.2 The cellular complexity of human lungs	41
1. 3 Molecular mechanisms for lung development and branching morphogenesis	46
1. 4 Animal models	49
1.5 Lung-In-Vitro Models	52
1.5.1 Two-dimensional cell monolayers in and air-liquid interface models	52
1.5.2 Organ-on-a-chip	54
1.5.3 Organoids	59
1. 5. 4 Literature survey: Available lung organoids	63
1.6 Context and Scope of the Thesis	72
1.6.1 Description of the Problem	72
1.6.2 Research Objectives	74
1.6.3 Rationale, and hypothesis	76
1.6.4 Thesis organization	77
Chapter 2 Fabrication methods and protocols.....	80
2. 1 Contributions	80
2.2 Introduction	80
2. 3 Results	82
2.3. 1 Alginate-Gelatine as substrate for fibroblasts encapsulation	82
2.3.2 Protocol for the Development of Human Lung Organoids from Primary or Immortalized Bronchial Epithelial Cells	83
2.3.3 Effects of fibroblast density on the organoid formation	87
2.3. 4 Comparative Analysis of Hydrogels and Impact on Organoid Development	89
2.3.5 Effect of Feeder Cell Sources for Organoid Cultures	92
2.3. 6 Effect of Culture Medium for Organoid Development	93

2.3.7 Investigation of organoid morphology by Transmission Electron Microscopy and Focused Ion Beam Microscopy.....	94
2.3.8 Investigation of bioprinting for the fabrication of lung organoids.	102
2. 4 Discussion	105
2. 5 Methods	111
2. 5.1 Cell culture.....	111
2.5.2 Induction of adult human lung organoids derived from airway epithelial cells.	111
2. 5. 3 Dialysis and lyophilisation of GelMA.....	112
2.5.4 Hydrogel synthesis.....	112
2.5.5 Live/Dead Assay.....	113
2.5.6 RGD conjugation	113
2.5. 7 Rheological measurements.....	114
2.5.8 Fourier-transform infrared spectroscopy.....	114
2.5.9 Immunofluorescence staining	114
2.5.10 Transmission electron microscopy of lung organoids	115
2.5. 11 Focused Ion Beam microscopy of lung organoids.	115
2.5.12 Bioprinting lung organoids	115
Chapter 3 Characterization of pulmonary organoids	117
3. 1 Contributions.....	117
3. 2 Introduction	117
3.3 Results	118
3.3.1 Evaluation of cellular markers and functional enrichment analysis	118
3. 3. 2 Proteomics profile of organoids and cell lines.....	134
3. 3.3 Comparative study between proteomic profile of organoids and adult lung tissues.....	146
3. 4 Discussion	154
3. 5 Methods	157
3. 5. 1 Cell culture.....	157
3. 5. 2 CFBE culture in air-liquid interface.....	158
3.5.3 Primary airway epithelium culture in air-liquid interface	158
3.5. 4 Bulk RNA sequencing and analysis.....	158
3.5. 5 Tandem Mass Tags.....	161
3.5. 6 Flow cytometry	164

3.5. 7 Immunofluorescence Staining	165
3. 5. 8 RNA isolation and quantitative PCR	165
Chapter 4 Modeling respiratory diseases with lung organoids	167
4. 1 Contributions	167
4. 2 Introduction	167
4. 3 Results	172
4.3. 1 Genes and proteins involved in Respiratory viral infections	172
4.3. 2 Lung organoids to model influenza infections.	180
4.3. 3 Lung organoids to model SARS-CoV-2.	181
4.3. 4 Lung organoids to model Asthma	183
4. 4 Discussion	189
4. 5 Methods	192
4. 5. 1 RNA sequencing analysis	192
4.5.2 SARS-CoV-2 infection in human lung organoids	193
4.5. 3 Influenza infection in human lung organoids	194
4.5.4 Quantification of SARS-CoV-2 RNA in Supernatant using RT–qPCR Error! Bookmark not defined.	
4.5. 5 Quantification of SARS-CoV-2 RNA in Cell Lysates using RT–qPCR	194
4.5. 6 Plaque Assay	195
4.5. 7 Quantification of Nucleocapsid protein for influenza infection using RT-qPCR	196
4.5. 8 Generation of asthmatic organoids	197
4.5. 9 Statistical analysis	198
Chapter 5: Conclusions and Perspectives.....	199
5.1 Summary and conclusions	199
5. 1.1 Protocol for developing lung organoids	200
5.1.2. Organoid phenotypes	202
5.1.3. Lung organoid as model of respiratory diseases	205
5. 2 Perspectives and Future work	206
5. 3 Final contributions	211
Bibliography	212
Appendix	224

List of Tables

Table 1.1 Lung-on-a-chip microdevices.	59
Table 1.2 Existing lung and LRT organoids. There are two main categories of lung organoids. 1) The organoids derived from adult stem cells, typically represent one region of the lung (either proximal or distal) but not both. They have a spheroidal morphology, and a relative short maturation time. They are made with primary cells extracted from deep lung tissues from patients with cancer. 2) iPSC-derived organoids. These organoids mimic the entire lung. They exhibit a branching morphogenesis, but their phenotype remains immature. They require long culture time conditions, increasing their cost. \$Commercially available model.	69
Table 1.3 Lung-on-a-chip microdevices. Medium to culture airway organoids. *Conditioned media were produced from stable cell lines for production of R-spondin1 and Noggin ⁶⁵	70
Table 1.4 Cell culture medium used for development of iPSC derived lung organoids. Obtained from ²¹	71
Table 2.1 Average diameter of bioprinted droplets of AIGe and lung fibroblasts for three different cell densities.	103
Table 4.1 Conditions tested and their outcomes for generation of organoids derived from a patient with asthma.	186
Table A.1 P. adjust value from multiple t-test comparisons between RNA sequencing of LOp vs cell monolayers: HBE, and IMR-90 ↑ means upregulation in LOp (p.adjust<0.05). ↓ means downregulation in LOp (p. adjust <0.05). Lower the p value, more significant the up or downregulation.	223

Table A.2 P. adjust value from multiple t-test comparisons between RNA sequencing of LOi vs cell monolayers: CFBE, and IMR-90. ↑ means upregulated in LOi (p.adjust<0.05).....	224
Table A.3 Key resources table for methods described in Chapter 3.....	226
Table A.4 Key resources table. Primer sequence used in chapter 3 as housekeeping gene.....	227
Table A.5 Key resources table. Primer sequences used in chapter 4 to evaluate infectability of SARS-CoV-2 and Influenza in the organoids.....	227

List of Figures

Fig. 1.1 Cellular composition of lower respiratory tract in humans and mice. The lower respiratory tract contains multiple epithelial cell types, which are underlined with heterogenous mesenchymal cells, including fibroblasts and airway smooth muscle cells (ASM). These cells provide extracellular matrix proteins and ligands, which modulate epithelial cell differentiation and control airway tube diameter. A) Schematic of the lower respiratory tract consisting of trachea and lungs, which are further subdivided into proximal (bronchi) and distal regions composed of bronchioles and alveoli. B) Schematic of large airways composed of trachea, and bronchi. Multiple epithelial cell types line up these regions, including basal cells, secretory cells, ciliated cells, and goblet cells. Other rare epithelial cell types such as brush cells, ionocytes, pulmonary neuroendocrinal cells (PNEC), and neuroendocrine bodies (NEB) are also found in these regions. Large airways harbor cartilaginous rings and submucosal glands containing serous cells, mucous cell, and myoepithelial cells. C) Schematic of the small airways in humans and mice and representative cells within it. Mice airways are distinct from those of humans. The former ones lack basal and goblet cells. Image obtained with permission of ¹ (License number: 5764250306282)..... 44

Fig. 1.2 Cellular composition of distal lung, in particular alveoli. A) Schematic showing the breathing process in small airways. Inhaled air is circulated, and oxygen and CO₂ exchange occurs within the endothelial capillary plexus. B) The alveoli are composed of two types of epithelial cells, alveolar type 1 (AT1) and alveolar type 2 (AT2) cells. In AT1 the gas exchange occurs, while AT2 produces surfactant proteins which help the breathing process, preventing the alveolus from collapsing. Other abundant cell types

are the mesenchymal alveolar niche cells (MANC). They support alveolar structures, epithelial proliferation, and differentiation. Interstitial fibroblast expressing Axin-2-positive myogenic precursors (AMPs) and Wnt2 expressing platelet-derived growth factor- α (PDGFR α) are subtypes of MANC. Immune cells, specifically interstitial macrophages, are part of the alveolar microenvironment. Image obtained with permission of ¹ (License number: 5764250306282)..... 45

Fig. 1.3. Lung branching morphogenesis mediated by epithelial-mesenchymal interactions and Wnt signaling. A) During embryonic development, the lung buds emerge, regulated by Wnt2/2b to establish NKX2 patterning. Endodermal Wnt ligands promote FGF10 in the mesenchyme allowing basal cell development. B) The pseudo glandular stage, lung buds undergo branching morphogenesis to develop terminal bronchioles. Suppression of Wnt is needed for branching morphogenesis. Wnt5a is the highest on the distal tip. It suppresses SHH and activates FGF10. Concurrently, FGF9 from epithelium and mesenchyme promotes Wnt2a, facilitating mesenchymal cell proliferation. C) The canicular stage of development, the terminal bronchioles become more defined and form epithelial sacs. Proximal and distal patterning occurs. The downregulation of Wnt by DKK1 generates proximal patterning. Conversely, high levels of Wnt drive distal phenotype through the expression of FGF, BMP4, and N-MYC. D) The alveolar structures mature. AXIN2 and Wnt signaling regulate AT2 alveologenesi. BMP4 suppresses the self-renewal of AT2 while inducing AT1 differentiation. The developmental period is indicated for humans in post-conception weeks (pcw). Image created with BioRender with information of ^{1,18}. 48

Fig. 1.4 Differences between mouse and human distal airways. A) Schematic showing the respiratory bronchioles (RB) in human and their absence in mouse lungs. **B)** Top figure: Haematoxylin-and-eosin-stained tissue showing the mouse conducting airways (CA) and the direct transition between the bronchioalveolar duct junction and the alveolar compartment (BADJ). Bottom gradual figure: Haematoxylin-and-eosin-stained tissue showing the transition between the terminal bronchioles and the alveolar duct (AD) through the respiratory bronchioles (RB). Scale bar, 100 μ m. Image modified from²⁴ (License number: 5764250570906)..... 50

Fig. 1.5 Key differences between epithelial cell components in mouse and human lungs. Image obtained with permission from²⁵ (License number: 1477-9129). 51

Fig. 1.6 Air-liquid-interface model of human bronchial epithelial cells. On day 0, epithelial cells are seeded on collagen-coated porous membranes. Until day 7, the cells grow completely immersed. On day 11, the apical side of the cells (top) is exposed to air, and cell differentiation medium is added to the basal side (bottom). Cells start to differentiate on day 14. Typically, the culture is maintained over 25 days..... 53

Fig. 1.7 First reported “*lung-on-chip*”. The model provides mechanical cues which mimic the breathing process. A) The device was characterized by compartmentalized PDMS microchannels to form an alveolar-capillary barrier. B) During inhalation in the living, the diaphragm contracts leading to distension of the alveoli. C) Three PDMS layers are aligned in irreversible bonds forming microfluidic channels. Scale Bar 200 μ m. D) After the permanent bonding vacuum is applied to cause mechanical stretching. Scale bar, 200 μ m. Image obtained with permission from³⁷. 55

Fig. 1.8 Methods and considerations for organoid formation. A) Physical characteristics of the environment. B) The self-organization of the organoid depends on exogenous and endogenous signals. Most models require at least initial exogenous signals, but some models require continuous exogenous signals. C) Possible starting cell conditions for organoid formation. Organoids can be derived from single cells, homogenous cell populations or heterogenous co-cultures. Image obtained with permission from ⁵¹ (License number: 5764251335262). 62

Fig. 1.9 The starting cell type stage determines the level of organoid maturation in-vitro. The horizontal axis shows the developmental stage of the initial cell culture. The vertical axis shows the degree of maturation of the organoid. Image obtained with permission from⁵¹ (License number: 5764251335262)..... 63

Fig. 2.1. Viability of Fibroblasts on AIge substrate. Representative images of fibroblasts encapsulated on AIge over time. Magnification 10X. Scale Bar 100 μm. 82

Fig. 2.2. Protocol for the development of lung organoids using co-culture of lung fibroblasts with airway epithelial cells from primary or immortalized origin..... 84

Fig. 2.3 Representative phase contrast pictures of lung organoids derived from immortal cell lines. Magnification 10X. Scale bar 200 μm. 85

Fig. 2.4. Representative phase contrast pictures of lung organoids derived from female primary airway epithelium on day 18. Magnification 10X. Scale bar 200 μm..... 86

Fig. 2.5 Representative images of independent lung organoid (LOi) cultures over time. Magnification 10X. Red-F-actin. Blue-Nuclei. Scale Bar 500 μm. 87

Fig. 2.6 Effect of fibroblasts on the formation of lung organoid (LOi). A) Airway epithelial cells in geltrex without lung fibroblasts. B) Images showing typical tubular morphology of

lung organoids on day 7. Red-F-actin. Blue-Nuclei. Magnification 10X. Scale Bar 200 μm 88

Fig. 2.7 Representative image of resulting cell aggregations on day 7 when fibroblasts are incorporated in equal density with airway epithelial cells. Magnification 10X. Red-F-actin. Blue-Nuclei. Scale Bar 100 μm 89

Fig. 2.8. 3D cellular structures generated in GelMA hydrogel on day 7. **Red-F-actin. Blue-Nuclei.** Magnification 10X. Scale Bar 100 μm 90

Fig. 2.9. Fourier Transformed Infrared Spectroscopy Analysis of Alginate (blue) and Alginate conjugated with RGD (red). 90

Fig. 2.10. Effects of AI-RGD-Ge substrate on organoid formation. A) Viability of organoids grown in AIGe (pink) and AI-RGD-Ge (purple) substrate images and percentages. Representative micrographs showing in Red-dead cells, and in green-live cells on day 7. Magnification 10X. Scale Bar 500 μm . Percentages of live cells in both substrates over time. N=3. Two-way ANOVA analysis shows no significant change. B) Organoid length over time (μm) N=3. Two-way ANOVA analysis shows no significant change. C) Stiffness of AIGe (pink) and AI-RGD-Ge (purple). N=3. Two-way ANOVA analysis. $P < 0.005$ 92

Fig. 2.11. Organoids derived using vocal fold fibroblasts as feeder cells on day 5. A) representative brightfield image. Magnification 4X. Scale Bar 500 μm . B) Immunofluorescence images. Red-F-actin. Blue-Nuclei. Magnification 10X. Scale Bar 100 μm 93

Fig. 2.12. Effect of cell medium on lung organoid culture over time. Representative images. Red-F-actin. Blue-Nuclei. Magnification 10X. Scale Bar 500 μm 94

Figure 2.13 Representative microphotographs of LOi using Transmission Electron Microscopy at 3300X Magnification. Scale Bar 5 μm . Arrows point to signs of autophagy. 95

Figure 2.14 Representative microphotographs of LOi using Transmission Electron Microscopy at 5500X Magnification. Scale Bar 2 μm 95

Figure 2.15 Representative microphotographs of LOi using Transmission Electron Microscopy at 7000 X Magnification. Scale Bar 2 μm 96

Figure 2.17 Representative microphotographs of LOi using Transmission Electron Microscopy at 11000 X Magnification. Scale Bar 1 μm 97

Fig. 2. 18. Overview of LOi at 21 days of culture using FIB microscopy. A) Magnification 10 X. Scale Bar 237.8 μm . B-E) Magnification 20 X. B) Scale Bar 118.9 μm C) Scale Bar 118.9 μm D) Scale Bar 59.4 μm E) Scale Bar 59. 4 μm 98

Fig. 2. 19 Microphotographs of airway epithelial cells forming an organoid structure. Visualized with FIB microscopy. Magnification 40X. Scale Bar 59.4 μm 98

Figure 2.20 Microphotographs of LOi at day 21 using FIB microscopy. A) Magnification 500X. B) Scale Bar 598X. Scale Bar 50 μm . Arrows indicate the airway epithelial cells in a tube-like structure..... 100

Figure 2.21 Microphotographs of LOi at day 21 using FIB microscopy with magnifications exceeding 1000X. The images reveal multilayers of airway epithelial cells exhibiting distinct morphologies, contributing to the formation of the organoid structure. Scale Bar 40 μm . A) Magnification 1069X. B-D) Magnification 1076X. E) Magnification 1087X..... 101

Figure 2.22 Microphotographs of LOi at day 21 using FIB microscopy with magnifications of A) 2000X and B) 3500X. Scale Bar 20 μm 101

Figure 2.23 Microphotographs of LOi at day 21 using FIB microscopy with magnifications of 5000X. Scale Bar 5 μm . Arrows indicate microvilli structures..... 102

Figure 2.24 Microphotographs of LOi at day 21 using FIB microscopy with magnifications of A) 8000X and B) 10000X. Scale Bar 5 μm . Arrows indicate microvilli structures. 102

Fig. 2.25 Bioprinting lung organoids. A) Schematic representing the overall protocol. Generated by Bio Render. B) AlGe droplet with 2 mm of height. C) Representative lung ‘organoid’ on day 21. Magnification 2X. D) Robustness of ‘organoids’ which can be handled with tweezers. E) Lung ‘organoids’ growth on spinning bioreactor. F) Organoids were retrieved after being cultured on a spinning bioreactor for 21 days. 105

Fig. 2.26 Lung organoid fabrication flow chart using bioprinting..... 116

Figure 3.1. Used markers for the identification of major and rare cell types in the lung, in either the proximal or the distal region. 119

Figure 3.2. RNA sequencing data showing proximal (A) and distal (B) markers of LOp, fibroblasts monolayers, and primary bronchial epithelial cells, respectively, in air-liquid-interface. N=3. Multiple T-test comparison, p.adjust <0.05 in comparison to IMR-90*, and in comparison to HBE*. 121

Figure 3.3 Flow cytometry to confirm AT2 cells of organoids derived by primary cells LOp. a-c) Percentage of SFTPC+ (AF594) cells detected in each organoid. d) Fluorescence minus one (FMO) 594 was used to calibrate the instrument. N=3 122

Figure 3.4. Functional enrichment analysis of genes with major change between cell monolayers and organoids (LOp) ($p_{adj} < 0.01$) using G: Profiler. Abbreviations: MF- Molecular Function, BP: Biological Process. CC-Cellular Component. KEGG-Kyoto Encyclopedia of Genes and Genomes. REAC - Reactome pathways. WP – WikiPathways. TF - Transcription factor binding site predictions. MIRNA - mirTarBase miRNA targets. HPA - Human Protein Atlas expression data. CORUM - Manually annotated protein complexes from mammalian organisms. HP - Human Phenotype Ontology, a standardized vocabulary of phenotypic abnormalities encountered in human disease. The display set of terms was selected according to their association with the lung, tissue development, and cell differentiation. 123

Fig. 3.5 Heatmap showing genes associated with respiratory system development pathway: Gene Ontology :0060541. Differential expressed genes analysis, comparing cell monolayers (HBE, IMR-90) and LOp, ($p_{adj} < 0.01$ & $abs(\log_2 \text{ Fold Change shrink} \Rightarrow 4)$). 125

Figure 3.6 Heatmap showing genes associated with tube development pathway: GO: 0035295. Differential expressed genes analysis, comparing cell monolayers (HBE, IMR-90) and LOp, ($p_{adj} < 0.01$ & $abs(\log_2 \text{ Fold change shrink} \Rightarrow 4)$). 126

Figure 3.7. Heatmap showing genes associated with alveolus development in all samples. Differential expressed genes analysis, comparing cell monolayers (HBE, IMR-90) and LOp, ($p_{adj} < 0.01$ & $abs(\log_2 \text{ Fold Change shrink} \Rightarrow 4)$). 127

Fig. 3.8 Characterization of lung organoids derived from immortal bronchial epithelial cells (LOi). A) RNA sequencing data showing markers of proximal cells of the lung including rare cell types in epithelial cell monolayers, fibroblasts, and derived organoids.

B) RNA sequencing data showing distal markers of cells of the lung. A-B) N=3. Multiple T-test comparisons, * p. adjust <0.05 in respect to IMR-90, *p. adjust <0.05 in respect to CFBE. C) Image of LOp organoid on day 21, showing distal markers of the lung. Red-SFTPC, Green-SFTPb. Blue-Nuclei. Magnification 10 X. Scale Bar 500 μm..... 130

Fig.3.9. Functional Enrichment analysis of genes with major change between cell monolayers and immortalized derived organoids (p adj.<0.01) by G: Profiler. Abbreviations: MF-Molecular Function, BP: Biological Process. CC-Cellular Component. KEGG- Kyoto Encyclopedia of Genes and Genomes. REAC - Reactome pathways. WP – WikiPathways. TF - Transfac transcription factor binding site predictions. MIRNA - mirTarBase miRNA targets. HPA - Human Protein Atlas expression data. CORUM - Manually annotated protein complexes from mammalian organisms. HP - Human Phenotype Ontology, a standardized vocabulary of phenotypic abnormalities encountered in human disease. 131

Fig. 3.10 Heatmap of genes associated with “epithelial tube branching involved in lung morphogenesis” Red shows up-regulation. Abundances grouped linked by Average. 132

Fig. 3.11 Genes associated with lung phenotype. Gene expression using qPCR in CFBE (pink) and LOi (white). SFTPb upregulated in organoids in comparison to CFBE. N=3. *p<0.05. 133

Fig. 3.12. Flow cytometry to evaluate the number of cells expressing SFTPC+ into organoids derived by immortalized cells. a-c) Percentage of SFTPC+ (AF594) cells detected in each organoid. d) Fluorescence minus one (FMO) 594 was used to calibrate the instrument. N=3..... 133

Fig. 3.13 Principal component analysis of cell monolayers, organoids, and tissues. Orange-primary bronchial epithelial cells. Blue-immortalized epithelial cells. Green-Fibroblasts. Purple-Lung organoids derived from primary cells (LOp). Red-Lung organoids derived from immortal cell lines (LOi). Grey-Lung Tissue from superior region. Pink-Lung Tissue from inferior region..... 135

Fig. 3.14 UpSet plot showing the proteomic profile of lung organoids derived by primary cells (LOp), and cell lines. A) Venn diagram comparing the number of proteins in LOp, IMR-90, and HBE. N=3. 136

Fig. 3.15 Section of heatmap (cluster 2) showing upregulated proteins in LOp in comparison to cell monolayers. Abundances grouped, linked by average. Red show upregulation and blue downregulation. N=3..... 137

Fig. 3.16 Upregulated proteins in LOp with high specificity to the lung showing connections on pathways. Generated by STRING. Pathways colors: Blue-from curated database, Pink-\experimentally determined. Green-Gene neighborhood. Red-Gene fusions. Blue-Gene co-occurrence. Yellow-Textmining. Black co-expression. Dark blue: protein homology..... 138

Fig. 3.17 Subset of proteins from the immune system upregulated in LOp organoids in comparison to cell lines. Generated by STRING. Pathways colors: Blue-from curated database, Pink-experimentally determined. Green-Gene neighborhood. Red-Gene fusions. Blue-Gene co-occurrence. Yellow-Textmining. Black co-expression. Dark blue: protein homology..... 139

Fig.3.18 Overrepresented terms from upregulated proteins (cluster 2) in LOp using gene ontology..... 141

Fig. 3.19 Volcano Plot shows the upregulated proteins in LOp (in red) and the downregulated proteins (blue) in comparison to pHBE monolayers. Generated by VolcaNoseR 142

Fig. 3.20. UpSet plot showing the proteomic profile of lung organoids derived by immortalized cells (LOi) and cell lines. 144

Fig. 3.21 Section of heatmap (cluster 3) showing upregulated proteins in LOi in comparison to cell monolayers. Abundances grouped, linked by average. Red show upregulation and blue downregulation. N=3..... 145

Fig. 3.22 Overrepresented terms from upregulated proteins (cluster 3) in LOi using gene ontology..... 146

Fig. 3.23 Comparison of proteomic profile of each type of lung organoids (LOp) and LOi. Volcano Plot generated by VolcaNoseR. Red upregulated proteins in LOp, Grey-unchanged proteins between samples. Blue-downregulated proteins in LOp. 147

Fig. 3.24 Heatmap showing the regulation of proteins in lung organoids (LOp and LOi) and adult lung tissues (Inferior and Superior). Abundances grouped, linked by average. Red show upregulation and blue downregulation. N=3 149

Fig. 3.25 Cluster 1 of heatmap showing the regulation of proteins in lung organoids (LOp and LOi) and adult lung tissues (Inferior and Superior). Abundances grouped, linked by average. Red show upregulation and blue downregulation. N=3 150

Fig. 3.26 UpSet plots visualizing the proteins shared between adult lung tissues and LOp (A) or LOi (B). 151

Fig. 3.27 Overrepresented terms from upregulated proteins in LOp and lung tissues (cluster 1), adult lung tissues (cluster 3) and lung organoids (cluster 6)..... 153

Fig. 3.28. Schematic showing the pipeline of proteomics analysis of cell monolayers, organoids, and adult lung tissues..... 163

Fig. 4.1 Schematics showing the structure of Coronaviruses and Influenza. Images modified from: Online Biology Notes: Influenza Virus (Influenza virus-Structure, Types, Nomenclature, Transmission, Pathogenesis, Diseases, Diagnosis and Treatment - Online Biology Notes) and Biophysical Society: Coronavirus Structure, Vaccine and Therapy Development (Coronavirus Structure, Vaccine and Therapy Development (biophysics.org)..... 169

Fig. 4.2 Viral tropism of influenza and SARS-CoV-2. Image obtained with permission from¹³⁷ (License number: 5764260448937). 171

Fig. 4.3 Expression of genes associated with critical illness of patients with SAR-CoV-2 on organoids and adult lung tissues. T-tests (LOp and LOi) * p. adjust<0.05. N=3. Upregulation shown in blue. 174

Fig. 4.4 Expression of interferon induced transmembrane genes associated with restriction of entry of viral pathogens SAR-CoV-2 on organoids and adult lung tissues. T-test (LOp vs LOi) adjust <0.05 in all comparisons. N=3. Upregulation shown in blue. 175

Fig. 4.5 Expression of human host factors required for influenza, classified in three different pathways. A) Coat Protein Complex I. B) Phosphoinositide 3-kinase- Protein kinase C. C) Endosomal uptake, maturation, acidification, and fusion. T-test (LOp vs LOi) *p adjust<0.05. N=3. Upregulation shown in blue..... 177

Fig. 4.6 Entry and priming mechanisms of respiratory viruses on organoids. A) Comparison between bulk RNA sequencing of proteins relevant to infection on

organoids and adult lung tissues. T-test (LOp vs LOi) *p. adjust <0.05 N=3. Upregulation shown in blue. B) Expression of ACE2, and TMPRSS2 on LOi and CFBE at day 21 using RT-qPCR. N=3. Two-way ANOVA *p<0.05. C) Representative images of LOi at day 7 expressing TMPRSS2, and ACE2, respectively. Magnification 10X. Scale Bar 100 μ m..... 179

Fig. 4.7. Representative viral titer (PFU/ml) on supernatant of infected organoids with influenza H3N2 (A) or H1N1 (B) at 24 and 48 hpi. N=3. ***p<0.005. Panel B shows representative plaque assay results obtained after inoculated serial viral dilutions in MDCK cells. 180

Fig. 4.8 Nucleocapsid protein load (log) in organoid lysate after 24 hpi, and 48 hpi of influenza H1N1-PR-8. N=3..... 181

Fig. 4.9 Viral copies /ml (log₁₀) on supernatant of organoids under MOI: 0.01 and 0.001 SARS-CoV-2 infected-purple, and non-infected-black, 24 hpi and 48 hpi (n=3). Two-way ANOVA p<0.0001 in all comparisons. 182

Fig. 4.10 Viral copies/ml (log₁₀) on cell lysate of organoids MOI: 0.01 and 0.001 SARS-CoV-2 infected-purple, and non-infected-black, 24 hpi and 48 hpi (n=3). Two-way ANOVA p<0.05 in every condition. LOD: Limit of detection. 183

Fig. 4.11 Brightfield pictures of airway epithelium cultured along different density of fibroblasts and Geltrex at day 7. No organoid formation was achieved under these conditions. A) 1 fibroblast per 2 epithelial cells. B) 1 fibroblast per 3 epithelial cells. Red arrows pointing airway epithelium. Magnification 10X. Scale Bar 100 μ m. 184

Fig. 4.12. Airway epithelial cells from an asthma donor cultured along with fibroblasts in “low” density. Final ration 10:1. Initially, some cells grouped together, but cell shedding,

and abnormal morphology was observed on day 14. Magnification 10X. Scale Bar 500 μm . Images processed with ImageJ using the tool “Enhance contrast”. 185

Fig. 4.13. Asthmatic airway epithelial cells cultured without fibroblasts on day 3. Elongations and bifurcations were observed. Magnification 10X. Scale Bar 500 μm . Images processed with ImageJ using the tool “Enhance contrast”. 185

Fig. 4.14. Asthmatic airway epithelial cells cultured without fibroblasts on day 6. Cell disassociation from the main structure was observed, shown in red squares. Magnification 10X. Scale Bar 500 μm . Images processed with ImageJ using the tool “Enhance contrast” 186

Fig. 4.15 asthmatic airway epithelial cells cultured without fibroblasts on day 11 and day 14. Structures are broken, and spheres like structures remain. Magnification 10X. Scale Bar 500 μm . Images processed with ImageJ using the tool “Enhance contrast”. 186

Fig. 4.16. Representative images of asthmatic organoids achieved by incorporation of IL-10 into the medium. No fibroblasts were incorporated into the culture. Magnification 10X. Scale Bar 500 μm 187

Fig. 4.17. Airway epithelial cells cultured with fibroblasts in 10:1 ratio in a medium supplemented with IL-10. Magnification 10X. Scale Bar 500 μm 188

Fig. 4.18. Viral infection of organoids with SARS-CoV-2. Organoid culture medium is substituted by viral solution in serum free media, during an absorption time of 3 h. Afterwards, the viral inoculum is removed and substituted by fresh medium. Infected organoids are cultured during 24 and 48 h at 37°C. Finally, supernatant and organoids are harvested for further analysis. Created with Mind the Graph. 193

Fig. 4.19. Plaque assay pipeline. Serial viral dilutions are made with the supernatant of infected organoids. These viral dilutions are used to infect MDCK cell monolayers during an absorption time of 1 hour. Media containing TPCK is used to cover cell monolayers for 72 h. MCDK are fixed with crystal violet to expose plaques. 196

Fig. 5.1 Potential strategy to increase complexity of lung organoids. Monocytes (THP-1) were cultured on top of 8 µm porous membranes using two different cell densities: 1:1000, and 1:10000, in relationship to airway epithelial cells (CFBE) during 24 h or 72 h after 4 days post organoid formation. Red arrows show cell debris from the main structure. Magnification 10X. Scale Bar 500 µm. 208

Figure A.1 Complete heatmap of proteins upregulated in LOp (cluster 2) in respect to cell monolayers HBE, IMR-90. Abundances grouped, linked by average. Red show upregulation and blue downregulation. N=3. 229

Figure A.3. Proteins downregulated in LOp in comparison to HBE. Color code: Pink-Lung. Yellow-Respiratory chain complex. Green-ATP. Generated by STRING. Pathways colors: Blue-from curated database, Pink-experimentally determined. Green-Gene neighborhood. Red-Gene fusions. Blue-Gene co-occurrence. Yellow-Textmining. Black co-expression. Dark blue: protein homology. 231

Figure A.4 Complete heatmap of proteins upregulated in LOi (cluster 3) in respect to cell monolayers CFBE, IMR-90. Abundances grouped, linked by average. Red show upregulation and blue downregulation. N=3. 232

Figure A.5 Complete heatmap of proteins in cell monolayers CFBE, IMR-90 and LOi organoids. Cluster 3, correspond to the proteins upregulated in the organoid.

Abundances grouped, linked by average. Red show upregulation and blue downregulation. N=3. 233

Fig. A6 Proteins upregulated in LOi in comparison to cell monolayers with specificity to the lung-red, and immune system-purple. Generated by STRING. Pathways colors: Blue-from curated database, Pink-experimentally determined. Green-Gene neighborhood. Red-Gene fusions. Blue-Gene co-occurrence. Yellow-Text mining. Black co-expression. Dark blue: protein homology. 234

Fig. A7 Proteins upregulated in LOp in comparison to LOi. Lung-Orange. Respiratory System-Purple. Throat-Green. Response to Stimulus-Pink. **Tissue development-Yellow**. Cell differentiation-Turquoise. Dark yellow-viral entry host cell. Generated by String. Pathways colors: Blue-from curated database, Pink-experimentally determined. Green-Gene neighborhood. Red-Gene fusions. Blue-Gene co-occurrence. Yellow-Textmining. Black co-expression. Dark blue: protein homology. 235

Contribution of original knowledge

In this section a list of journal articles and conference proceedings published by the author during her doctoral studies is presented in chronological order.

Peer-review journal articles

1. **Alicia Reyes Valenzuela**, Mark Turner, Nathan Makarian, Christophe Lachance-Brais, Charlotte Fouquet, Silvia Vidal, John Hanrahan, Luc Mongeau, “Fabrication and analysis of heterogenous lung organoids derived from adult bronchial cells and fetal fibroblasts for SARS-CoV-2 infection.” **Under review. 2024**

Contributions: This article reports the highlights of the present dissertation.

Alicia Reyes Valenzuela conceived the idea, developed the outline, designed the experiments, conducted such experiments, analyzed the results, and drafted the manuscript.

2. Christophe Lachance Brais+, Chihyu Yao+, **Alicia Reyes Valenzuela**, Jathavan Asohan, Elizabeth Guettler, Hanadi Sleiman. “Exceptional Nuclease Resistance Induced in DNA and RNA Through the Addition of Inexpensive Nucleobase Mimic.” JACS. **Accepted. 2023**

Contributions: Alicia Reyes Valenzuela performed the viability and morphological analysis of epithelial cells. She analyzed the results and write the respective section on the paper.

3. **Alicia Reyes**, Guangyu Bao, Abigail Vikstrom, Luc Mongeau, Satya Prakash. “Polymeric microspheres containing human vocal fold fibroblasts for the regeneration of vocal fold lamina propria: Preparation and In vitro analysis”. The Laryngoscope. **Published 2020**.

Contributions: Alicia Reyes Valenzuela conceived the idea, created alginate microspheres by electroporation, encapsulated cells, and evaluated the biocompatibility and mechanical properties of the substrate.

4. Guangyu Bao, Tao Jiang, Hossein Ravanbakhsh, **Alicia Reyes**, Zhenwei Ma, Mitchell Strong, Huijie Wang, Joseph M. Kinsella, Jianyu Li, and Luc Mongeau. “Triggered Micropore Forming Bioprinting of Porous Viscoelastic Hydrogels” Science Advances. **Published. 2020**.

Contributions: Alicia Reyes Valenzuela performed the morphological analysis of cells in response to hydrogel over time.

Journal articles in preparation.

1. **Alicia Reyes Valenzuela**, Lan Anh Huynh, Cameron Hastie, Luc Mongeau. “Next Generation of bioprinted Lung Organoids: Expanding Possibilities with High Throughput” **Under Preparation**.

2. Alicia Reyes Valenzuela, Virginie Calderon, Ludovic Malet, Luc Mongeau. "A quantitative comparison of existing lung organoids using RNA sequencing."

Under Preparation.

3. **Alicia Reyes Valenzuela**, Charlotte Fouquet, Priya Nagpal, Nathan Makarian, Silvia Vidal, Luc Mongeau. "Lung multi-cellular organoids to model infectivity of Influenza type A and seasonal coronaviruses". **Under preparation.**

Patents and disclosures

1. **Alicia Reyes Valenzuela**, Luc Mongeau. Mark Turner. Silvia Vidal. Guangyu Bao. "Microfluidic Lung Organoid for High Throughput drug Screening" No. 63/500,144. 2023.

2. Ravanbakhsh, H., Mohammadi, S., Mongeau, L., Bao, G., **Reyes, Alicia**, "Novel Method for the Fabrication of Hydrogel Microparticles using Microfluidics". 2020.

Peer-reviewed conferences proceedings

1. **Alicia Reyes Valenzuela**, Luc Mongeau. "Tandem Mass Tags of lung organoids unveil upregulation and expression of lung associated proteins in comparison to cell monolayers." Proteomics in Cell Biology and Disease Mechanisms. Heidelberg. Germany 25-27 October 2023. Oral and poster presentation.

2. **Alicia Reyes Valenzuela**. Mark Turner, Silvia Vidal, Luc Mongeau. "From bronchial adult cells to lower respiratory tract organoids: A multicellular leap towards enhanced disease modeling" Organoids: modelling organ development and disease in 3D culture. Heidelberg. Germany. 18-23 October 2023. Poster Presentation.
3. **Alicia Reyes Valenzuela**, Luc Mongeau. "Generation and Characterization of heterogenous lung organoids derived from adult bronchial cells and fetal fibroblasts" Voice Foundation. USA. 2023. Oral Presentation
4. **Alicia Reyes Valenzuela**, Mark Turner, Silvia Vidal, Luc Mongeau. "Rapidly Generated Lung Organoids as a Physiologically Relevant In-Vitro Model for Studying Respiratory Viral Infections and Host-Virus Interactions" Biomedical Engineering Society Annual Meeting. Seattle. USA. 11-14 October 2023. Poster Presentation.
5. Lan Anh Huynh, **Alicia Reyes Valenzuela**, Luc Mongeau. "Simplistic High-throughput Bioprinting of Lung Organoids". McGill University. SURE Project. Montreal. Canada. 2023.
6. **Alicia Reyes Valenzuela**. Luc Mongeau. Silvia Vidal. "Generation and characterization of lower respiratory tract multicellular organoids derived by adult

bronchial cells” Infectious Disease and Immunity in Global Health (IDIGH). Montreal, Canada. 5 May. 2023. Oral Presentation.

7. **Alicia Reyes Valenzuela**, Luc Mongeau. “Lung Organoids Derived by Multiple Cellular Interactions into hydrogel substrates mimic the lower respiratory tract’s morphogenesis, structure and breathing function by induction of Surfactant Protein B.” Lung In Vitro Event (LIVE). Nice, France. 2022. Oral Presentation.
8. **Alicia Reyes Valenzuela**. Mark Turner, Silvia Vidal, John Hanrahan, Luc Mongeau^{1,4} “Generation of Macro-Scale and Mature Lung Organoids Through Engineering Cell Microenvironment”. TERMIS Conference. Toronto. 2022. Poster Presentation.
9. Ravanbakhsh, H., Mohammadi, S., Bao, G., Tang, G., Taheri, F., **Reyes, Alicia.**, and Mongeau, L., "Microfluidic-based Fabrication of Hydrogel Microspheres with a Controllable Size Using an Oil-free Approach", TERMIS World Conference, Maastricht, Netherlands, Nov. 2021.
10. **Alicia Reyes Valenzuela**, Luc Mongeau. “Engineering cell microenvironment for lung organoids”. iPSC Seminars: Early Drug Discovery Unit (EDDU). Montreal, Canada. 2021. Oral presentation.
11. **Alicia Reyes Valenzuela**. Luc Mongeau. “Morphological evaluation of airway epithelium and fibroblasts using biinks for 3D culture”. Innovative Science Without Animals. John Hopkins. June 2020. Virtual Oral Presentation.

12. Alicia Reyes Valenzuela. Guangyu Bao, Karen Kost, Satya Prakash, Luc Mongeau. "Polymeric microspheres containing human vocal fold fibroblasts for vocal fold lamina propria regeneration: Preparation and In-Vitro Analysis". COSM. Atlanta. Virtual. 2020. Oral and poster presentation.

Abbreviations

2D Two dimensional	C14 Cytokeratin 14
3D Three dimensional	CALCA Calcitonin related polypeptide alpha
ACE2 Angiotensin-converting enzyme 2	CC Cellular Component
AKAP5 A-Kinase Anchoring Protein 5	CCL2 Chemokine C-C motif ligand 2
AQP5 Aquaporin 5	CFBE Cystic Fibrosis derived Bronchial Epithelium
AGER Advanced Glycosylation End-product specific Receptor	COPD Chronic Obstructive Pulmonary Disease
AIge Alginate Gelatine	COPI Coat Protein Complex I
ALI Air Liquid Interface	COVID-19 Coronavirus 19 pandemic
Alox5ap Arachidonate 5-lipoxygenase activating protein	CMC Carboxymethyl cellulose
ASC adult stem cells	DKK1 Dickkopf1
ASCL1 Achaete-Scute homolog 1	DPP9 Dipeptidyl peptidase 9
ASM Airway Smooth Muscle	DMEM Dulbecco's Modified Eagle Medium
AT1 Alveolar type I cells	DNA Deoxyribonucleic acid
AT2 Alveolar type II cells	dNTP Deoxynucleotide triphosphate
ATP6AP1 ATPase H ⁺ Transporting Accessory Protein 1	E embryonic days
ATP6V0B ATPase H ⁺ Transporting V0 Subunit B	FGF Fibroblast Growth Factor
ATP6V0C ATPase H ⁺ Transporting V0 Subunit C	FIB Focused Ion Beam Microscopy
ATP6V1A ATPase H ⁺ Transporting V1 Subunit A	FOXJ1 Forkhead box protein J1
ATP6V1B2 ATPase H ⁺ Transporting V1 Subunit B2	FOXP4 Forkhead box protein P4
BMZ Base Membrane Zone proteins	FURIN Paired basic Amino acid Cleaving Enzyme
BNC1 Zinc finger protein basoonuclin-1	GeIMA Gelatin methacryloyl
BP Biological process	GO Gene Ontology
	GM-CSF Granulocyte-macrophage colony-stimulating factor

GRAMD 2A GRAM domain containing 2A
HA Haemagglutini
HBE Human Bronchial Epithelial Cells
HCoV Human Coronavirus
HMVECS human microvasculature endothelial cells
HOPX Homeodomain-only protein
HPA Human Protein Atlas expression data
Hpi H post infection
IL-4 Interleukin 4
IL-5 Interleukin 5
IL-6 Interleukin 6
IL-10 Interleukin 10
IL-13 Interleukin 13
IL-25 Interleukin 25
iPSC induced Pluripotent Stem Cells
IAV Influenza A virus
IBV Influenza B Virus
ICV Influenza C Virus
IDV Influenza D Virus
IFNAR1 Interferon-alpha/beta receptor alpha chain 1
IFNAR2 Interferon-alpha/beta receptor alpha chain 2'
IFTM1 Interferon Induced Transmembrane 1
IFITM2 Interferon Induced Transmembrane 2
IFITM3 Interferon Induced Transmembrane 3

IP3-PCK Phosphoinositide 3-kinase- Protein kinase C
KEGG Kyoto Encyclopedia of Genes and Genomes
KRT5 Keratin 5
RT-qPCR Real Time quantitative Polymerase Chain Reaction
LPS Lipopolysaccharide
LRT Lower Respiratory Tract
LO Lung organoids
LOD Limit of detection
LOi Lung organoids derived from immortal cell lines
LOp Lung organoids derived from primary cells
MANC Mesenchymal Alveolar Niche Cells
MEM Minimum Essential Medium Eagle
MERS Middle East respiratory syndrome
MDCK Madin-Darby canine kidney
MIRNA mirTarBase miRNA targets
MF Molecular Function
MOI Multiplicity of Infection
MUC15 Mucin 15, cell surface associated
MUC2 Mucin 2, oligomeric mucus gel-forming
MUC5AC Mucin 5AC, oligomeric mucus gel-forming
MUC5B Mucin 5B, oligomeric mucus gel-forming

NA neuraminidase

NKX2 NK homeobox 2

Ng nanogram

N-MYC N-myc proto-oncogene

NP Nucleocapsid protein

OAS Oligoadenylate synthetase

OAS1 Oligoadenylate Synthetase 1

OAS2 Oligoadenylate Synthetase 2

OAS3 2'-5'-Oligoadenylate Synthetase 3

OG Original cell density

P postnatal days

P63 Tumor protein p63

Pa Pascals

p.adj adjusted p value

PC Principal Component

Pcw post-conception weeks

PDGFR α platelet-derived growth factor- α

PDMS Polydimethylsiloxane

PDPN Podoplanin

PET polyethylene terephthalate

PNES Pulmonary Neuroendocrinal Cells

POU2F3 POU class 2 homeobox 3

REAC Reactome pathways

RGD Arginine-Glycine-Aspartic Acid.

RNA Ribonucleic acid

ROCK1 Rho Associated Coiled-Coil Containing Protein Kinase

Rpm Revolutions per minute

SARS-CoV Severe acute respiratory syndrome coronavirus

SARS-CoV-2 severe acute respiratory syndrome coronavirus 2

SCGB1A1 Secretoglobin family 1A member 1

SCGB3A2 Secretoglobin family 2A member 2

SCNN1G Sodium Channel epithelial 1 subunit Gamma

SFTPA1 pulmonary Surfactant-associated protein A1

SFTPB Surfactant protein B

SFTPC Surfactant protein C

SFTPD Surfactant protein D

SLC6A2 Solute carrier family 6 member 2

SMC small smooth muscle cells

SOX2 SRY-box transcription factor 2

SOX9 SRY-box transcription factor 9

TEM Transmission Electron Microscopy

TF Transfect transcription factor binding site predictions

TMT Tandem Mass Tags

Trpm5 Transient receptor potential cation channel subfamily M member 5

TMPRSS2 Transmembrane Serine Protease 2

TPCK Tosyl phenylalanyl chloromethyl ketone (TPCK)-treated trypsin

TYK2 Tyrosine Kinase 2

USE1 SNARE In the ER 1

VEGF Vascular endothelial growth factor

WP Wiki Pathways

Chapter 1: Introduction

1.1 Introduction Outline

Over the ages, one of the most pivotal features of evolution of vertebrates has been the acquisition of lungs, allowing life above the water, breathing and the disposal of waste products such as carbon dioxide^{1,2}. To maintain their core function of gas exchange with the cardiovascular system, the lungs require critical cellular interactions¹. This chapter describes the cellular complexity of the lungs and its functions. One focus is the molecular regulation of lung development through branching morphogenesis, a highly regulated and repetitive process in which an arborized network is generated³. The limitations of animal models and 2D cell monolayers for the study of human lung development, function and diseases are stated, in particular on the differences between human and mouse lungs. Lung organoids constitute a promising alternative to animal models for drug testing. The state of the art of lung organoids is described. Finally, the rationale and objectives of the present study are stated.

1.2 The cellular complexity of human lungs

The lower respiratory tract (LRT) is a complex system comprising bronchi, themselves branching out into bronchioles terminated with alveoli⁴. The functions of these distinct anatomical structures are enabled by a heterogeneous cell population, featuring at least 58 recognizable phenotypes populating both the proximal (bronchi) and distal (bronchiole, and alveoli)⁵⁻⁷ lung regions (Fig 1.1. Fig. 1.2). Within the proximal region, epithelial cell sub-types such as goblet, basal and ciliated cells contribute to innate immunity functions such as mucociliary clearance (Fig 1 B). Mucins, secreted by goblet

cells, trap inhaled pathogens. These are then removed through the coordinated beating of cilia on ciliated cells, thus preventing pathogens from reaching the distal regions of the lungs⁵. Airway epithelial cells produce and release cytokines directly, in response to pathogens. Cytokines promote the recruitment of immune cells, thereby initiating the immune response.^{8,9} Basal cells constitute a pool of adult stem cells. They play a leading role in lung regeneration following injury¹⁰. Rare cell types are also found, in small number, in the proximal airways, including pulmonary neuroendocrinal cells (PNEC), Tuft cells and Ionocytes. Pulmonary neuroendocrinal cells influence smooth muscle tone and regulate immune responses¹. They can detect hypoxic conditions and communicate with immune and nervous systems. They also have stem cell properties, in particular in pathological conditions¹¹. Brush or Tuft cells, may have important adaptive immunomodulation functions¹². Ionocytes are associated with liquid absorption and salt in the airways¹³.

The distal airways are formed by bronchioles and alveolar ducts (Fig.1A-Fig.1.2) which ultimately connect to alveolar sacs populated by type I (AT1) and type II cells (AT2)^{5,7,8}. Bronchioles are lined with secretory cells that express the SCGB3A2 protein. These cells serve as progenitors for alveolar cells⁸. The gas exchange between air and blood is performed by AT1 cells; it is also facilitated by AT2 cells through the production of surfactant proteins⁴. Acting as stem cells within the alveolar region, AT2 cells can self-renew and generate AT1 cells via alveologensis^{5,14}.

Fibroblasts are found abundantly within both proximal and distal regions of the lungs. They support the maintenance and survival of AT2 and basal cells through the secretion of Fibroblast Growth Factor^{5,15}. They synthesize extracellular matrix (ECM) proteins,

which are vital to efficient gas exchange. Fibroblasts support multiple cellular functions⁵. They regulate lung morphogenesis during fetal development^{5,16}. They also perform immune functions, such as antigen presentation and bioactive molecules secretion¹⁵. The pulmonary immune response maintains a delicate balance between defense and gas exchange functions, ensuring efficient clearance of pathogens and pollutants. Such balance minimizes inflammation and tissue damage, preserving the respiratory system's integrity and gas exchange efficiency¹⁷.

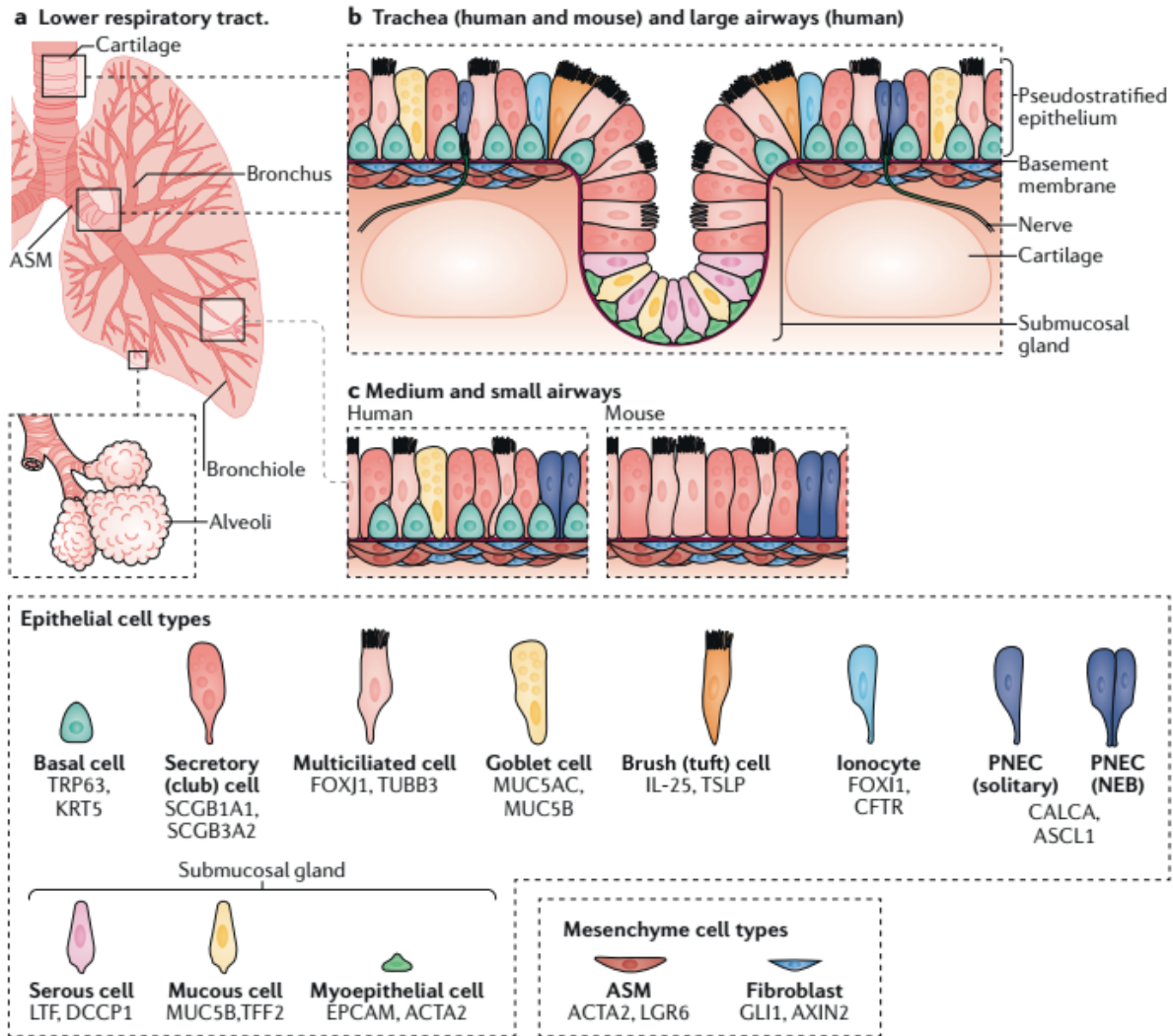


Fig. 1.1 Cellular composition of lower respiratory tract in humans and mice. The lower respiratory tract contains multiple epithelial cell types, which are underlined with heterogeneous mesenchymal cells, including fibroblasts and airway smooth muscle cells (ASM). These cells provide extracellular matrix proteins and ligands, which modulate epithelial cell differentiation and control airway tube diameter. A) Schematic of the lower respiratory tract consisting of trachea and lungs, which are further subdivided into proximal (bronchi) and distal regions composed of bronchioles and alveoli. B) Schematic of large airways composed of trachea, and bronchi. Multiple epithelial cell types line up these regions, including basal cells, secretory cells, ciliated cells, and goblet cells. Other rare epithelial cell types such as brush cells, ionocytes, pulmonary neuroendocrine cells (PNEC), and neuroendocrine bodies (NEB) are also found in these regions. Large airways harbor cartilaginous rings and submucosal glands containing serous cells, mucous cell, and myoepithelial cells. C) Schematic of the small airways in humans and mice and representative cells within it. Mice airways are distinct from those of humans. The former ones lack basal and goblet cells. Image obtained with permission of ¹ (License number: 5764250306282).

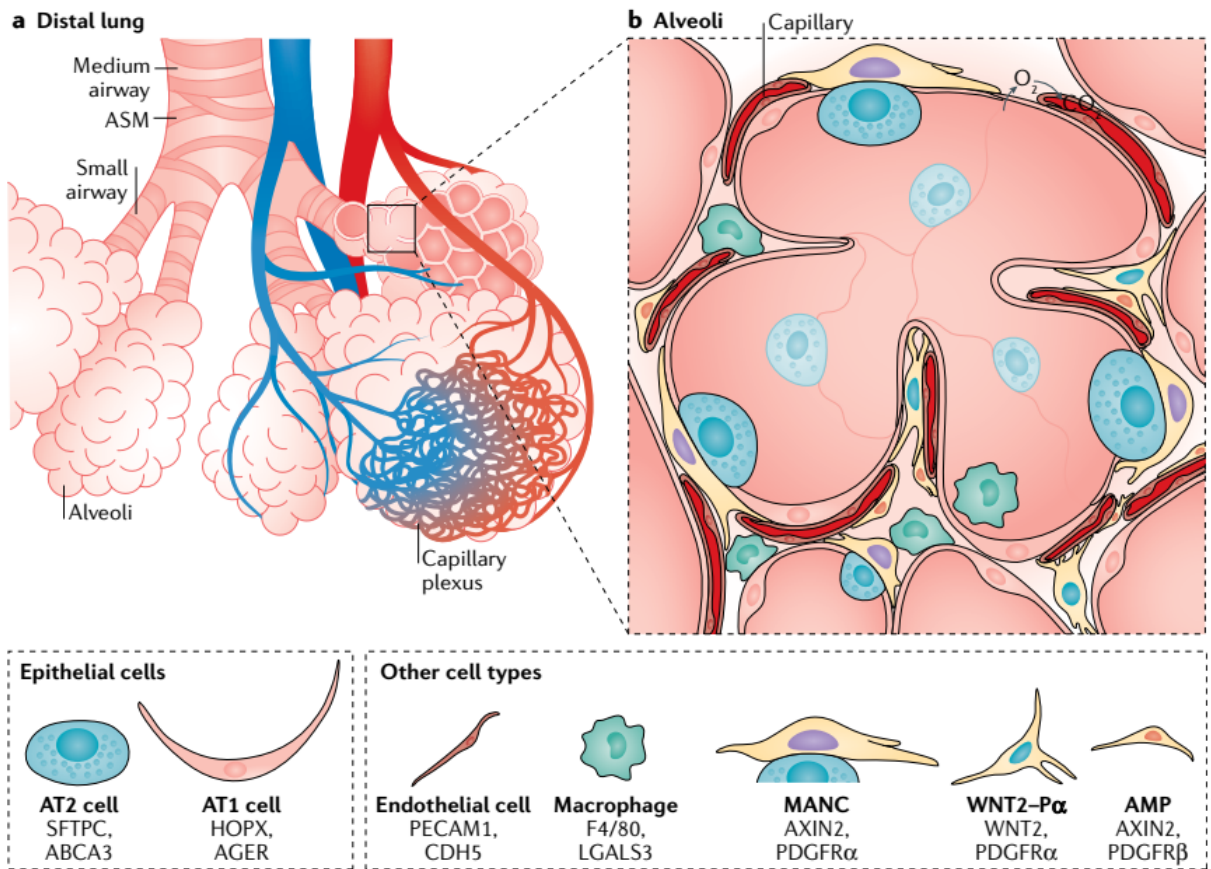


Fig. 1.2 Cellular composition of distal lung, in particular alveoli. A) Schematic showing the breathing process in small airways. Inhaled air is circulated, and oxygen and CO₂ exchange occurs within the endothelial capillary plexus. B) The alveoli are composed of two types of epithelial cells, alveolar type 1 (AT1) and alveolar type 2 (AT2) cells. In AT1 the gas exchange occurs, while AT2 produces surfactant proteins which help the breathing process, preventing the alveolus from collapsing. Other abundant cell types are the mesenchymal alveolar niche cells (MANC). They support alveolar structures, epithelial proliferation, and differentiation. Interstitial fibroblast expressing Axin-2-positive myogenic precursors (AMPs) and Wnt2 expressing platelet-derived growth factor- α (PDGFR α) are subtypes of MANC. Immune cells, specifically interstitial macrophages, are part of the alveolar microenvironment. Image obtained with permission of ¹ (License number: 5764250306282).

1. 3 Molecular mechanisms for lung development and branching morphogenesis.

The development of the human LRT requires the interaction between airway epithelium and mesenchyme^{1,5,6,8}. The morphological stages of lung development includes: (Fig. 1.3) (1) embryonic (2) pseudo glandular (3) canalicular/saccular and (4) alveolar stages^{1,18,19}. During human embryo development, at approximately 4-5 weeks' gestation, the lung endoderm is specified. The anterior foregut endoderm is characterized by the expression of the transcription factor NKX2. To activate NKX2, the lateral plate mesoderm expresses Wnt2 and Wnt2b, by B-catenin, resulting in the upregulation of SOX2. The early respiratory primordium, expressing NKX2, starts to elongate to eventually form the tracheal tube. Concurrently, signals activated by FGF10 from the mesenchyme promote its outgrowth and differentiation. During the pseudo glandular stage, 5-17 weeks after conception, Wntless (Wls)-regulated Notum suppresses mesenchymal Wnt. This initiates the branching morphogenesis process to develop terminal bronchioles and the extensive arborized network of the lung. This process is highly supported by Wnt5a, which activates sonic hedgehog (SHH) in the respiratory endoderm. SHH represses FGF10 expression^{1,19}. Signaling from Wnt7b-BMP4 promotes epithelial, small smooth muscle cells (SMC) proliferation, and mesenchymal vascular cell (VSMC) differentiation. The epithelium and mesothelium produce FGF9, which promotes Wnt2a, facilitating mesenchymal cell proliferation. At the same time, SOX9 is expressed in the distal tip of the endoderm¹. During the saccular or canicular stage (16-26 post conception weeks), the bronchioles become more defined and form epithelial sacs. The expression of DKK1 downregulates Wnt, which induces the proximal patterning of the epithelium. The distal airway phenotype is

patterned by high levels of Wnt signaling mediated by BMP4, FGF, and N-myc proto-oncogene, N-MYC^{1,19}.

The alveolarization stage (36 post conception week to 10 years after birth) concludes the maturation of alveolar structures. Alveolar type II cells (AT2) cells respond to AXIN2 and Wnt signaling to regulate lung alveologenesi. Alveolar type II cells (AC2) cells constitute alveolar epithelial progenitors, which can self-renew and differentiate into AT1 cells^{1,19}. Low Wnt signaling triggers cellular fate towards an alveolar type I (AT1) lineage^{19,20}. Although lung alveologenesi begins at around 36 weeks of pregnancy^{1,18}, it persists over at least the first decade of life¹.

As shown in Fig. 1.3, this process is highly complex, and dynamic. It is initiated by the mesenchyme and the production of FGF10^{1,19}.

This complex in-vivo morphogenesis process has inspired the organoid formation approach followed in the present study, as many others²¹. In this work lung fibroblasts were used as main resource of mesenchymal signals and as the producers of fibroblasts growth factors needed to induce the lung organoid formation of airway epithelial cells.

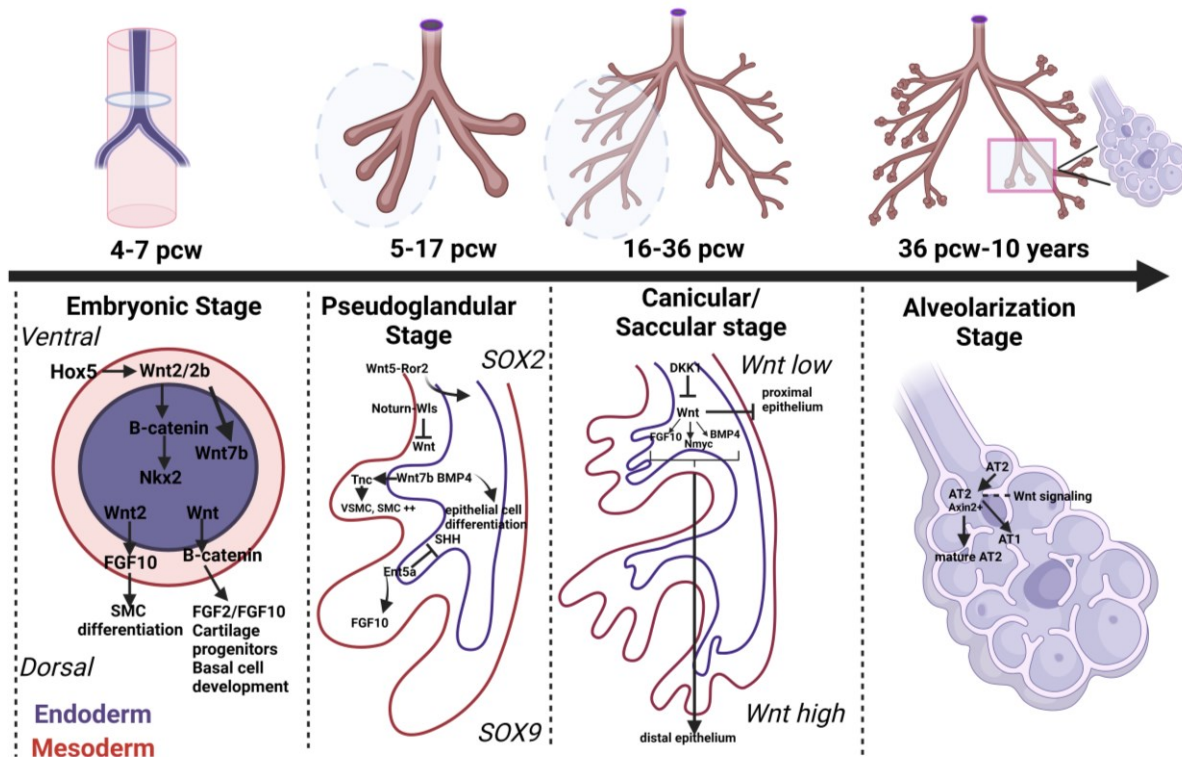


Fig. 1.3. Lung branching morphogenesis mediated by epithelial-mesenchymal interactions and Wnt signaling. A) During embryonic development, the lung buds emerge, regulated by Wnt2/2b to establish NKX2 patterning. Endodermal Wnt ligands promote FGF10 in the mesenchyme allowing basal cell development. B) The pseudo glandular stage, lung buds undergo branching morphogenesis to develop terminal bronchioles. Suppression of Wnt is needed for branching morphogenesis. Wnt5a is the highest on the distal tip. It suppresses SHH and activates FGF10. Concurrently, FGF9 from epithelium and mesenchyme promotes Wnt2a, facilitating mesenchymal cell proliferation. C) The canicular stage of development, the terminal bronchioles become more defined and form epithelial sacs. Proximal and distal patterning occurs. The downregulation of Wnt by DKK1 generates proximal patterning. Conversely, high levels of Wnt drive distal phenotype through the expression of FGF, BMP4, and N-MYC. D) The alveolar structures mature. AXIN2 and Wnt signaling regulate AT2 alveologenesis. BMP4 suppresses the self-renewal of AT2 while inducing AT1 differentiation. The developmental period is indicated for humans in post-conception weeks (pcw). Image created with BioRender with information of ^{1,18}.

1. 4 Animal models

In biomedical research, various living organisms, such as mice, zebrafish, fruit flies, and nematodes, serve as human models owing to the remarkable conservation of fundamental biological mechanisms across species due to evolutionary processes. These mechanisms include genetic pathways, cellular processes, metabolic pathways, and physiological functions. Conservation allows researchers to study development, immune response, and disease pathways across species, aiding in the understanding of human health and the discovery of therapeutic targets. Fast-growing species, which can generate a large offspring are often preferred in the laboratory such as mice. In addition, there is more information and tools to enable genetic engineering in mice than in other animals²². However, their maintenance is costly. There are significant physiological, and metabolic differences between mice and humans. Several drugs effective in humans are toxic for animals, for example ibuprofen and warfarin. One important limitation of the mouse models is their inability to include the effect of the human genetic diversity on drug response²².

Intrinsic differences between the signalling pathways activated in mouse stem cells and human stem cells have been reported. These are required for their maintenance, development, immune response, and disease progression including viral infections^{22,23}.

Anatomically, the human lung differs substantially from the mouse lung as shown in Fig. 1.4. The human lung is characterized by respiratory bronchioles (RB) and alveolar ducts, which are connected to the alveoli. In contrast, the conducting airways of the mouse lungs end directly at the bronchoalveolar junction. This has hampered the study of molecular and cellular mechanisms of the human respiratory bronchioles²⁴.

A new subtype of epithelial cells, known as secretory cells (SCGB3A2+), was recently found in the distal human airways of the RB. This cell type is a progenitor of AT2 cells, regulated by Notch and Wnt signaling²⁴. The downregulation of this cell type appears to be associated with multiple respiratory pathologies such as chronic obstructive pulmonary disease. Mouse distal airways lack these cell types²⁴.

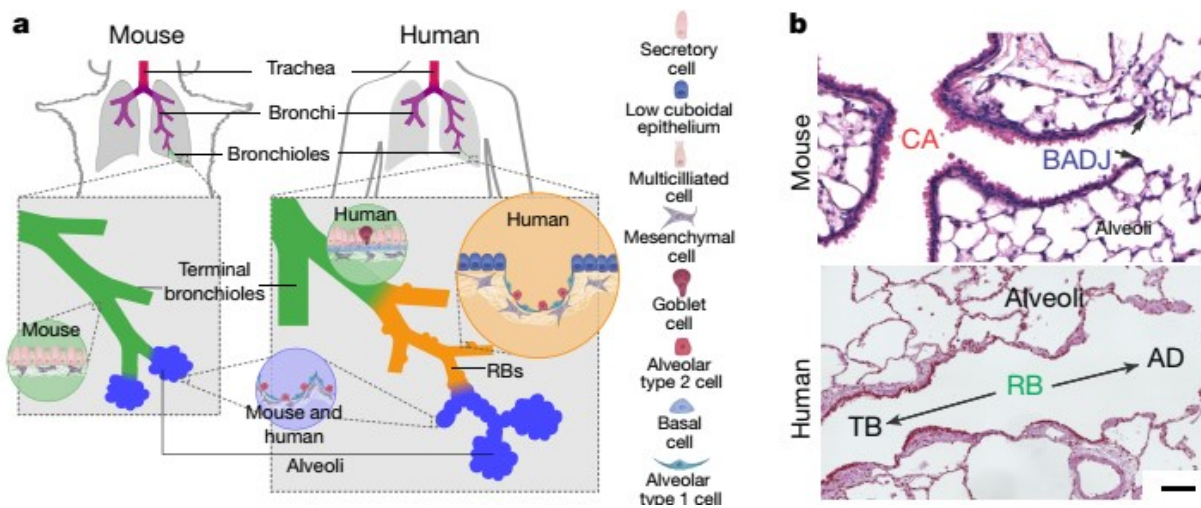


Fig. 1.4 Differences between mouse and human distal airways. **A)** Schematic showing the respiratory bronchioles (RB) in human and their absence in mouse lungs. **B)** Top figure: Haematoxylin-and-eosin-stained tissue showing the mouse conducting airways (CA) and the direct transition between the bronchioalveolar duct junction and the alveolar compartment (BADJ). Bottom gradual figure: Haematoxylin-and-eosin-stained tissue showing the transition between the terminal bronchioles and the alveolar duct (AD) through the respiratory bronchioles (RB). Scale bar, 100 μ m. Image modified from²⁴ (License number: 5764250570906).

Additionally, the small airways of human and mice have different cell populations (Fig. 1.1, 1.5). Basal cells, for example, are only located in the mice trachea, but not in the small airways. Instead, the major cell types in mouse lungs are secretory type I (previously known as club cells), and ciliated cells, with very few numbers of goblet

cells. Following the absence of basal cells in mouse lungs, the secretory cells type I respond to injury and differentiate into ciliated cells²⁵.

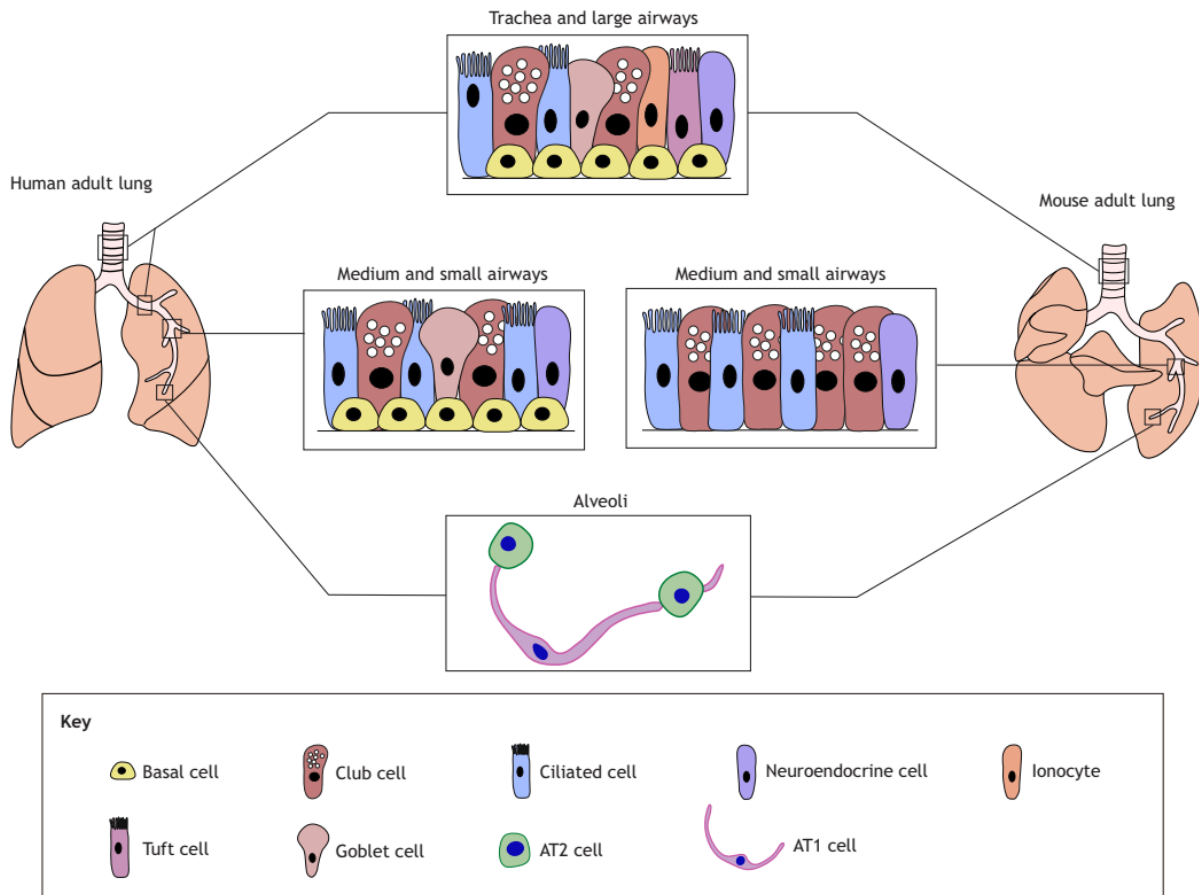


Fig. 1.5 Key differences between epithelial cell components in mouse and human lungs. Image obtained with permission from²⁵ (License number: 1477-9129).

According to the FDA, 92% to 96% of all drugs that pass animal tests do not reach the market²⁶. The poor translation of animal preclinical models to human patients has increased the social and ethical concerns linked to the use of animals in research. Government legislation stemming from social aims at ending animal experimentation²⁷.

In response to this pressure, in 2022, the *FDA modernization Act 2.0*, was approved. This legislation does not ban the use of animals in research, but it recognizes their

limitations. It promotes and validates the use of alternative non-animal methods, including cell-based assays²⁸.

The main objective of this thesis, as described in the next sections, is motivated by the new legislations and the need to develop more physiological relevant human models.

1.5 Lung-In-Vitro Models.

1.5.1 Two-dimensional cell monolayers and air-liquid interface models

Two-dimensional cell monolayers are the most used approach in biomedical research today. Their use has improved our understanding of cellular signaling pathways in health and disease. They are robust platforms for the identification of potential drug candidates, and for the design of drugs for infectious diseases and other pathologies²². These models, however, do not recreate the tissue architecture and physiology of organs²². The culture of primary bronchial epithelial cells in two dimensional cultures, does not allow cell differentiation, or polarization^{29,30}.

Human bronchial epithelial cells (HBE) cultured in porous membrane to form air-liquid-interface (ALI) constitute the gold standard for the study of human proximal airways. In this type of model, the ALI conditions promote cell differentiation and pseudo-stratification. It also allows mucus secretion and ciliated differentiation³⁰. Typically, the establishment of ALI models requires seeding HBE on a porous polyethylene terephthalate (PET) membrane coated with collagen and Fibronectin. Differentiation media is added on the basal side of the membrane, while the apical side is exposed to air (Fig.1.6). The differentiation media includes insulin, hydrocortisone, retinoic acid, transferrin, epinephrine, and epithelial growth factors²⁹. The exposure of cells to air, a

small change in the cell culture conditions, improves HBE polarization and differentiation in comparison to 2D immersed models.

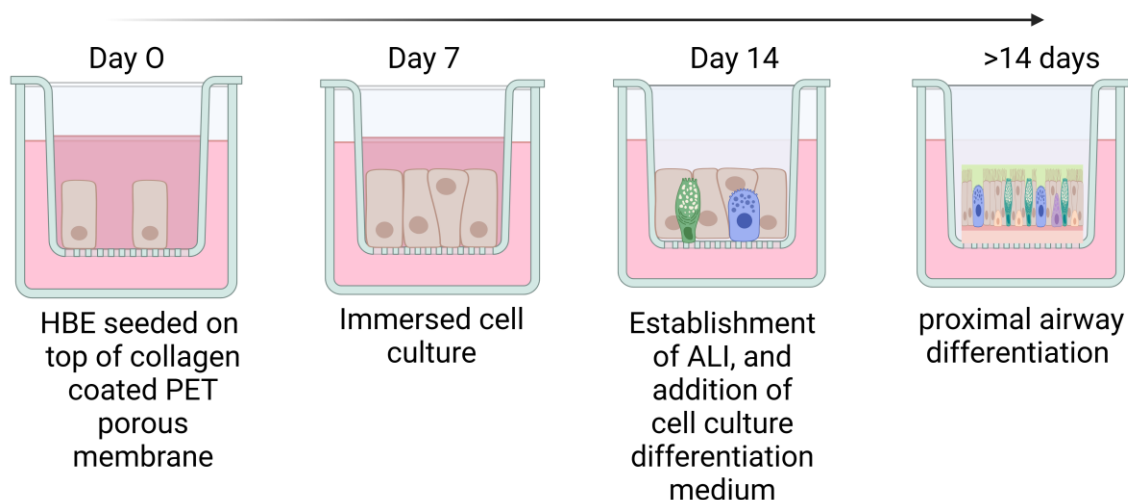


Fig. 1.6 Air-liquid-interface model of human bronchial epithelial cells. On day 0, epithelial cells are seeded on collagen-coated porous membranes. Until day 7, the cells grow completely immersed. On day 11, the apical side of the cells (top) is exposed to air, and cell differentiation medium is added to the basal side (bottom). Cells start to differentiate on day 14. Typically, the culture is maintained over 25 days.

In addition to culturing primary HBE on ALI, immortalized cells line such as Calu-3, NCI-H441, and A549 have been cultured using similar conditions. Calu-3 derived from the adenocarcinoma, form a columnar monolayer with mucin and microvilli expression. NCI-H441, derived from the papillary adenocarcinoma, forms a polarized monolayer with AT2 and secretory cells. A549, derived from the alveolar adenocarcinoma, forms a monolayer of AT2 cells, which secretes surfactant proteins³¹.

Variations of ALI models use induced pluripotent stem cells (iPSC) instead of airway epithelial cells to model proximal airways. In this case, cells are first guided to differentiate into endoderm progenitors, followed by anterior foregut progenitors, to

eventually form immature lung cells through the incorporation of FGF10, FGF7, BMP4, and FGF18 into BEGM medium. Over a period of 26 days, the cells are cultured submerged into the medium. The cells are exposed to air in the apical side over a period of 40 days. By the end of this period, cells have reached maturation and resemble the proximal airways, expressing ciliated cells markers, along with goblet cells, and in lower amounts of basal cell markers³².

Some degree of complexity has been added to these models by co-culturing airway epithelial cells with other cell types such as macrophages³³ in the basal side, and/or fibroblasts in the apical side of the chamber³⁴.

Currently, commercially available airways plates are in ALI format from HiTrach³⁵ representing either the proximal or distal regions of the lung³⁵. These ALI models are useful for the study of viral infections, toxicology, cancer, asthma, and cystic fibrosis in a high throughput-manner^{29,29-31}. But they lack integration between proximal and distal airway components, 3D architecture²², and active mechanical microenvironmental cues³⁶. To overcome the latter limitation, advances in microsystems engineering have created biomimetic cell-culture devices, know as organs-on-a-chip³⁶.

1.5.2 Organ-on-a-chip

The first organ-on-a-chip fabrication was reported in 2010 in the journal *Science*, it was a representation of the lung³⁷. This system aimed to mimic the alveolar region of the lungs by culturing airway epithelial cells and endothelial cells in a microfluidic device. Airway epithelium was seeded on the top part of a thin, porous, flexible PDMS membrane coated with collagen, while endothelial cells were seeded on the bottom of the same membrane, forming a co-culture interface, Fig. 1.7. The airway epithelial cells

were exposed to air, while the endothelial cells were cultured immersed. The main differences with ALI interfaces, described previously (section 1.5.1), was that the device offered a dynamic microenvironment. This model recreated the breathing movements by applying vacuum to the side chambers, inducing stretching on the PDMS membrane^{37,38}.

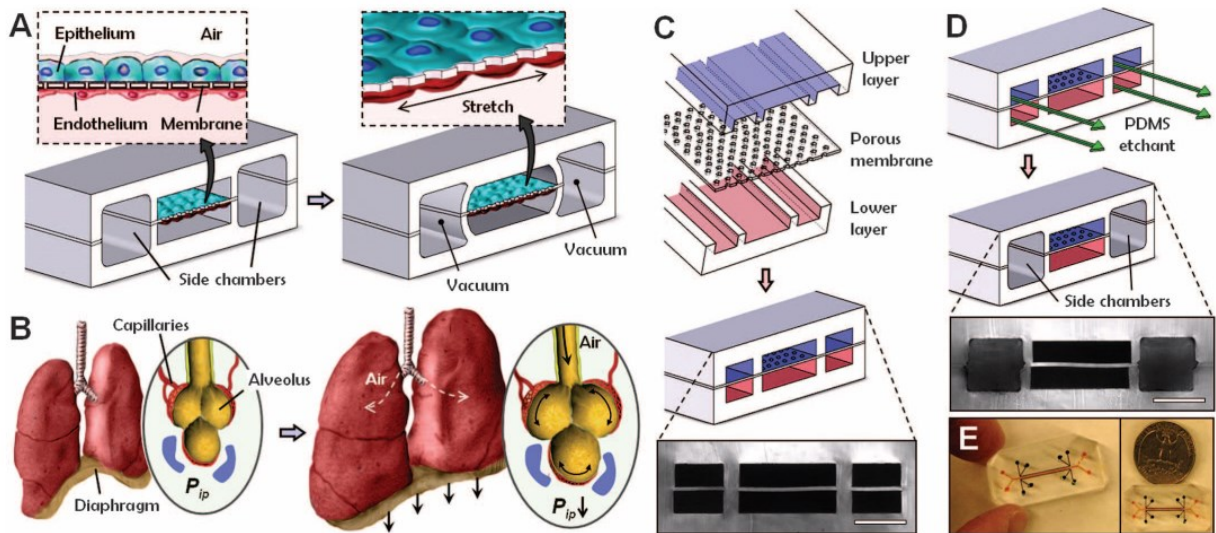


Fig. 1.7 First reported “*lung-on-chip*”. The model provides mechanical cues which mimic the breathing process. A) The device was characterized by compartmentalized PDMS microchannels to form an alveolar-capillary barrier. B) During inhalation in the living, the diaphragm contracts leading to distension of the alveoli. C) Three PDMS layers are aligned in irreversible bonds forming microfluidic channels. Scale Bar 200 μ m. D) After the permanent bonding vacuum is applied to cause mechanical stretching. Scale bar, 200 μ m. Image obtained with permission from³⁷.

Subsequent organ-on-a-chips are described in Table 1.1. In the case of lungs, the vacuum chambers were removed from the original design²³, probably for simplification. Instead, fluid flow is circulated into the lower chamber corresponding to the endothelial component. This design is extremely common nowadays. It has been used for studying SARS-CoV-2, and for repurposing drugs²³.

One limitation of the *lung-on-a-chip* is that PDMS, used as porous membrane, tends to absorb biomolecules and compounds. This can complicate drug assessment³⁹. Alternative membrane concepts have been investigated, shown in Table 1.1, with patterns characteristics of the alveoli, while preventing biomolecules absorption⁴⁰.

The cellular complexity of these models has evolved over the years, going from the culture of immortalized cells^{37,41–44} to the use of primary bronchial or alveolar epithelial cells^{40,45–47} along with endothelial cell lines, as shown in Table 1.1. Tri-cultures systems have been created using airway epithelial cells, endothelial cells and fibroblasts⁴³ or T-helper cells⁴⁶. Matrigel has been used to support the growth of alveolar cells⁴⁷ instead of collagen and fibronectin coatings typical of lungs-on-a-chip⁴¹.

The incorporation of mechanical cues into cell cultures, have resulted in different responses to drugs, and treatments than static conditions⁴¹. Fluid flow within the endothelial compartment leads to tighter cellular junctions than when cells are cultured in normal settings^{39,41}. These models have proved the relevance of mechanical stresses and multicellular cultures under ALI⁴⁸. They have been used for modelling asthma by induction of IL-13 on healthy cells⁴⁶, to study viral infections such as rhinovirus⁴⁶, influenza and SARS-CoV-2²³, drug screening^{23,40,43,44}, and other toxicological studies^{37,47}, as well as model cancer^{43,44}, thrombosis⁴⁵, and pulmonary edema⁴².

There are several companies which commercialize *lung-on-a-chip* devices representing either the bronchi^{49,50} or the alveolar region of the lung^{49,50}. All these models are inspired by the original *lung-on-a-chip* system²³, having typically a porous membrane, co-culture system, and continuous fluid flow in the endothelial compartment^{49,50}.

As for static ALI models, *lung-on-a-chip* systems have the main disadvantage of not representing the 3D architecture of the lung. The cells, although cultured in dynamic conditions, are still in a “2D planar configuration”^{22,51}. This constrains the cells to grow in substrates with a high stiffness unrepresentative of the lung. For instance, PDMS stiffness varies between 1 MPa to 10 MPa⁵², while lung stiffness is in the range of a few kPa⁵³.

Cell behavior and structure vary depending on culture conditions⁵⁴. In 3D matrices cells can better communicate with surrounding cells. Changes in migratory characteristics of the cells are also observed. These migratory changes alter subcellular structures⁵⁵.

Additionally, *lung-on-a-chip* devices, partially represent only one portion of the lung. They model either the bronchi or alveoli, which limits the study of disease progression, including viral tropism^{23,40,43,45,45–48}.

Organ-on-a-chip name	Source of cells	Mechanical cues	Product description	Limitations	Applications
Lung-on-a-chip ³⁷	Immortalized airway epithelium and endothelium	Vacuum chamber to mimic dynamic breathing.	Co-culture of epithelial and endothelial cells with mechanical stresses. ALI	Use of immortal cell types. Representation of distal region of the lung with proximal epithelium cell type.	Nanoparticle uptake study
Human airway-on-a chip ⁴¹	Primary HBE	Continuous Fluid flow in endothelial component.	Representing proximal region of the lung. ALI	PDMS absorbs molecules. Lack of “breathing” motion Lack of representation of distal lung regions.	SARS-CoV-2. Drug repurposing

Primary human lung alveolus on-a-chip⁴⁵	Primary AT1 and AT2 and vascular endothelial cells (HUVEC)	Continuous fluid flow on the basal chamber.	Co-culture of epithelial and endothelial cells. Endothelial cells covered the 4 walls of the basal chamber. Perfusion of whole blood on the basal chamber. ALI	PDMS membrane has some absorption problems. Use of immortalized endothelial cells. Lack of representation of the proximal region. Lack of mechanical "Breathing"	Intravascular thrombosis
Second generation Alveoli-on-a-chip⁴⁰	Primary lung epithelial cells, and HUVEC	Cyclic negative pressure on the basal chamber causing membrane deflection.	Use biological membrane done of ECM, collagen, and elastin, mimicking the array of alveoli. ALI	Lack of representation of proximal regions of the lung. No continuous fluid flow.	Drug toxicology.
Microengineering lung-on-a-chip⁴⁶	Primary healthy human airways, and human microvasculature endothelial cells (HMVECS).	Fluid flow on basal chamber (endothelial cells components)	Induction of asthma by IL-13, while simultaneously infecting with Rhinovirus. Incorporation of T-helper cells by endothelial channel. ALI	Lack of mechanical "breathing" motion. Lack of representation of distal lung regions	Viral induced exacerbation of asthma.
3D human lung-on-a-chip⁴⁷	Primary human alveolar epithelial cells and HUVEC	Fluid flow on basal chamber (endothelial cells components)	Matrigel is used to culture alveolar epithelial cells. ALI	Lack of mechanical "breathing" motion. Lack of representation of proximal lung regions	Evaluation of toxicity of nanoparticles
Pulmonary Edema on a lung-on-a-chip⁴²	Alveolar epithelial cells (NC1-H441) and HMVECS	Vacuum chamber to mimic dynamic breathing.	Co-culture of alveolar cells and endothelial cells under mechanical stresses. ALI	Use of immortalized cells. Lack of representation of proximal lung region/	Pulmonary Edema
Nanofiber membrane for lung-on-a-chip⁴³	A549 non-small lung cancer cells, human fetal lung fibroblasts HFL1, and human endothelial cells	NA	Tri-culture of alveolar cells and lung fibroblasts. ALI. Use of Poly (lactic-co-glycolic	Use of immortalized cells. Static culture conditions. Lack of representation of proximal region of the lung	Anti-cancer drug treatment

			acid) (PLGA) electrospinning nanofiber membrane.		
Lung cancer on - a-chip platform⁴⁴	Lung cancer cell line: NCI-H1437	NA	Collagen coated glass membrane contained the lung cancer cells. Electrodes were integrated on the chip to monitor TEER.	Monoculture of cells Static conditions	Drug testing for cancer.

Table 1.1 Lung-on-a-chip microdevices.

1.5.3 Organoids

Organoids are multi-cellular 3D organ models that mimic specific physiological functions, with potential applications in drug screening. Organoids have been shown in recent years to address some of the intrinsic challenges of viral infection modeling⁴. Organoids can better recapitulate the cellular organization and physiology of original organs, including cell communication²². Physiological mimicry is particularly useful, if not essential, for the study of viral-host interactions, which involve more than one cell type in the targeted tissue. As an example, severe acute respiratory syndrome-2, SARS-CoV-2, first infects airway epithelial cells, along with ciliated and goblet cells of the proximal lung. If the virus is not cleared, it later infects AT2 cells in the distal lungs as its primary target⁵⁶. Gut, brain, vascular, kidney, and lung organoids have been used to model SARS-CoV-2 and other infectious diseases⁵⁷. Altogether, these organoids have yielded predictive results for drug testing before clinical trials and their use has been adopted by pharmaceutical companies⁵⁸.

Organoid development typically involves a self-organization process, in which the initially disordered cell population is reordered under the guidance of

microenvironmental cues⁵¹. The architectural rearrangement is triggered by differentiation, cell migration, contraction, and cell shape^{51,59}. The successful derivation of organoids and their characteristics depends on 1) the physical characteristics of the environment, 2) exogenous or endogenous signals, 3) and the initial cell types, as shown in Fig. 1.8.

To promote 3D culture, natural substrates such as Matrigel are most commonly used⁵¹. Matrigel contains ECM proteins and growth factors purified from Engelbreth-Holm-Swarm mouse sarcoma. Geltrex is a similar substrate in composition and purification method^{51,60}. Intestinal, gastric, mammary gland and lung organoids use Matrigel^{21,51,57,61–66}. Collagen is another natural substrate which has been used to grow organoids^{51,67}. Alternatively, synthetic chemically-defined substrates have been explored for the generation of colon^{68,69} and brain organoids^{51,69,70} to overcome the variability of natural derived substrates⁵¹. But these hydrogels are less bioactive than natural substrates⁵¹.

Suspension is another strategy to culture organoids (Fig. 1.8a). It is more commonly used in brain organoids with lower concentrations of Matrigel^{51,71}. Spinning bioreactors promote the diffusion of Oxygen and nutrients, preserving organoids over a longer time^{71,72}. Finally, organoids, particularly kidney organoids, have been reported to grow on air-liquid-interface⁷³. In this method cells are cultured on a thin, porous membrane, with cell culture medium only on the basal side of the cells⁵¹(Fig. 1.8a).

In most cases, during the organoid formation, the initial cell population needs to be exposed to morphogens at specific time points, which will activate the desired signaling pathways, cell differentiation and proper self-organization⁵¹. Some models, for instance

mouse optic cup organoids⁷⁴, rely primarily on their endogenous factors. The initial cell population then meets all the requirements to self-organize. But most organoids require initial exogenous signals, and in some cases, continuous exogenous signals throughout the culture. This is the case for organoids derived from induced pluripotent stem cells (iPSC) or embryonic stem cells⁵¹, including lung organoids^{21,57}, and organoids derived from adult stem cells (ASC)^{63,65,67,75}.

The initial cell type and concentration constitute the “input” of the system. They vary according to specific protocols. The degree of differentiation and patterning depends on the initial cell stage. When organoids are derived from single cell populations, the cells must go through the complete morphogenesis process, including symmetry breaking, differentiation, and maturation (Fig.1.8c)⁵¹. More frequently, organoids are derived from homogenous cell aggregates (Fig.1.8c). Other protocols, for liver organoids, involve the co-culture of already pre-differentiated cell types. Self organization, then, depends on architectural rearrangements^{51,76}. These conditions facilitate and speed up the maturation process⁵¹.

The degree of maturation of the final organoid depends on the initial cell type. Organoids derived from ASC, reach maturation in-vitro, while organoids derived from iPSC remain immature, shown in Fig.1.9. This is also the case for lung organoids derived from iPSC^{21,77}. Additionally, organoids derived from iPSC, require longer culture time than ASC derived organoids, increasing their cost and the complexity of culture conditions^{21,51}. Organoids derived from fetal cells, dissected directly from fetal tissues, mature further than iPSC-derived organoids, but less than ASC-derived organoids. The generation of this type of organoids creates ethical concerns, which limits their

availability⁵¹. Immature organoids are normally used for developmental biology purposes^{21,51,77,78}. The study of adult diseases requires more mature organoids^{51,61–63,65,66,75}. Both models are useful depending on their application⁵¹.

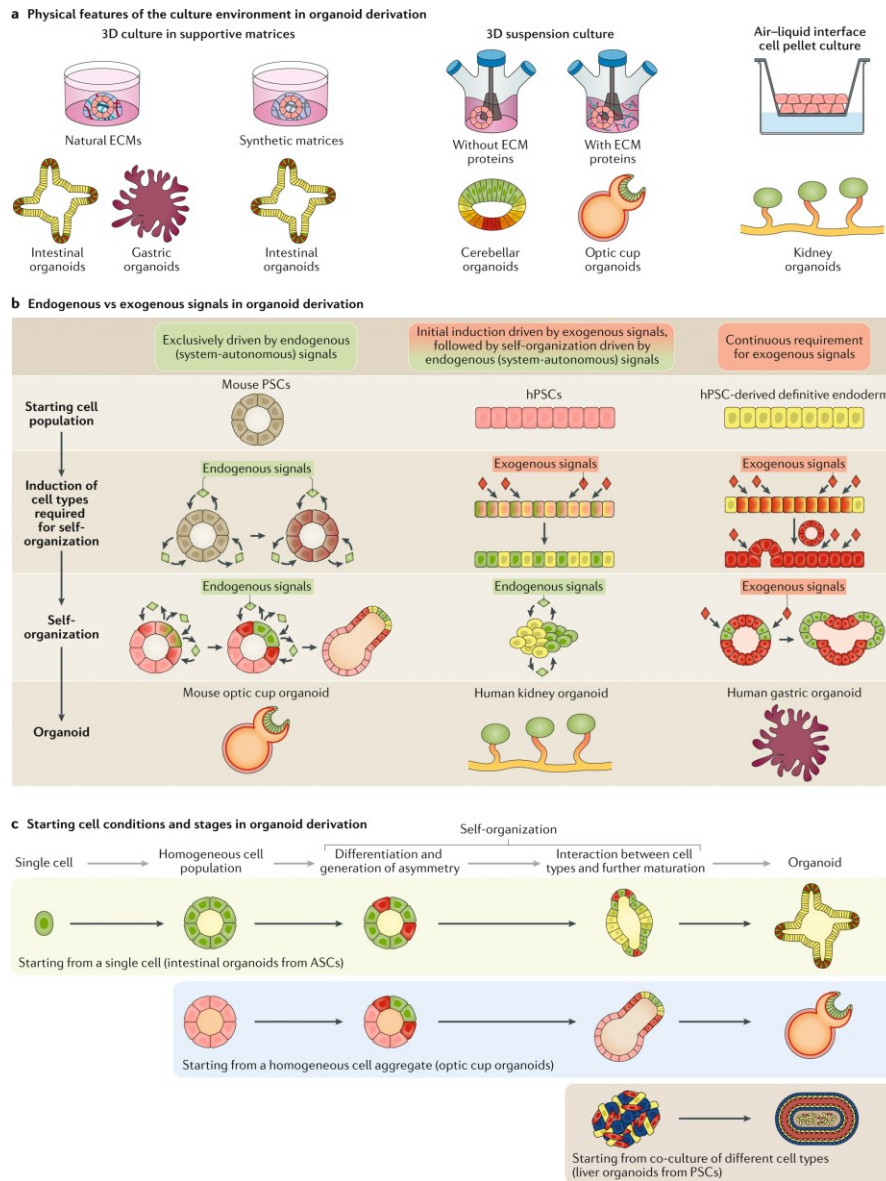


Fig. 1.8 Methods and considerations for organoid formation. A) Physical characteristics of the environment. B) The self-organization of the organoid depends on exogenous and endogenous signals. Most models require at least initial exogenous signals, but some models require continuous exogenous signals. C) Possible starting cell conditions for organoid formation. Organoids can be derived from single cells, homogenous cell populations or heterogenous co-cultures. Image obtained with permission from ⁵¹ (License number: 5764251335262).

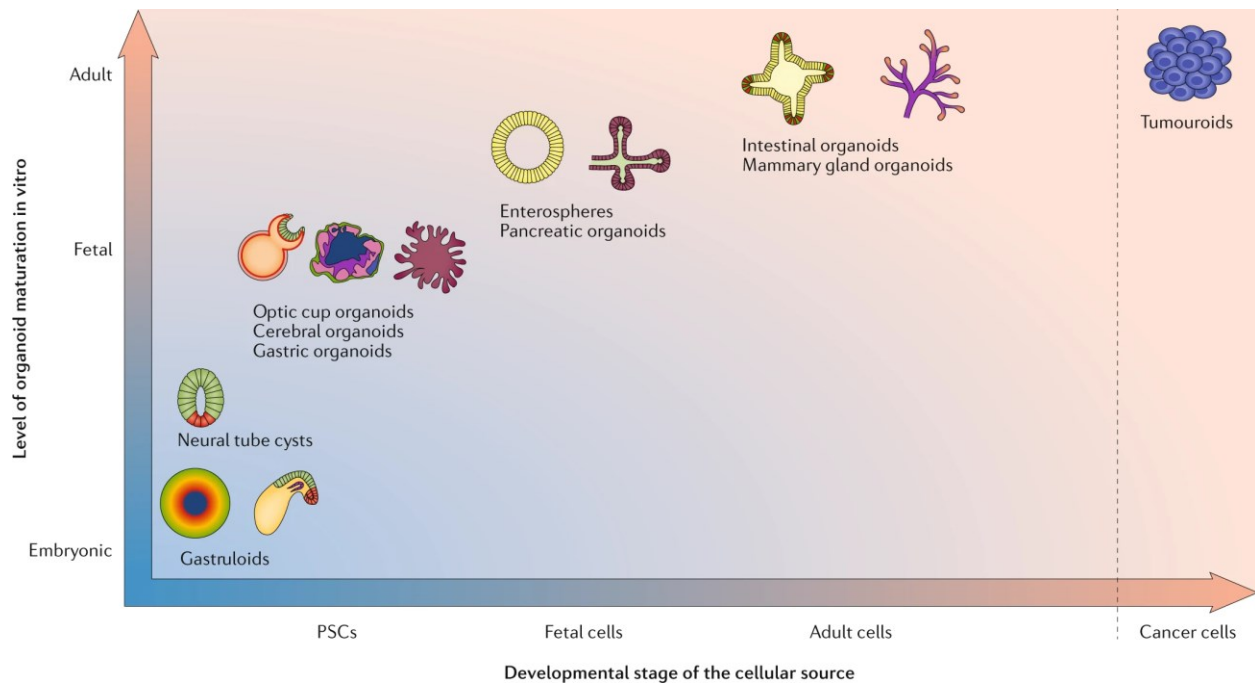


Fig. 1.9 The starting cell type stage determines the level of organoid maturation in-vitro. The horizontal axis shows the developmental stage of the initial cell culture. The vertical axis shows the degree of maturation of the organoid. Image obtained with permission from⁵¹ (License number: 5764251335262).

1. 5. 4 Literature survey: Available lung organoids

Existing protocols for the generation of lung organoids vary depending on the initial cell type. Initial cell type also determines final organoid characteristics. Such organoids are shown in Table 1.2. Two categories of lung organoids have been reported” 1) derived from iPSC. And 2) derived from ASC^{6,21,61–66,75}, commonly dissected from deep lung tissue fragments^{61,63,66,75}. Existing models do not take advantage of technological advances such as bioreactors, composite substrates, mechanical cues, or organ-on-a-chip culture^{21,62–65,65,75,77,78}.

“Organoids derived from ASC have been designed to mimic only one region of the lung, either proximal or distal, for instance alveolospheres⁶¹, broncheospheres⁶², tracheospheres^{6,64} or human airways organoids^{65,10}. All previous models display a spheroidal morphology, and do not reproduce the complex branching structures of the lung^{1,61–63,65,75}. Alveolospheres, as described in Table 1.2, are derived from primary alveolar type I and type II cells. They use a combination of lung fibroblasts, Matrigel, and exogenous factors during the entire culture period. Alveolospheres have been used to model SARS-CoV-2, and to test diverse antiviral drugs⁶¹. Broncheospheres, Table 1.2, have been used to study the effects of bacteria and LPS. This model is derived from primary bronchial cells using Notch2 as morphogen to trigger the differentiation of goblet cells. Alternatively, IL-17A has been used, but yielded reduced numbers of ciliated cells^{62,79}. Airway organoids are made using bronchial epithelial cells embedded in Matrigel and cultured in enriched growth factor medium (Table 1.2). The associated media composition is shown in Table 1.3. These organoids have been used for modeling influenza strains⁶⁵, cystic fibrosis, lung cancer and respiratory syncytial virus infection (RSV)⁶⁶. Variations in the culture medium resulted in greater numbers of ciliated, secretory and goblet cells⁶⁵. Airway Organoids can be expanded up to 19 passages while preserving their initial characteristics⁶⁶. Broncheospheres and human airway organoids represent only the proximal region of the lung^{62,65,66}. The medium composition in Table 1.3 became the gold standard to develop ASC organoids^{63,65,75}. Some variations in this medium composition have generated models with different characteristics. For instance, a variation of the airway organoids protocol was explored in order to guide epithelial cells into distal lung regions⁷⁵, Table 1.2. Epithelial cells

cultured on Matrigel and in distal differentiation medium gave rise to organoids with AT2 and AT1 cells. These organoids were named “biopotential organoids”. These organoids can be tuned to represent proximal regions or distal regions according to the selected medium, but not both simultaneously⁷⁵. Biopotential organoids have been used to test omicron infection⁷⁵.

The incorporation of TGF- β receptor inhibitor, antioxidants, and p38 MAPK inhibitor, into the airway organoid culture medium (Table 1.3), lead to a fast differentiation and maturation of the organoids with a proximal and distal mixed phenotype⁶³. This model was named ‘complete’ lung organoid (Table 1.2). It has been used for SARS-CoV-2 infection⁶³. The model allows viral replication as well as overzealous host response, but its morphology is spheroidal⁶³.

Tracheospheres derived from ASC as their name indicates, are used to model the trachea. They use mouse or human epithelial cells embedded on Matrigel and cultured with epidermal growth factor and retinoic acid. Tracheospheres, Table 1.2, contain basal, and ciliated cells, and they can be expanded at least twice⁶⁴.

Since ASC-derived organoids are isolated regional models, they are not optimal for the reproduction of viral tropism that evolve heterogeneously in the human body⁷⁵. The infection of these organoids requires their 3D structure and physiological mimicry to be mechanically disrupted. Once disrupted, the cellular components of the organoids are grown as 2D cell monolayers^{63,65,75}, thereby preventing the opportunity to mimic disease progression in a physiological relevant manner. The paucity of ASC, specially obtained from deep lung tissue, hampers their scalability. In many cases, LO are formed with

already diseased cells, such as cancer cells^{63,65,66,75}. Most of these models are only epithelial cell based, lacking a lung mesenchyme^{62,63,65,66,75}.

Organoid Type	Source of cells	Methods and exogenous factors used	Product description	Limitations	Applications
ASC derived organoids					
Alveolospheres	Primary human Alveolar type I and type II cells ⁶¹	Distal lung epithelial cells are mixed in Matrigel with human lung fibroblasts (MRC5). Pneumacult ALI medium is used to culture the organoids on thin, porous membranes. Exogenous factors are used during the entire time of the culture: 50 mg per ml of Gentamycin for the first 24 hr. 10mM Rho kinase inhibitor for the first 48 hr. 2 mM of the Wnt pathway activator is used during the entire time of the culture.	Express surfactant protein C. Maturation time 11 to 18 days.	Only resembles the distal region of the lung. Spherical morphology.	SARS-CoV-2 infection. Drug-screening: Remdesivir, hydroxychloroquine, interferon β
Broncheospheres	Primary human bronchial epithelial cells ^{62,79}	Bronchial epithelial cells cultured in differentiation medium with Matrigel are plated in 96-well plate containing Matrigel. Exogenous factors: 100 ng/ml of Pam3CSK4 is applied during the whole time of culture, and Notch2 to induce goblet cell differentiation.	Presence of goblet, basal and ciliated cells. Notch2 and IL-17A induces goblet cell differentiation. Maturation time 30 days.	Only resembles proximal region of the lung, without secretory or other rare cell types. Spherical morphology	Effect of bacterial flagellin and LPS.
Human Airway organoids	Primary human bronchial epithelial cells from deep lung tissues of patients with cancer ⁶⁵ .	Bronchial epithelial cells cultured in human airway organoid medium and 'PneumaCult' medium immersed in Matrigel. Human organoid medium containing multiple exogenous factors such as: FGF10, FGF7, Noggin, Rspondin1.	Presence of ciliated, basal, secretory, and goblet cells. Higher percentage of ciliated, secretory and goblet cells when cultured in	Only resembles proximal region of the lung. Spherical morphology. The 3D structure of the organoids needs to be disrupted to be	Assess influenza virus strains: H1N1, H7N9, H7N2 ⁶⁵ Study of cystic fibrosis, lung cancer and Respiratory syncytial virus infection ⁶⁶ .

		'Pneumacult' medium.	'PneumaCult' medium. Maturation time 19-23 days.	infected.	
Vascularized human airway organoid	Primary epithelium, endothelium, and lung fibroblasts ⁸⁰ .	Mixed cell population embedded on Matrigel and cultured with 'Pneumacult'.	Spherical model with small protuberances. Expression of goblet, ciliated, basal, AT1 and AT2 cells. Maturation time 21 days.		Possible regenerative medicine applications.
Tracheospheres	Primary epithelium from mouse/human tracheas ^{6,64} .	Tracheal epithelial cells embedded in Matrigel cultured in thin, porous membrane. Cultured in ALI interface. MTEC/Plus medium containing Retinoic acid, Insulin, Epidermal Growth Factor, and FBS ^{64,81} .	Expressing basal, secretory, and ciliated cells. Maturation time 9 days. Organoids can be expanded at least twice.	Only resembles the proximal airways (trachea) without goblet or secretory cells.	NA
Biopotential organoid	Primary lung epithelial cells from diseased-deep tissues ⁷⁵ .	To derive proximal lung organoids, airway organoids culture medium was used (Table 1.2) To derive distal lung organoids, distal differentiation medium was used supplemented with 50 nM dexamethasone, 100 µM 8-bromo-cAMP, 100 µM IBMX, 2% B-27, Wnt agonist CHIR99021. Organoids were embedded in Matrigel in low attachment plates.	Distal lung organoids have AT1 and AT2 cells.	Spherical organoids. The organoids represent either proximal or distal regions of the lung (no both) The 3D structure of the organoids needs to be broken and cultured as 2D, before infection	SARS-CoV-2 Omicron Variant infection
'Complete' lung organoid	Primary lung epithelial cell obtained from deep lung biopsies obtained from the normal regions of lung lobes	Organoids were embedded in Matrigel and cultured with lung expansion medium. Lung expansion medium containing Wnt3, Rspodin, and Noggin, supplemented with	Presence of secretory, basal, goblet, ciliated cells, as well as AT1 and AT2 cells. Maturation time: 7-10 days.	Spherical lung organoids without specific patterning. To be infected the organoids need to be broken and	SARS-CoV-2 infection.

	surgically resected from lung cancer tissues ⁶³ .	recombinant growth factors: B27, TGF- β receptor inhibitor, antioxidants, p38 MAPK inhibitor, FGF 7, FGF 10, and ROCK inhibitor.	Organoids can be expanded.	culture in 2D.	
\$3dGRO™ Human Lung Organoids (PDXO.149-Sigma Aldrich)	Primary lung cancer cells from various lung regions (squamous, acinar, papillary, solid, mucinous) ⁸² .	Not available	Presence of AT2 cells, basal, goblet, and ciliated cells, as well as pulmonary endoderm. Expression of ACE2 and TMPRSS receptors Maturation time 40-60 days.	Long maturation time. Only cancer organoids available. No expression of AT1 cells, and secretory cells.	Possibility to use them for viral infections studies.
iPSC derived organoids					
Lung organoid	iPSC ²¹	iPSC differentiated into foregut were embedded in Matrigel. Organoid culture medium was supplemented with diverse exogenous factors varying according to specific culture times. As specified in Table 1.3 some of these molecules are FGF10, FGF4, FGF7.	Fetal airway like epithelium surrounded by mesenchyme. Presence of goblet, ciliated, basal, AT1 and AT2 cells. Tubular and branching morphology. Maturation time 85-185 days (considering the initial iPSC differentiation into foregut endoderm)	Lack of maturation, it represents the fetal stage of the lung. Inability to study adult viral diseases. Long term culture. Required to be transplanted into mice to improve maturation.	Evaluate human fetal lung malformations ⁷⁷ . Model RSV ²¹ .
Airway lung organoid	iPSC ⁸³	Definitive endoderm stage cells were embedded on Matrigel and cultured with medium containing FGF10, retinoic acid, Wnt suppressor, and Notch inhibitor at different times.	Resembles the proximal airways of the lung expressing secretory, ciliated, and basal cells. Maturation time	The organoids mimic only the proximal region of the lung. Spherical morphology Long maturation	Cystic fibrosis study.

			around 46 days (considering initial cell differentiation)	time	
Proximal airway epithelial spheroids	iPSC ⁸⁴	Organoids cultured in medium with Noggin, BMP4. Followed by medium with Notch inhibitor to promote ciliated cells differentiation.	Presence of ciliated, goblet, basal, and secretory cells Maturation time 42 days-56 days (long time higher number of ciliated cells)	The organoids mimic only on the proximal region of the lung. Spherical morphology Long maturation time	NA
Lung organoids	Embryonic cells, and iPSC ⁸⁵	Stem cells were seeded on decellularized human lung matrices on 96 well plates in presence of FGF10.	Presence of Basal, ciliated, and secretory cells, and AT2 cells in lower number, with adjacent mesenchyme. Maturation time 110 days.	Spherical structure. Immature phenotype	NA

Table 1.2 Existing lung and LRT organoids. There are two main categories of lung organoids. 1) The organoids derived from adult stem cells, typically represent one region of the lung (either proximal or distal) but not both. They have a spheroidal morphology, and a relative short maturation time. They are made with primary cells extracted from deep lung tissues from patients with cancer. 2) iPSC-derived organoids. These organoids mimic the entire lung. They exhibit a branching morphogenesis, but their phenotype remains immature. They require long culture time conditions, increasing their cost. \$Commercially available model.

Reagents	Company	Catalog No.	Working concentration
Advanced DMEM/F12	Invitrogen	12634010	n/a
HEPES	Invitrogen	15630-056	1%
GlutaMAX	Invitrogen	35050061	1%
Penicillin-Streptomycin	Invitrogen	15140-122	1%
Rspondin1* (conditioned medium)	n/a	n/a	10%
Noggin* (conditioned medium)	n/a	n/a	10%
B27 supplement	Invitrogen	17504-044	2%
N-acetylcysteine	Sigma	A9165	1.25mM
Nicotinamide	Sigma	N0636	10mM
Y-27632	Tocris	1254	5μM
A8301	Tocris	2939	500nM
SB202190	Sigma	S7067	1μM
FGF-7	Peprtech	100-19	5ng/ml
FGF-10	Peprtech	100-26	20ng/ml
Primocin	InvivoGen	ant-pm-1	100μg/ml
Heregulin beta-1	Peprtech	100-03	5nM

*Table 1.3 Medium to culture airway organoids. *Conditioned media were produced from stable cell lines for production of R-spondin1 and Noggin⁶⁵.*

Media	Definitive endoderm, Day 1	Definitive endoderm, Day 2	Definitive endoderm, Day 3	Definitive endoderm, Day 4	Anterior foregut endoderm, days 5-9	Human lung organoid maintenance	Bud tip progenitor organoid medium
Basal Media	RPM1 1640	RPM1 1640 0.2% HyClone FBS	RPM1 1640 2% HyClone FBS	RPM1 1640 2% HyClone FBS	(Foregut basal) Advanced DMEM/F12 10 mM HEPES 2 mM L-glutamine 5,000 U/ml penicillin-streptomycin	(Foregut basal) Advanced DMEM/F12 10 mM HEPES 2 mM L-glutamine 5,000 U/ml penicillin-streptomycin	(Bud tip basal) DMEM F12 200 mM L-glutamine 5000 U/ml (vol/vol) BSA
Add on day of use	Activin A 100 ng/ml	Activin A 100 ng/ml	Activin A 100 ng/ml	Activin A 100 ng/ml	10 µM SB431542 200 ng/ml Noggin 1 µM SAG 500 ng/ml FGF4 2 µM CHIR-99021	500 ng/ml FGF10 1% FBS	0.4 µM monothioglycerol 50 µg/ml Ascorbic acid 10 ng/ml FGF7 50 nM ATRA 3 µM CHIR-99021

Table 1.4 Cell culture medium used for development of iPSC derived lung organoids. Obtained from²¹.

In contrast, lung organoids derived from iPSC are generally more complex (Table 1.2). They typically exhibit an arborized morphology as the native lungs. Unlike to the ASC-derived lung organoids, most of these models recapitulate both proximal and distal regions of the lungs. They are well-suited for the study of lung development^{77,78,85}. Some iPSC-derived lung organoids resemble only one region of the lung. Their fate, proximal or distal, appears to be determined by the exogenous molecules and patterning factors included in the medium. For example Notch inhibitor promotes the ciliated differentiation of the proximal airway^{83,84}. But all iPSC-derived lung organoids display immature phenotypes resembling those of fetal lung tissues^{77,78,83–85}. This hampers their use for viral infection models. These models can only be infected with

fetal viral diseases as RSV, excluding Influenza H1N1 and H3N2, and SARS-CoV-2^{21,77,78}. In addition, these organoids require around 85-150 days to grow^{77,78,85}, along with costly and complex culture conditions^{21,78,85} (Table 1.4). Such growth rate is too low to track epidemic progression and viral evolution in the eventuality of an epidemic.

Among all lung organoids models, ASC-derived and iPSC-derived, only one is commercially available. It is named 3DGRO™ (Table 1.2). This model uses primary lung cancer cells from various lung regions (squamous, acinar, papillary, solid, and mucinous)⁸². The model has been reported to express AT2, basal, goblet, ciliated cells, and pulmonary endoderm. But it apparently lacks secretory and AT1 cells. Its maturation time varies between 40 to 60 days, and its application is limited to lung cancer research purposes⁸².

There is an unmet need for a novel LO that can model mature and diverse structures and cellular populations of the LRT involved in viral infections such as influenza and COVID. The model should be scalable made from readily accessible cells with simple and timely culture conditions.

1.6 Context and Scope of the Thesis

1.6.1 Description of the Problem

The wide use of animal models for the study of disease progression, toxicology, and developmental biology, rise ethical concerns, and often fail to guide human clinical trials²⁶. Mouse lungs differ substantially from human lungs^{24 25}. This has created a need for using *lung-in-vitro* models with human cells. 2D cell monolayers are robust systems easy to implement at low cost²². Modifications in the cell cultures, such as the addition of a ALI interface, have significant effects on cell differentiation and polarization,

specifically for human bronchial epithelial cells³⁰. Small changes in the cell culture conditions have profound impact on the cell behavior^{30,31}.

Organs-on-a-chip have provided useful tools to add mechanical cues representative of the breathing motions of the lung^{37,38}. Over the years, cellular applications of these devices have been improved by using primary cells^{40,45–47}, instead of immortalized cells^{37,41–44}. Additionally, co-culture and even tri-cultures^{43,46} of different cell types of the lung have been used. However, these culture methods do not represent the architecture of the lung. They consist of “flat cells” which behavior differs from 3D^{22,51}. PDMS used to grow lung cells, is stiffer than the tissue^{52,53}. The migration characteristics of cells change between 2D and 3D substrates leading to alteration in subcellular structure⁵⁴.

One of the most limiting characteristics of the *lung-on-a-chip* models is their lack of integration between different lung regions. They model individually either the bronchi or the alveoli^{23,40,43,45,45–48}.

Lung organoids have emerged providing 3D self-induced cell cultures⁵¹. iPSC derived lung organoids resemble the complete lung by having airway epithelial cells from proximal and distal lung regions. They display an arborized and sophisticated morphology similar to that of the lungs. Unfortunately, these organoids remain immature. As such, their applications are restricted to developmental biology, and to the study of fetal pediatric diseases. Additionally, the growth of organoids is a slow, and costly process^{21,77,78}. Conversely, ASC-derived lung organoids reach a maturation representative of adult lungs, which expands their applications. Typically, their culture is shorter than that with iPSC-derived lung organoids. But they fail to integrate proximal and distal lung regions. Their morphology remains spheroidal^{21,62–65,65,75,77,78}, and the

benefits of 3D culturing are lost when such organoids are disassociated to study LRT diseases^{63,65,75}. Because these organoids are derived from ASC, they depend on harvested deep lung tissue biopsies¹⁹⁻²⁵. Given the invasive nature and the cost of lung tissue biopsies^{86,87} cellular availability is limited from healthy donors^{63,65,66,75}.

1.6.2 Research Objectives

The objective of the work described in this thesis was the creation of a novel *lung-organoid* model, which can mimic the tubular and arborized architecture of the lungs and integrate some of their proximal and distal components, as illustrated in Fig. 1.10. One goal was to use airway epithelial cells as input cells from the large airways: Trachea/Bronchi, to improve cell accessibility. Another related goal was to induce lung organoid formation using immortal cell lines to reduce costs and increase scalability. The central objective was to demonstrate the applicability of the model to study LRT diseases, such as viral infections, and other pathological conditions.

The specific aims to deliver the main objective were the following:

Aim 1: To develop an innovative and standardized methodology for the creation of lung organoids with a focus on simplicity and reproducibility. This objective encompasses the deliberate manipulation of microenvironmental variables to assess their impact on the morphology and viability of lung organoids. Following the establishment of the protocol, in-depth analysis of organoid morphology was conducted utilizing focused ion beam microscopy to elucidate their structural orientation and cellular architecture.

Aim 2: To characterize the phenotype of lung organoids derived from both primary and immortalized cells. Specifically, this objective aimed to analyze the transcriptome and

proteome of the organoids and compare them with the input cells, as well as adult lung tissues, providing insight into their molecular profile and functional relevance.

Aim 3: To evaluate the applicability of lung organoids by investigating the expression of key genes associated with susceptibility to Influenza A and coronaviruses. Subsequently, the organoids were infected to assess viral replication within the model without prior disruption. Additionally, within this aim, efforts were made to establish organoids derived from donors with asthma, enabling the examination of disease-specific responses and potential therapeutic avenues.

The strategies and rationale of these objectives are described in the following subsection.

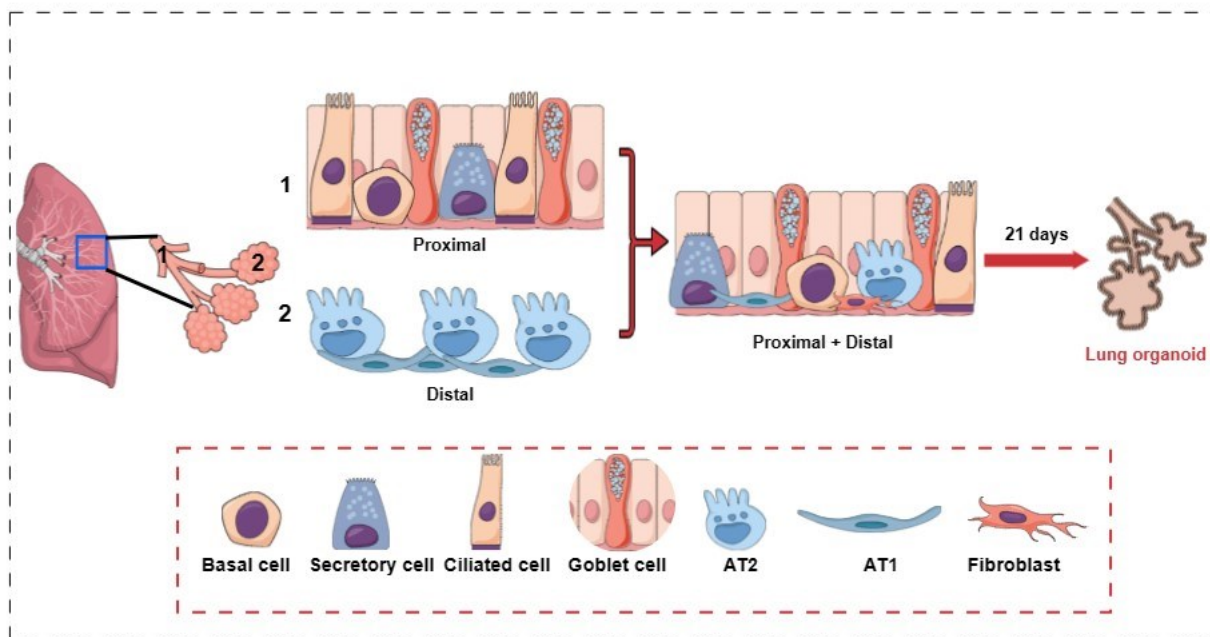


Fig. 1.10 Schematic of the lung organoid concept.

1.6.3 Rationale, and hypothesis

As described already in section 1.3, lung development is a dynamic process initiated by epithelial progenitors surrounded by mesenchymal interactions^{21,62–65,65,75,77,78}. The elongation of the tracheal tube is activated by FGF10 from the mesenchyme, promoting basal cell development. Later, during the pseudo glandular stage, FGF10 and FGF9 facilitate mesenchymal cell proliferation and branching morphogenesis. During the canicular stage, proximal and distal patterning of the lungs occurs, guided by gradient levels of WNT, FGF, and BMP4. High levels of these molecules are found in distal lung regions. The terminal bronchioles become more defined, forming epithelial sacs. During the alveolarization stage, the alveolar structures mature^{1,18}. IL-6 and FGF7, produced by fibroblasts and BMP inhibitors promote AT2 alveogenesis^{1,18,88}. Elastin and collagen secreted by lung fibroblasts has also been linked to AT2 regeneration⁸⁸. BMP4 suppresses the self-renewal of AT2, while inducing AT1 differentiation^{1,18}.

Often, lung organoid formation requires the addition of FGF10, FGF7, FGF9, and FGF18, along with other biomolecules, listed in Table 1.3, and 1.4, into the culture medium at different times^{21 65}. It is clear the FGFs play a critical role for lung development and maintenance^{5,15,88}. The protocol in the present study relies on lung fibroblasts encapsulated in a soft substrate, in contact with adult airway epithelial cells from the large airways (Trachea/bronchi). It was hypothesized that the interaction between these cells in a soft substrate containing base membrane zone proteins, would yield a sophisticated morphology, different from the spheroidal morphology of the current lung organoids^{21,62–65,65,75,77,78}. Another hypothesis was that airway epithelial cells, from the proximal region would differentiate into distal lung regions in response to

the fibroblast's interactions, while preserving some of their initial characteristics (proximal phenotype). There is evidence of lung development derived from trachea^{1,18}. Lung distal organoids have even been developed from bronchial epithelial progenitors⁷⁵. *Organ-on-a-chip*, and *ALI* cultures have shown that small changes in the cellular microenvironment generate significant changes in cell behavior, even when using immortalized cells^{29 30,31}. It is well known that the immortalization process of primary and stem cells may lead to a loss of their differentiation potential⁸⁹. It has been suggested, however, that the culture of these cells into a tailored microenvironment may temper their loss of stemness^{89–93}. A few studies have shown that the culture conditions may trigger immortalized cell line differentiation^{92,93}. It was hypothesized that our protocol would provide a microenvironment favorable to the differentiation of CFBE41-o, a cell line, to induce a lung organoid formation with similar characteristics than the organoids derived from primary airway epithelium.

1.6.4 Thesis organization

This thesis includes five chapters. Chapter 1 is the Introduction. Chapters 2, 3 and 4 present the results of this work. Each one of these chapters starts with the individual contributions of collaborators, professors, and students involved in the project, followed by a brief introduction, results, methodology used, and discussion. Chapter 5 describes the conclusions and perspectives of this work.

Chapter 1 provides an overview of the cellular complexity of human lungs and delves into the branching morphogenesis process crucial for lung development. It discusses the limitations of current animal models used in lung studies and introduces various in-vitro models, including 2D cellular models, air-liquid-interface (ALI) variations, lung-on-

a-chip models, and organoids. The chapter explores the methodology, applications, and limitations of lung organoids, along with a detailed comparison of media components. Finally, it outlines the issues with existing models, the objectives of the present work, and the underlying rationale.

Chapter 2 describes the optimization and development of a novel methodology to induce lung organoid formation with primary and immortalized cells. Variations in the culture conditions, such as cell density, substrate, cell culture medium, and cell origin were evaluated using morphological assays. This protocol was adapted to bioprinting techniques, and preliminary results are shown.

Chapter 3 describes the characterization of pulmonary organoids. Bulk RNA sequencing, and tandem mass tags were mainly used to compare the organoid fate with their counterparts: human bronchial epithelial cells grow in cell culture inserts in ALI interface, and lung fibroblasts. The genetic profile of organoids derived from primary and immortalized cells is compared to that of adult lung tissues. Gene Ontology databases and String were used to develop an in-depth functional enrichment analysis of the organoids. Particular attention was paid to specific cellular markers from proximal and distal regions of the lung. Flow cytometry, and qPCR were used to support the findings.

Chapter 4 explores applications of the developed organoids. The chapter starts by introducing some of the most frequent respiratory diseases. It shows the upregulation of genes on the organoids which are related to viral infectivity of SARS-CoV-2, influenza, and their relationship with critical illness. The results of infection of immortalized derived organoids, LOi, with influenza H1N1, H3N2, and SARS-CoV-2 are presented, in support

of the validity of the model to study adult viral infections. Finally, the chapter explores the formation of the organoids with cells from asthmatic patients.

Chapter 5 summarizes the main conclusions, and the outcomes of the present work.

The contribution to knowledge in the field of *lung-in-vitro models* is discussed, as well as the evaluation of our initial hypothesis. The last section of this chapter presents limitations of our study, future work, and perspectives.

Chapter 2 Fabrication methods and protocols

2.1 Contributions

Alicia Reyes Valenzuela developed the protocol for lung organoids. She monitored the growth of organoids, their viability, length, and morphology over time. She evaluated the effects of different parameters, described in this chapter. She fabricated AIGe, GelMA and AI-RGD-Ge hydrogels. Hossein Ravanbakhsh kindly provided lyophilised GelMA. Abigail Vikstrom performed the conjugation of alginate with RGD (section 2.3.4). Rheological measurements of hydrogels were performed by Guangyu Bao (section 2.3.4). Lan Anh Hyun adapted the protocol for bioprinting (section 2.3.7) under the supervision of Alicia Reyes Valenzuela and Luc Mongeau.

2.2 Introduction

This chapter describes a novel, reproducible and facile protocol for lung organoid formation from primary and immortalized airway epithelial cells.

The organoid conceptually relies on the interactions between airway epithelial cells and fibroblasts, and their growth factors secretion. Given the role of fibroblasts growth factors in lung development^{1,16}, cell proliferation, and maintenance of stem cell stemness^{6,15,94}, we hypothesized that fibroblast cues would induce differentiation into cell types typical of distal regions of the lung, including AT2 and AT1 cells. This approach is different from typical monoculture of airway epithelium cells with exogenous fibroblast growth factors^{61–66,75}. Epithelial progenitors, surrounded by mesenchyme, trigger the lung development process^{1,16}. To mimic this process, we applied a co-culture method of fetal fibroblasts and airway epithelial cells described in detail in this chapter. The chapter starts with the evaluation of the biocompatibility of alginate, a commonly

used hydrogel for 3D culture, with lung fibroblasts. After determining the safety of the substrate, the protocol was optimized in terms of cell density, and cell morphology. An elongated morphology was sought rather than a spherical one, as it closely resembles the tubular structure and branching patterns observed in the lung³. This choice is crucial since the arborized morphology of the lungs is strongly linked to their functionality^{3,95}. The intricate branching network of the lung facilitates efficient gas exchange and optimal airflow distribution, both essential for respiratory function. Additionally, studies have shown that the specific morphological features of the lung are closely tied to its gene expression profile, further emphasizing the significance of morphology-function relationship^{1,18,96–98}.

The reproducibility of the protocol for different cell cultures and hydrogel batches was evaluated. The effects of the substrate on the organoid formation, cell medium, and fibroblast origin were evaluated. These variations were tested using immortalized epithelial cells, due to their availability. The resulting organoids were monitored using microscopy.

AIGe was determined to be as the most suitable substrate in conjunction with lung fibroblasts, in a density 2 to 1. The incorporation of base membrane proteins (BMZ) was needed to induce the organoid formation. The possibility of using bioprinting to decrease costs and to enhance the production rate of the model was explored.

The best parameters for organoid formation were used to further characterize the phenotype of the organoids, as described in Chapter 3, and to use them for modeling viral infections, as described in Chapter 4.

2. 3 Results

2.3. 1 Alginate-Gelatine as substrate for fibroblasts encapsulation

Alginate is a frequently used substrate for 3D cell culture due to its biocompatibility, biodegradability, and non-antigenicity^{99–101}. Alginate hydrogels, often crosslinked with CaCl_2 , have mechanical properties similar to those soft tissues such as lung, cartilage, smooth and striated muscle^{102,103}. Alginate hydrogels retain a high-water fraction content useful for many cellular physiological processes¹⁰⁴. Gelatin is often incorporated into alginate to improve adhesion and cohesion¹⁰⁵. Among the mixtures that have been used for cell encapsulation, 2% alginate and 5% gelatin hydrogels have yielded optimal results¹⁰⁵. Lung fibroblasts were encapsulated in alginate-gelatine gel, and their viability was tested for 7 days. The percentage of cells alive in AIGe at day 0 was found to be 94.83%. It was 90.6% at day 5, and 81.16% at day 7, as shown in Fig. 2.1.

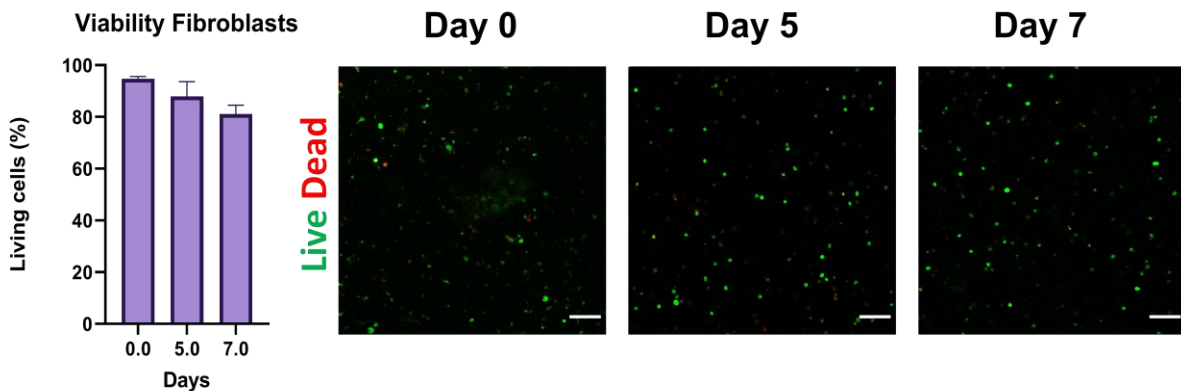


Fig. 2.1. Viability of Fibroblasts on AIGe substrate. Representative images of fibroblasts encapsulated on AIGe over time. Magnification 10X. Scale Bar 100 μm .

2.3.2 Protocol for the Development of Human Lung Organoids from Primary or Immortalized Bronchial Epithelial Cells

Lung fibroblasts (IMR-90) were co-cultured with airway epithelial cells to mimic the lung development process. After fibroblasts were encapsulated in AIGe, and the hydrogel formed, the culture was maintained overnight with Dulbecco's Modified Eagle Medium (DMEM). "The following day, BMZ proteins within Geltrex, such as laminin, collagen IV, entactin, and heparin sulfate proteoglycans were incorporated into the superior portion of the hydrogel to form a secondary thin layer"¹⁰. Base membrane zone proteins are thin sheets underlie the basal side of epithelial cells. These proteins regulate epithelial proliferation, differentiation, survival and structural support¹⁰⁶. Geltrex, particularly, is purified from Engelbreth-Holm-Swarm (EHS) tumor proteins.

"Primary human bronchial epithelial cells were isolated from human bronchus/trachea donors of both sexes, namely one 53-year-old female and one 51-year-old male. The bronchus/trachea cells were seeded on top of the secondary layer and cultured with Bronchial Epithelial Cell Growth Medium (BEGM). The input cell population contained basal cells, positive for p63. These cells can differentiate into all other types of airway epithelial cells, including cells normally found in distal regions, as observed in actual lungs following lung injury⁵. At day 3 of culture, cells were maintained in a mixture of BEGM: DMEM media with a 1:1 ratio until day 21. The media were changed every two days. A similar approach was followed when using cell lines, where parental human cystic fibrosis bronchial epithelial cells CFBE41-o, were used. This cell line was originally derived from patients with cystic fibrosis expressing F508 Del mutation ¹⁰⁷. Once immortalized, however, these cells are devoid of any CFTR expression ^{107,108} and

they constitute a good source of bronchial epithelial cells given their commercial availability”¹⁰. The protocol which provided reproducible and robust results is shown in Fig. 2.2, and further detailed in the method section.

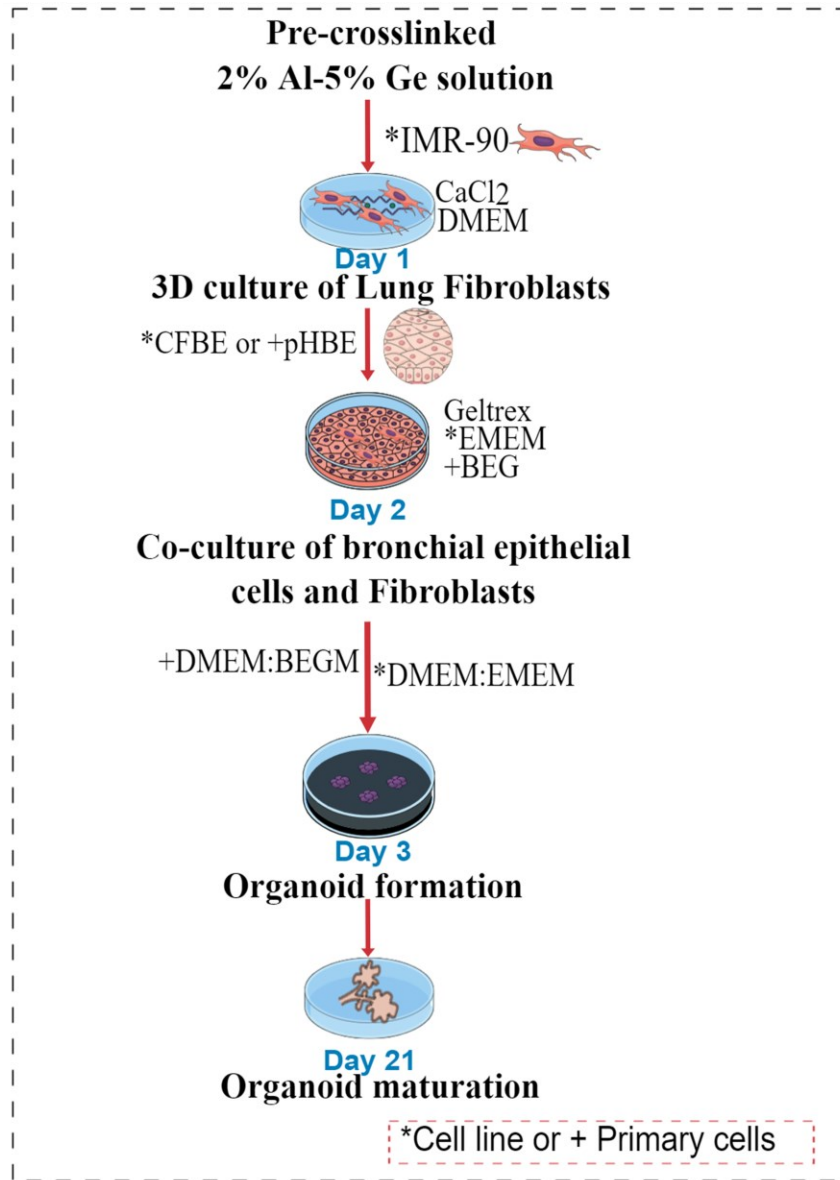


Fig. 2.2. Protocol for the development of lung organoids using co-culture of lung fibroblasts with airway epithelial cells from primary or immortalized origin.

It is well known that the immortalization process of primary and stem cells may lead to a loss of their differentiation potential⁸⁹. It has been suggested, however, that the culture of these cells into a tailored microenvironment may temper their loss of stemness^{89–93}. A few studies have shown that the culture conditions may trigger immortalized cell line differentiation^{92,93}. We hypothesized that the hydrogel and fibroblasts provided a microenvironment favorable to the differentiation of CFBE41-o to induce a lung organoid formation representative of the proximal and distal regions. We monitored the development of lung organoids generated either with primary cells (LOp) or immortalized cells (LOi) using low phase contrast microscopy.

Figure 2.3 shows representative pictures of the derived LOi organoids and their inhomogeneous morphology. The elongated structure of the organoids grew in thickness and diameter over time.

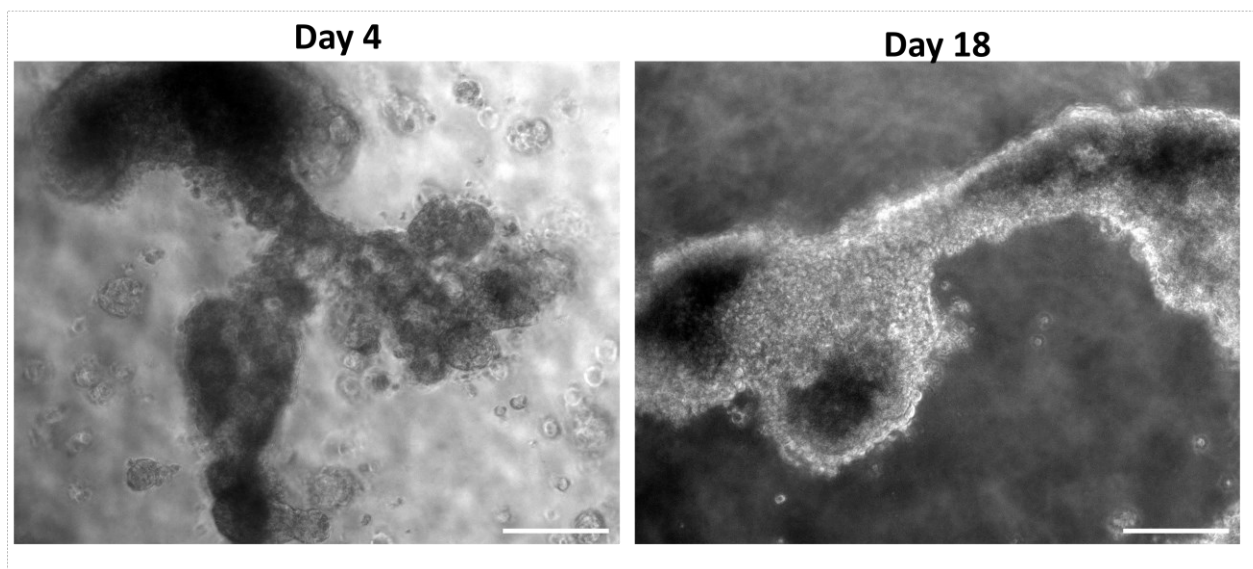


Fig. 2.3 Representative phase contrast pictures of lung organoids derived from immortal cell lines. Magnification 10X. Scale bar 200 μ m.

Figure 2.4. Shows representative images of organoids derived from primary cells on day 18. Their morphology is similar to that for the organoids generated with immortal cell lines.

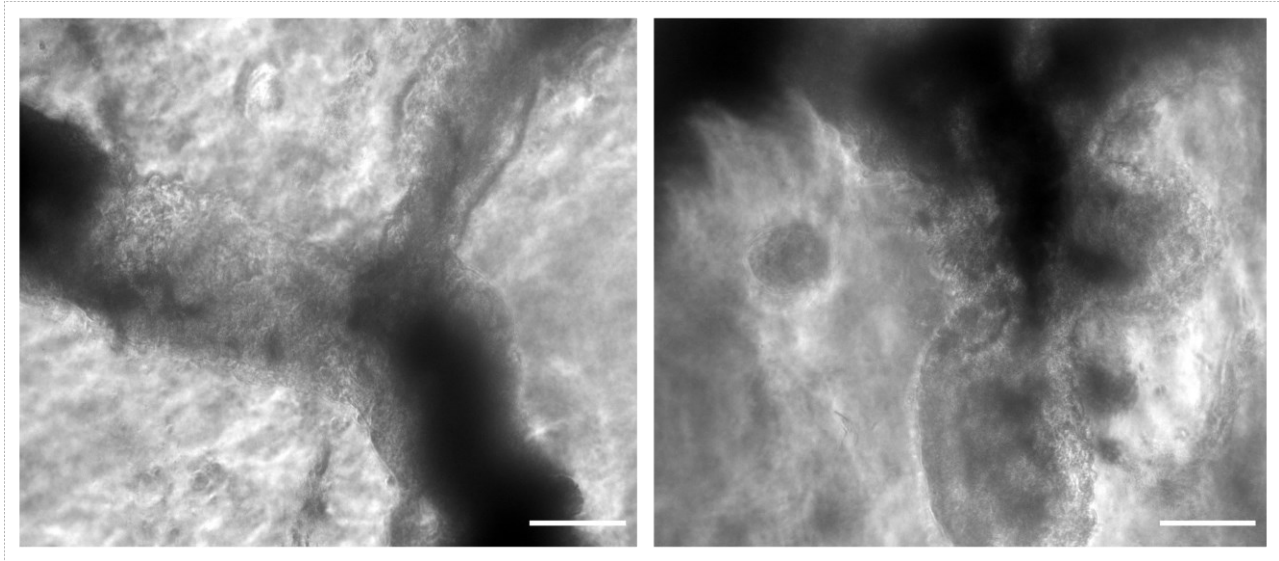


Fig. 2.4. Representative phase contrast pictures of lung organoids derived from female primary airway epithelium on day 18. Magnification 10X. Scale bar 200 μm .

The reproducibility of the protocol was verified by repeating the protocol three times independently. Small variations in the number of elongations and specific shapes were observed between batch to batch. But the overall pattern was very similar. Cells formed small clusters within the first week of culture. These elongated into a tubular shape by day 7. These tubes increased in length and diameter by day 14, and further ramifications were formed by day 21. This pattern is illustrated in Fig. 2.5. No obvious morphological changes were observed by day 30. After day 30, the organoid became more brittle and difficult to handle, and disintegration of the organoid was observed.

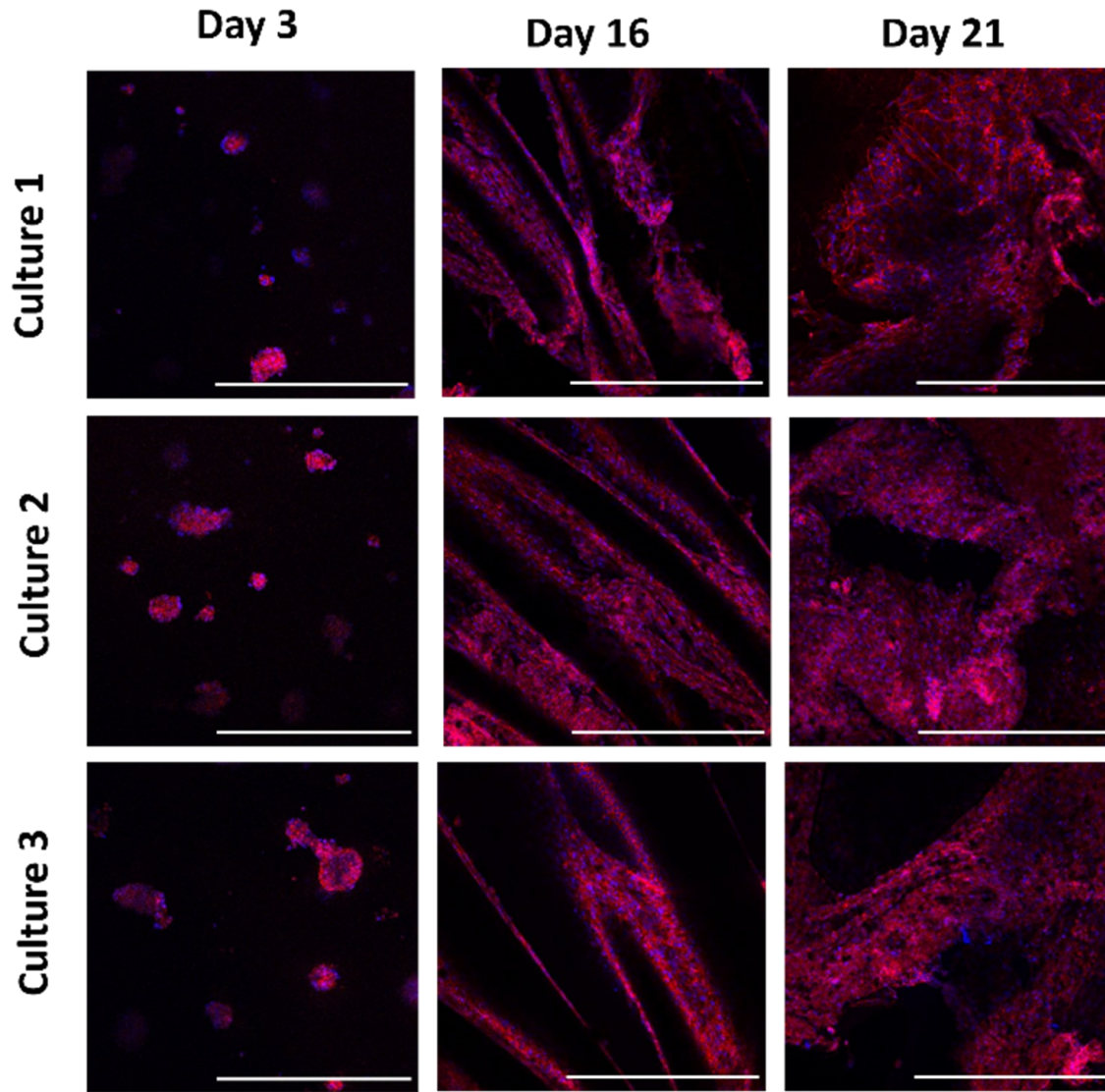


Fig. 2.5 Representative images of independent lung organoid (LOi) cultures over time. Magnification 10X. Red-F-actin. Blue-Nuclei. Scale Bar 500 μ m.

2.3.3 Effects of fibroblast density on the organoid formation

To evaluate the effect of fibroblasts on the organoid formation, the protocol for the organoid formation was repeated without fibroblast encapsulation. Instead of tubular structures, airway epithelial cells formed spheroidal structures, as shown in Fig. 2.6A. In a few cases elongated shapes were formed at around day 5, but they disintegrated by

day 7. The consistent incorporation of fibroblasts resulted in the formation of tubular shapes as shown in Fig. 2.6B

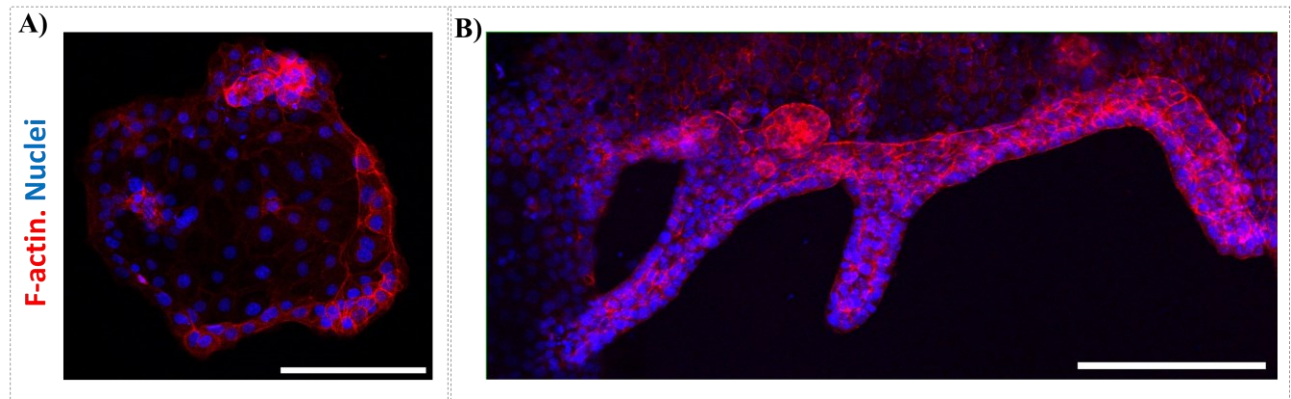


Fig. 2.6 Effect of fibroblasts on the formation of lung organoid (LOi). A) Airway epithelial cells in geltrex without lung fibroblasts. B) Images showing typical tubular morphology of lung organoids on day 7. Red-F-actin. Blue-Nuclei. Magnification 10X. Scale Bar 200 μm .

Different input densities of fibroblasts were tested. Organoids were successfully formed when using a density of one fibroblast for every two epithelial cells. Reducing the number of fibroblasts of one fibroblast for three epithelial cells also resulted in the formation of organoids. A larger number of fibroblasts per epithelial cells, in a 1 to 1 ratio, disrupted the organoid formation. This caused cells to remain rounded and form aggregations with loose packing, as shown in Fig. 2.7. To maintain consistency between batches, a 1/2 cell ratio was selected to induce organoid formation.

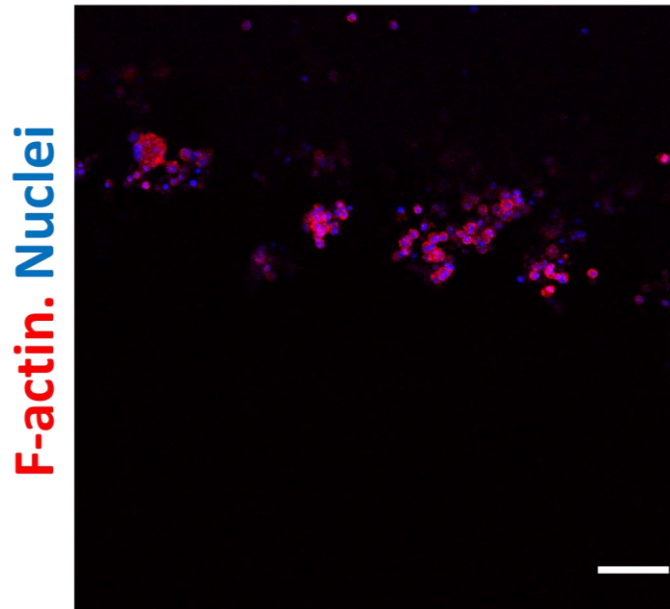


Fig. 2.7 Representative image of resulting cell aggregations on day 7 when fibroblasts are incorporated in equal density with airway epithelial cells. Magnification 10X. Red-F-actin. Blue-Nuclei. Scale Bar 100 μ m.

2.3. 4 Comparative Analysis of Hydrogels and Impact on Organoid Development

Two hydrogel configurations were used to test their impact on organoid formation and to evaluate if they can potentially overcome the limitations of AIGe. Gelatin methacryloyl (GelMA)-based hydrogels have been used as biocompatible and reproducible substrates to allow 3D cell culture, in particular spheroids, and cancer models¹⁰⁹. Lung fibroblasts were embedded in a GelMA precursor solution and polymerized with UV light, as stated in the methods chapter (2.5.4). On the next day, geltrex was added as a second layer followed by CFBE in optimized density (5×10^7 /ml). A 3D cellular structure was observed in one-half of the samples (Fig.2.8A) with variability in their morphology (Fig.2.A). No 3D cellular structure was formed in the remaining samples. Instead, cells remained rounded (Fig.2.8B). After day 7 of culture, the 3D structures were disrupted, with individual cells clustered together without specific structure like Fig.2.8B.

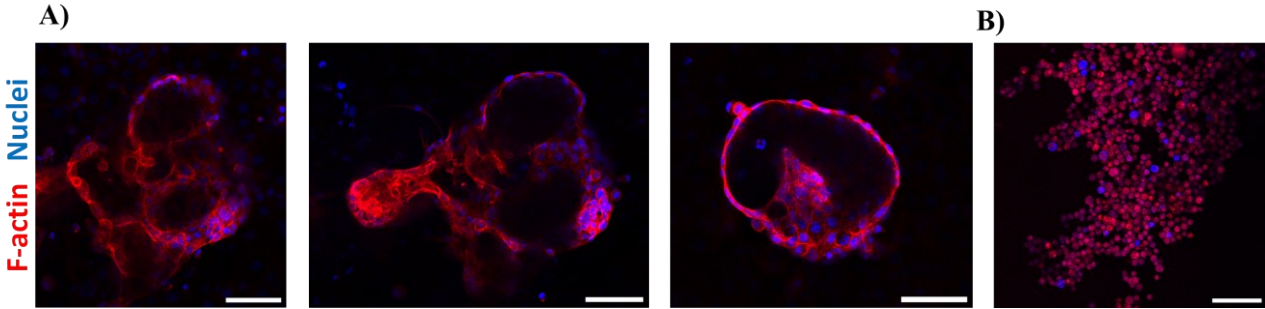


Fig. 2.8. 3D cellular structures generated in GelMA hydrogel on day 7. **Red-F-actin**. **Blue-Nuclei**. Magnification 10X. Scale Bar 100 μ m.

Alginate, modified with *Arginine-Glycine-Aspartic Acid* (RGD), was mixed with 5% Gelatin (Al-RGD-Ge) to encapsulate lung fibroblasts. RGD conjugation was confirmed using Fourier-transform infrared spectroscopy, as show in Fig. 2.9.

The adhesion of epithelial cells to the hydrogel surface without geltrex was first tested. Epithelial cells were not binding to the surface for this RGD concentration. Therefore, AlGe was substituted for Al-RGD-Ge as substrate for fibroblast encapsulation.

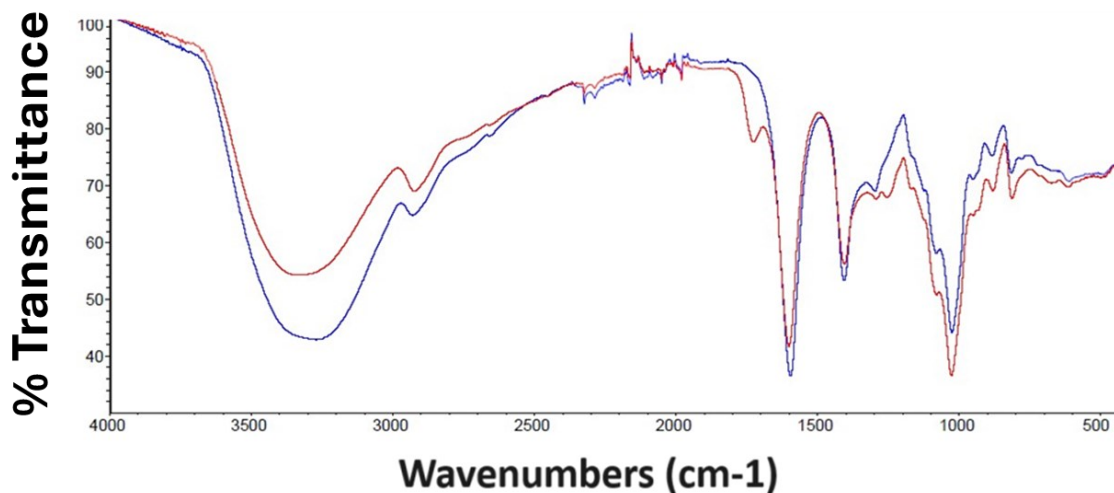


Fig. 2.9. Fourier Transformed Infrared Spectroscopy Analysis of **Alginate** (blue) and Alginate conjugated with **RGD** (red).

The morphology of organoids in AI-RGD-Ge was found to be similar to the ones generated using AI-Ge as substrate. The incorporation of RGD did not significantly affect the size or the viability of the organoids (Fig. 2. 10A, B). The percentage of live cells cultured in AI-Ge at day 30 was 58.42 ± 1.44 . In AI-RGD-Ge, it was 55.61 ± 4.22 . The length of organoids grown in AI-Ge and AI-RGD-Ge substrate at day 30 was 1.1 cm. The stiffness (Fig.2.10C), of AI-Ge was initially 2.02 kPa. It decreased to 1.56 kPa at day 7. AI-RGD-Ge had an initial stiffness of 1.27 kPa which decreased to 481 Pa at day 7. These stiffness values are representative of the lung, at around 1.50 kPa⁵³. AI-RGD-Ge was found to be more brittle than AI-Ge, which makes it more difficult to handle. There were no significant advantages of using AI-RGD-Ge. Given the complexity and cost, AI-Ge was selected for subsequent studies.

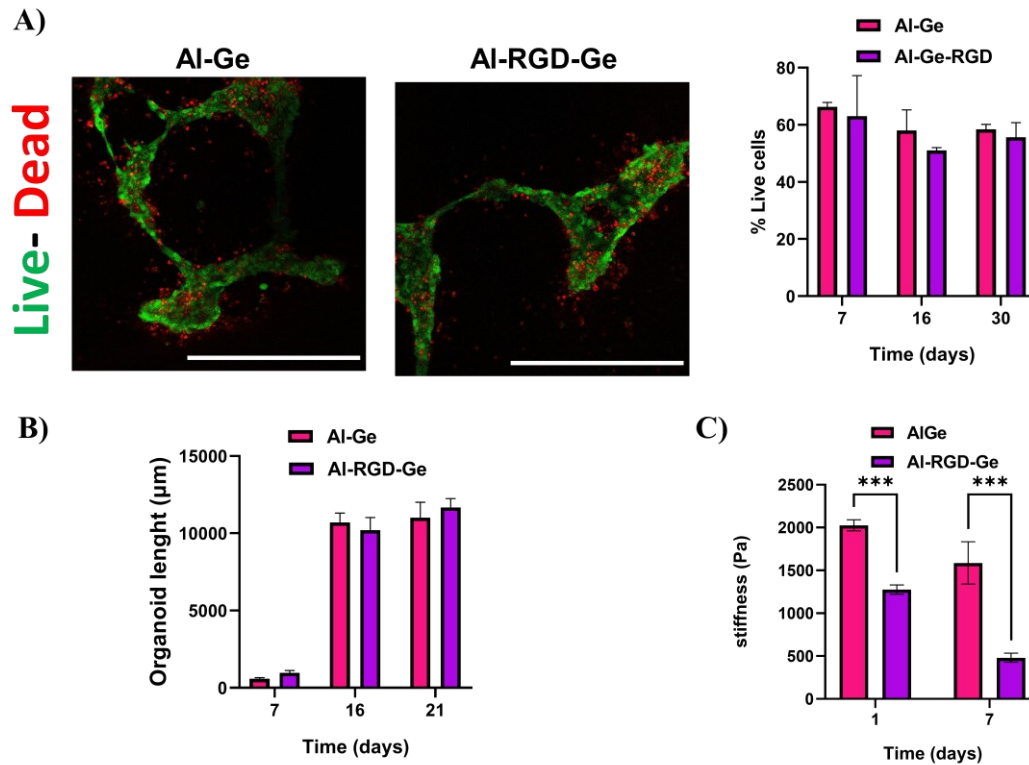


Fig. 2.10. Effects of AI-RGD-Ge substrate on organoid formation. A) Viability of organoids grown in AI-Ge (pink) and AI-RGD-Ge (purple) substrate images and percentages. Representative micrographs showing in Red-dead cells, and in green-live cells on day 7. Magnification 10X. Scale Bar 500 µm. Percentages of live cells in both substrates over time. N=3. Two-way ANOVA analysis shows no significant change. B) Organoid length over time (µm) N=3. Two-way ANOVA analysis shows no significant change. C) Stiffness of AI-Ge (pink) and AI-RGD-Ge (purple). N=3. Two-way ANOVA analysis. $P < 0.005$.

2.3.5 Effect of Feeder Cell Sources for Organoid Cultures

To elucidate the role of feeder cells on the organoid morphology, human vocal fold fibroblasts (hVFF) were used instead of lung fibroblasts. The hVFF derived organoids had a different morphology than that of the ones derived from lung fibroblasts, as shown in Fig. 2.11. Instead of one main tubular structure with ramifications, two prominent tubular structures were formed enclosed together. This striking difference suggests a

significant role of feeder cells in directing the fate of the organoids and influencing the branching morphogenesis process. By utilizing hVFF as feeder cells, we provide further evidence supporting the hypothesis that the cellular microenvironment, particularly the choice of feeder cells, exerts profound effects on the structural organization and development of lung organoids.

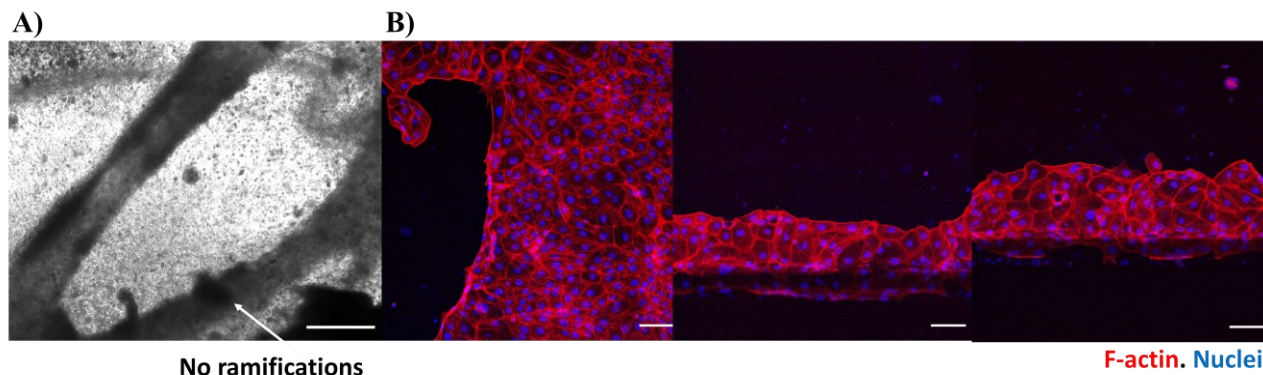


Fig. 2.11. Organoids derived using vocal fold fibroblasts as feeder cells on day 5. A) representative brightfield image. Magnification 4X. Scale Bar 500 μm . B) Immunofluorescence images. Red-F-actin. Blue-Nuclei. Magnification 10X. Scale Bar 100 μm .

2.3. 6 Effect of Culture Medium for Organoid Development

Lung Organoid Maturation Medium (3dGRO™) was used to culture organoids instead of the mixture of DMEM: MEM medium. 3dGRO™ is enriched with epithelial growth factors, Noggin, and Wnt3A. According to the supplier, this medium helps to the maturation of lung organoids and promotes an arborized morphology. But there was not apparent advantage of using this product over DMEM: MEM. The organoids grown in both media had a similar morphology at day 7, Fig.2. 12. At day 16, the organoids grown using 3dGRO™ were smaller in size with a lower cell density than the ones grown in DMEM: MEM.

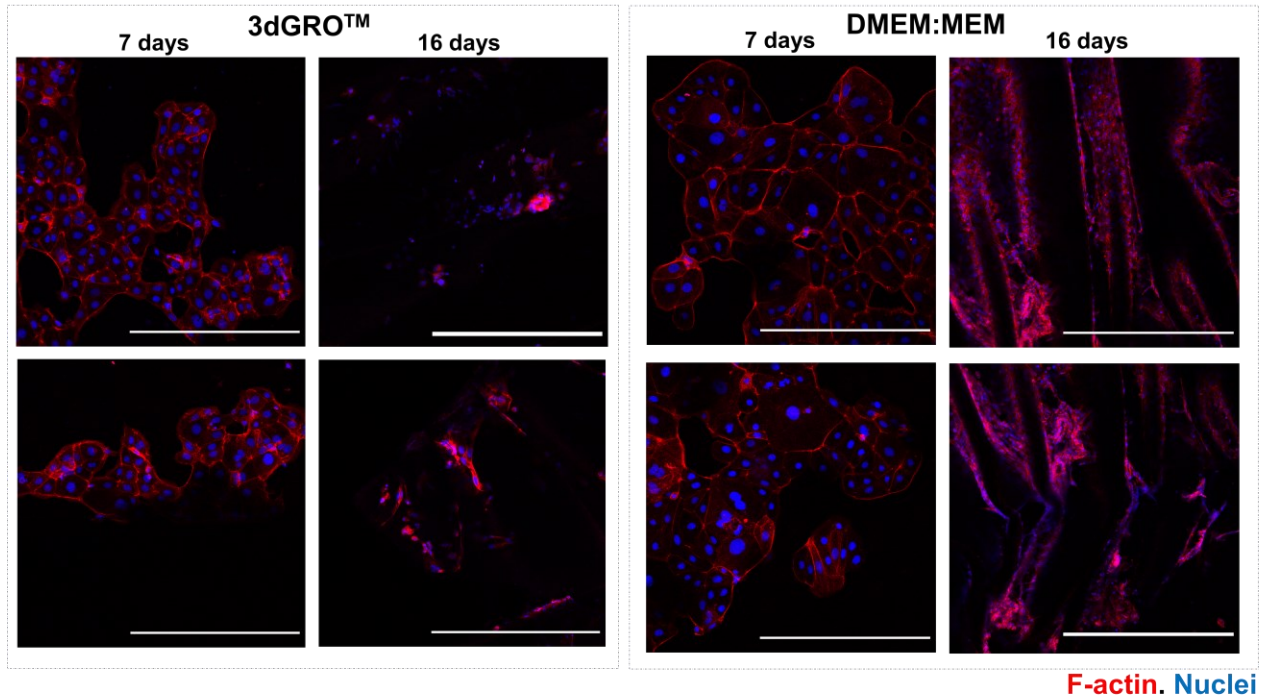


Fig. 2.12. Effect of cell medium on lung organoid culture over time. Representative images. Red-F-actin. Blue-Nuclei. Magnification 10X. Scale Bar 500 μ m.

2.3.7 Investigation of organoid morphology by Transmission Electron Microscopy and Focused Ion Beam Microscopy.

Organoids derived from immortalized cells (LOi) were visualized using Transmission Electron Microscopy (TEM) following a 21-day culture period. Figure 2.13 depicts the subcellular architecture of LOi along with their extracellular matrix (ECM) interface, observed at a magnification of 3300X. Evidence of autophagy was discerned. Additionally, Figure 2.14 showcases the subcellular structure of the organoids at a magnification of 5500X, while Figure 2.15 presents representative microphotographs of LO at a magnification of 7000X. Figure 2.16 shows representative microphotographs of LOi using Transmission Electron Microscopy at 8600 X, while Figure 2.17 shows the structures at 11000X magnification.

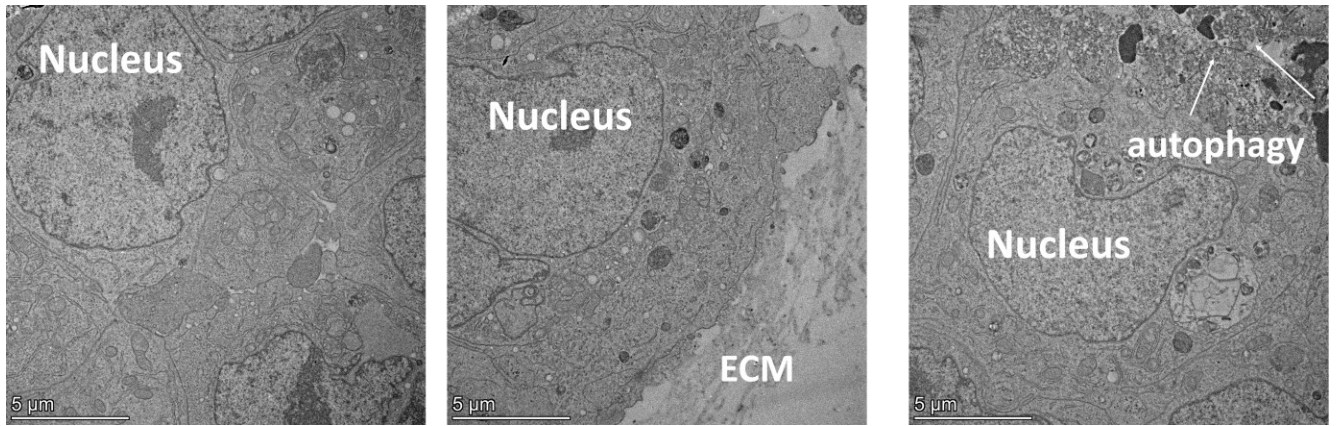


Figure 2.13 Representative microphotographs of LOi using Transmission Electron Microscopy at 3300X Magnification. Scale Bar 5 μm . Arrows point to signs of autophagy.

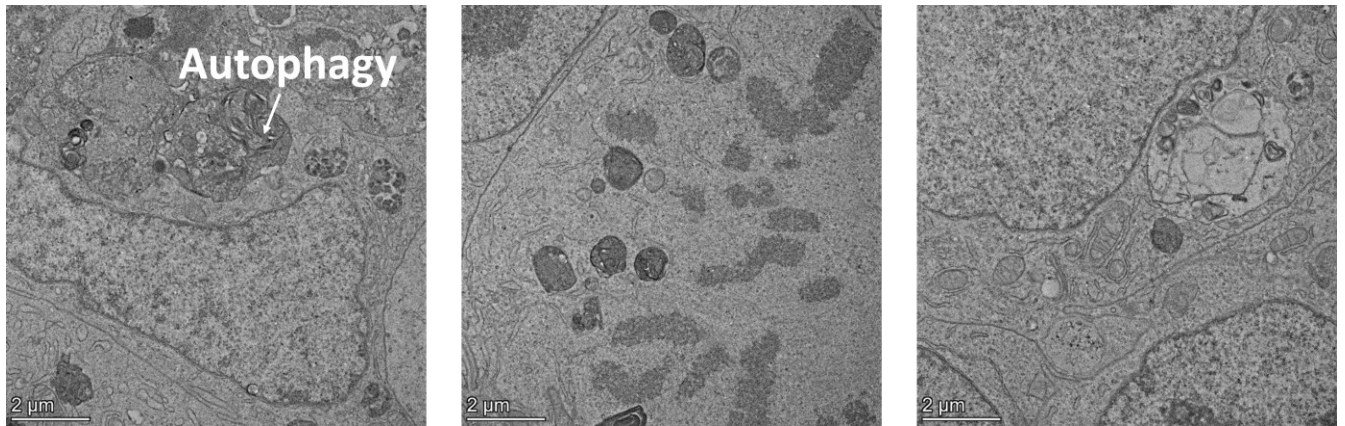


Figure 2.14 Representative microphotographs of LOi using Transmission Electron Microscopy at 5500X Magnification. Scale Bar 2 μm .

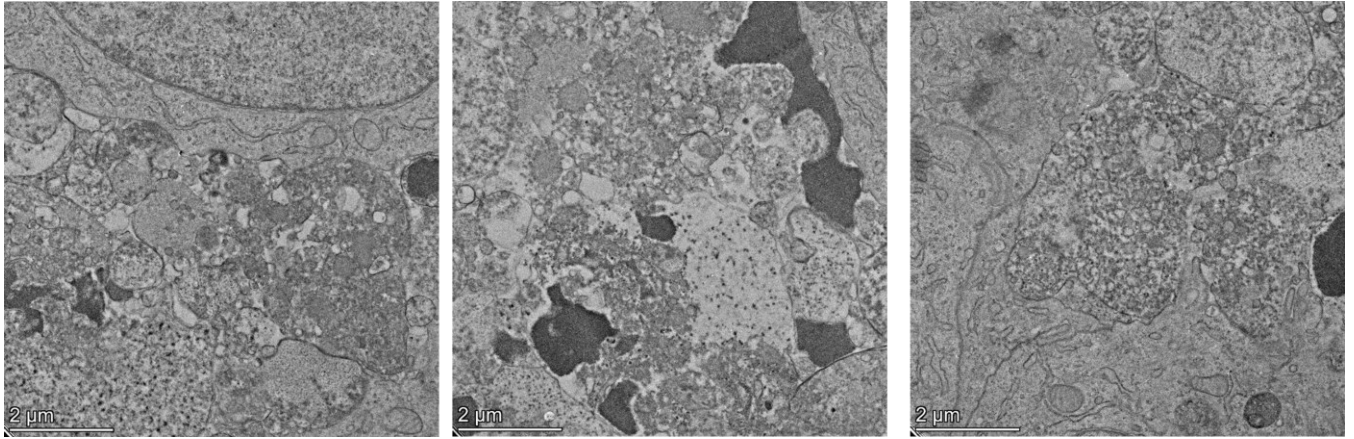


Figure 2.15 Representative microphotographs of LOi using Transmission Electron Microscopy at 7000 X Magnification. Scale Bar 2 μm

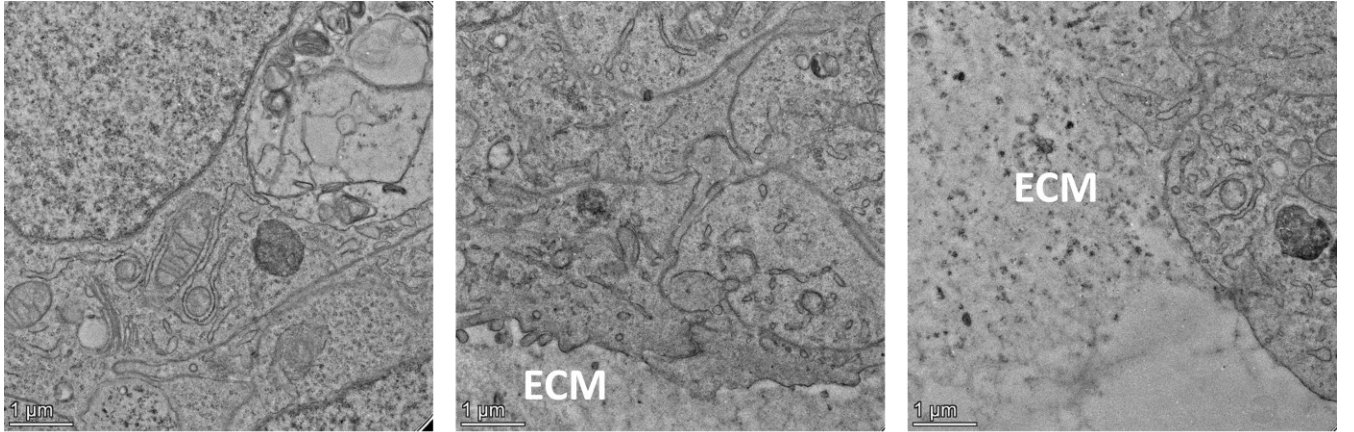


Figure 2.16 Representative microphotographs of LOi using Transmission Electron Microscopy at 8600 X Magnification. Scale Bar 1 μm.

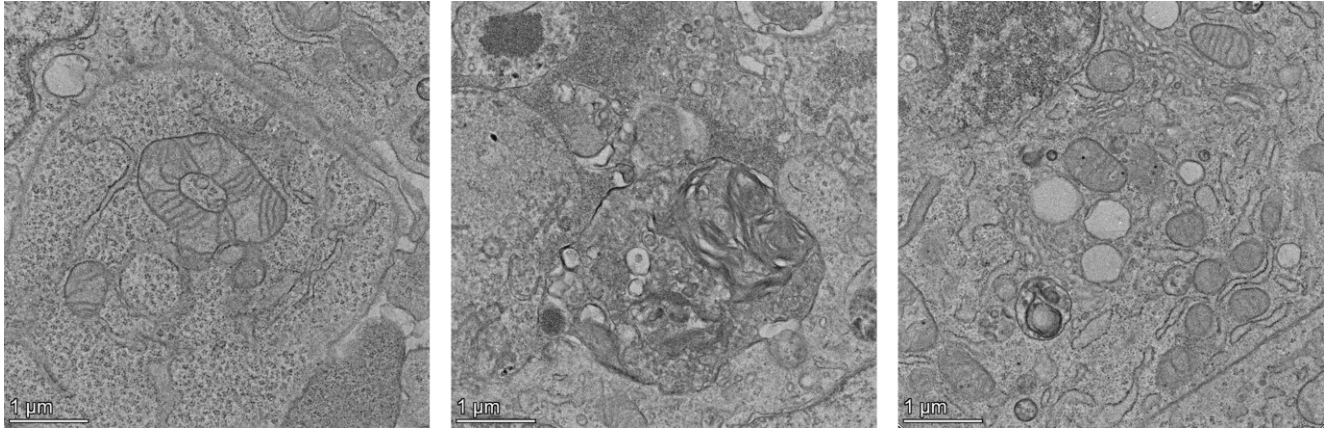


Figure 2.17 Representative microphotographs of LOi using Transmission Electron Microscopy at 11000 X Magnification. Scale Bar 1 μm .

Concurrently, an investigation of LOi was carried out utilizing Focused Ion Beam (FIB) Microscopy. Figure 2.18 provides an overview of select regions within an organoid cultured for 21 days, captured at lower magnifications. Notably, airway epithelial cells are discernible, forming a tubular-like structure. This architectural feature is further illustrated in Figure 2.19 at a magnification of 40X.

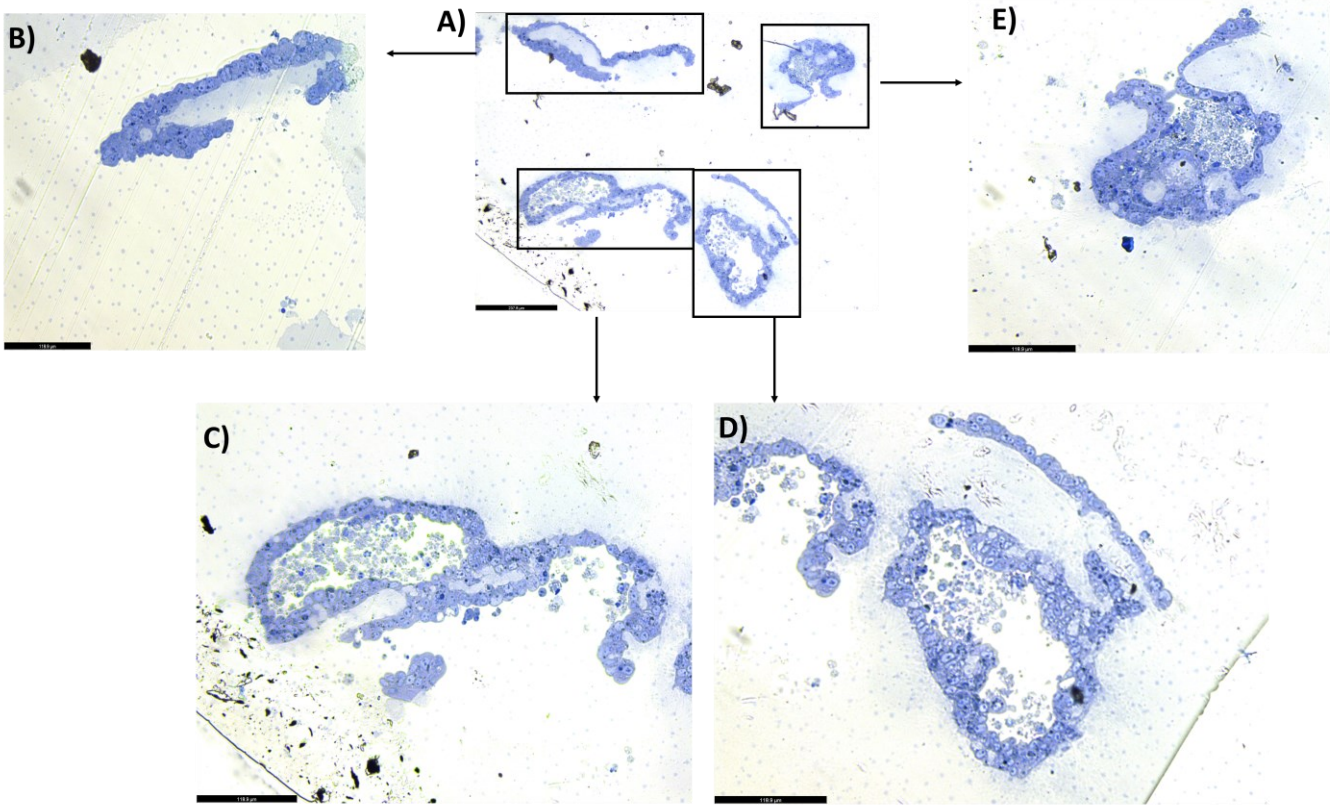


Fig. 2. 18. Overview of LOi at 21 days of culture using light microscopy. A) Magnification 10 X. Scale Bar 237.8 μm . B-E) Magnification 20 X. B) Scale Bar 118.9 μm C) Scale Bar 118.9 μm D) Scale Bar 59.4 μm E) Scale Bar 59.4 μm .

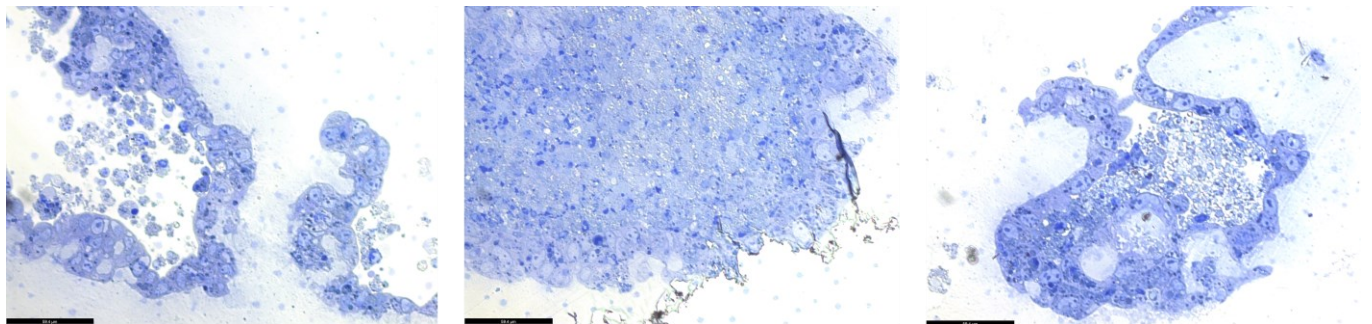


Fig. 2. 19 Microphotographs of airway epithelial cells forming an organoid structure. Visualized with light microscopy. Magnification 40X. Scale Bar 59.4 μm .

The organoid was imaged at varying higher magnifications, including 500X, 1000X, 2000X, and 3500X as depicted in Figures 2.20-2.22. These close observations revealed intriguing features, including the alignment of cells within the organoid structure and

discernible morphological variations among individual cells. Particularly noteworthy were the distinct cellular arrangements observed within different regions of the organoid. Some regions exhibited stratified airway epithelial cells, characterized by multiple layers of epithelial cells stacked upon each other, while in other regions, a pseudostratified arrangement was apparent, where only a single layer of epithelial cells was observed. These findings underscore the complexity and heterogeneity of cellular organization within the organoid, shedding light on its structural diversity.

Additionally, images captured at magnifications of 5000X, 8000X, and 10000X are presented in Figures 2.23-2.27. These images reveal detailed subcellular structures, indications of autophagy, and the presence of microvilli structures (indicated with arrows). Microvilli are microscopic membrane cellular protrusions which are involved in the process of absorption of nutrients and cellular secretion¹¹⁰. They have a significant function in transmitting signals that trigger immune responses¹¹¹. The emergence of microvilli suggests a level of cellular differentiation and specialization within the organoids, despite their origin from cell lines that are traditionally considered homogeneous^{29,30}. This finding challenges the notion of cellular homogeneity within the organoids and underscores their dynamic nature, potentially reflecting a degree of cellular plasticity and functional diversity. Notably, the identification of microvilli, which are typically associated with brush cells in the lung¹¹², further highlights the organoids' ability to mimic essential characteristics of native lung tissue. This aspect emphasizes their relevance as a model system for studying respiratory physiology and pathology.

Autophagy is the process of degrading cytoplasmic components within lysosomes¹¹³. This process, which is abundant in LOi, serves various physiological functions, including

adaptation to starvation, clearance of intracellular proteins and organelles, development, anti-aging, elimination of microorganisms, cell death, tumor suppression, and antigen presentation¹¹³. Interestingly, autophagy has been associated with the regulation of lamellar body formation¹¹⁴. Lamellar bodies are concentric structures loaded with surfactant proteins specific to AT2 cells¹¹⁴. While the reason for the high presence of autophagy in the organoids is not certain, one possibility could be its involvement in the development of these organelles.

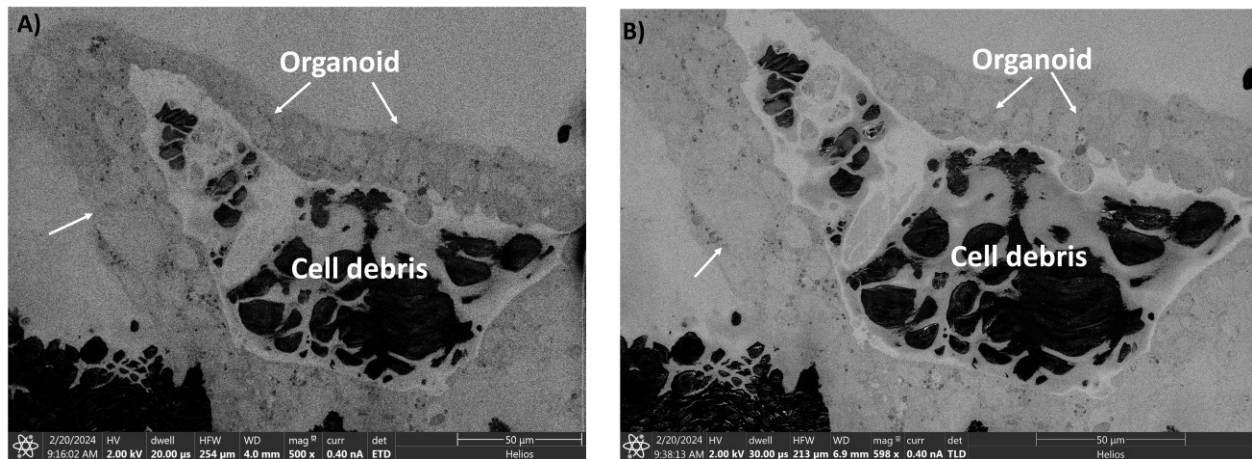


Figure 2.20 Microphotographs of LOi at day 21 using FIB microscopy. A) Magnification 500X. B) Scale Bar 598X. Scale Bar 50 µm. Arrows indicate the airway epithelial cells in a tube-like structure.

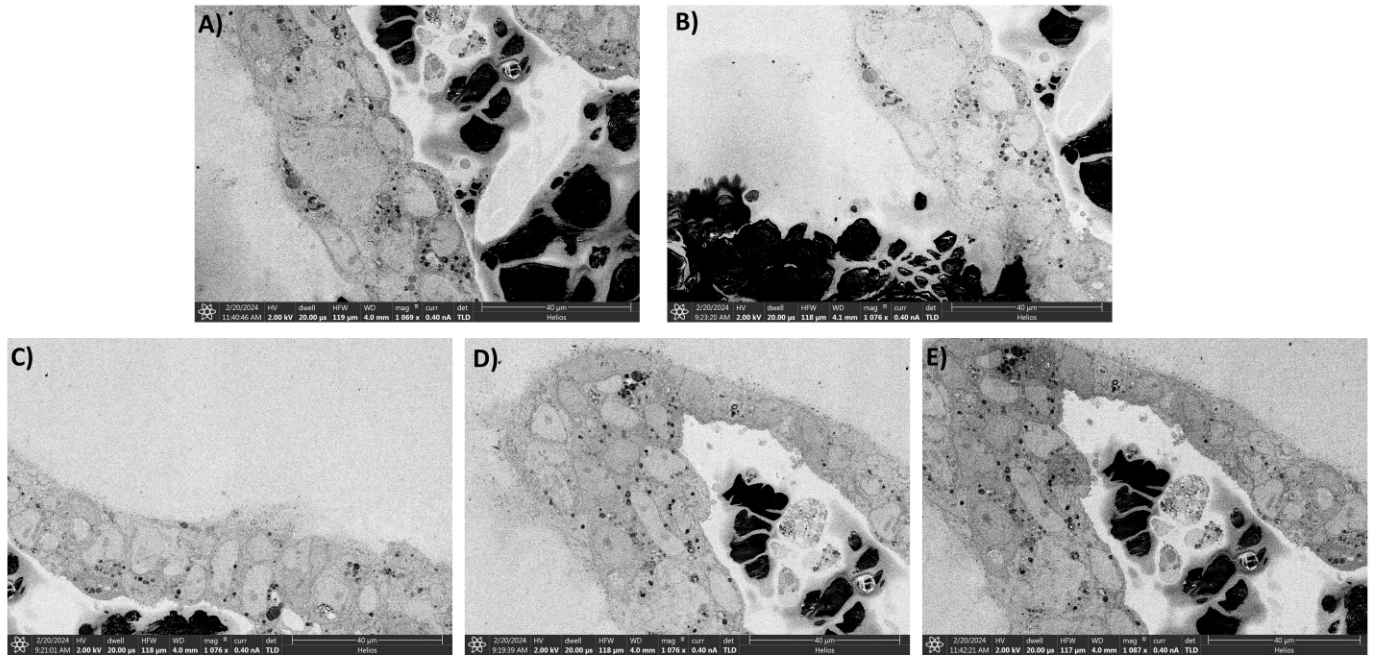


Figure 2.21 Microphotographs of LOi at day 21 using FIB microscopy with magnifications exceeding 1000X. The images reveal multilayers of airway epithelial cells exhibiting distinct morphologies, contributing to the formation of the organoid structure. Scale Bar 40 µm. A) Magnification 1069X. B-D) Magnification 1076X. E) Magnification 1087X.

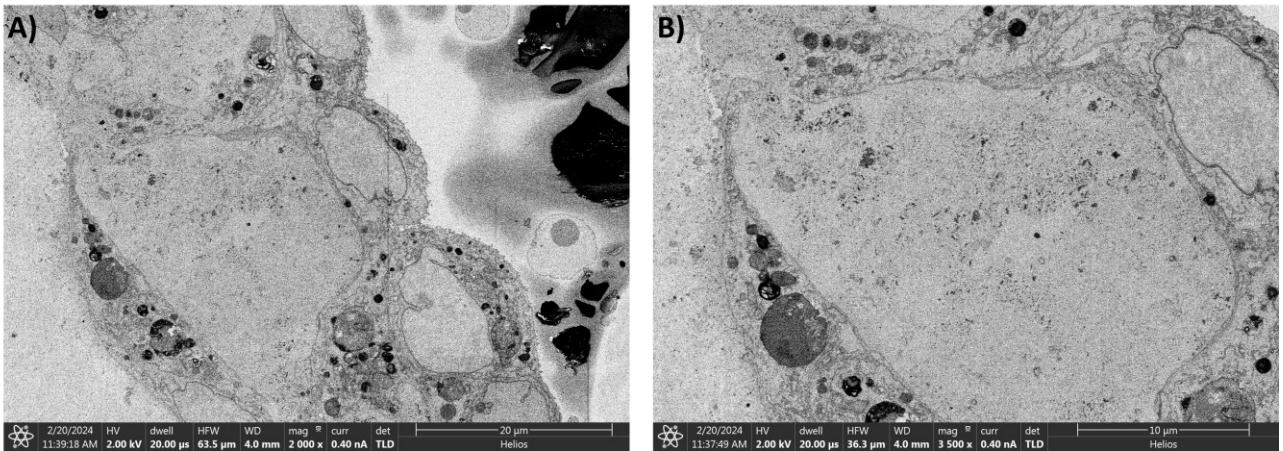


Figure 2.22 Microphotographs of LOi at day 21 using FIB microscopy with magnifications of A) 2000X and B) 3500X. Scale Bar 20 µm.

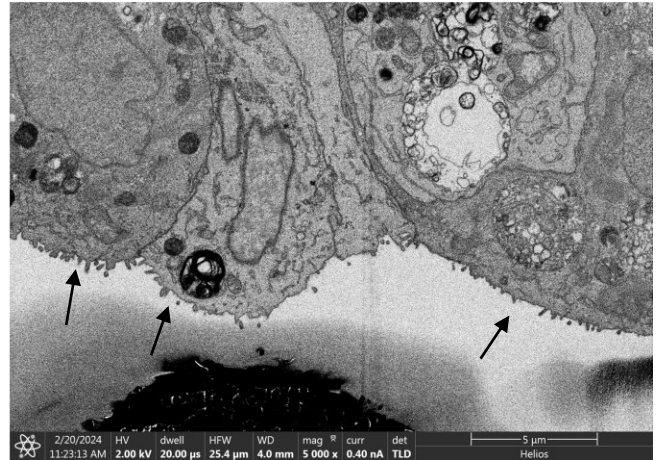
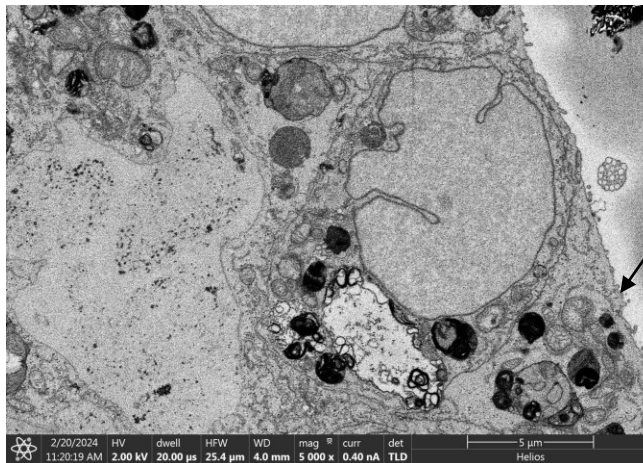


Figure 2.23 Microphotographs of LOi at day 21 using FIB microscopy with magnifications of 5000X. Scale Bar 5 μm . Arrows indicate microvilli structures.

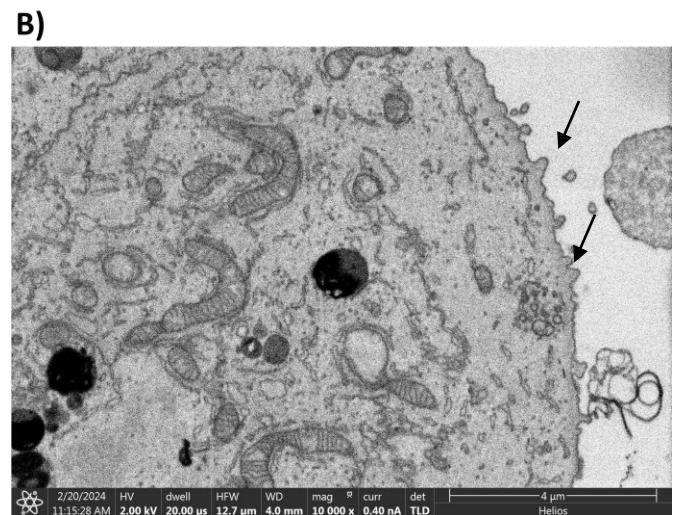
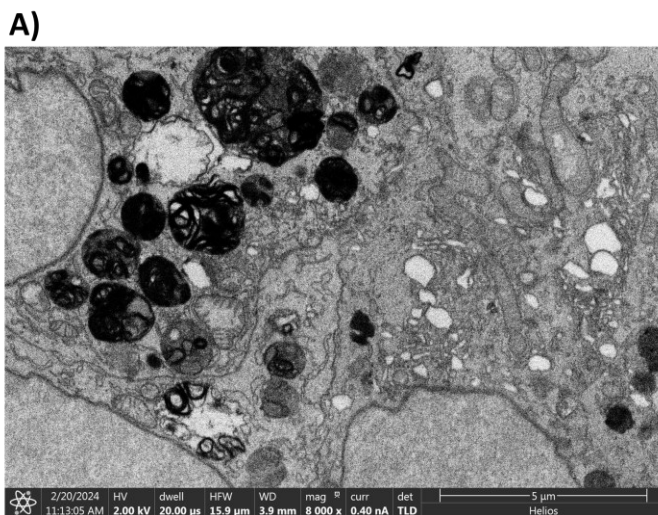


Figure 2.24 Microphotographs of LOi at day 21 using FIB microscopy with magnifications of A) 8000X and B) 10000X. Scale Bar 5 μm . Arrows indicate microvilli structures.

2.3.8 Investigation of bioprinting for the fabrication of lung organoids.

Bioprinting was explored to automate the fabrication of lung organoids to reduce costs and reduce variability due to manipulations. The goal is to improve the robustness of the model and ease their handling. Biofabricated models can easily be transported to a

spinning bioreactor⁷¹. The use of spinning bioreactors for culturing organoids enhances oxygen and nutrients absorption, allowing preservation over a longer time^{71,115}.

The LO generated in this study can be used until day 30. Afterwards, some degree of disintegration of the organoid is observed. Manipulation of the organoid grown in transwells is difficult, hampering potential high throughput characterizations.

A 3D bioprinter (BioX Cellink) was used to extrude AIge containing lung fibroblasts solution into 96-well plates. A “Droplet” configuration was used while extruding the solution. On the second day, a layer of geltrex was used to coat the droplets. After polymerization, airway epithelial cells, CFBE, were added on the top of the gel.

Three different densities were tested. During manual fabrication every organoid had an initial cell density of 250,000 cells deposited in 100 μ l of AIge. To keep the cell original density, OG, per organoid, 10 million IMR-90 cells per ml were used in bioprinting. Every droplet included 25 μ l of solution, and approximately 250, 000 cells. To reduce the cell concentration, solutions were diluted 100 times, 0.01 OG, or 10 times, 0.1 OG.

The diameter of the droplets was measured using widefield microscopy. The results of the first step of fabrication are illustrated in Table 2.1. It was observed that the droplets shrunk over time regardless of the cell density. They were robust and maintained their shape beyond 30 days of culture. The thickness of the droplets was 2 mm, much greater than that of 100 μ m, achieved by manual methods, thereby improving their cohesiveness for handling. The 0.01 OG cell concentration was used for the deposition of Geltrex and CFBE.

The resulting lung ‘organoids’ were kept for more than 30 days in static conditions, without evident disassociation. Organoids could be handled with tweezers and cultured

them into a spinning bioreactor over 21 days with no signs of damage. These results are illustrated in Fig. 2.25.

Time after printing (days)	Diameter (mm)			Average diameter (mm)	Standard Deviation (mm)	% Shrinkage
	Concentration					
	OG	0.1 OG	0.01 OG			
2	4724	4729	4368	4607	207	NA
3	4523	4583	4294	4467	152	3.04
7	3924	3716	3723	3788	117	15.20
14	3761	3714	3800	3759	43	0.76
21	3747	3777	3754	3759	15	0.02

Table 2.1 Average diameter of bioprinted droplets of AIGe and lung fibroblasts for three different cell densities.

Based on the preliminary characterisation results, automated biofabrication has the potential to achieve a faster fabrication rate (35 seconds per droplet), higher reproducibility (in terms of size), a higher flexibility in varying cell density, and greater organoids robustness.

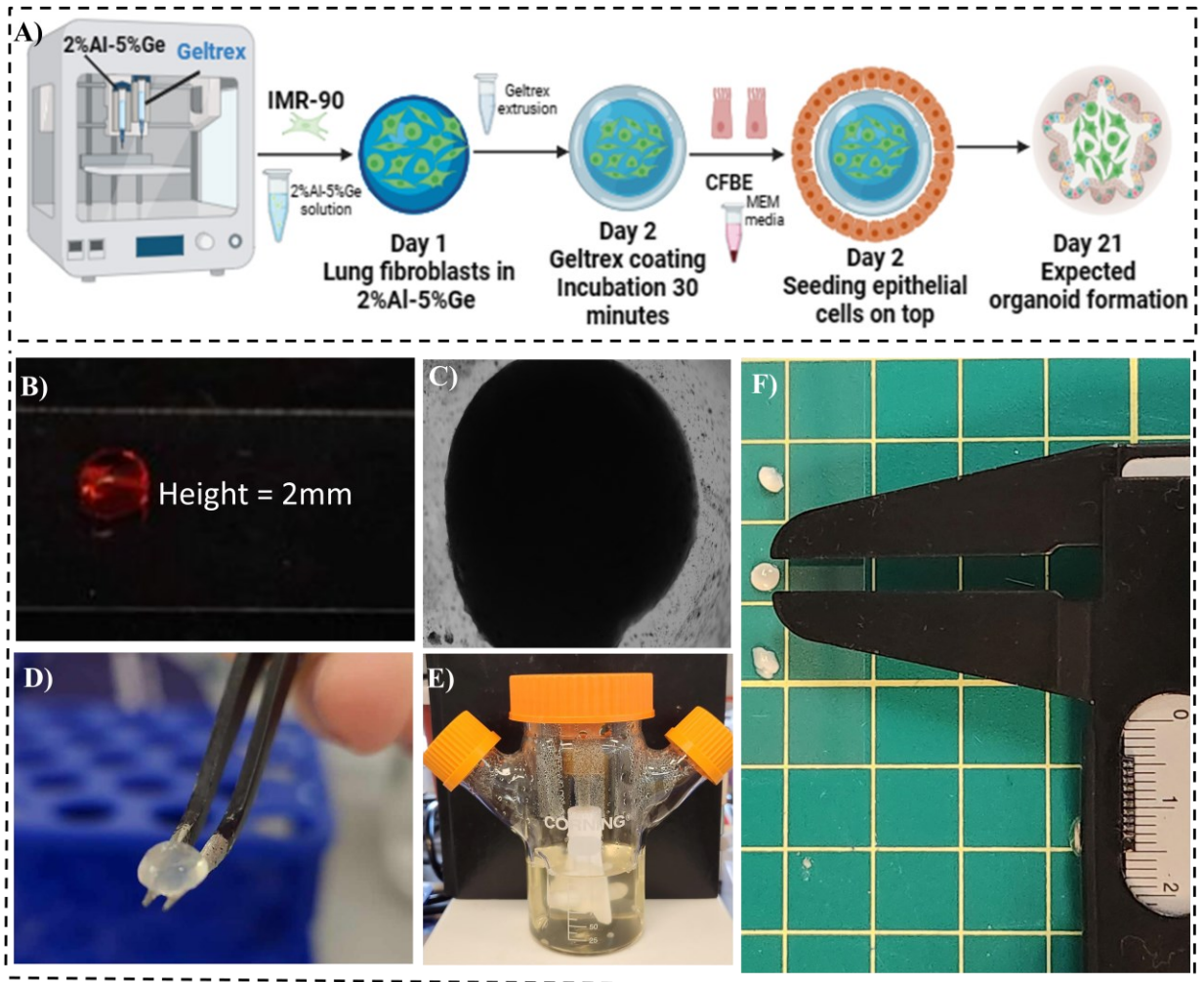


Fig. 2.25 Bioprinting lung organoids. A) Schematic representing the overall protocol. Generated by Bio Render. B) AlGe droplet with 2 mm of height. C) Representative lung 'organoid' on day 21. Magnification 2X. D) Robustness of 'organoids' which can be handled with tweezers. E) Lung 'organoids' growth on spinning bioreactor. F) Organoids were retrieved after being cultured on a spinning bioreactor for 21 days.

2. 4 Discussion

The protocol to induce the formation of lung organoids consists of encapsulating lung fibroblasts in 2%Al and 5%Ge. On day 2, BMZ proteins from geltrex are used to cover the hydrogel, and airway epithelial cells are seeded on top. The organoids are formed early, and over time they form tubular structures with some ramifications. They can be kept in culture until day 30. This protocol could be used for both primary airway

epithelial cells from trachea/bronchi and immortalized epithelial cells, CFBE. The organoids morphology was similar for both type of cell inputs.

Adjustment of fibroblasts density was instrumental to the formation of organoids. Fibroblasts act as feeder or supporting cells to the epithelium. Therefore, the use of an equal or greater fibroblasts concentration than that of airway epithelial cells was detrimental for the formation of the organoid. Since fibroblasts are encapsulated in hydrogels, the hydrogel properties are extremely important to maintain an adequate balance between cell viability and proliferation. Alginate-gelatin mixture was found to maintain a fibroblasts viability over 80% on day 7 and did not induce their proliferation. Conversely, GelMA induced the proliferation of fibroblasts leading to premature disruption of the organoid. Another problem with GelMa is the need for crosslinking by using UV light. This hydrogel has successfully been used to make spheroids¹⁰⁹. But not for organoids, which are more complex structures⁵¹. UV light can damage the cells resulting in carcinogenesis and DNA mutations¹¹⁶. This may explain the propensity for organoid dissociation and their variable morphology.

The incorporation of RGD was expected to improve the surface adhesion of the hydrogel to support epithelial cells growth without geltrex. But the AI-RGD-Ge hydrogel did not offer any evident advantage over AI-Ge and added complexity to the fabrication process. Additionally, 2%AI and 5%Ge was found to have a stiffness representative of that of the lung, making it a compliant substrate. It is also inexpensive, and its preparation is relatively simple in comparison to more sophisticated hydrogels.

Organoids so far, rely extensively on the use of extracellular matrix proteins contained in Matrigel or Geltrex. To induce further differentiation, they use exogenous factors in

cell medium⁵¹. For airway organoids (proximal) FGF is added, specifically FGF7, FGF10, noggin, R-spondin-1, Primocin and other differentiation molecules^{65,66}. For alveolar organoids (distal) Wnt3a, dexamethasone and Primocin are normally used⁷⁵. Other protocols use Wnt activator and Rho kinase inhibitor⁶¹. For proximal and distal patterning of immature lung organoids, medium is supplemented with FGF4, FGF7, Noggin, Wnt inhibitor (CHIR99021) at different times of culture²¹. Branching media and Lung Organoid Maturation Medium (3dGRO™) are also used to induce maturation of lung organoids⁷⁷. According to the information of the product, this medium contains Wnt3a, R-spondin-3, and Noggin. We used this medium since it contains a mixture of molecules to induce proximal and distal differentiation of the lung. We compared the organoids cultured on DMEM: MEM, with the ones cultured using 3dGRO™. Organoids grown in DMEM: MEM display more elongated structures and ramifications, as well as higher cell density, they look overall more robust than the ones grown in 3dGRO™. Our protocol, distinct from others, does not use exogenous molecules since fibroblasts are incorporated in the model to produce these factors. Although we are uncertain about the quantities and exact molecules that fibroblasts produce under the established culture conditions, they seem to be equivalent or even superior to the mixture of differentiation molecules normally used. This aspect simplifies the protocol and culture conditions to maintain the organoids. Additionally, it reduces the cost per organoid. For instance, 3dGRO™ (Millipore SIGMA) cost cad \$622 for 250 ml, while DMEM and MEM cost of cad \$34 per 500 ml¹¹⁷.

Our protocol as others relies on BMZ proteins^{5,21,65,66,77}. This is a key component of the protocol in the generation of the organoid. However, the use of geltrex alone is not

sufficient to induce consistent tubular organoids, which can be maintained over long time periods.

Interestingly, the source of feeder cells affects the morphology, and probably phenotype of the organoid. When VFF were used, an atypical morphology was observed. Instead of tube with ramifications, two tubes were enclosed together. Future work can be directed to the study of the molecules secreted by the two different types of fibroblasts to elucidate how they are involved in the branching morphogenesis process.

Further morphological examination of LOi using FIB microscopy revealed heterogeneous structures within the organoids. Some regions exhibited stratified epithelium, whereas others displayed pseudostratified epithelium. Microvilli were observed on the surface of certain cells, indicating the differentiation potential of the CFBE cell line within the provided microenvironment post-organoid formation. Interestingly, previous reports indicated that this cell line retained its differentiation characteristics similar to primary airway epithelium¹¹⁸. Typically, microvilli are found on brush cells in the lung¹¹² and play roles in nutrient secretion and absorption, as well as in the activation of immune cells¹¹¹. Some regions of the organoids are characterized by stratified epithelium, while others are characterized by pseudostratified epithelium. This underscores the relevance of the organoid model since it partially mimics the heterogeneity and complexity of the lungs. Transmission electron microscopy and FIB microscopy revealed that autophagy was notably abundant in LOi organoids. This process has several physiological roles, such as promoting development, adaptation to starvation, clearing proteins, and remarkably in the regulation of lamellar body formation^{113,114}. Lamellar bodies are specialized organelles containing surfactant proteins specific to AT2 cells¹¹⁴. While the exact reason

for the heightened presence of autophagy in the organoids remains uncertain, it is plausible that it plays a role in their organelle development.

The low viability of organoids is a common problem in the field¹¹⁹. Our LOi has a viability around 55% on day 30, which can be improved. One strategy to improve this issue, is culturing the organoids on spinning bioreactors to allow higher diffusion of oxygen and nutrients⁷¹. To do this, and to automatize our protocol, we explored the use of bioprinting. Further characterization of the 'organoids' made with this technique is needed to confirm the similarities with manual organoids. Nevertheless, the printed 'organoids' show robustness even when grown on spinning bioreactors. This method holds potential to reduce fibroblast density, to enhance organoid viability and to improve their manageability.

Attempts were made to reduce the number of steps in the protocol. For instance, fibroblasts and epithelial cells were incorporated simultaneously in geltrex. This led to the formation of random cell aggregates, which disassociated easily. Airway epithelial cells seeded on geltrex were cultured with fibroblast supernatant. This led to spherical lung organoids. Therefore, we confirmed that each step in the protocol developed in this chapter is essential for the successful formation of tubular organoids. The protocol was reproducible. The organoids reached a length of 1.2 cm at day 21. Such large size has only been reported when bioprinting was used to fabricate the model¹²⁰. Our model is the largest self-grown lung organoid.

Organoid formation depends on living cells, which may be subject to variations between cultures and culture conditions. For instance, slight differences in incubator conditions, may lead to variation in the proliferation rate of fibroblasts. The protocol developed in

this study accounts for these variations, yielding a working range between 1:3 to 1:2 of fibroblast per epithelial cells. BMZ proteins are derived from tumor cell lines. There are possible variations from batch to batch, mainly reported when using Matrigel⁶⁰. Fibroblast co-culture seems to help to overcome those variations.

The goal of the protocol was to induce the formation of lung organoids which represent the entire phenotype of the lung, including proximal and distal regions using either primary airway epithelium or immortalized epithelium. Based on the morphology obtained, we were encouraged to fully characterize these organoids and compare them against traditional 2D cultures and adult lung tissues. The results of these experiments are presented in Chapter 3.

2. 5 Methods

2. 5.1 Cell culture

CFBE and IMR-90 were cultured in Eagle's minimum essential medium (VWR, CA45000-380) supplemented with 10% (vol/vol) FBS (Sigma-Aldrich, F1051), 2 mM L-glutamine (Thermo Fisher, A2916801), 1% Penicillin Streptomycin (Fisher Scientific, SV30010), and incubated at 37°C in 5% CO₂-95% O₂. Human Vocal Fold Fibroblasts were cultured in DMEM medium supplemented with 10% (vol/vol) FBS (Sigma-Aldrich, F1051), 1 % Amino acids (ThermoFisher, 11130051) 1% Penicillin Streptomycin (Fisher Scientific, SV30010), and incubated at 37°C in 5% CO₂-95% O₂.

2.5.2 Induction of adult human lung organoids derived from airway epithelial cells.

Human fetal lung, IMR90, cells were cultured overnight in different alginate-gelatin hydrogels with a density of 250,000 cells per/cm² using DMEM (Corning, 15-017-CV) with Penicillin-Streptomycin (Fisher Scientific, SV30010) non-essential aminoacids (Fisher Scientific, LS11140050) and FBS (Sigma-Aldrich, F1051) at 37°C. The media was removed, and the hydrogels were coated using 100 µl/cm² of Geltrex (Thermo Fisher, A1413202) for 30 min at 37°C. Afterwards, Human Bronchial CF Epithelial cells were seeded on the top with a density of 500,000 cells per/cm² using EMEM (Corning) and L-Glutamine (Thermo Fisher, A2916801) forming a co-culture interface. When primary organoids were made, BEGM media (PACB) was used instead of EMEM. The next day the medium was substituted by a combination of DMEM and EMEM in a ration 1:1 supplemented with 3 mM CaCl₂ (Sigma, Aldrich, C4901). The organoids were

formed by cellular and extracellular matrix interactions. After 5 days of culture, the maturation, branching of the organoids was observed. The organoids were cultured in solution until day 21 at 37°C under a humidified atmosphere with 5% CO₂ and 95% air. During culture, the medium was refreshed every two days at most.

2. 5. 3 Dialysis and lyophilisation of GelMA

GelMA dialysis was done as previously described¹⁰⁹. Gelatin was soaked to a final concentration of 10% (wt/vol) in Milli-Q water at room temperature. While stirring, gelatin solution was heated at 50°C in a water bath until gelatin was fully dissolved and the solution looked clear. A concentration of 0.6 g methacrylic anhydride per 1 g of dissolved gelatin was added. The solution was stirred vigorously over a period of one hour until it looked opaque. The solution was centrifuged for 3 min to remove unreacted methacrylic anhydride. Supernatant solution was diluted with two volumes of preheated Milli-Q water and transferred into a dialysis membrane with 12 kDa molecular weight cutoff and dialyzed at 40 °C against a large volume of Milli-Q water for 5-7 days until GelMa solution was cleared. The water was changing daily. The pH of GelMA solution was adjusted to 7.4 using 1 M NaHCO₃. GelMA solution was sterilized using 0.2 µm filters (SLFGL25BS, SIGMA). The solution was transferred to freeze dryer and they were lyophilized for 7 days¹⁰⁹.

2.5.4 Hydrogel synthesis

2. 5. 4.1 GelMA.

Lyophilized GelMA (10%) was added into PBS at 37 °C and mixed with 2.5 x10⁶/ ml of lung fibroblasts to obtain the precursor solution. The solution was added into ibidi plates

and crosslinked with UV to enable the formation of the hydrogel by photo-polymerization for 10 min with an exposure of 2.7 mW/cm².

2.5.4. 2 A/Ge.

A solution of 2% Alginic acid molecular weight (MW) 212.121 g/mol (Sigma, A0682) was prepared in MilliQ water and sterilized with 0.2 µm PES filter (Fisher Scientific, FB12566502). The solution was mixed with 5% sterile Gelatin type A (Sigma, G2500). The hydrogel was formed by the incubation with 100 mM CaCl₂, MW 147.02 g/mol (ACP, C-0360) for 15 min.

2.5.5 Live/Dead Assay

The viability of the organoids was evaluated after 7, 16 and 30 days of culture using a live/dead kit (Fisher Scientific, L3224). The confocal images were acquired using an inverted confocal laser scanning microscope (LSM710, Zeiss). Live cells were shown in green fluorescence and dead cells were shown in red.

2.5.6 RGD conjugation

RGD conjugation was adapted from previous protocols^{121–124}. Overnight 1% of alginate (A0682, SIGMA) was dissolved in 0.1 M MES buffer, 0.5 M NaCl, at pH 6. Next day, 2 mM of EDC and 5 mM NCH (ThermoFisher, 24510) were added into alginate solution, allowing its reaction for 15 min. Subsequently, pH was raised to 7.3 and 0.1% RGD (AB141092, ABCAM) was incorporated, and let to react for 2 h. 10 mM of Hydroxylamine-HCl was used for quenching the NHS. Dialysis was done for 4 h, and the solution placed in the freeze-dryer.

2.5.7 Rheological measurements

The shear moduli were determined using a torsional rheometer with parallel plates (Discovery HR-2). Isothermal time sweeps were applied at a frequency of 0.1 Hz and 0.1 % strain at 37 °C. The shear moduli were recorded and analyzed using TA instruments software. The Young's modulus (stiffness) was calculated by multiplying the shear modulus by 3. Experiments were conducted in triplicate.

2.5.8 Fourier-transform infrared spectroscopy

FTIR spectra were obtained in ATR mode by placing thin pieces (~ 1mm) of the different hydrogel's compositions in the window of a Perkin-Elmer Spectrum II with diamond crystal. The 4000 to 400 cm^{-1} region was measured with a resolution of 0.5 cm^{-1} .

2.5.9 Immunofluorescence staining

A morphological analysis of the organoids was performed at day 3, 7, 16, and 21 according to the study design. Organoids were washed with PBS (Fisher Scientific, 10-010-049) supplemented with 10 mM CaCl_2 (Sigma, Aldrich, C4901) three times for 3 min. Afterwards, the organoids were fixed with 3.7% paraformaldehyde, permeabilized with 0.3% Triton X-100 (Sigma Aldrich, T9284), and blocked for 2 h with 10% Goat serum (Thermo Fisher, 50062Z) at room temperature. Organoids were cultured with in 10% goat serum at 4°C for 1 hour. Nuclei and actin filaments were counterstained with Hoechst dye (Thermo Fisher H3569) and Phalloidin-647 (Fisher Scientific, A22287) respectively. The confocal images were acquired using a Zeiss LSM-710 inverted confocal microscope.

2.5.10 Transmission electron microscopy of lung organoids

Organoids derived from immortalized cells at 21 days of culture were embedded in resin after sequential fixation in 2.5% glutaraldehyde in 0.1 M cacodylate buffer (pH 7.2) at 4 °C. The ultrathin sections were stained with uranyl acetate and examined under an FEI Tecnai 12 BioTwin 120 kV scanning transmission electron microscope.

2.5. 11 Focused Ion Beam microscopy of lung organoids.

Organoids derived from immortalized cells at 21 days of culture were embedded in resin after sequential fixation in 2.5% glutaraldehyde in 0.1 M cacodylate buffer (pH 7.2) at 4 °C. The sections were examined under 2.5 nm at 30 kV Focused Ion Beam Microscope.

2.5.12 Bioprinting lung organoids

A 3D bioprinter (BioX Cellink) was used to extrude 2% alginate and 5% gelatin containing lung fibroblasts solution into ultra-low attachment round bottom 96-well plate (Thermo Fisher, 7007). The plate was cold before use. The hydrogel was crosslinked with CaCl₂ for 15 min at room temperature. After, the droplets were covered in DMEM (Life Technologies 12430054) and incubated overnight at 37°C. On the next day, cell medium was removed, and geltrex was extruded in the droplets-maintained 4°C (print bead). The samples were incubated at 37°C for 30 min, and CFBE were added into MEM medium (VWR, CA45000-380). The proportion of the IMR-90 to CFBE was keep it 1:1. The media was changed on day 3, using a combination if DMEM and MEM into 1:1 ratio. A flow chart of this protocol is illustrated in figure 2.26.

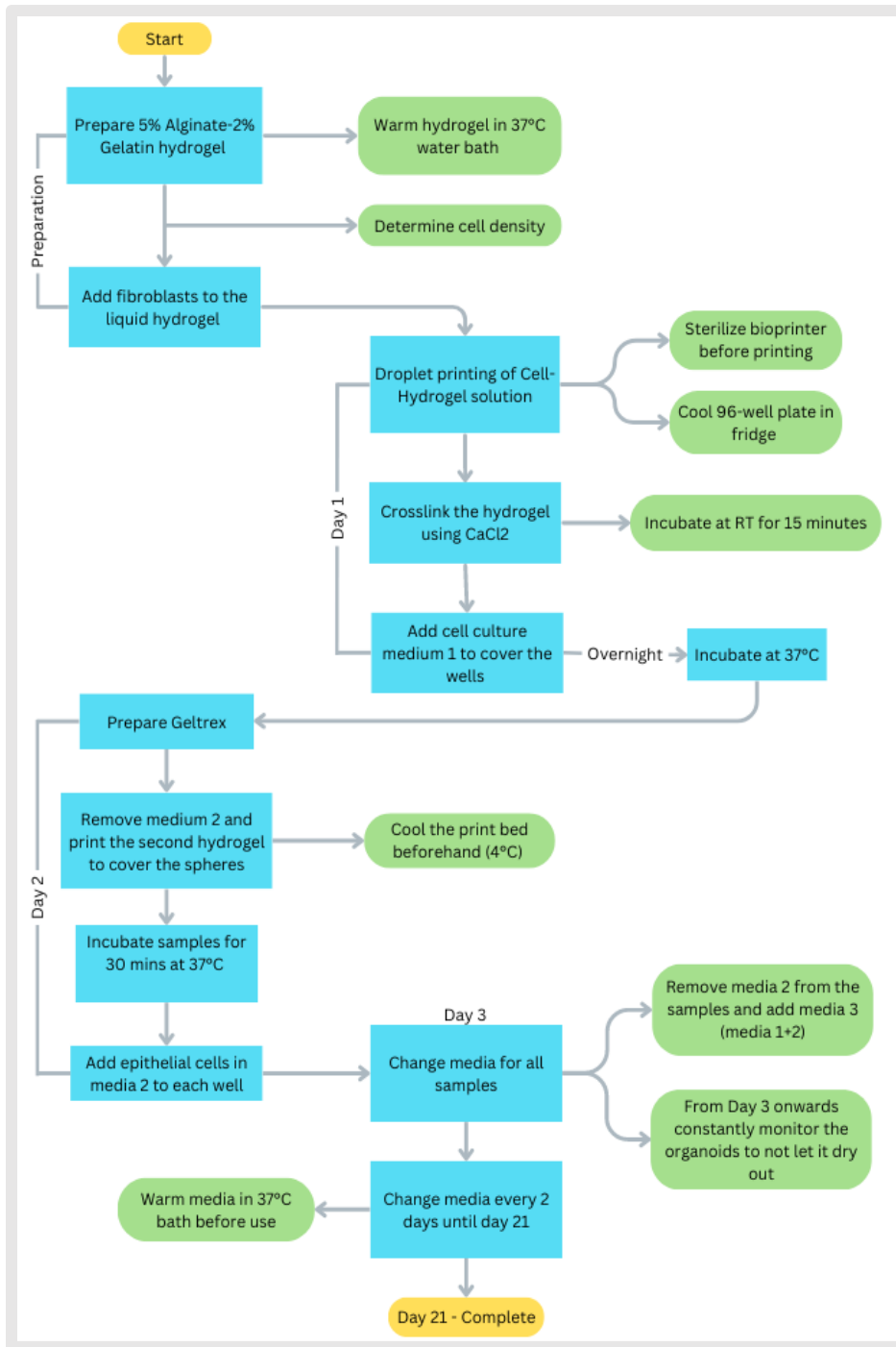


Fig. 2.26 Lung organoid fabrication flow chart using bioprinting.

Chapter 3 Characterization of pulmonary organoids

3. 1 Contributions

Alicia Reyes Valenzuela designed the study and the methodologies. She cultured primary and immortalized cells and prepared the organoids needed for the experiments. She performed all characterization experiments such as immunofluorescence and RT-qPCR, and downstream analysis of RNA sequencing data and proteomics. Mark Turner designed HPRT primers and provided training on qPCR, and the culture of airway epithelial cells. The RNA extraction, library preparation and sequencing services were provided by Génome Québec. Upstream bioinformatics analysis of RNA sequencing data was performed by Virginie Calderon at the Montreal Clinical Research Institute (IRCM). Proteomics analysis was performed using the Proteomics and molecular Analysis Platform at Research Institute of the McGill University Health Centre (RI-MUHC). Jennifer Nedow processed the samples for Tandem Mass Tags. Lorne Taylor and Jenna Cleyle performed the upstream data analysis and provided insights for into downstream analysis. Flow cytometry analysis was done with the help of Julien Leconte of the Flow Cytometer Core Facility at McGill University. John Harahan provided the ethics protocol to use human cell lines. Luc Mongeau supervised the study and provided guidance and oversight over the entire duration of the project. The data of this chapter is included in a manuscript to be submitted.

3. 2 Introduction

A robust protocol for inducing 3D cellular structures with elongated and tubular morphology was described in the previous chapter. Reproducibility, morphology, and facile fabrication were considered key factors for protocol selection. In chapter 3, the

phenotype of the organoids was investigated by using bulk RNA sequencing and proteomics. Additional data included RT-qPCR, immunofluorescence, and flow cytometry. RNA sequencing and proteomics allow the study of the expression of multiple RNA and proteins simultaneously and the networks they form. The cross examination of two complementary methods provides a holistic view of cellular phenotypes¹²⁵. These methods have more relevance than the study of individual molecules since genes or proteins rarely act alone or have one single function¹²⁵.

The present chapter starts with a comparison between the RNA-sequencing and proteomics of lung organoids and traditional 2D cellular monolayers from which the organoids are derived from. This analysis confirms the superiority of 3D cultures over 2D models in reproducing relevant pathways associated with the lung tissue.

A functional enrichment analysis of the organoids was performed to identify the function of the genes upregulated in the organoid. The phenotype of the organoids was then compared to that one of adult lung tissues. One common disadvantage of organoids derived from iPSC is their fetal phenotype, which hampers their applications to development biology and pediatric diseases⁷⁷. In contrast, the organoids generated in the present study show similarities with adult lung tissues, which widen their potential applications.

3.3 Results

3.3.1 Evaluation of cellular markers and functional enrichment analysis

Differentiation of six major lung epithelial cells commonly found in lung proximal and distal regions^{7,63,65,66,75} was evaluated using bulk RNA sequencing. Markers for rare cell types were also evaluated^{1,7,24}. For this, nine organoids were processed and divided

into three samples, each consisting of three organoids (n=3 per sample), to ensure an adequate amount of RNA for analysis. This number was determined based on the number of cells per organoid.

We used multiple markers for different cell types as illustrated in Fig.3.1. All these markers have been extensively used before in other studies for identification of specific cell types. We used SOX2 as the main marker to evaluate the multipotency of the proximal region of the lung^{1,77,126}, while the marker SOX9 was used to evaluate the multipotency of the distal region of the lung^{1,77}. Other markers were used to identify rare and recently discovered cells, such as brush cells¹, and PNECS¹, both located within proximal lung regions.

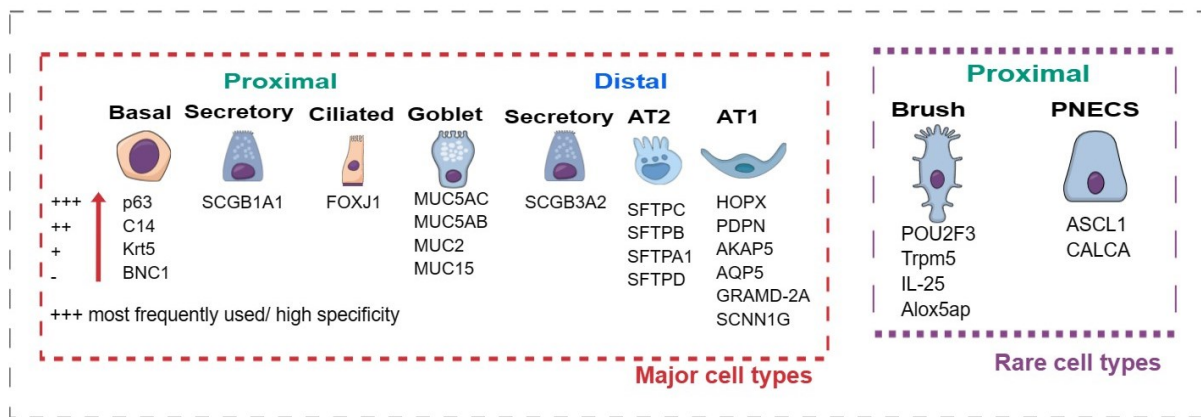


Figure 3.1. Used markers for the identification of major and rare cell types in the lung, in either the proximal or the distal region.

3.3.1.1 Organoids derived from primary cells.

We compared the organoid's gene expression with that from primary bronchial epithelial cells (HBE) cultured in filters coated with collagen IV (see methods details), creating an air-liquid interface (n=3). The latter model is well-known, and served as the gold

standard for proximal airways modelling.³⁰ The genetic expression of organoids was also compared with that from fibroblasts cultured in traditional monolayers (n=3).

As shown in Fig.3.2 and Table 3.1, the signals used to identify basal cells (Cytokeratin 14, Keratin 5, BNC1, and Tp63) remained the same in the organoids as in the input HBE cells. As expected, monolayers of IMR-90 were devoid of any marker of basal cells, nor any other cell types from the proximal lung region. It was found that markers for secretory cells (SCGB1A1+), ciliated cells (FOXJ1+), and multipotency (SOX2+) decreased in level within the organoid in comparison to HBE. Yet, their expression was significantly greater than in IMR-90 cell monolayers. It was found that markers of goblet cells (MUC5AC, MUC5B, and MUC15) were upregulated within HBE cells in comparison to LOp. All cell markers used to identify brush cells and PNECs, except for IL-25, were found to be upregulated within the organoid in comparison to HBE and IMR-90 (Fig. 3.2A). Markers of cells from distal regions of the lung such as secretory (SCGB3A2+), Alveolar type II (SFTPC+, SFTPB+, SFTPA1+, SFTPD+) and Alveolar type I (HOPX+, PDPN+, AKAP5+) were mostly upregulated within the organoid in comparison to HBE and/or IMR-90 cell monolayers, as shown in Fig.3.2B.

The SFTPB and SFTPA1 remained the same in HBE and LOp. The SFTPC, and SFTPD were significantly upregulated in the organoid.

Generally, markers associated with proximal regions of the lung were downregulated in the organoid, while markers associated with distal regions of the lung were upregulated. These observations suggest that the input epithelial cells, from proximal regions, differentiate into multiple cell types from distal regions while retaining some markers of

the proximal regions. Specific adjusted p values, resulting from multiple t-test comparisons between IMR-90 and LOp, and HBE and LOp are shown in the Appendix (Table A1). The expression of representative genes of alveolar type II cells (SFTPC+) was confirmed by parallel flow cytometry results, as shown in Fig.3.3.

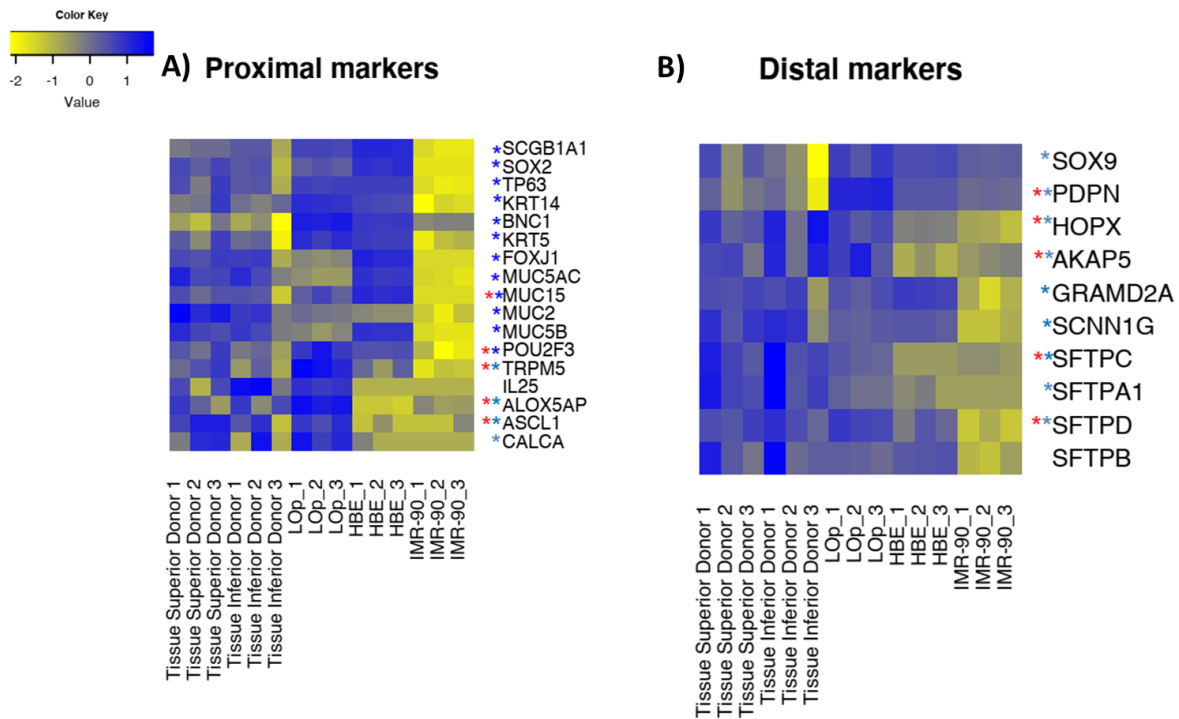


Figure 3.2. RNA sequencing data showing proximal (A) and distal (B) markers of LOp, fibroblasts monolayers, and primary bronchial epithelial cells, respectively, in air-liquid-interface. N=3. Multiple T-test comparison, p.adjust <0.05 in comparison to IMR-90*, and in comparison to HBE*.

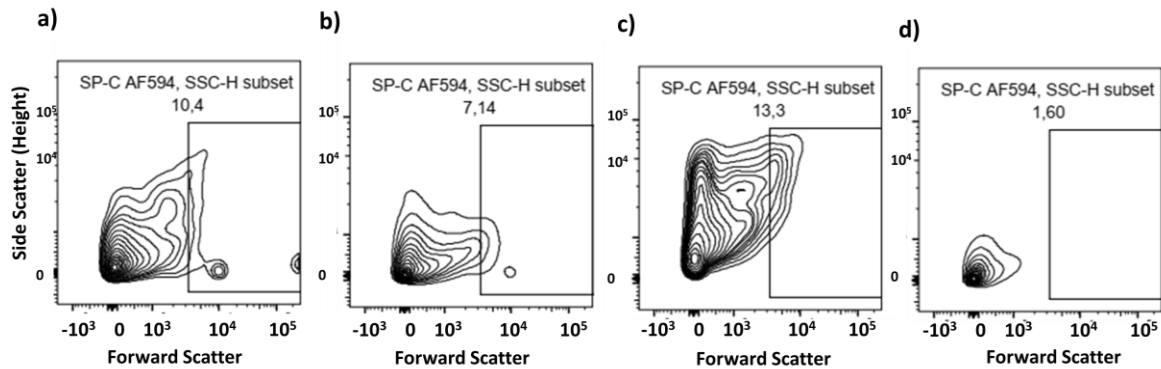


Figure 3.3 Flow cytometry to confirm AT2 cells of organoids derived by primary cells LOp. a-c) Percentage of SFTPC+ (AF594) cells detected in each organoid. d) Fluorescence minus one (FMO) 594 was used to calibrate the instrument. N=3

Differential expression analysis between cell monolayers and LOp, revealed that 153 genes were up- or downregulated in a statistically significant manner ($p \text{ adj} < 0.01$ & $\text{abs}(\log_2 \text{ Fold Change shrink}) \geq 4$). A functional enrichment analysis of those genes was performed using g: Profiler to access to a collection of genes¹²⁷. This analysis, referred as Gene Ontology (GO), allowed the identification of genes from several domains such as Molecular function (MF), Biological Process (BP), and cellular components (CC), as well as other biological databases¹²⁷ as shown in Fig. 3.4.

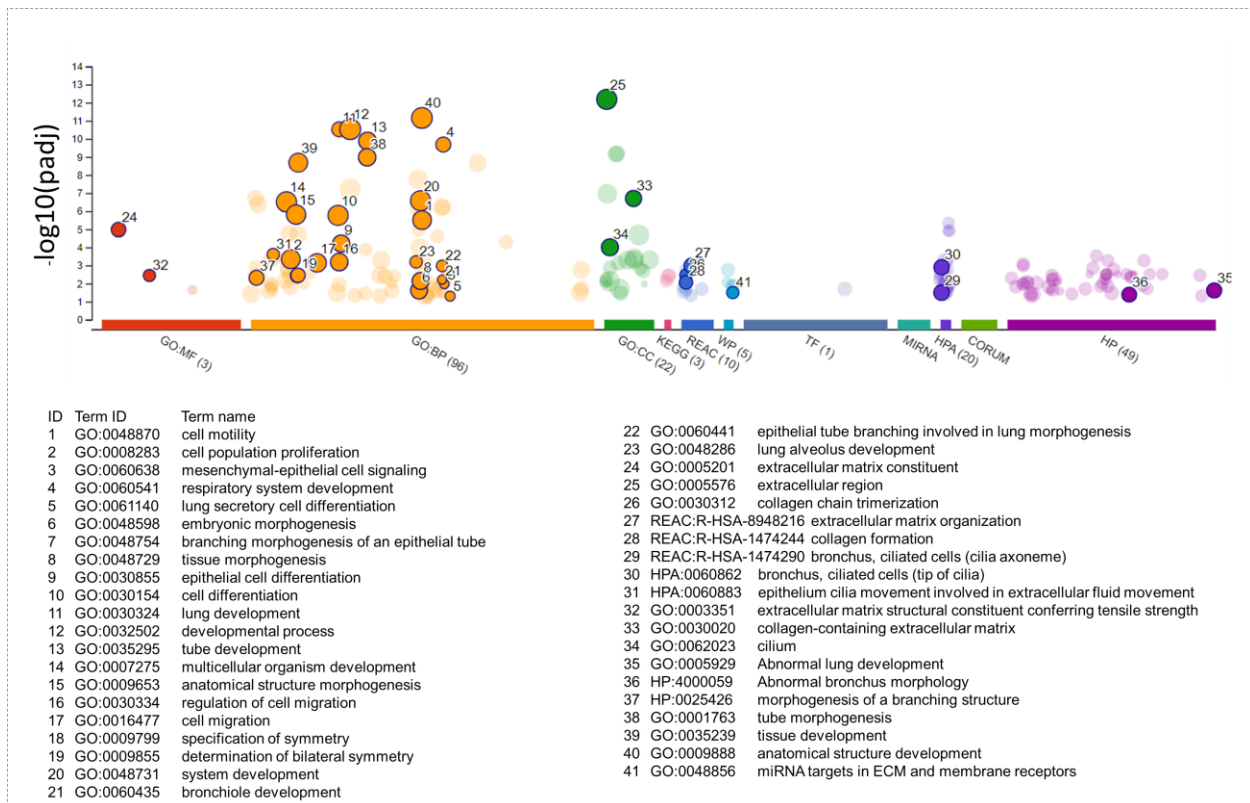


Figure 3.4. Functional enrichment analysis of genes with major change between cell monolayers and organoids (LOp) (padj. <0.01) using G: Profiler. Abbreviations: MF- Molecular Function, BP: Biological Process. CC-Cellular Component. KEGG-Kyoto Encyclopedia of Genes and Genomes. REAC - Reactome pathways. WP – WikiPathways. TF - Transcription factor binding site predictions. MIRNA - mirTarBase miRNA targets. HPA - Human Protein Atlas expression data. CORUM - Manually annotated protein complexes from mammalian organisms. HP - Human Phenotype Ontology, a standardized vocabulary of phenotypic abnormalities encountered in human disease. The display set of terms was selected according to their association with the lung, tissue development, and cell differentiation.

Figures 3.5-3.7 show several Biological Process ‘terms’ (set of genes associated with specific functions) identified from the functional enrichment analysis associated with respiratory system development, tube development and lung alveolus development. Many genes from each term were upregulated in the organoid versus cell monolayers. As shown in Fig. 3.5, many genes associated with respiratory system development appear in HBE and IMR-90. But once the organoids are formed, they combine both of

the upregulated genes of each individual cell type. Additional genes are original and not abundantly present in the input cells. This shows that the organoids are more than the sum of the characteristics of the initial input of cells used at the beginning of the process.

These results suggest that the organoid constitutes a more heterogeneous respiratory system model than HBE or fibroblasts alone. Similarly, all genes associated with tube development were upregulated within the organoid versus cell monolayers (Fig. 3.6). This suggests that the tubular morphology of the organoids may be a consequence of well orchestrated and complex processes similar to those involved during embryonic lung development. This observation is also supported by trends for other related terms such as alveolar development (Fig. 3.7), branching morphogenesis, tube morphogenesis, and morphogenesis of branching structure.

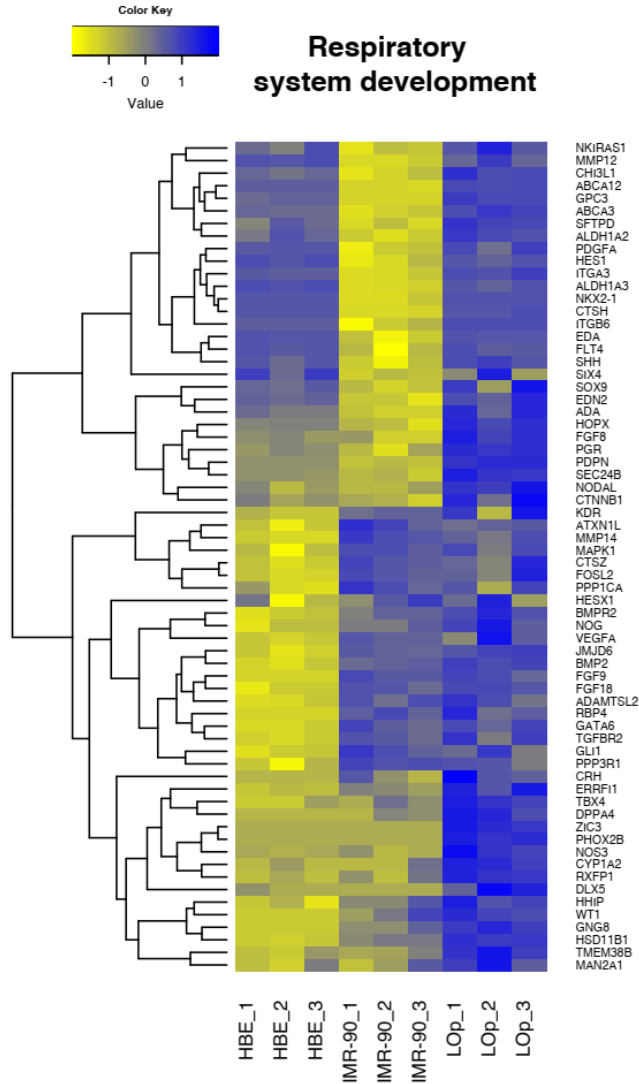


Fig. 3.5 Heatmap showing genes associated with respiratory system development pathway: Gene Ontology :0060541. Differential expressed genes analysis, comparing cell monolayers (HBE, IMR-90) and LOp, ($p_{adj} < 0.01$ & $abs(\log_2 \text{ Fold Change shrink}) \geq 4$).

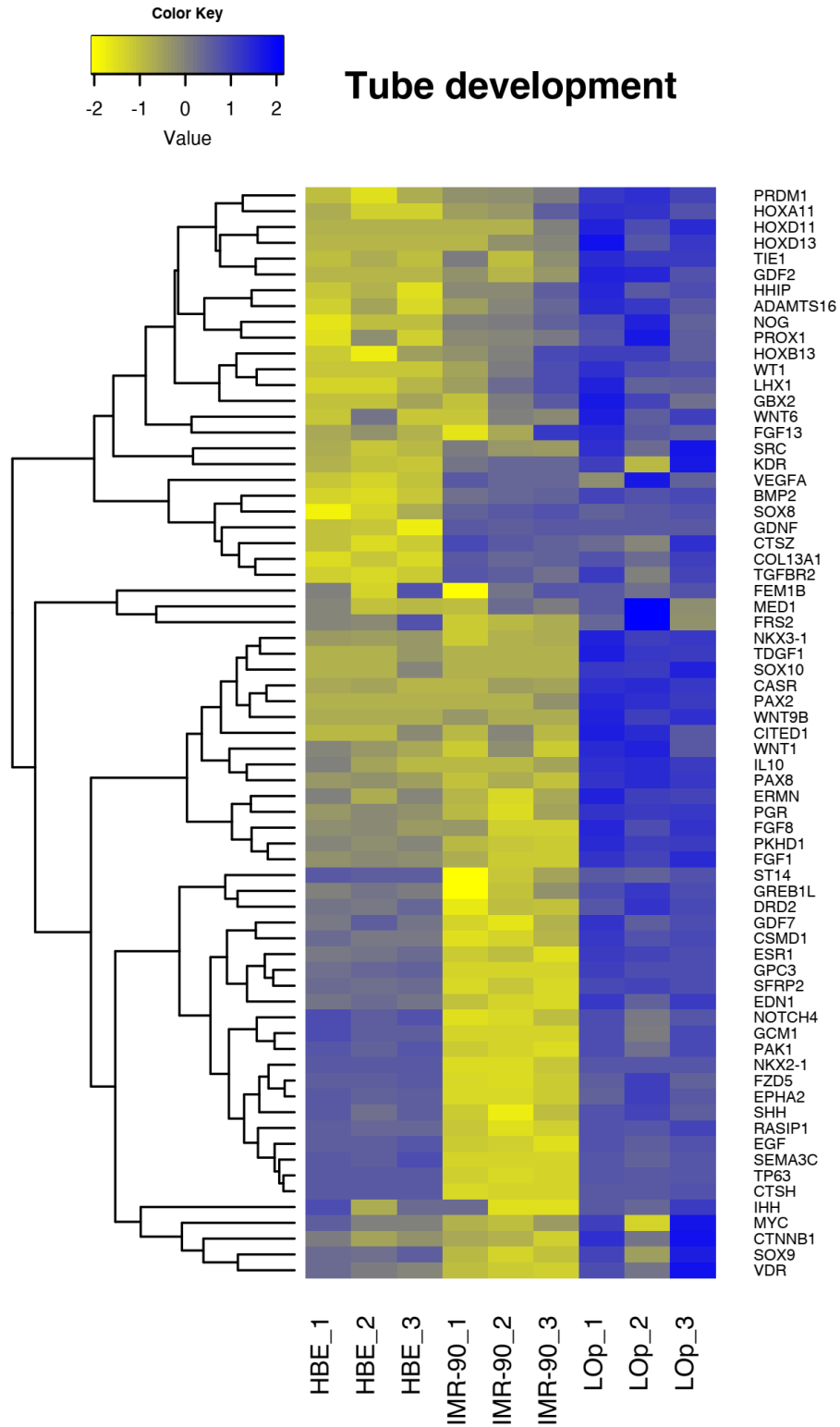


Figure 3.6 Heatmap showing genes associated with tube development pathway: GO: 0035295. Differential expressed genes analysis, comparing cell monolayers (HBE, IMR-90) and LOp, ($p \text{ adj} < 0.01$ & $\text{abs}(\log_2 \text{ Fold change shrink}) \geq 4$).

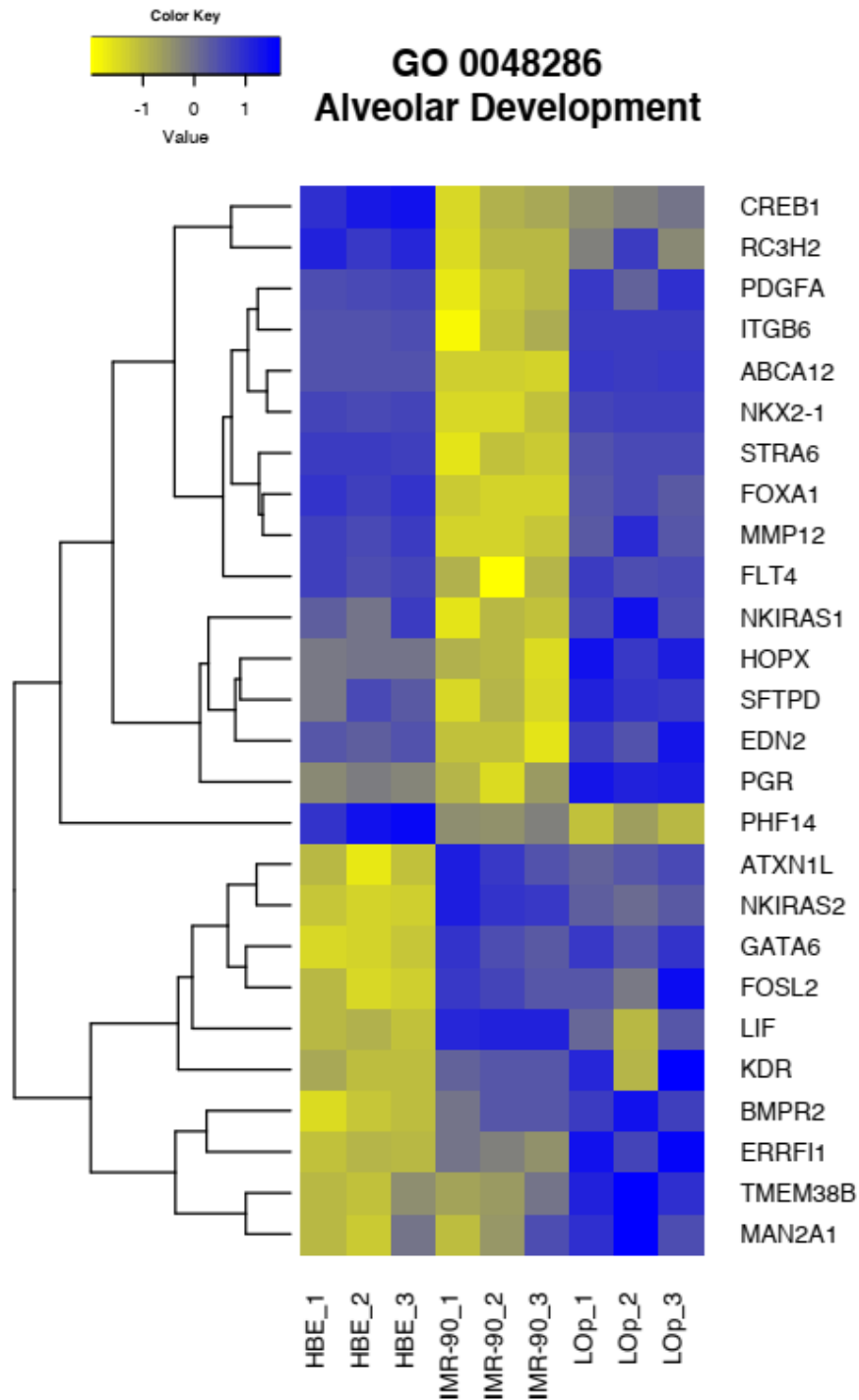


Figure 3.7. Heatmap showing genes associated with alveolus development in all samples. Differential expressed genes analysis, comparing cell monolayers (HBE, IMR-90) and LOp, ($p_{adj} < 0.01$ & $abs(\log_2 \text{Fold Change shrink}) \geq 4$).

3.3.1.2 Organoids derived from immortalized cells.

Lung organoids fabricated using immortalized cell lines (LOi) in lieu of primary epithelial cells were investigated. Markers of basal cells (Cytokeratin 14, p63, and BNC1) were absent from the initial cell monolayers (Fig. 3. 8A), as expected given their stage of immortalization. Although the expression of these specific genes increased after the organoid was formed, relative to CFBE and IMR-90, the increment was not significant, except for TP63 which expression was upregulated with respect to CFBE and IMR90. This could perhaps indicate that the microenvironment plays a beneficial role in the genome even after cells are immortalized^{92,128}. Markers of secretory cells (SGB1A1+) from the proximal region, goblet (MUC5B+, MUC2+), brush (TRMP5+, IL25+, ALOX5AP+), and PNECS (ASCL1+), were all undetectable or minimal in cell monolayers, but they were all significantly upregulated in LOi (Fig.3. 8A). Similarly, secretory cells (SGC3A2+) were upregulated in the organoids (Fig.3.8B). These results suggest that, regardless of the immortalization of the cells, CFBE have the potential to change their phenotype according to their culture conditions, albeit with some limitations. Markers for AT2 cells (SFTPC+, SFTPB+, SFTPA1+, SFTPD+) were not significantly upregulated in the organoids with respect to CFBE, but SFTPA1+ and SFTPD+ increased in LOi in respect to IMR-90 (Fig.3.8B). Interestingly, the expression of SFTPC, and SFTPB in LOi was confirmed by parallel immunofluorescence (Fig. 3.8C). Based on these findings, it is inappropriate to attribute the expression of AT2 markers in the CFBE cell line to differentiation into AT2 cells. Instead, it is more likely that the immortalization process induces changes in the cellular characteristics, leading

to the expression of these markers. For markers of AT1, only GRAMD2A+ and SCNN1G+, were significantly upregulated in the organoid relative to cell monolayers (Fig. 3.8B). PDPN was upregulated in the initial cohort of fibroblasts, and therefore it cannot be used to determine the specificity of AT1 cells. For this reason, HOPX was used instead. This marker was found to be minimally expressed in all the groups (Fig.3.8B). Therefore, proper differentiation into AT1 could not be confirmed in LOi. Specific adjusted p values, resulting from multiple t-test comparisons between IMR-90 and LOi, and CFBE and LOi are shown in the Appendix (Table A.2).

Based on the data presented, it is apparent that LOi exhibits a distinct lung tissue phenotype. When compared to the input cell types, LOi primarily regulates markers associated with the proximal region of the lung. One notable difference between LOi and LOp is the lack of upregulation of AT2 and AT1 markers in LOi.

A functional enrichment analysis was performed to identify the 25 genes that changed the most among cell monolayers and LOi with $p \text{ adj.} < 0.01$. Fig.3.9 shows these 'terms' (set of genes associated with specific functions) along with their function. Most of the functions are associated with extracellular matrix changes. This was expected, given the use of BMZ proteins within the gel. There was a total of 259 genes upregulated in the organoids. Since a tubular morphology was observed in LOi (Fig.3.10B), the term GO:0060441 from gene ontology database corresponding to epithelial tube branching for lung morphogenesis was analyzed. Several genes of this term were upregulated in LOi in comparison to epithelial cells (Fig. 3.10). Interestingly, some genes needed for adequate branching morphogenesis during lung development, such as RSPO2, SPRY2^{129,130}, were upregulated in the fibroblasts (Fig.3.10), thereby highlighting the

relevance of these cells during lung development. These genes could be used to improve branching of the organoid by increasing the fibroblasts density or adding fibroblasts growth factors into the media.

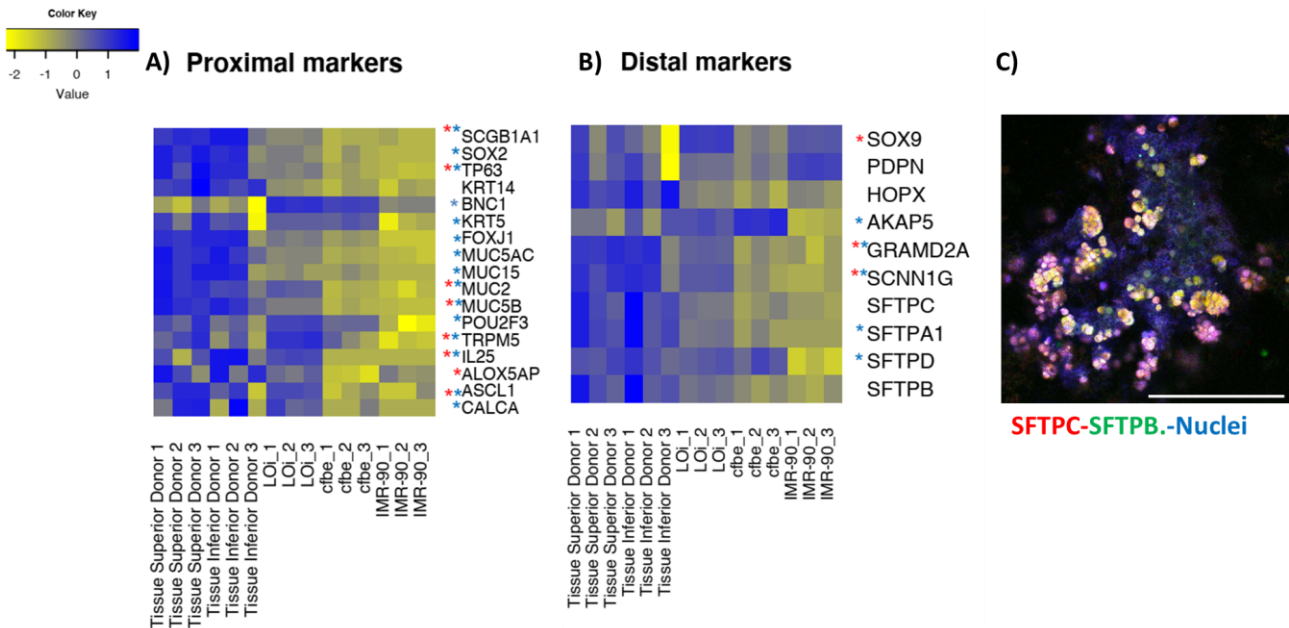


Fig. 3.8 Characterization of lung organoids derived from immortal bronchial epithelial cells (LOi). A) RNA sequencing data showing markers of proximal cells of the lung including rare cell types in epithelial cell monolayers, fibroblasts, and derived organoids. B) RNA sequencing data showing distal markers of cells of the lung. A-B) N=3. Multiple T-test comparisons, * p. adjust <0.05 in respect to IMR-90, **p. adjust <0.05 in respect to CFBE. C) Image of LOp organoid on day 21, showing distal markers of the lung. Red-SFTPC, Green-SFTPB. Blue-Nuclei. Magnification 10 X. Scale Bar 500 µm.

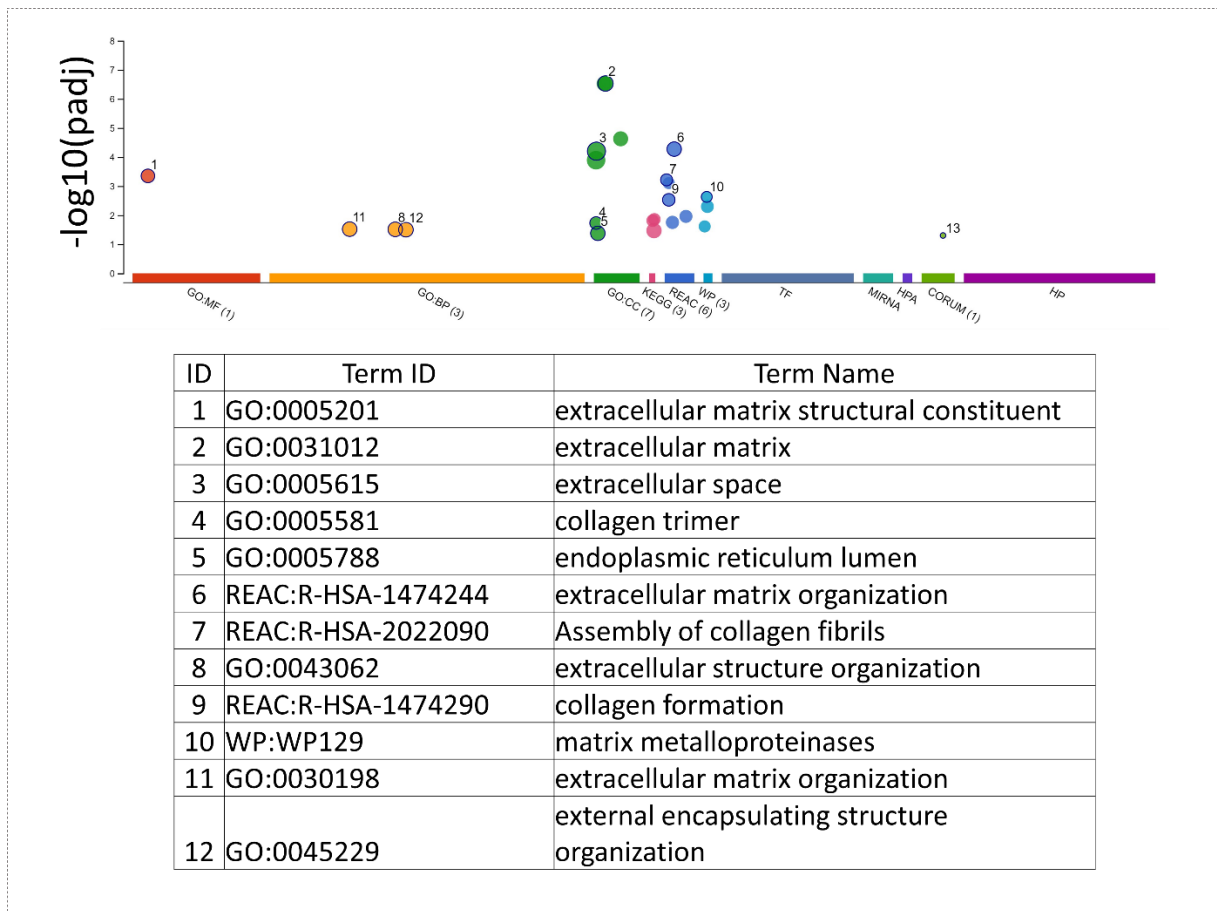


Fig.3.9. Functional Enrichment analysis of genes with major change between cell monolayers and immortalized derived organoids ($p_{adj} < 0.01$) by G: Profiler. Abbreviations: MF-Molecular Function, BP: Biological Process. CC-Cellular Component. KEGG- Kyoto Encyclopedia of Genes and Genomes. REAC - Reactome pathways. WP – WikiPathways. TF - Transfac transcription factor binding site predictions. MIRNA - mirTarBase miRNA targets. HPA - Human Protein Atlas expression data. CORUM - Manually annotated protein complexes from mammalian organisms. HP - Human Phenotype Ontology, a standardized vocabulary of phenotypic abnormalities encountered in human disease.

Quantitative PCR was used to confirm the lung fate of LOi (Fig.3.11) using homeobox protein Nkx-2 (NKX2) and Advanced Glycosylation End-Product Specific Receptor (AGER), as well as HOPX, and SFTPB, SFTPC. The expression of AT2 markers was also confirmed by flow cytometry (Fig.3.12). However, attributing the presence of surfactant protein markers (SFTPC and SFTPB) in LOi solely to differentiation into AT2

cells is incorrect, as these markers are initially present in the epithelial cells (CFBE). Immortalization likely prompts alterations in cellular properties, leading to the expression of these markers. Also, the expression of the various markers used was less abundant than that in organoids derived from primary cells. Interestingly, the heatmaps showing the gene expression of proximal and distal markers in adult lung tissue shows a greater resemblance with LOi than with cell monolayers. However, few genes were upregulated in LOi in comparison to CFBE. Therefore, although some degree of improvement was achieved in LOi relative to the individual cell lines, this does not necessarily imply cell differentiation, or that the expression of markers is equivalent to specific cell types.

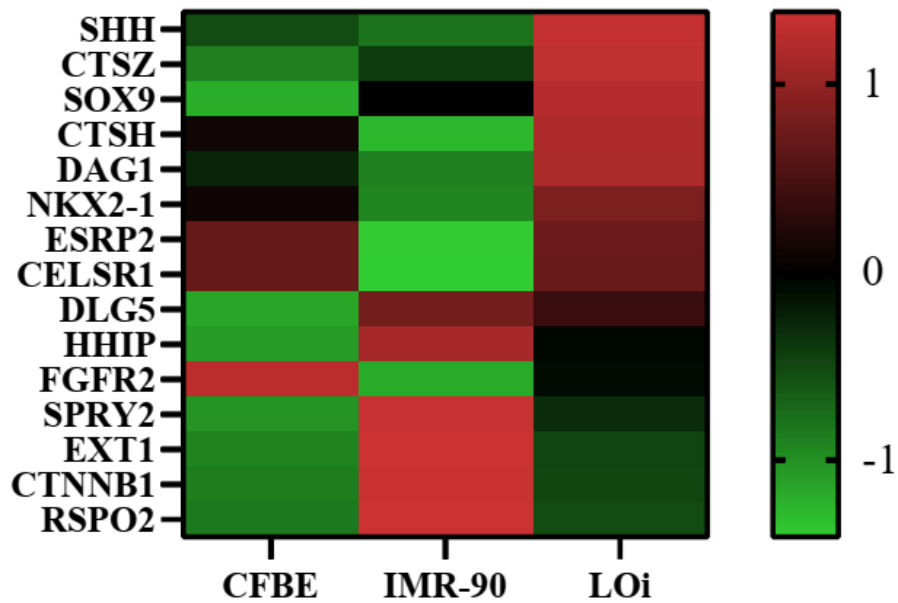


Fig. 3.10 Heatmap of genes associated with “epithelial tube branching involved in lung morphogenesis” Red shows up-regulation. Abundances grouped linked by Average.

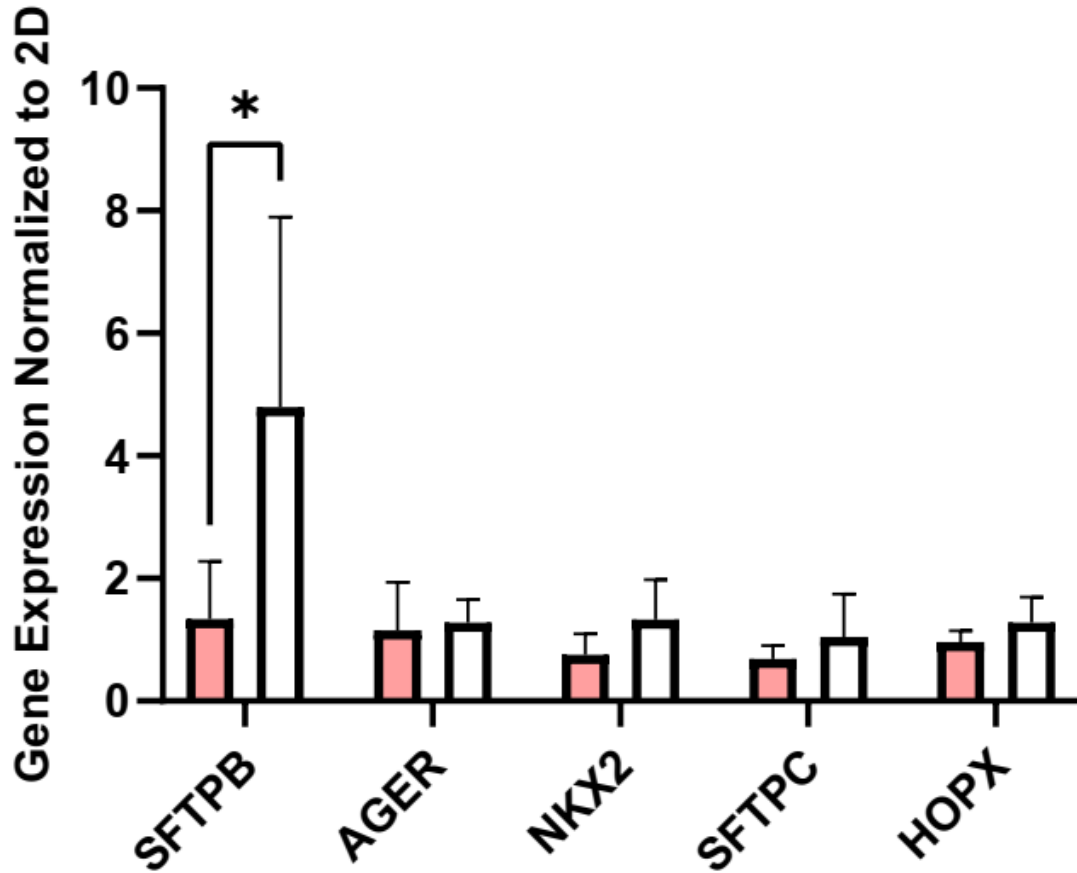


Fig. 3.11 Genes associated with lung phenotype. Gene expression using qPCR in CFBE (pink) and LOi (white). SFTPB upregulated in organoids in comparison to CFBE. N=3. *p<0.05.

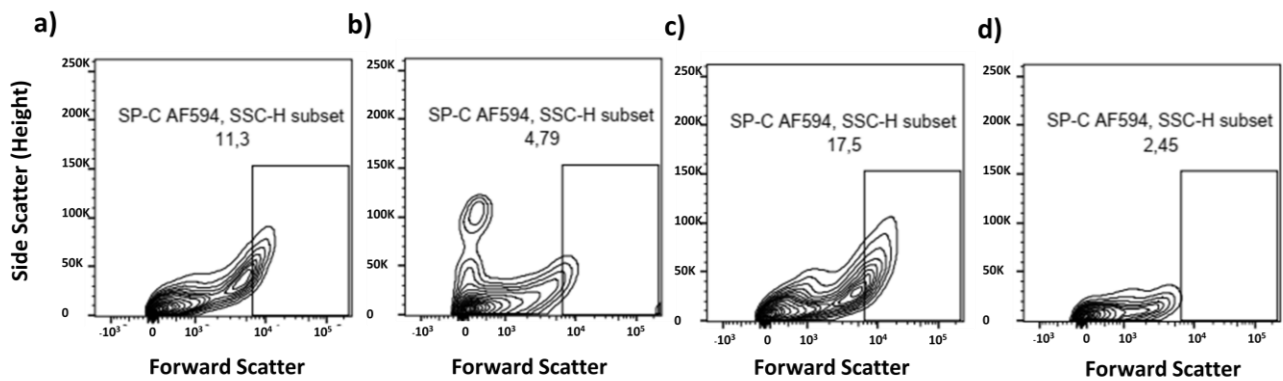


Fig. 3.12. Flow cytometry to evaluate the number of cells expressing SFTPC+ into organoids derived by immortalized cells. a-c) Percentage of SFTPC+ (AF594) cells detected in each organoid. d) Fluorescence minus one (FMO) 594 was used to calibrate the instrument. N=3

3. 3. 2 Proteomics profile of organoids and cell lines

To gain further insight into cellular dynamics, a proteomic analysis was performed using Tandem Mass Tags (TMT). The principal component analysis of all samples is shown along with that of lung tissues in Fig.3.13, indicated that both types of organoids (LOp and LOi) are reproducible. Three samples (n=3) of each type were used for the analysis. A detailed quantitative analysis of initial cells, HBE, IMR-90, and LOp is shown in Fig. 3. 14. A number 1361 proteins were shared among these samples. A total of 180 proteins were found only in LOp and not in the cell monolayers. A representation of the proteins upregulated in LOp respect to cell monolayers are shown in Fig. 3.15. The heatmap showing the complete list of upregulated proteins (cluster 2) can be found in the appendix (Fig. A1 and Fig. A2). These proteins were analyzed using the STRING software to collect information from multiple sources, including text mining data from the literature, databases of interaction experiments and complex pathways¹³¹. Only nodes and networks with high strength ($p < 0.05$) and low false discovery (≤ 0.001) rate were considered. 122 proteins were specific to the respiratory system, 18 were specific to the throat, and 105 proteins were specific to lung tissue as shown in Fig. 3.16. These proteins form interconnected networks, facilitating coordinated communication and regulation of essential cellular functions. Operating within networks enables signal amplification, pathway regulation, and adaptation to changing conditions more effectively than if they were isolated¹²⁵. Interestingly a subset of 46 proteins were associated with the immune system (Fig. 3.17), and 33 were associated with response

to stress, including chemical and oxidative stress, as well as response to external stimulus.

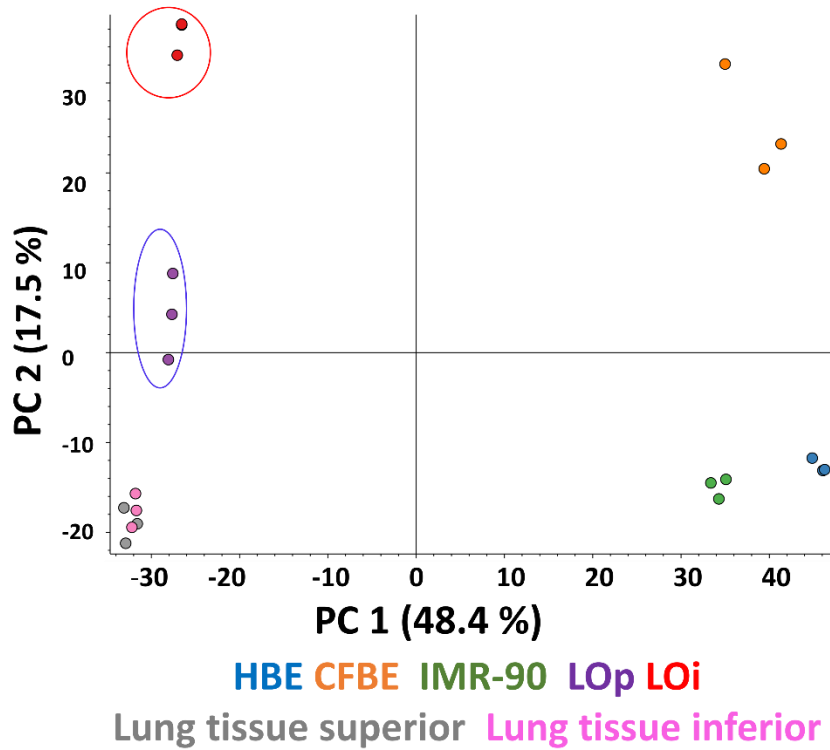


Fig. 3.13 Principal component analysis of cell monolayers, organoids, and tissues. Blue-primary bronchial epithelial cells. Orange-immortalized epithelial cells. Green-Fibroblasts. Purple-Lung organoids derived from primary cells (LOp). Red-Lung organoids derived from immortal cell lines (LOi). Grey-Lung Tissue from superior region. Pink-Lung Tissue from inferior region.

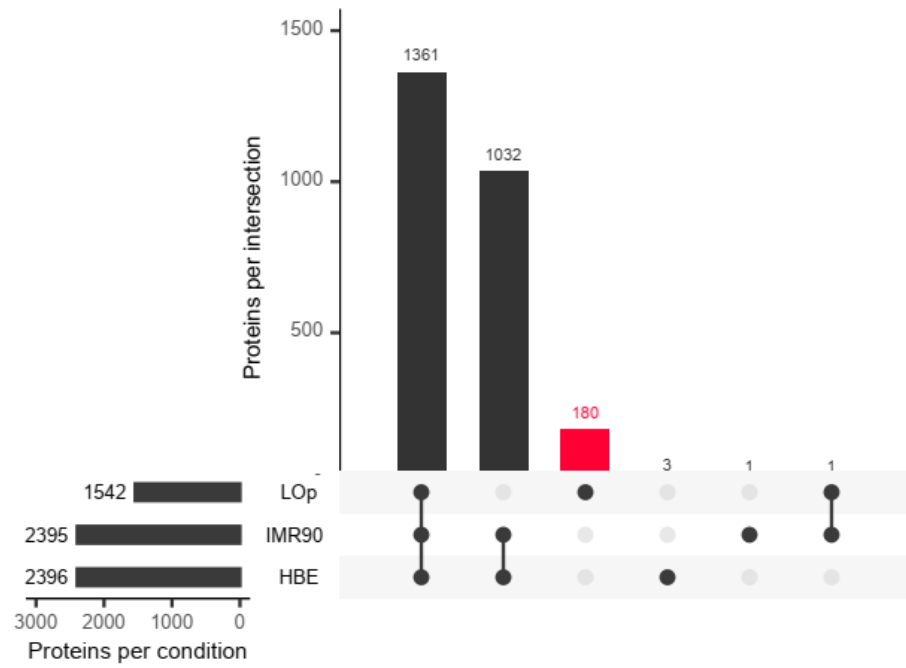


Fig. 3.14 UpSet plot showing the proteomic profile of lung organoids derived by primary cells (LOp), and cell lines.

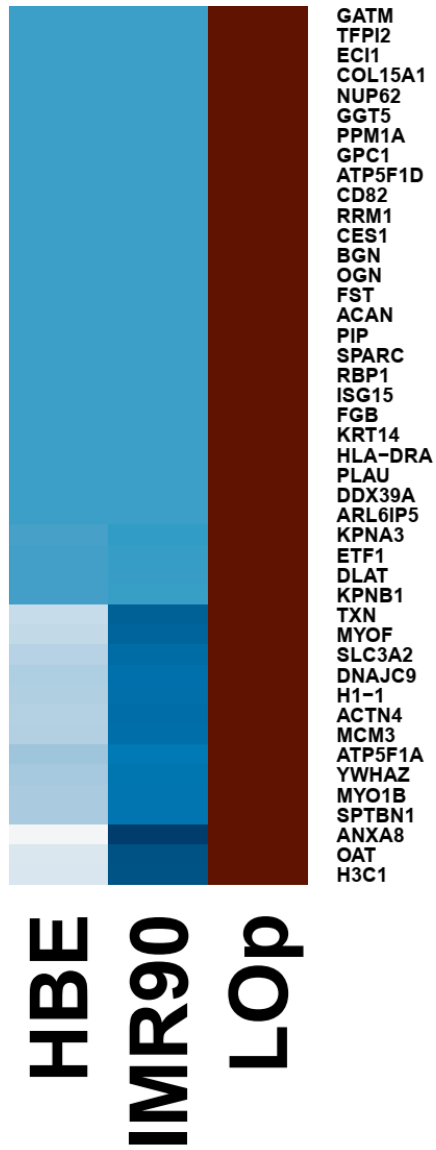


Fig. 3.15 Section of heatmap (cluster 2) showing upregulated proteins in LOp in comparison to cell monolayers. Abundances grouped, linked by average. Red show upregulation and blue downregulation. N=3.

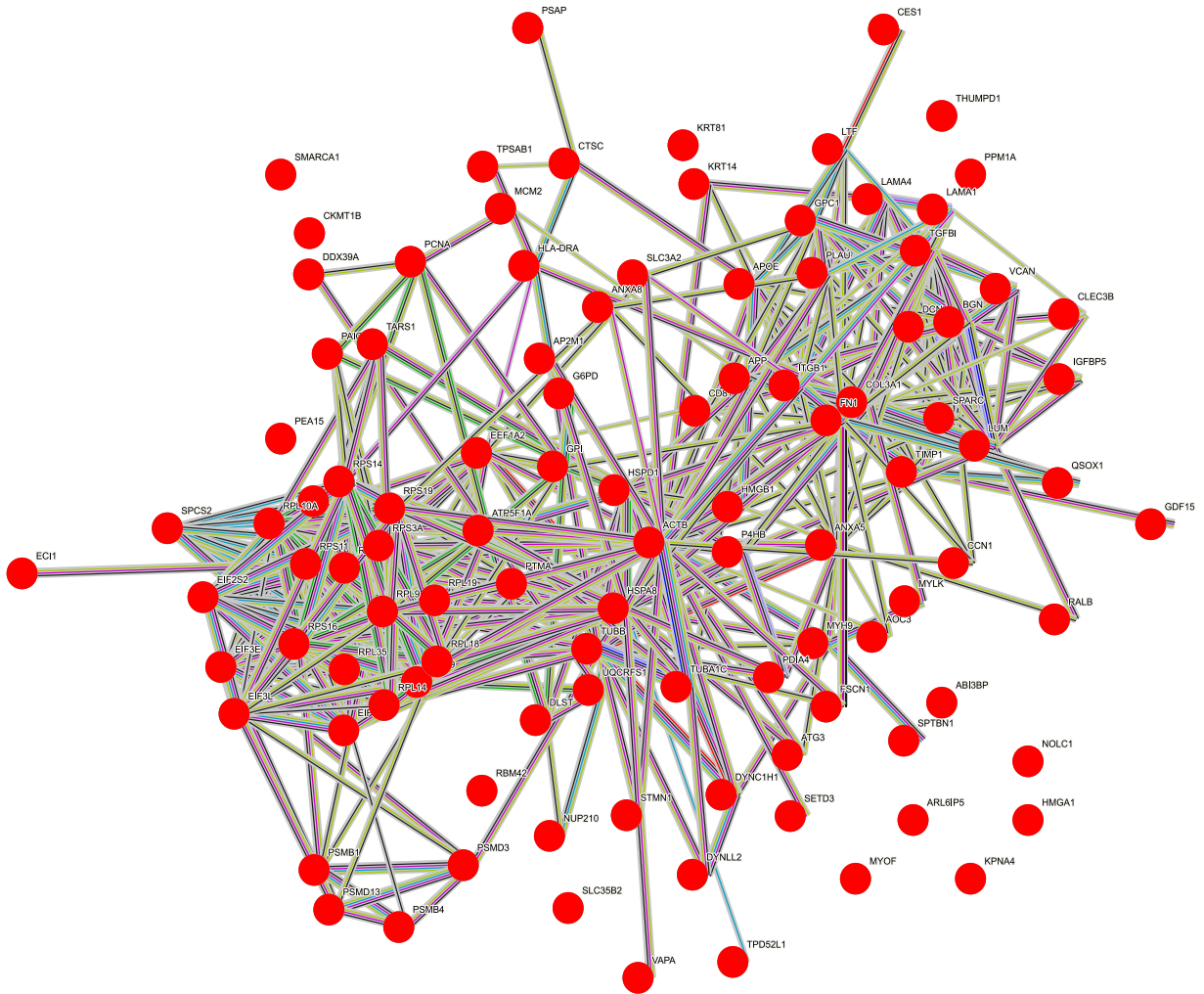


Fig. 3.16 Upregulated proteins in LOp with high specificity to the lung showing connections on pathways. Generated by STRING. Pathways colors: Blue-from curated database, Pink-\experimentally determined. Green-Gene neighborhood. Red-Gene fusions. Blue-Gene co-occurrence. Yellow-Textmining. Black co-expression. Dark blue: protein homology.

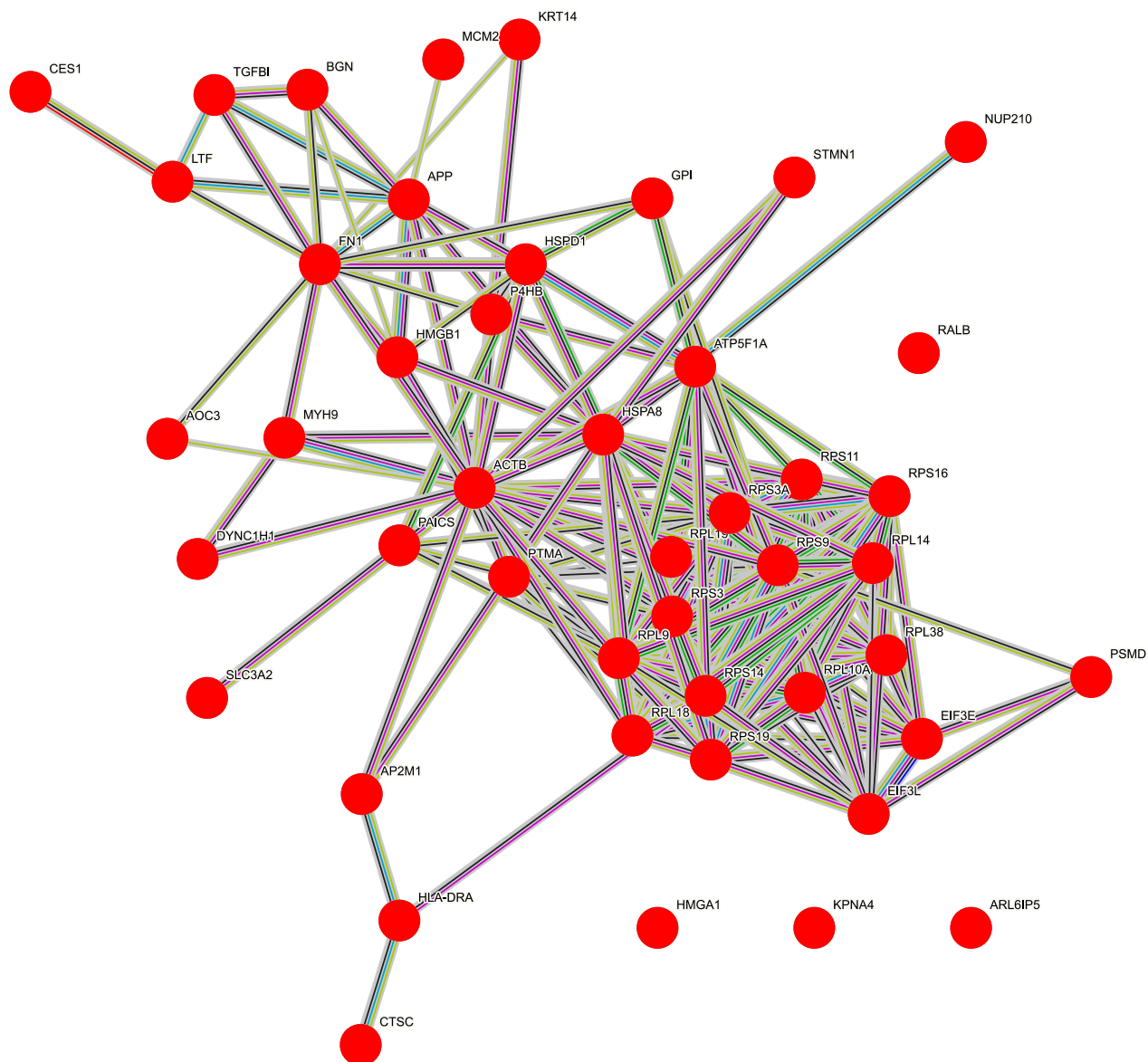


Fig. 3.17 Subset of proteins from the immune system upregulated in LOp organoids in comparison to cell lines. Generated by STRING. Pathways colors: Blue-from curated database, Pink-experimentally determined. Green-Gene neighborhood. Red-Gene fusions. Blue-Gene co-occurrence. Yellow-Textmining. Black co-expression. Dark blue: protein homology.

Wingless related-integrated site (Wnt) was found to be upregulated in LOp, including 12 proteins from the non-canonical pathway and 28 proteins from the signaling pathway.

Wnt has been found to regulate epithelial-mesenchymal interactions during lung

development¹⁹. Notably, wingless related-integrated site typically requires supplementation by media for organoid formation²¹. Here the co-culture of epithelial cells and fibroblasts alone provided sufficient signaling and growth factors without need for additional processing. Additionally, gene ontology (GO) analysis was conducted on the upregulated proteins of LOp. Figure 3.18 presents a summary of overrepresented terms, categorizing proteins based on their biological roles or properties in LOp. The figure illustrates the number of proteins corresponding to each term and their statistical significance. The terms depicted in Figure 3.18 offer insight into the varied biological roles and properties of the proteins identified in LOp. Many proteins are associated with lung tissue, including lung AT2 cells, lung macrophages, and bronchus and respiratory epithelial cells. Additionally, proteins involved in cell differentiation, biogenesis, structural development, cell differentiation, and cell migration are represented. The proteins upregulated in the organoid are not randomly selected; rather, they play key roles in essential functionalities crucial for lung development and function. Together, these findings highlight the targeted and purposeful nature of the protein expression profile observed in the organoid.

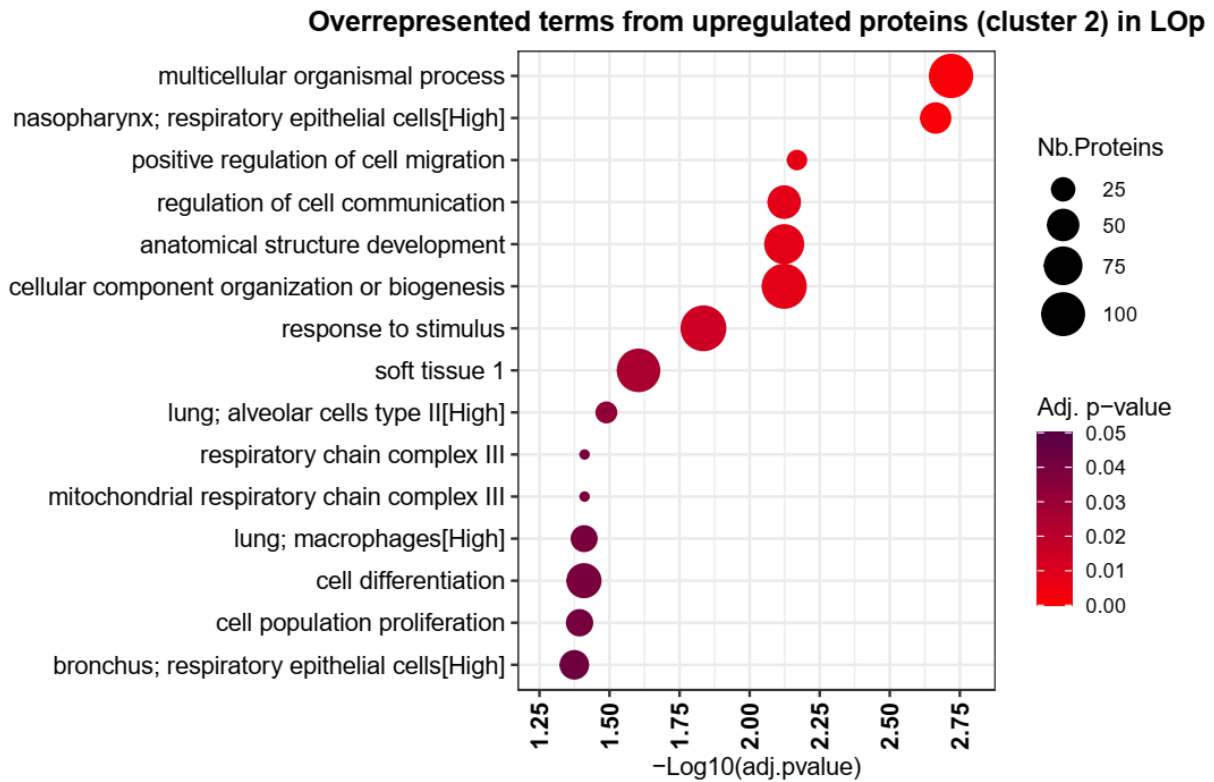


Fig.3.18 Overrepresented terms from upregulated proteins (cluster 2) in LOp using gene ontology.

The LOp proteins that were downregulated in comparison to HBE were analyzed using STRING and found to be associated with cellular and aerobic respiration, as well as mitochondrial ATP synthesis (Fig.3.19, Appendix Fig.A3). We speculate that this could be due to the ALI culture condition of HBE while the organoids were submerged.

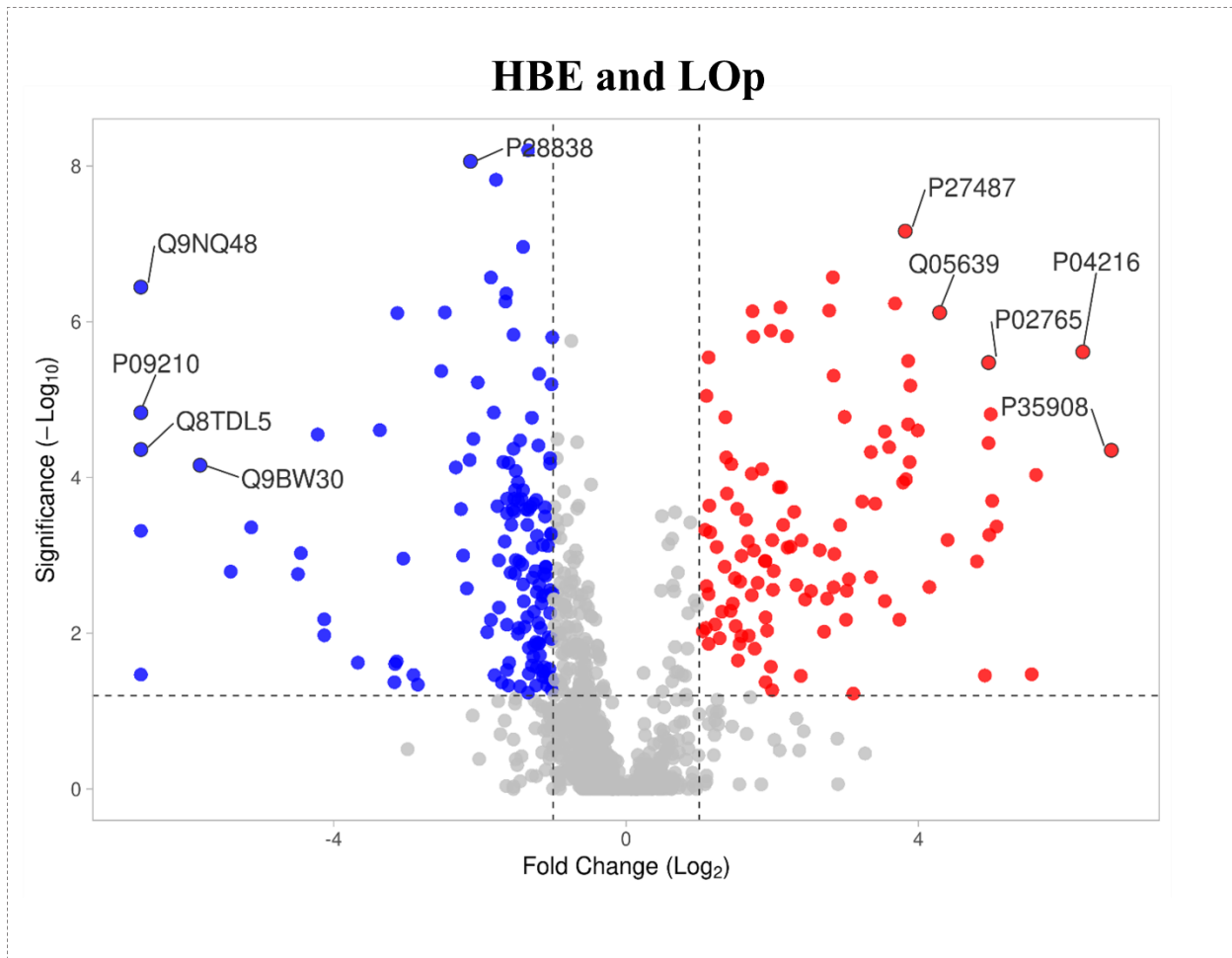


Fig. 3.19 Volcano Plot shows the upregulated proteins in LOp (in red) and the downregulated proteins (blue) in comparison to pHBE monolayers. Generated by VolcaNoseR

The proteomes from organoids derived from immortal cell lines and cell monolayers were compared (Fig. 3.20, Fig. 3.23). 1357 proteins were shared between all samples. A significant number of 180 proteins were found to be exclusive to the organoids and were not identified in the cell monolayers (Fig.3.20). A representation of the proteins upregulated in LOi respect to cell monolayers are shown in Fig. 3.21. The heatmap showing the complete list of upregulated proteins in LOi (cluster 3) can be found in the appendix (Fig. A4 and Fig. A5). Using STRING it was found that proteins upregulated in

LOi were specific to the lung (Appendix Fig.A5-orange) and the immune system (Appendix Fig. A5-purple). These two functions are valuable since the models aim to be used to model lung infections *in vitro*. The associated biological functions included humoral immune response, antimicrobial humoral response, immune system process, viral process, and innate immune response. Surfactant protein A stands out, as it plays an important role in the host-defense mechanisms of the lung, including opsonizing virus, bacteria, and apoptotic cells; it also modulates the production of cytokines and mediators of the inflammatory response¹³². Similar to the upregulated proteins in LOp, the upregulated proteins in LOi also interact with each other, forming interconnected networks that facilitate coordinated communication and regulation of essential cellular functions (Appendix Fig.A5). Working within these networks allows for more effective signal amplification, pathway regulation, and adaptation to changing conditions than if the proteins were isolated¹²⁵.

Gene ontology (GO) analysis of upregulated proteins in LOi revealed interesting biological functions. Fig. 3.22 provides an overview of terms that are overrepresented, organizing proteins according to their biological roles or properties in LOi. It shows the number of proteins associated with each term and their statistical significance. The biological functions associated with the upregulated proteins in LOi are tissue development, biogenesis, cell differentiation, and response to stress. This analysis also revealed an extensive pool of proteins specific to the lung such as lung macrophages, lung AT2 cells, respiratory epithelial cells, and lung mucosa. The presence of autophagy in the organoids, as discussed in Chapter 2 (section 2.3.7), suggests a potential connection to proteins associated with AT2 cells. Conversely, the cell lines CFBE and

IMR-90 have a broad collection of proteins without lung specificity, likely responsible for maintaining housekeeping functions¹³³. These proteins were downregulated in LOi.

Clearly, the proteomic profiles of organoids derived from both cell lines and primary cells are more specifically related to the lung and respiratory system than the cell monolayers from which they are derived. The organoids also display an upregulation of proteins indicative of tissue development, innate immune response, response to stimulus, cell differentiation, and viral processes.

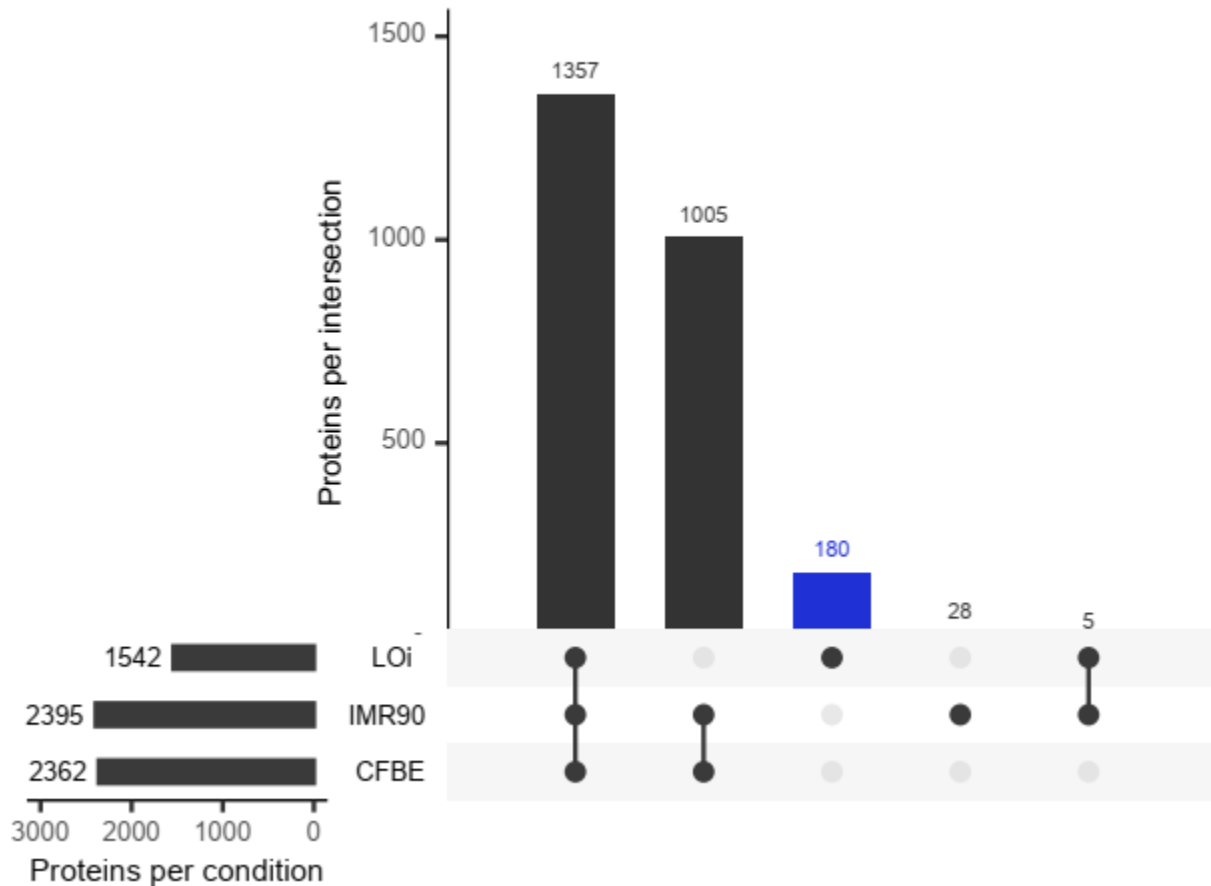


Fig. 3.20. UpSet plot showing the proteomic profile of lung organoids derived by immortalized cells (LOi) and cell lines.

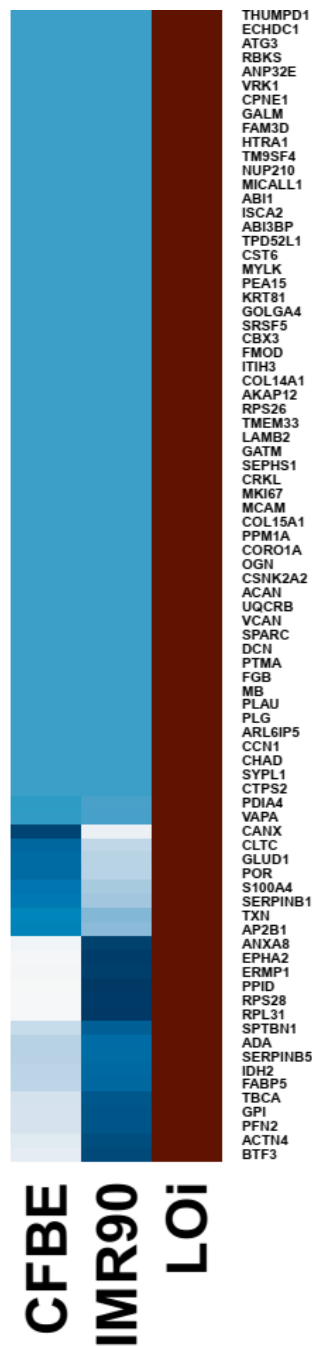


Fig. 3.21 Section of heatmap (cluster 3) showing upregulated proteins in LOi in comparison to cell monolayers. Abundances grouped, linked by average. Red show upregulation and blue downregulation. N=3

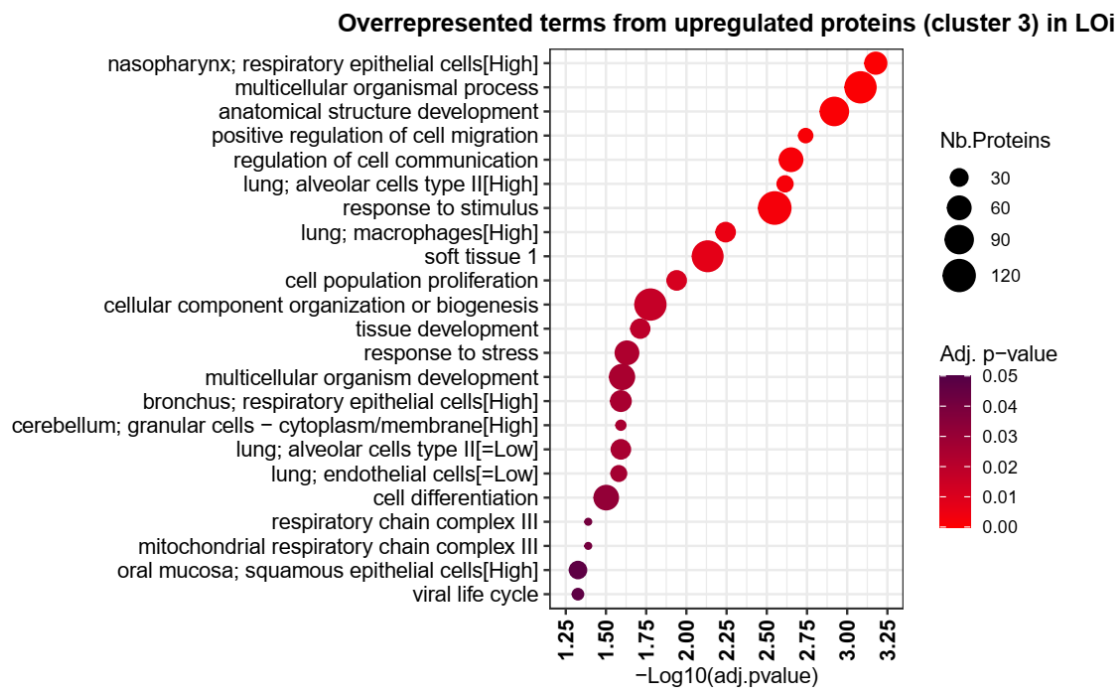


Fig. 3.22 Overrepresented terms from upregulated proteins (cluster 3) in LOi using gene ontology.

3. 3.3 Comparative study between proteomic profile of organoids and adult lung tissues

Significant differences were observed between the proteomes of both types of organoids, LOp and LOi. Upregulated proteins in LOp are shown in red (Fig. 3.23) while downregulated proteins are shown in blue (Fig. 3.23). Identified using STRING, the biological function and specificity of 102 proteins that were upregulated in LOp relative to LOi were specific to the lung and respiratory system. They were associated with tissue development, multicellular organismal process, response to stimulus, cell differentiation, anatomic structure morphogenesis, and viral entry into host cells (Appendix Fig. A6). Conversely, proteins that were upregulated in LOi in respect to LOp displayed relatively less specific biological functions; they were mostly associated with

changes at the DNA level such as DNA repair, DNA metabolic process, and DNA conformational change. Only 10 proteins were specific to the lung.

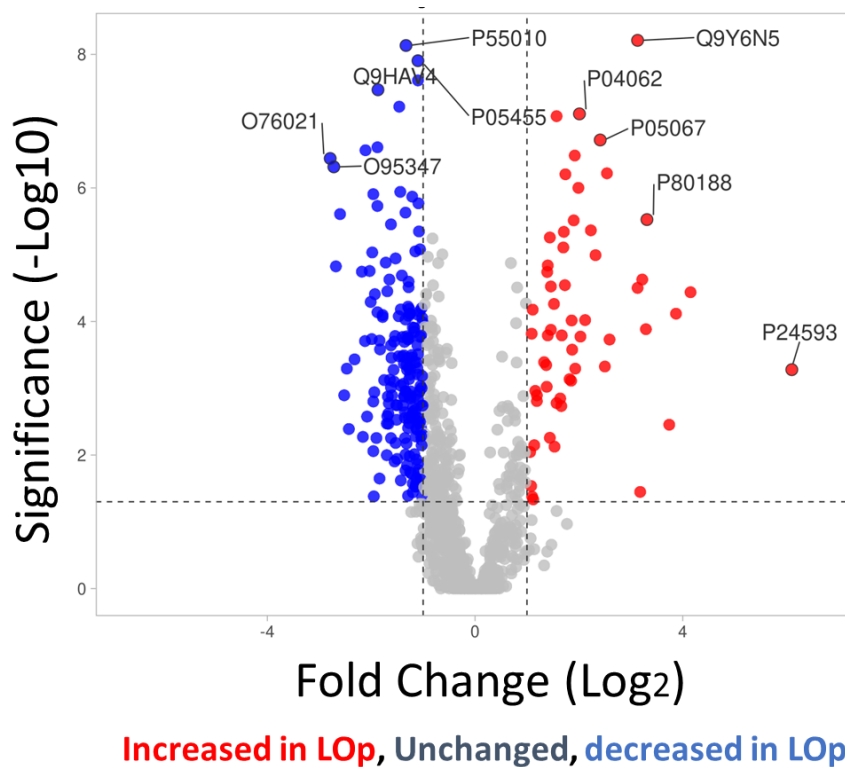


Fig. 3.23 Comparison of proteomic profile of each type of lung organoids (LOp) and LOi. Volcano Plot generated by VolcanoR. Red upregulated proteins in LOp, Grey-unchanged proteins between samples. Blue-downregulated proteins in LOp.

Both proteomic profiles were then compared with that of adult lung tissue from three male donors aged 42, 51, and 66 years. Males of this age were chosen because of their susceptibility to COVID-19. Tissue from both superior and inferior regions was used to account for any potential differences in protein levels between the two regions.

The complete heatmap of proteins in lung tissue and organoids is shown in Fig. 3.24. The proteome of these samples was clustered into six groups. Cluster 1 demonstrates the similarity of proteins between lung tissues and LOp. Cluster 2 illustrates the similarity of proteins in LOi with those in lung tissues. Cluster 3 indicates the

upregulation of proteins in lung tissues compared to the organoids. Cluster 4 shows the upregulation of proteins in LOi compared to those in lung tissue. Clusters 5 and 6 represent the proteins upregulated in both organoids compared to lung tissues.

As shown in Fig. 3.25, cluster 1, the proteomic profile of LOp has similarities with the one of adult lung tissue. It shows resemblance to both lung regions: superior and inferior. To reiterate, the primary cells are taken from proximal tissues. There is a benefit for the future development of the organoids, to allow easier and safer collection of cells from proximal regions of the tissues (throat and bronchi) to reproduce the proteome of further distal tissue, itself harder and riskier to collect^{86,87}.

A numerical analysis was performed to quantify differences between all samples (Fig.3.26). As shown in Fig. 3.26A, adult lung tissue and LOp shared 1518 proteins, from which 5 were exclusively found in the tissues, and 6 in the organoids. Adult lung tissues and LOi shared 1519 proteins, with only 4 proteins absent from the organoids (Fig. 3.26B).

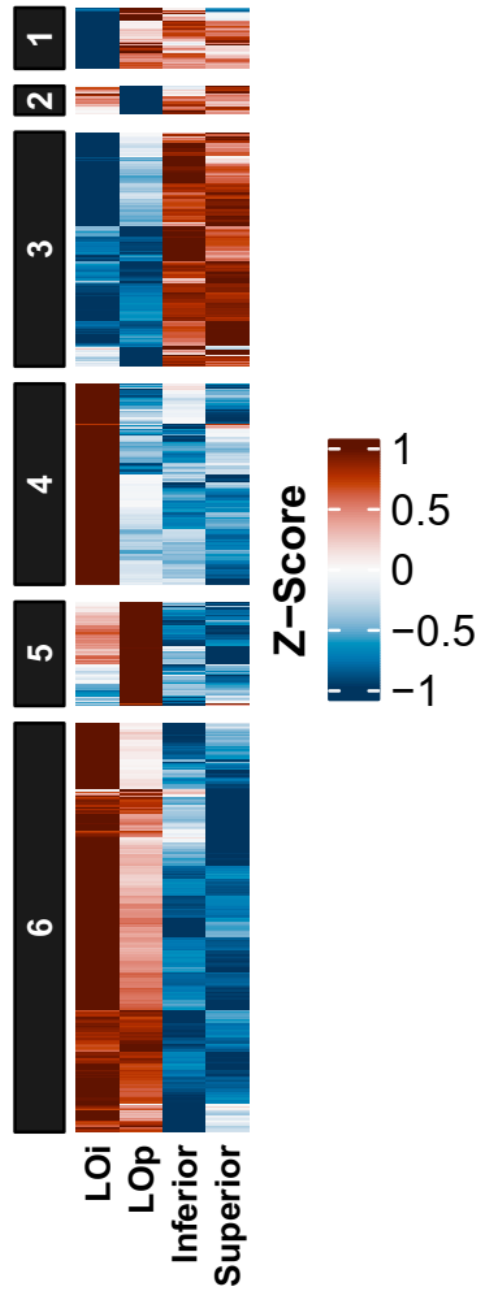


Fig. 3.24 Heatmap showing the regulation of proteins in lung organoids (LOp and LOi) and adult lung tissues (Inferior and Superior). Abundances grouped, linked by average. Red show upregulation and blue downregulation. N=3

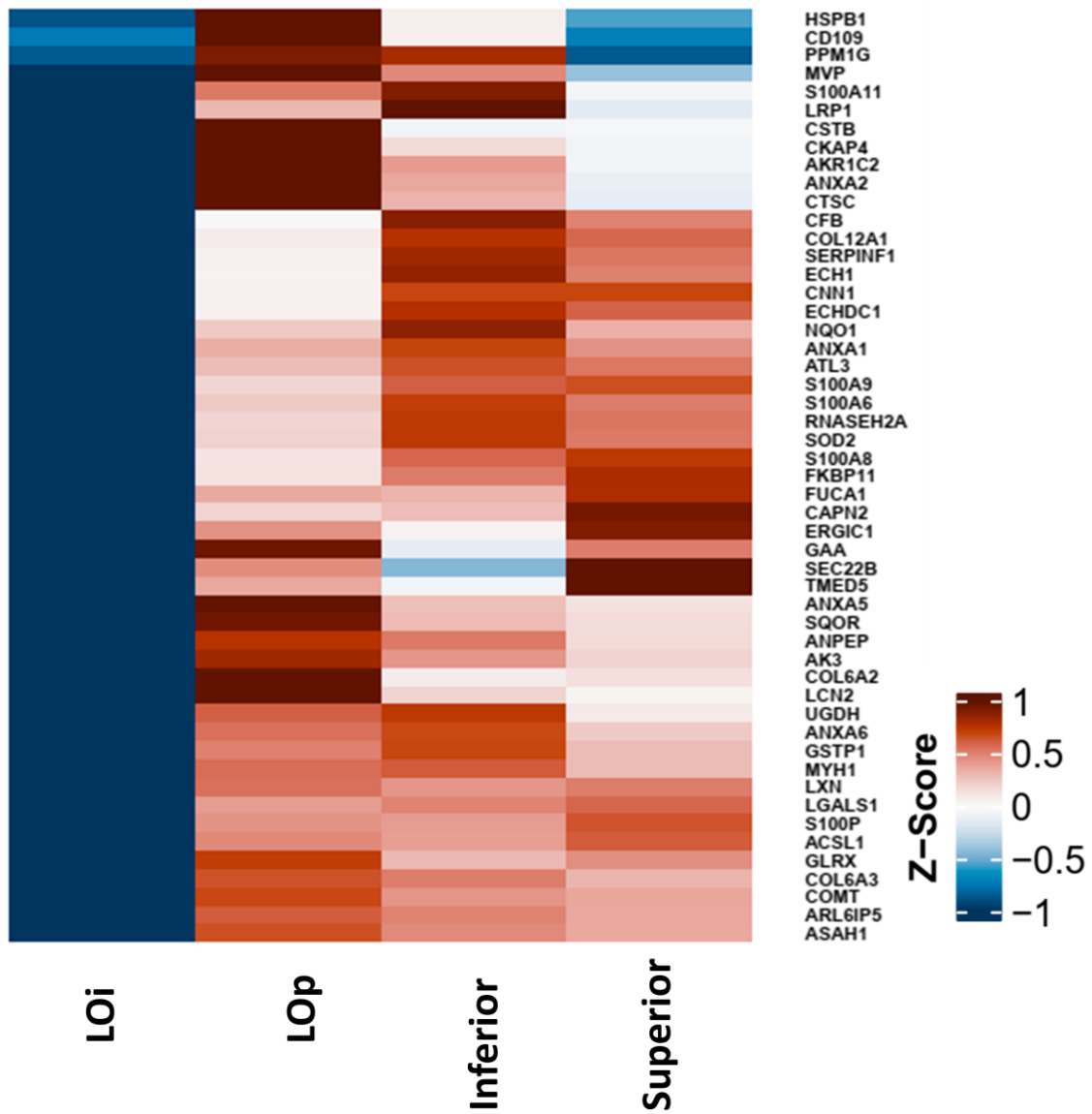


Fig. 3.25 Cluster 1 of heatmap showing the regulation of proteins in lung organoids (LOp and LOi) and adult lung tissues (Inferior and Superior). Abundances grouped, linked by average. Red show upregulation and blue downregulation. N=3

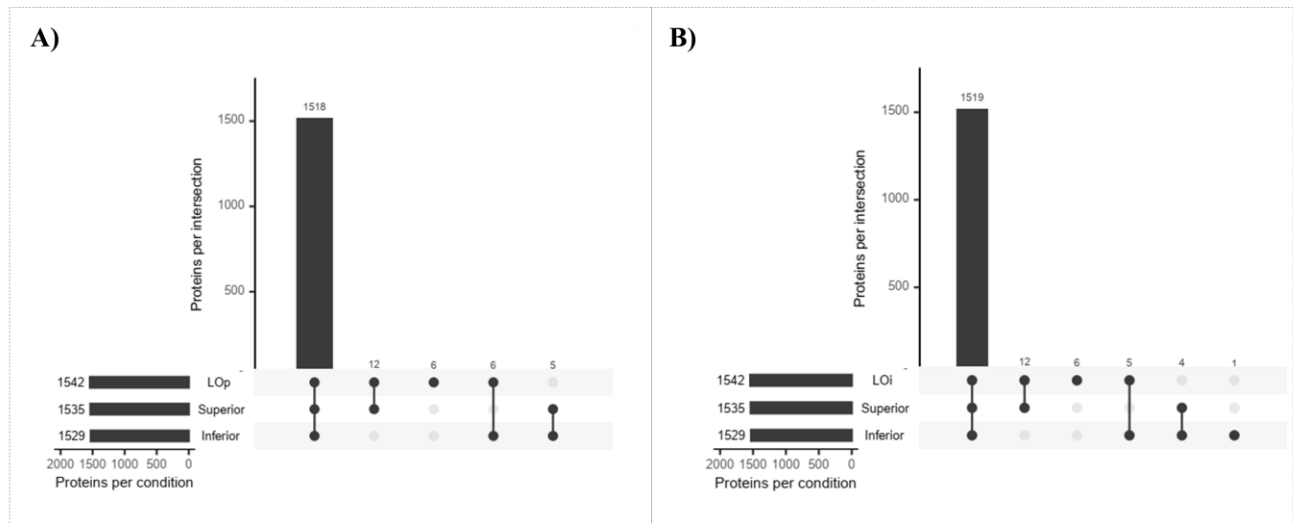


Fig. 3.26 UpSet plots visualizing the proteins shared between adult lung tissues and LOp (A) or LOi (B).

Gene ontology (GO) analysis was conducted on clusters 1, 3, and 6 of the proteome of adult lung tissues and organoids. These clusters correspond to sections of the proteome representing similarities between LOp and tissues, upregulated proteins in the tissues, and upregulated proteins in the organoids, respectively. Fig. 3.27 shows an overview of the terms overrepresented in these clusters, organizing proteins according to their biological roles or properties. It shows the number of proteins associated with each term and their statistical significance. The overrepresented terms in cluster 1 show that the proteins in LOp and adult tissues are related to alveolar type II cells, inflammatory response, lung macrophages, basal layer, epithelial migration, and response to stress. The proteins upregulated in lung tissues in respect to organoids (cluster 3) show overrepresented terms related to goblet cells, indicating a higher number of these cells in the tissue. Lung epithelial and lung cell differentiation, as well

as proteins related to secretory cells, were also found to be functionalities of the upregulated proteins in the tissue. On the other hand, the functionalities of the proteins upregulated in the organoids in respect to adult lung tissues (cluster 6) are related to bronchus respiratory epithelium, oral mucosa, and nasopharynx epithelium. This suggests that some of the proteins of the organoids correspond to the proximal lung region. Additionally, several proteins related to viruses were found in the organoids, such as coronavirus disease, virus replication, viral transmission, and response to virus, highlighting the potential application of the model for the study of viral diseases. Proteins associated with endothelial cells, alveolar cells, and lung macrophages were also found in this cluster.

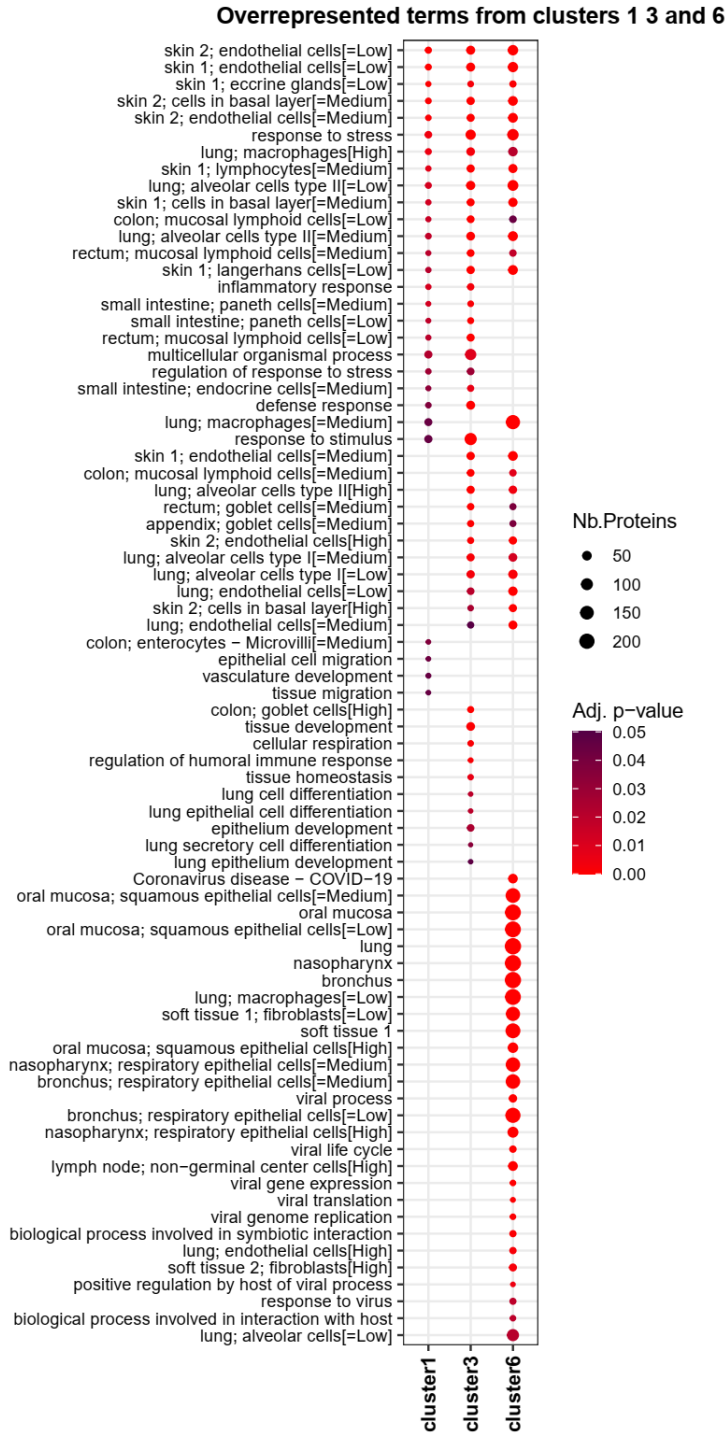


Fig. 3.27 Overrepresented terms from upregulated proteins in LOp and lung tissues (cluster 1), adult lung tissues (cluster 3) and lung organoids (cluster 6).

In summary, the proteome of organoids was found to be much more similar to that of adult lung tissues than the cell monolayers. Only 4 or 5 proteins are found exclusively in the tissue and not in the LOi or LOp, respectively. In terms of regulation, the similarity was strongest for organoids derived from primary cell lines, as could be expected from their increased differentiation capacity.

Lung organoids derived from primary cells (LOp) offer many advantages, such as elevated levels of innate immune response proteins, an enriched pool of lung and respiratory system-specific proteins, and clear differentiation into multiple cell types. But the lung organoids derived by immortalized cell lines (LOi) remain potentially useful as they also present multiple enriched pathway specific to the lung and respiratory system, albeit less than their LOp counter parts. Their morphology is also tubular. Their use would circumvent the need for primary cells, which are more expensive and challenging to acquire and culture than cell lines.

3. 4 Discussion

In this section, we have utilized the tools of proteomics and transcriptomics to examine in depth the lung phenotype of the organoids and in turn quantified their degree of similarity to the lung tissue over a wealth of specific respiratory system markers.

Using differential expression, the results demonstrate that lung organoids are more similar to lung tissue than their constituent cell types, thus probably providing better predictive models for in vitro screening. Beyond this, we have examined quantitatively the similarity of each type of organoid (LOi and LOp) with the adult lung tissue. In terms of regulation, lung organoids derived from primary cells showed the greater degree of

similarity to tissue. But both organoids share a high number of proteins with adult lung tissues.

One of the primary goals of the development of these new lung organoids is to generate in vitro models that were more complex than cell monolayers but remained easy to generate for further clinical applications. It is in that lens that the organoids derived from primary cells were taken from trachea/bronchi. These cells are more readily accessible than previously used primary cells from deeper lung tissues²⁴⁻²⁶. The data from this omics study demonstrate that despite their proximal origin, these cells yield lung organoids with upregulated genes that are known to be associated with respiratory system development (i.e. TBX4, ZIC3), tube development (i.e. HIP, NOG), and lung alveolus development (i.e. HOPX, SFTPD) of the entire lung^{1,16}.

The easiest organoids to generate remain the ones generated from immortalized cell lines (LOi). In the previous chapter, we have described how the use of immortalized cells could still lead to differentiation and organoid formation, as evidenced by the emergence of tubular morphology. In this chapter, the use of omics supports the differentiation of these cell lines into an organoid that mimics in some key functions the lung tissue. While the degree of similarity to the lung tissue is decreased compared to the more “naïve” primary organoids, it is still improved over cellular monolayers, and benefits from the ease of culture of immortalized cell lines.

One distinction of the present lung organoid (LOp) is the representation of both the proximal and distal regions of the lung. Most organoid models only capture one of the regions. Our organoids seem to have the advantage of representing both regions in key aspects. RNA sequencing data shows co-expression of markers of proximal (i.e.

MUC5B, TPR63) and distal (i.e. SFTPC, PDPN) regions of the lung for the LOp. This suggests that these models capture some of the heterogeneity of native lung tissue, which add more physiological accuracy than models which only partially represent specific lung regions. The presumed benefits of this remains to be demonstrated, which is the topic of ongoing investigation.

Except for basal cells, the expression of proximal markers of these organoids was found to decrease as the expression of distal markers increased, including surfactant proteins produced by AT2 cells. Surfactant proteins have innate immune functions¹³². This also highlights the cell differentiation process within the organoids.

In the second chapter of this thesis, we described the tubular and elongated morphology of the organoids induced by the incorporation of fibroblasts. Here, we found upregulated genes within the organoid associated with tube development, branching morphogenesis of epithelial tube, and epithelial tube branching involved in lung morphogenesis which suggest a well orchestrated process for the formation of these structures. The results show that morphological features are logically associated with cellular functions, molecular mechanisms and gene expression patterns^{134,135}. Interestingly lung organoids representing proximal or distal regions originated by adult cells are spherical, while iPSC derived organoids present a branched morphology and a more heterogenous phenotype⁷⁷.

Both RNA sequencing and proteome data shown that even in LOi (derived from cell lines), there is upregulation of mucin, TP63, Trmp5 and IL-15, markers of goblet, basal cells, and brush cells, respectively. The upregulation of markers of brush cells is consistent with the microvilli structure identified with FIB microscopy in chapter 2

(section 2.3.7). This further support the idea that there is some degree of plasticity on these organoids regardless of their cell origin. The proteomics data of the organoids show quantitatively their superiority in comparison to 2D cellular monolayers, even when comparing them to ALI models which are considered the gold standard³⁰.

Although LOp organoids have higher specificity towards the lung than LOi and show distal markers. LOi improves accessibility, and model scalability while reducing costs. While the cellular composition of these organoids was limited to an immortal bronchial cell line, the observed cellular output suggests that, although full differentiation may not have been achieved, significant improvements have been made towards a more heterogenous model. This indicates the potential for the environment to be auspicious for immortal cell differentiation in this case.

The accuracy of the model could be further improved. For example, endothelial, lymphoid, and immune cells could be incorporated. Interestingly proteins from the innate immune system, and viral receptor proteins were found upregulated in the organoids, which may be beneficial to model viral infections. This aspect will be further discussed in Chapter 4.

3. 5 Methods

3. 5. 1 Cell culture

CFBE and IMR-90 were cultured in Eagle's minimum essential medium (VWR, CA45000-380) supplemented with 10% (vol/vol) FBS (Sigma-Aldrich, F1051), 2 mM L-glutamine (Thermo Fisher, A2916801), 1% Penicillin Streptomycin (Fisher Scientific, SV30010), and incubated at 37°C in 5% CO₂-95% O₂.

3. 5. 2 CFBE culture in air-liquid interface

For establishment of ALI, CFBE were seeded on fibronectin (Promo cell, C-43060) coated permeable cell culture inserts (Fisher Scientific, 08-771-10) and cultured for 21 days before the study.

3.5.3 Primary airway epithelium culture in air-liquid interface

Primary human bronchial epithelial were provided by Primary Airway Cell Biobank (PACB) in the Cystic Fibrosis Translational Research Centre at McGill University. Cell from male and female donors of 51 and 53 years old, respectively were used. Cells were seeded on collagen IV coated cell culture inserts (Fisher Scientific, 08-771-10) and cultured in ALI medium provided by PACB. After 3 days, the apical medium was removed, and cells were allowed to differentiate for 28 days at the air-liquid interface before study. The medium in the basolateral chamber was changed every two days. Once a week, the apical mucus was aspirated carefully to avoid disruption of the monolayer. This was followed by washing the apical side with PBS without Ca²⁺.

3.5. 4 Bulk RNA sequencing and analysis

RNA extraction was performed according to the sample type, as follows.

Lung, RNeasy Plus Universal mini kit (QIAGEN) was used. Frozen tissue samples were weighed and processed on ice to prevent thawing. For homogenisation: 900 µl of RNeasy Plus Universal Mini Kit provided lysis buffer reagent (i.e. QIAzol) was added to the tissues and homogenized using a QIAGEN TissueLyser II with 2,8 mm ceramic beads, for 2 cycles of 30 Hz x 2 min plus 1 cycle of 30 Hz x 1 min. Extraction was performed according to the manufacturer's instructions. RNA was eluted in 35 µl buffer provided with the extraction kit. RNA quality was determined by the RNA Integrity

Number (RIN), measured by 2100 Bioanalyzer (Agilent Technologies) using RNA 6000 Nano kit, following the manufacturer's protocol.

Organoid, three organoids were disassociated and integrated as one sample to obtain enough RNA per sample. This was done on three independent sets of organoids. Therefore 9 organoids were processed and divided in 3 samples. RNeasy Plus Universal mini kit (QIAGEN) was used. For homogenisation 900 µl Trizol reagent was added to the samples and homogenized using a QIAGEN TissueLyser II with 2,8 mm ceramic beads, for 3 cycles of 30 Hz x 2 min. Extraction was performed according to the manufacturer's instructions. RNA was eluted in 35 µl buffer provided with the extraction kit.

RNA quality was determined by the RNA Integrity Number (RIN), measured by 2100 Bioanalyzer (Agilent Technologies) using RNA 6000 Nano kit, following the manufacturer's protocol.

Cells, miRNeasy mini kit (QIAGEN) was used. Cell samples were homogenized in the TRizol lysis reagent by passing the lysate 10 times through a 20-gauge needle attached to a sterile 3 ml plastic syringe.

Extraction was performed according to the manufacturer's instructions. RNA was eluted in 35 µl buffer provided with the extraction kit. RNA quality was determined by the RNA Integrity Number (RIN), measured by 2100 Bioanalyzer (Agilent Technologies) using RNA 6000 Nano kit, following the manufacturer's protocol.

Library preparation

Ribosomal RNA was depleted from 250 ng of total RNA using QIAseq FastSelect. cDNA synthesis was achieved with the NEBNext RNA First Strand Synthesis and

NEBNext Ultra Directional RNA Second Strand Synthesis Modules (New England BioLabs). The remaining steps of library preparation were done using and the NEBNext Ultra II DNA Library Prep Kit for Illumina (New England BioLabs). Adapters and PCR primers were purchased from New England BioLabs.

Library QC

Libraries were quantified using the KAPA Library Quantification Kits - Complete kit (Universal) (Kapa Biosystems). Average size fragment was determined using a LabChip GX II (PerkinElmer) instrument.

Sequencing

The libraries were normalized and pooled and then denatured in 0.02N NaOH and neutralized using HT1 buffer. The pool was loaded at 175 pM on a Illumina NovaSeq S4 lane using Xp protocol as per the manufacturer's recommendations. The run was performed for 2x100 cycles (paired-end mode). A phiX library was used as a control and mixed with libraries at 1% level. Base calling was performed with RTA v3. Program bcl2fastq2 v2.20 was then used to demultiplex samples and generate FASTQ reads.

Analysis

The quality of the raw reads was assessed with FASTQC v0.11.8. After examining the quality of the raw reads, no trimming was deemed necessary. The reads were aligned to the GRCh38 human reference genome with STAR v2.7.6a, with an average of 90 % of reads uniquely mapped. The raw counts were calculated with FeatureCounts v1.6.0 based on the human reference genome (release 108). Differential expression was performed using DESeq2 R package. Differentially expressed genes were define using $\text{adj-pvalue} < X$ and $|\log_2\text{FCshrink}| \geq 4 X$ leading respectively X, Y, Z DEGs for A vs B, A

vs C and B vs C. DEGs heatmap were drawn based on z-score of normalized count. Bioinformatics analyses were performed at the Bioinformatics core facility from Montreal Clinical Research Institute (IRCM).

3.5. 5 Tandem Mass Tags

Sample preparation

Cells monolayers and organoids were washed with cold PBS (X3) following by incubation on ice cold RIPA buffer (Sigma, R0278). The cell monolayers and organoids are broken using a plastic cell scraper. Organoids are passed by 21G needle until completely disassociated. Cells are collected and centrifuged at 16000 G for 50 min at 4°C. The supernatants were collected, protein quantification was performed with Qubit Protein Assay (ThermoFisher, Q33211), and normalized to 45 ng of protein. Samples were stored at -80 °C until their analysis. All the reported proteins had 95% of threshold.

Experimental procedure

Samples were treated with TMT-16plex reagents (ThermoFisher Scientific) according to the manufacturer's instructions. Labelled peptides were fractionated using Pierce™ High pH Reversed-Phase Peptide Fractionation Kit into 8 fractions. Each fraction was re-solubilized in 0.1% aqueous formic acid and 2 ug of each was loaded onto a Thermo Acclaim Pepmap (Thermo, 75 uM ID X 2cm C18 3 uM beads) precolumn and then onto an Acclaim Pepmap Easyspray (Thermo, 75uM X 15cm with 2uM C18 beads) analytical column separation using a Dionex Ultimate 3000 uHPLC at 250 nl/min with a gradient of 2-35% organic (0.1% formic acid in acetonitrile) over three h running the default settings for MS3-level SPS TMT quantitation (McAlister et al, 2014 - Anal Chem. 2014 Jul 15;86(14):7150-8. doi: 10.1021/ac502040v.), on an Orbitrap Fusion instrument

(ThermoFisher Scientific) was operated in DDA-MS3 mode. Briefly, MS1 scans were collected at 120,000 resolutions, scanning from 375-1500 m/z, collecting ions for 50ms or until the AGC target of $4e5$ was reached. Precursors with a charge state of 2-5 were included for MS2 analysis, which were isolated with an isolation window of 0.7 m/z. Ions were collected for up to 50 ms or until an AGC target value of $1e4$ was reached and fragmented using CID at 35% energy; these were then read out on the linear ion trap in rapid mode. Subsequently, the top 10 (height) sequential precursor notches were selected from MS2 spectra for MS quantitative TMT reporter ion analysis, isolated with an m/z window of 2 m/z and fragmented with HCD at 65% energy. Resulting fragments were read out in the Orbitrap at 60,000 resolutions, with a maximum injection time of 105ms or until the AGC target value of $1e5$ was reached.

Mass Spectrometry Raw Data Analysis

To translate .raw files into protein identifications and TMT reporter ion intensities, Proteome Discoverer 2.2 (ThermoFisher Scientific) was used with the built-in TMT Reporter ion quantification workflows. Default settings were applied, with Trypsin as enzyme specificity. Spectra were matched against the human protein fasta database obtained from Uniprot (2022). Dynamic modifications were set as Oxidation (M), and Acetylation on protein N-termini. Cysteine carbamidomethyl was set as a static modification, together with the TMT tag on both peptide N-termini and K residues. All results were filtered to a 1% FDR.

Analysis

ANOVA (individual proteins). Ratios were calculated based on protein abundances, and three biological replicates. For volcano plots, these values were graph as Log₂ (Fold

Change), versus Log10 p-value (Significance). Changes in the proteome were considered only when $2 \leq \text{Fold Change} \leq 2$, and Significance > 2 .

The set of changing proteins of each group was analyzed using the STRING software database, available online. <https://string-db.org/>. STRING collect and scores evidence from several sources including text mining of scientific literature, databases of interaction experiments and complex pathways, computational interactions, and predictions from co-expression³⁰. Only nodes and networks with high strength ($p < 0.05$) and low false discovery rate are shown.

The pipeline of Tandem Mass Tags analysis for all samples is shown in Fig.3.28

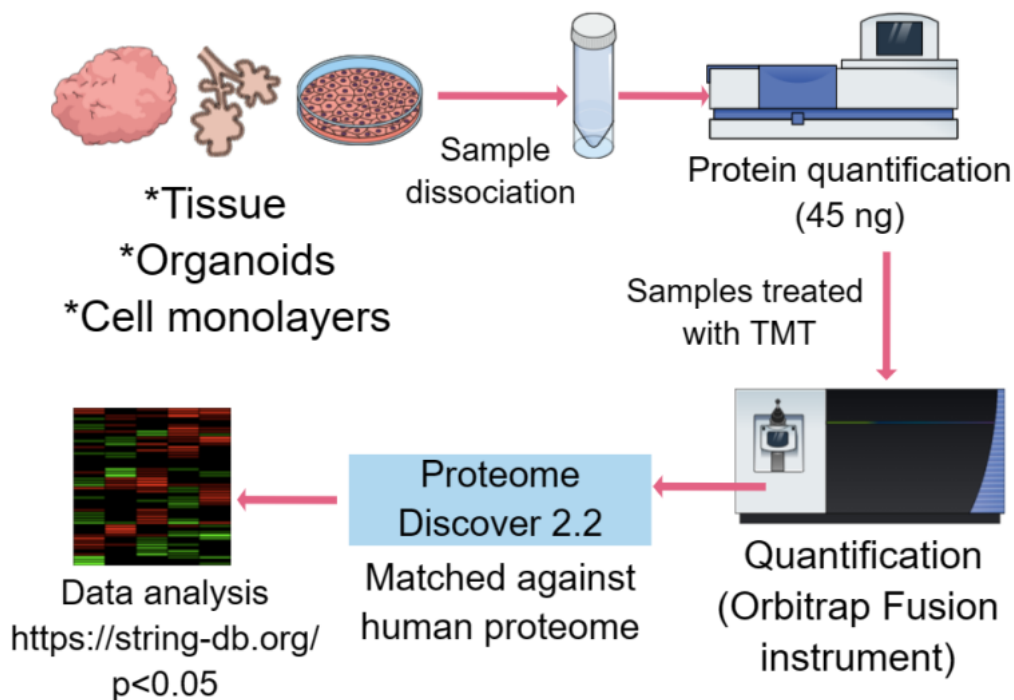


Fig. 3.28. Schematic showing the pipeline of proteomics analysis of cell monolayers, organoids, and adult lung tissues.

For gene ontology analysis, protein abundances across different conditions were collected in a matrix, and unidentified proteins were imputed with a value of zero. A

pseudo-count of one was then added to the matrix, and a z-score was calculated for each protein (row-wise). Heatmaps were created in R with the ComplexHeatmap package, employing the ward.D2 clustering method on Canberra distances. Clusters of proteins were extracted, and overrepresentation analyses were performed on Gene Ontology (GO) terms, KEGG pathways, Human Protein Atlas (HPA) tissues, and CORUM complexes with the R package gprofiler2 (PMID 31066453). The p-values were statistically corrected with the false discovery rate (FDR) correction method. Statistically significant terms with adjusted p-values < 0.05 were selected and presented in dotplots using the R package ggplot2. Additionally, UpSet plots were created in R with the upsetR package to enumerate non-redundant interactions identified among the different condition

3.5. 6 Flow cytometry

To assess the percentages of the types of cells, the LOs were analyzed by flow cytometry. Briefly, the organoids were dissociated with Trypsin-EDTA (Fisher Scientific, MT25053CI) for 30 min at 37°C. Clumps were disassociated with 21G gauge needle. Cell suspension was collected and centrifuged for 5 min. Supernatants were discarded and the cell pellets were wash twice with PBS. Samples were fixed with 4% PFA, and permeabilized with 0.1% Triton X-100. Subsequently, cells were incubated with 10% Goat serum for 15 min. The cells were incubated with antibodies conjugated (Key Resources Table) in flow cytometer staining buffer (ThermoFisher, 00-4222-57) for 20 min. Beads were incubated with single antibodies, and fluorescence minus one (FMO) organoid were used to calibrate the instrument. A BD FACS LSR Fortessa was used to analyze the samples. Gating strategy was based on scattering samples by size and

granularity. The samples were focused on singlets (height: FSC-H vs width: FSC-W). Double screen was done for size scattering. Percentages was graph against histogram. Percentages represent one individual marker.

3.5. 7 Immunofluorescence Staining

Organoids were washed with PBS (Fisher Scientific, 10-010-049) supplemented with 10 mM CaCl₂ (Sigma, Aldrich, C4901) three times for 3 min. Afterwards, the organoids were fixed with 3.7% paraformaldehyde, permeabilized with 0.3% Triton X-100 (Sigma Aldrich, T9284), and blocked for 2 h with 10% Goat serum (Thermo Fisher, 50062Z) at room temperature. Organoids were cultured with primary antibodies conjugated with fluorochromes, diluted in 10% goat serum at 4°C overnight. Nuclei with Hoechst dye (Thermo Fisher H3569). The confocal images were acquired using an LSM-710 inverted confocal microscope. Surfactant protein B (Santa Cruz-133143-AF488) and Surfactant protein C (Santa Cruz, 518029, AF594) were used as markers of alveolar type II cells (1:100). Three different organoids were imaged for Surfactant protein B and C.

3. 5. 8 RNA isolation and quantitative PCR

RNA was extracted using Illustra RNA Spin Mini kit (Ge Healthcare, GE25-0500-71) according to the manufacturer's instructions. RNA (500 ng) was reverse transcribed with 5X RT Master Mix (Diamed, ABMG486) with incubation at 25°C for 10 min, 42°C for 1 h, and 85°C for 5 min. Quantitative PCR (qPCR) was performed using Power track SYBR green (ThermoFisher, A46109). The reaction was performed using a QuantStudio 7 Flex Real-Time PCR system and the following protocol: 20 s at 95°C and 40 cycles at 95°C (1 s) and 60°C (20 s). Change in gene expression relative to housekeeping gene

($\Delta\Delta C_t$) was calculated using the manufacturer's software package. Primers were predesigned for IDT, except for the house keeping gene HPRT, listed in key Resources Table II (Appendix)

Chapter 4 Modeling respiratory diseases with lung organoids

4. 1 Contributions

Alicia Reyes Valenzuela cultured primary and immortalized cells, and prepared the organoids needed for the experiments. She infected organoids with influenza H1N1 and H3N2. She modified the original organoid protocol to allow the growth of asthmatic organoids and monitor their growth. In addition, she analyzed RNA sequencing data of non-infected organoids and tissues. Nathan Markarian performed the organoid infection with SARS-CoV-2. He along with Charlotte Fouquet performed RNA extraction of infected organoids. In addition, Nathan analyzed viral RNA copies in the organoid lysate and supernatant. Charlotte Fouquet analyzed viral supernatant of organoids infected with influenza using plaque assay. Silvia Vidal designed the experiments for viral infection and provided extensive guidance for the viral study. Luc Mongeau provided guidance and oversight during the study.

4. 2 Introduction

Lower respiratory infections are among the leading cause of death worldwide¹³⁶. Among them, influenza and coronaviruses are the two major respiratory viruses with pandemic potential¹³⁷. One example of this is the past SARS-CoV-2 pandemic, which emerged at the end of 2019¹³⁸. According to the World Health Organization, the pandemic resulted in over 15 million deaths worldwide, with a significant decrease in economic growth¹³⁹.

Coronaviruses are characterized by their envelope in single-stranded non segmented RNA virus. They have the largest genome of any RNA virus. To date, seven coronaviruses which can infect humans have been identified. Some of them are mild seasonal respiratory infections, and others have severe clinical manifestations. Examples of the former are HCoV-229E, HCoV-NL63, HCoV-OC43 and HCoV-HKU1¹⁴⁰. On the contrary, SARS-CoV, SARS-CoV-2, and MERS are highly pathogenic and transmissible coronaviruses¹⁴¹.

Influenza viruses are enveloped viruses, classified in four genera: IAV, IBV, ICV and IDV, all from the *Orthomyxoviridae* family. IAVs are particularly concerning as they cause annual epidemics and occasional human pandemics. They are subdivided based on two surface glycoproteins: haemagglutinin (HA) and neuraminidase (NA). The IAVs H1N1 and H3N2 currently cause most epidemic diseases in humans. Influenza viruses are in constant mutation, in specific in HA and NA, altering their fitness for human infections¹⁴⁰. Coronaviruses, on the other hand, experience low mutation rates¹³⁸.

The overall structure of coronaviruses and influenza are shown in Fig. 4.1. To infect humans, influenza viruses, in particular HA, preferentially bind sialic acids inked to galactose by α (2,6). This is further processed by trypsin-like proteases. The spike protein S of coronaviruses binds to ACE2 receptor, which requires activation by a host protease, normally TMPRSS-2¹⁴⁰. TMPRSS-2 is also used for cleavage of influenza¹⁴².

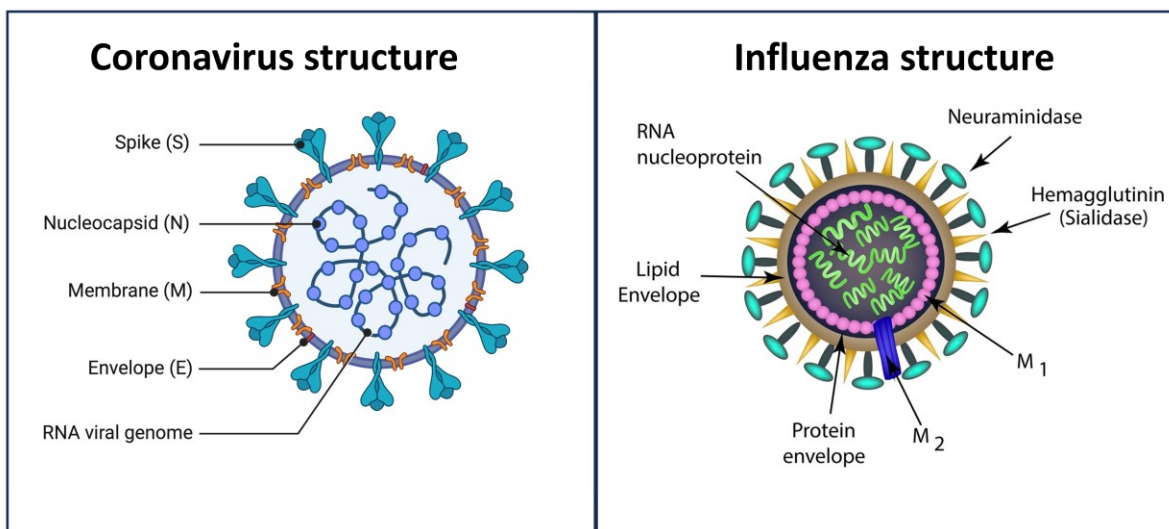


Fig. 4.1 Schematics showing the structure of Coronaviruses and Influenza. Images modified from: Online Biology Notes: Influenza Virus (Influenza virus-Structure, Types, Nomenclature, Transmission, Pathogenesis, Diseases, Diagnosis and Treatment - Online Biology Notes) and Biophysical Society: Coronavirus Structure, Vaccine and Therapy Development (Coronavirus Structure, Vaccine and Therapy Development (biophysics.org))

Viral infections from influenza and coronaviruses depend on host-specific mechanisms, in addition of their molecular evolution, fitness and pathogenesis^{78,137,140}.

Given their rapid adaptation to the host environment, the circulating viruses are genetically distinct from those grown on 2D monolayers⁷⁸. This has been reported for the human parainfluenza virus⁷⁸. Such genetic alterations often occur in virus envelope proteins involved in viral entry and transmission⁷⁸. This problem has been solved using organoids, preserving the viral genetics characteristics, and features as they are in natural viral infections¹³. It is still common, when using lung organoids for viral infection, to disrupt their 3D cellular structure to form a monolayer of cells prior to infection⁷⁵.

Another disadvantage of current lung organoids to model SARS-CoV-2, and influenza is the lack of cellular tropism. For instance, IVA, infects airway epithelium enriched with

sialic acid from trachea to bronchioles. Eventually, if the virus is not cleared, it infects alveoli¹⁴⁰. SARS-CoV-2 infects olfactory epithelium cells as well as secretory and ciliated cells from the nose, as well as secretory, ciliated and goblet cells from the bronchi (proximal) and ultimately AT2 cells (distal)^{10,140}. Both cellular tropisms of influenza and SARS-CoV-2 are illustrated in Fig. 4.2.

As described in chapter 1, lung organoid models typically represent only one lung region, for example alveospheres⁶¹, broncheospheres⁶², tracheospheres^{6,64} or human airways organoids⁶⁵. They fail to accurately reproduce natural viral infections.

The growth period for iPSC-derived lung organoid models spans several months²¹, rendering them impractical in the context of a pandemic marked by the rapid emergence of new variants¹⁴¹. Furthermore, these organoids retain an immature state, rendering them unsuitable for accurately modeling adult viral diseases^{21,51}.

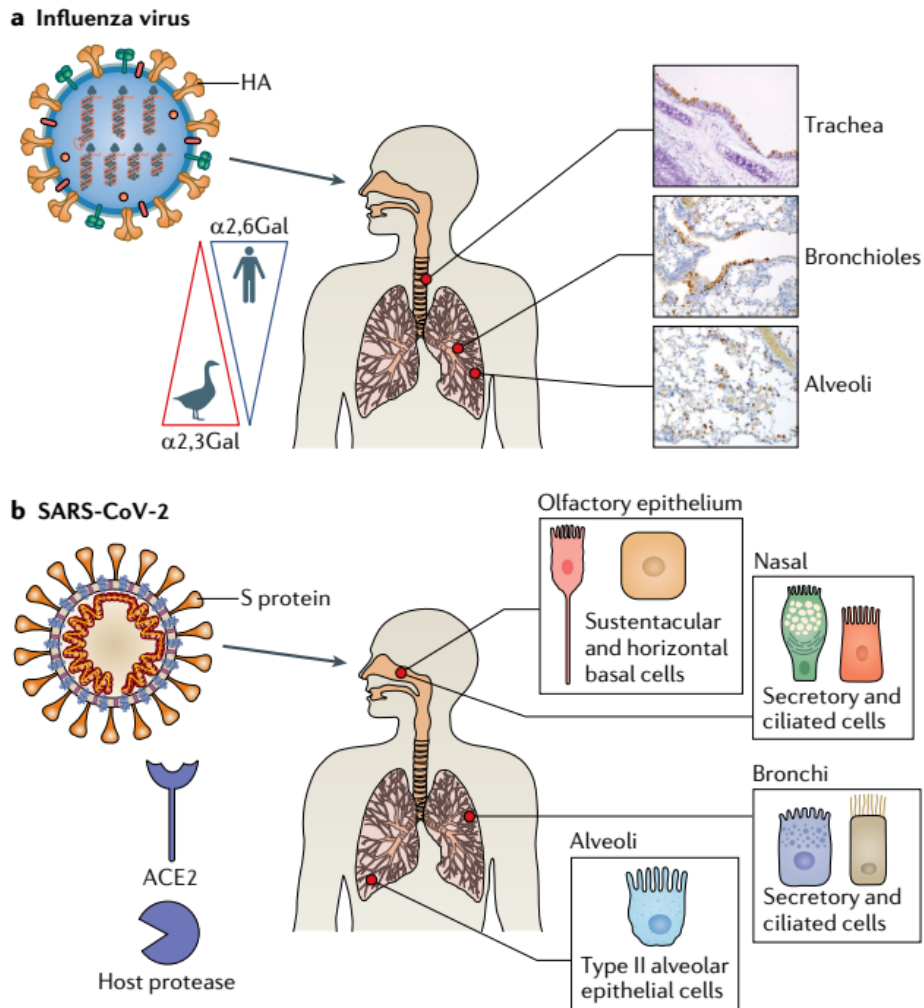


Fig. 4.2 Viral tropism of influenza and SARS-CoV-2. Image obtained with permission from¹⁴⁰ (License number: 5764260448937).

In addition to respiratory viral infections, chronic respiratory diseases are also a common cause of death worldwide. In 2019, they were the third leading cause of death, including specific diseases such as asthma, pneumoconiosis, chronic obstructive pulmonary disease (COPD), interstitial lung diseases and pulmonary sarcoidosis¹⁴³. From these diseases, asthma has the greatest prevalence¹⁴³.

Asthma involves proximal and distal regions of the lung. It is characterized by a stage of chronic inflammation and continuous structural changes. The former condition is

associated with airway hyper-responsiveness and reversible airflow obstruction by expansion of mucus glands and excessive proliferation of mucus-secreting cells. The increasing susceptibility of airway epithelium to damage triggers the release of growth factors, which in turn induce remodelling by mesenchymal cells sustaining chronic inflammation¹⁴⁴. To the best of our knowledge, no organoid has been used for the modelling of asthma so far.

In this chapter, we aim to explore applications of our heterogenous lung organoids to model diseases. The chapter starts by analyzing genes and proteins involved during influenza and coronaviruses infections in the organoids and in adult lung tissues. We show that organoids have receptors and proteases to allow infectibility by influenza A and SARS-CoV-2. Our model was then infected with influenza H1N1 and H3N2, and SARS-CoV-2. Our model shows viral infection and replication. The last application we explored, was the generation of organoids derived from asthmatic patients, in which variations in our original protocol were made to promote organoid formation.

4. 3 Results

4.3. 1 Genes and proteins involved in Respiratory viral infections.

Using RNA sequencing data obtained in Chapter 3, genes associated with critical illness in patients with COVID-19 were further analyzed for both type of organoids and adult lung tissues. Genes SLC6A2, IFNAR1, IFNAR2, OAS3, OAS1, FOXP4, DPP9, TYK2¹⁴⁵ were identified in 244 critical ill patients with COVID-19. Low levels of IFNAR2 and high levels of TYK2 were associated with life threatening disease¹⁴⁵. It was observed that IFNAR2 was downregulated in the organoids in comparison to the tissue, and TYK2 was upregulated, as shown in Fig. 4.3. This suggests the potential benefit of using

these organoids for modeling severe SARS-CoV-2 infection. In particular, LOi had the highest expression of TYK2 and the lowest expression of IFNAR2. Interestingly, organoids upregulated OAS complex, including OAS1, OAS2, and OAS3. Of these, OAS3 was the most abundant in LOi. “This is an antiviral enzyme which plays a role in cellular innate antiviral response. When activated, it inhibits protein synthesis, thus terminating viral replication¹⁴⁶.¹⁰ Therefore, OAS cluster has been associated with potential therapeutic target against COVID-19¹⁴⁵.

Other studies have highlight SCL6A2 as a putative mediator of severity of SARS-CoV-2. Indicating that this gene interacts with angiotensin, converting enzyme 2, and allowing viral infection¹⁴⁷. SCL6A2 is upregulated in adult lung tissues but not in organoids. Dipeptidyl peptidase 9, DPP9, has been found to increase in patients with severe COVID-19 in male and female patients. It was deemed to contribute to the induction of inflammatory response¹⁴⁸. Interestingly, this gene was upregulated in organoids, with higher expression in LOi, followed by LOp. Similarly, Forkhead box protein P4, FOXP4, active in lungs and immune cells, has been associated with higher odds of developing long COVID¹⁴⁹. This gene was found more abundantly in organoids derived from immortal cell lines.

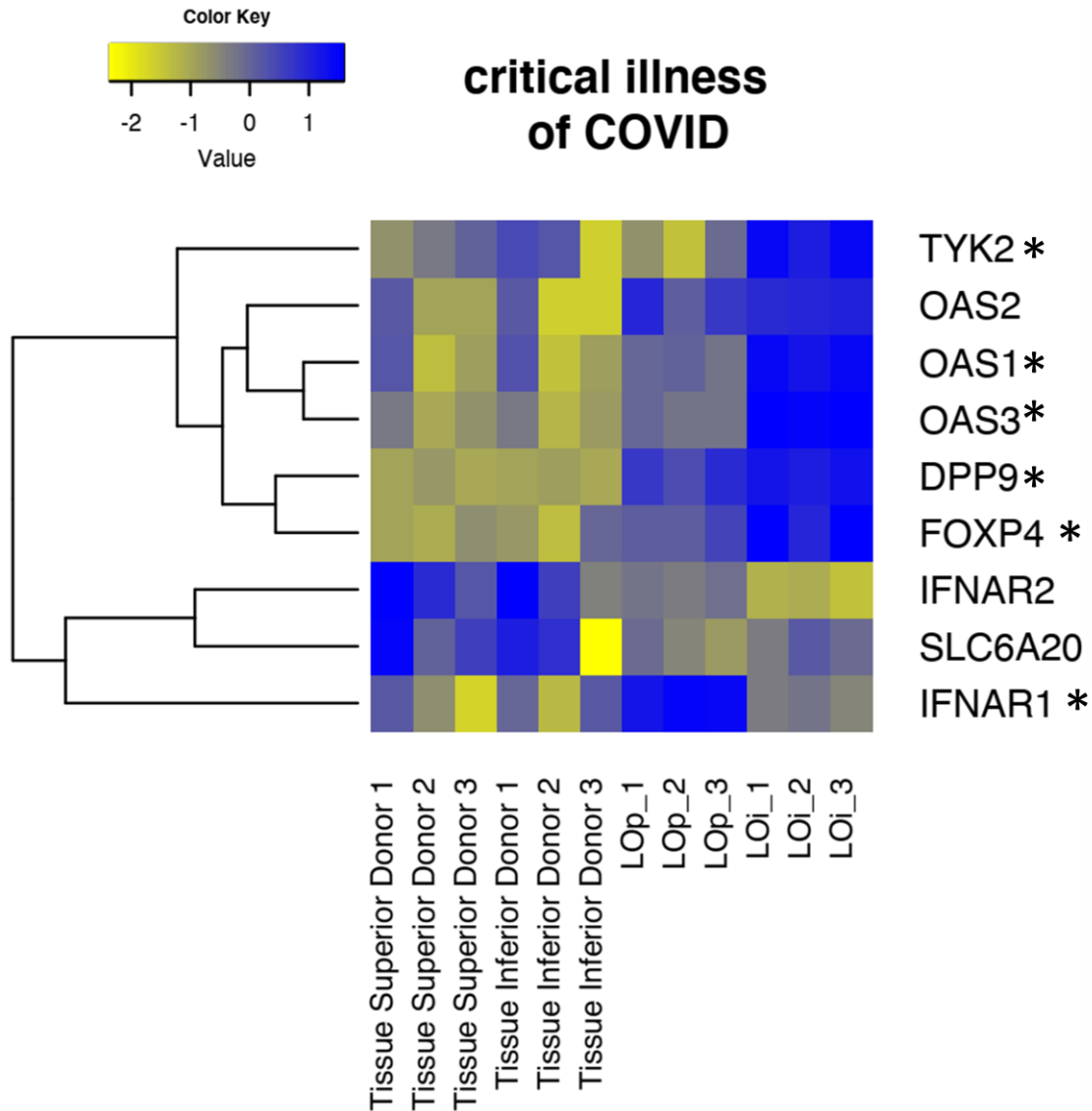


Fig. 4.3 Expression of genes associated with critical illness of patients with SAR-CoV-2 on organoids and adult lung tissues. T-tests (LOp and LOi) * p. adjust<0.05. N=3. Upregulation shown in blue.

Interferon induced transmembrane genes were also studied. These genes restrict the cellular entry of diverse viral pathogens such as influenza A, COVID-19, and Ebola virus¹⁵⁰. Interferon Induced Transmembrane 3 (IFITM3) was the most abundant transmembrane in all the samples,¹⁰ as shown in Fig.4.4. It was also significantly increased in LOi.

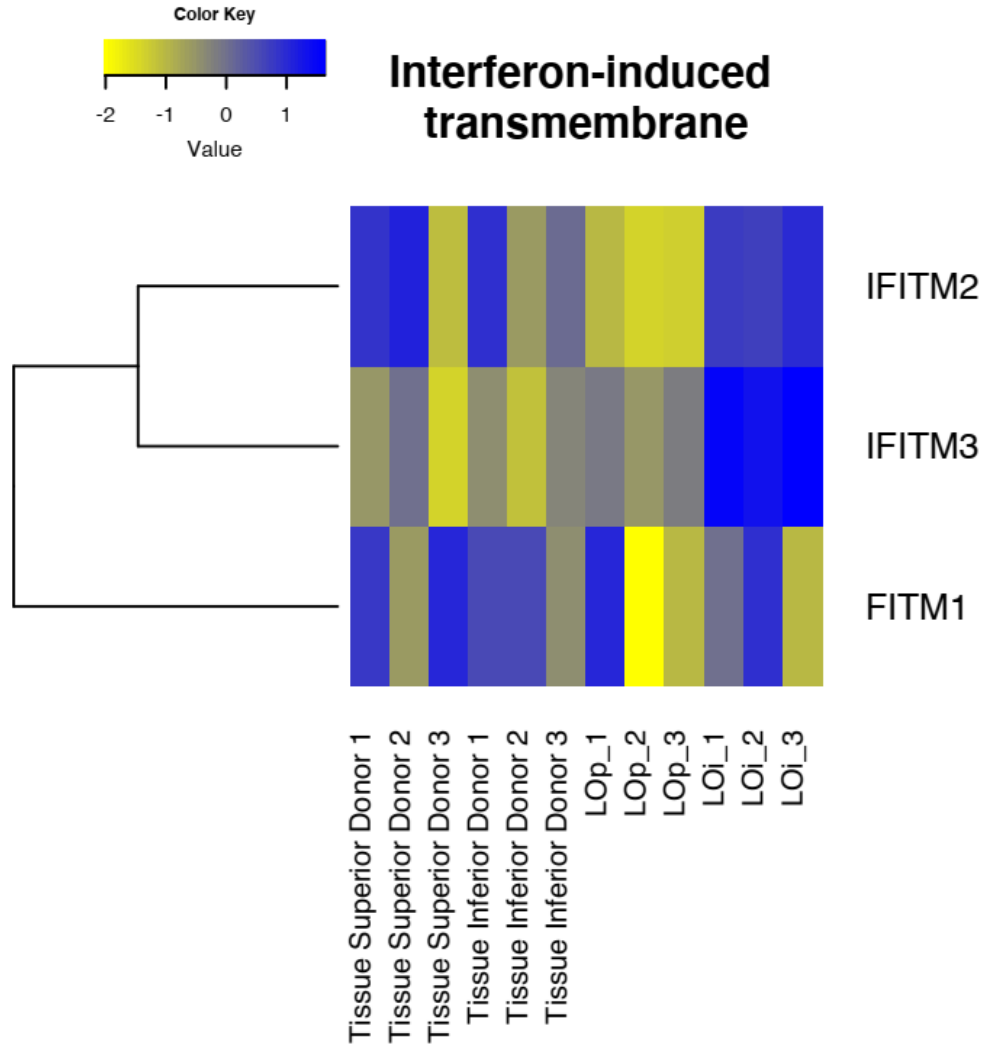


Fig. 4.4 Expression of interferon induced transmembrane genes associated with restriction of entry of viral pathogens SAR-CoV-2 on organoids and adult lung tissues. T-test (LOp vs LOi) adjust <0.05 in all comparisons. N=3. Upregulation shown in blue.

Human host factors required for influenza were investigated through different pathways illustrated in Fig. 4.5. These pathways are Coat Protein Complex I (COPI), Phosphoinositide 3-kinase- Protein kinase C (IP3-PCK), and endosomal uptake, maturation, and acidification. COPI genes are associated with the entry of virus by endosomal trafficking^{151,152}. Except for Unconventional SNARE In the ER 1 (USE1), all

other COPI genes were upregulated on LOp, in comparison to tissues and LOi (Fig.4.5A).

The set of genes classified as part of the IP3-PCK pathway help viral entry and enhance viral replication¹⁵². “In this case, all genes, except for Rho Associated Coiled-Coil Containing Protein Kinase (ROCK1), were upregulated in the organoids in comparison to the tissues. Between the organoids, LOp has the highest expression of this set of genes, as illustrated in Fig.4.5B.

Endosomal uptake, maturation, acidification, and fusion genes were also investigated mainly for their capacity to acidify intracellular organelles allowing viral entry¹⁵². These genes were upregulated in lung organoids derived from both primary and immortalized cell lines compared to tissues. Fig. 4.5C. From these genes, ATPase H⁺ Transporting V1 Subunit A (ATP6V1A), and ATPase H⁺ Transporting V1 Subunit B2 (ATP6V1B2) exhibited the highest expression levels in LOp. While ATPase H⁺ Transporting V0 Subunit B (ATP6V0B), ATPase H⁺ Transporting V0 Subunit C (ATP6V0C), and ATPase H⁺ Transporting Accessory Protein 1 (ATP6AP1) were most expressed in LOi.

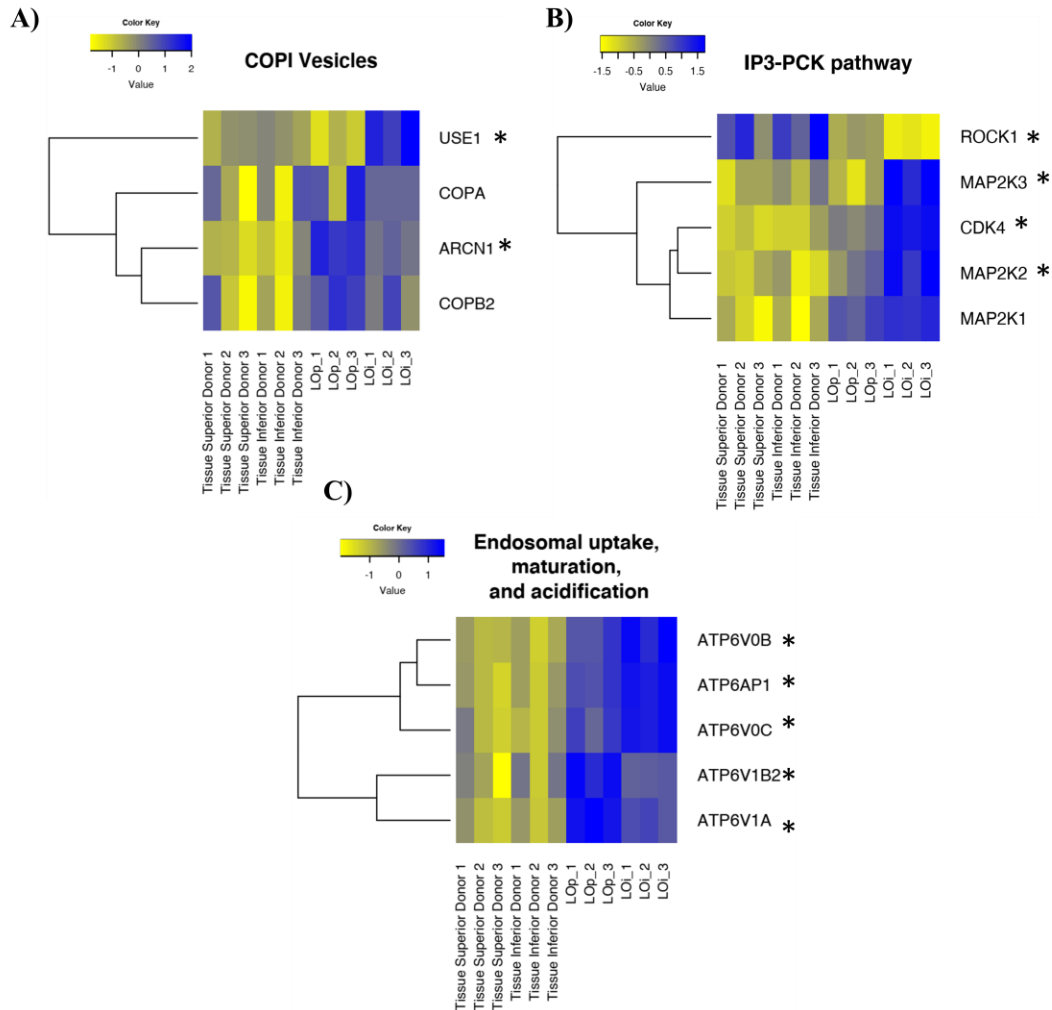


Fig. 4.5 Expression of human host factors required for influenza, classified in three different pathways. A) Coat Protein Complex I. B) Phosphoinositide 3-kinase- Protein kinase C. C) Endosomal uptake, maturation, acidification, and fusion. T-test (LOp vs LOi) * p adjust<0.05. N=3. Upregulation shown in blue.

Furthermore, entry and priming mechanisms of respiratory viruses, such as Angiotensin-Converting-Enzyme 2 (ACE2) and Transmembrane serine protease 2 (TMPRSS2), were also studied, as shown in Fig. 4.6. The former is the main mechanism of entry of SARS-CoV-2¹⁵³, while the latter is involved in the priming of SARS-CoV-2¹⁵³ or other coronaviruses and influenza¹⁵⁴. TMPRSS2 was found abundantly in LOP in comparison to the tissues and LOi; ACE2 was found more highly

upregulated in tissues than in LOp, and less abundant in LOi. FURIN, was also investigated since this protease has the potential to cleave the viral envelope glycoprotein, enhancing viral fusion with the host membrane^{155,156}. Several studies have discussed its role in SARS-CoV-2 infectivity^{156,157}. FURIN was upregulated in LOi relative to LOp¹⁰. RT-qPCR was performed on LOi at day 21 to confirm the expression of ACE2 and TMPRSS2. Their expression was confirmed, and it was found upregulated in LOi in comparison to CFBE (Fig. 4.6B). In addition, immunofluorescence was performed on LOi at day 7, showing ACE2 and TMPRSS2 on the organoids, as shown in Fig. 4.6C.

The presence, and in some cases upregulation, of these pathways crucial to the infectivity of SARS-CoV-2 or Influenza A led us to believe our lung organoids could act as good potential models for the progression of these diseases. Towards a fast, and scalable model for infection, we chose to focus our infectivity studies on the LOi organoids, since their generation from immortalized cell lines make them easier for other laboratories to generate.

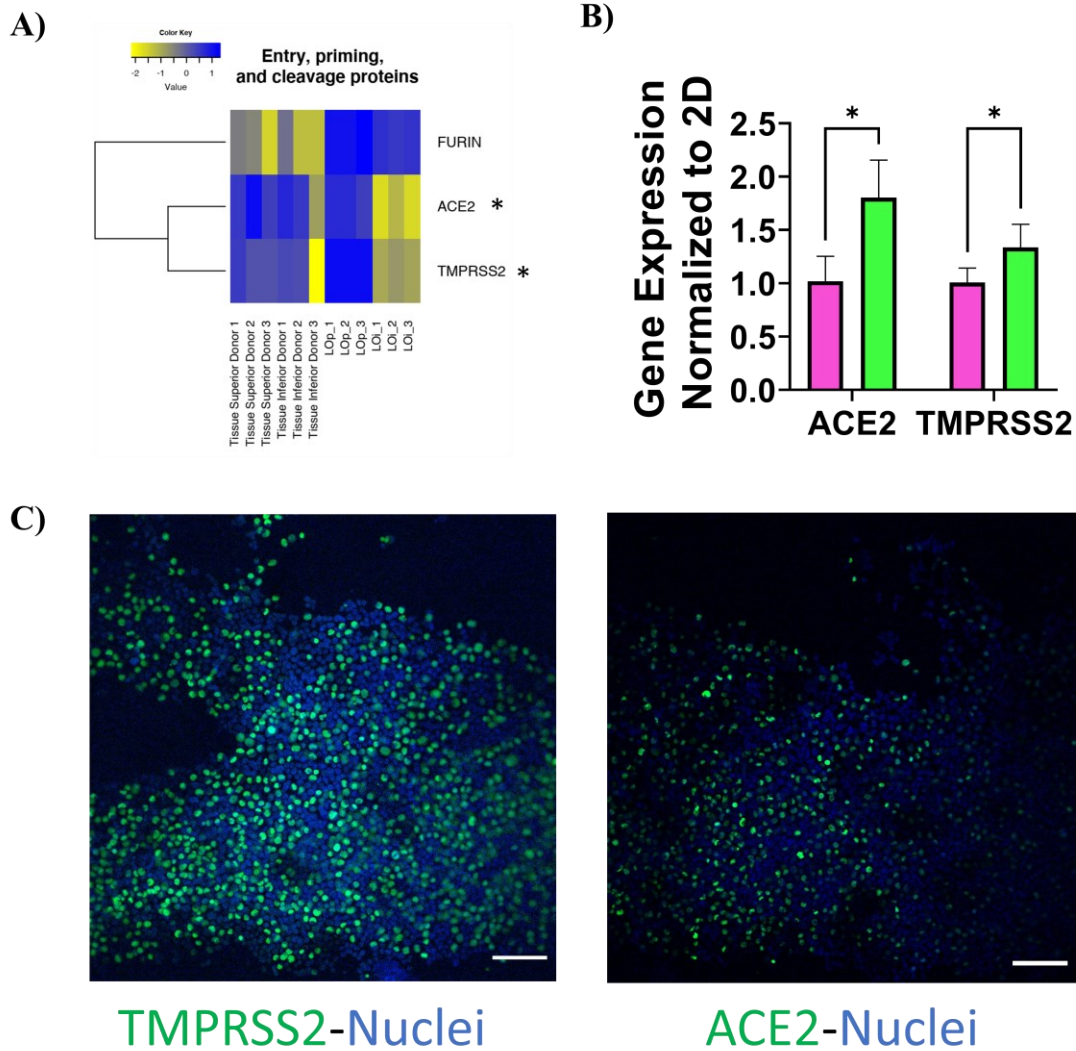


Fig. 4.6 Entry and priming mechanisms of respiratory viruses on organoids. A) Comparison between bulk RNA sequencing of proteins relevant to infection on organoids and adult lung tissues. T-test (LOp vs LOi) * p . adjust <0.05 $N=3$. Upregulation shown in blue. B) Expression of ACE2, and TMPRSS2 on LOi (green) and CFBE (pink) at day 21 using RT-qPCR. $N=3$. Two-way ANOVA * $p<0.05$. C) Representative images of LOi at day 7 expressing TMPRSS2, and ACE2, respectively. Magnification 10X. Scale Bar 100 μm .

4.3. 2 Lung organoids to model influenza infections.

Organoids derived from immortalized cells were infected with influenza H3N2 A/Hong Kong/1/68 (COVAR) or influenza H1N1-PR-8 (COVAR) using a multiplicity of infection (MOI) of 0.1 for 3 h. Viral replication was evaluated 24 and 48 h post infection using plaque assay. Results are shown in Fig. 4.7. Viral infection and replication were found from an analysis of the organoid supernatant, while no infection was found in the control group.

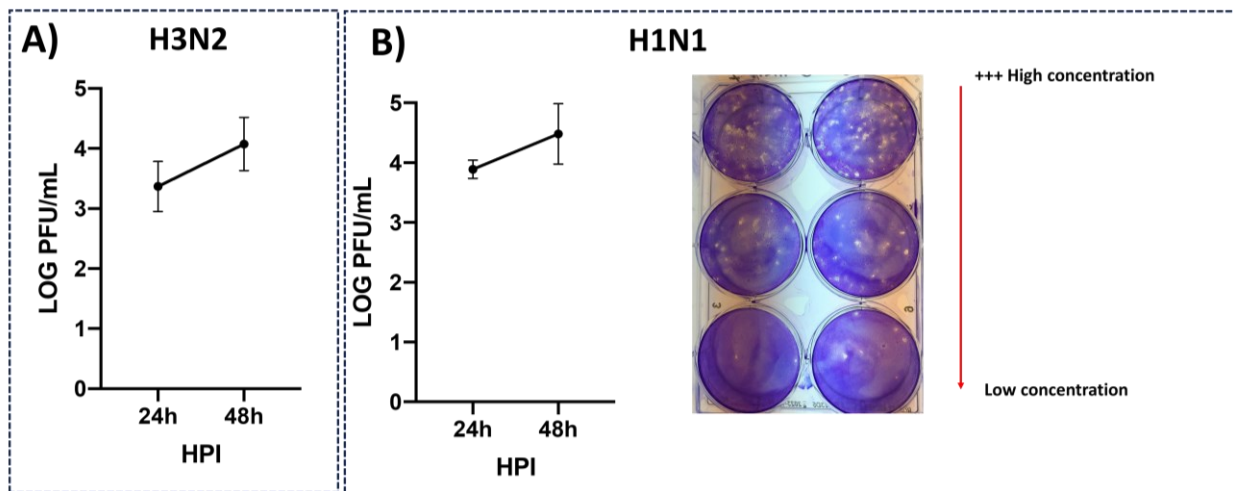


Fig. 4.7. Representative viral titer (PFU/ml) on supernatant of infected organoids with influenza H3N2 (A) or H1N1 (B) at 24 and 48 hpi. N=3. *** $p < 0.005$. Panel B shows representative plaque assay results obtained after inoculated serial viral dilutions in MDCK cells.

Cell lysate of organoids infected with influenza H1N1-PR-8 was analyzed using nucleocapsid protein (NP) and RT-qPCR. Results are shown in Fig. 4.8. As observed, viral replication was observed in the organoid lysate, highlighting the infectability of the model.

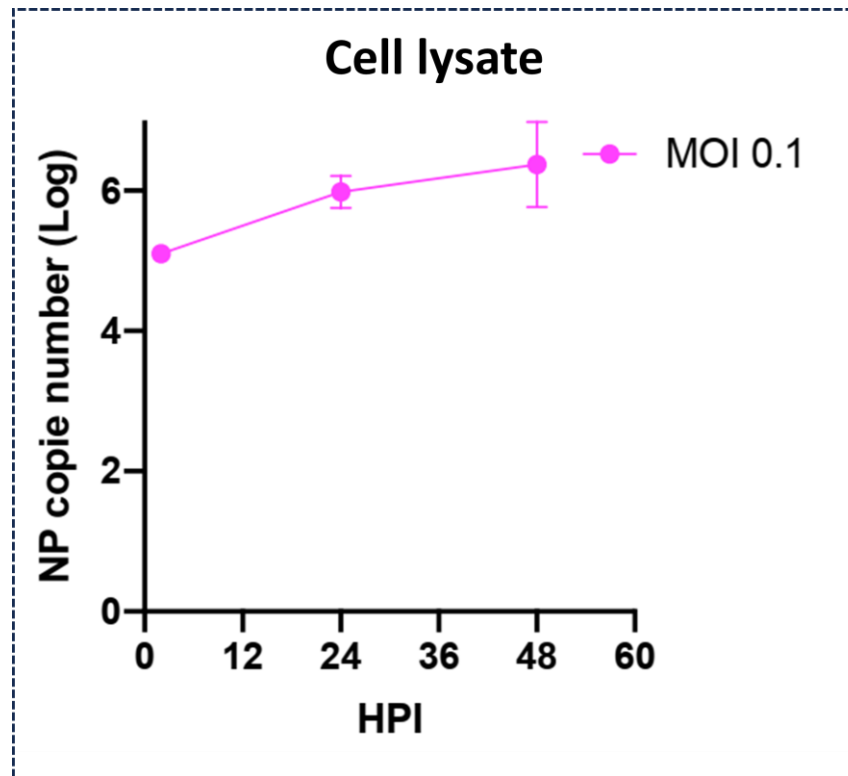


Fig. 4.8 Nucleocapsid protein load (log) in organoid lysate after 24 hpi, and 48 hpi of influenza H1N1-PR-8. N=3

4.3. 3 Lung organoids to model SARS-CoV-2.

Organoids derived from immortalized cells were infected with two MOI of 0.01 and 0.001 for 3 h, and viral replication was evaluated 24 and 48 hpi.

Viral replication on supernatant and organoid lysate was evaluated. Fig. 4.9 and Fig. 4.10 shows the results of this evaluation, where LOD represent the limit of detection of the used method. Significant SARS CoV-2 RNA was detected in the supernatants of infected organoids, and not for the negative controls, indicating successful infection (Fig.4.9). There was significant association between the MOI and the number of viral copies detected, indicating that the extent of infection in organoids is sensitive to the initial viral load. Similarly, a slight increase in the viral replication between 24 and 48 hpi

was found. Viral copies were also detected only in the lysate of infected organoids, as it shows in Fig. 4.10. As for the supernatant, there was an increment in the viral RNA copies of the organoids as the hpi and MOI were increased.

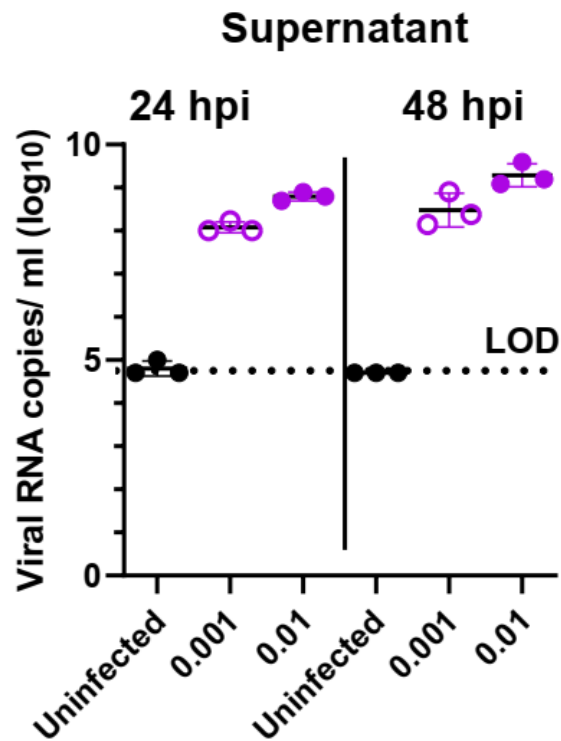


Fig. 4.9 Viral copies /ml (log10) on supernatant of organoids under MOI: 0.01 and 0.001 SARS-CoV-2 infected-purple, and non-infected-black, 24 hpi and 48 hpi (n=3). Two-way ANOVA $p < 0.0001$ in all comparisons. LOD: Limit of detection.

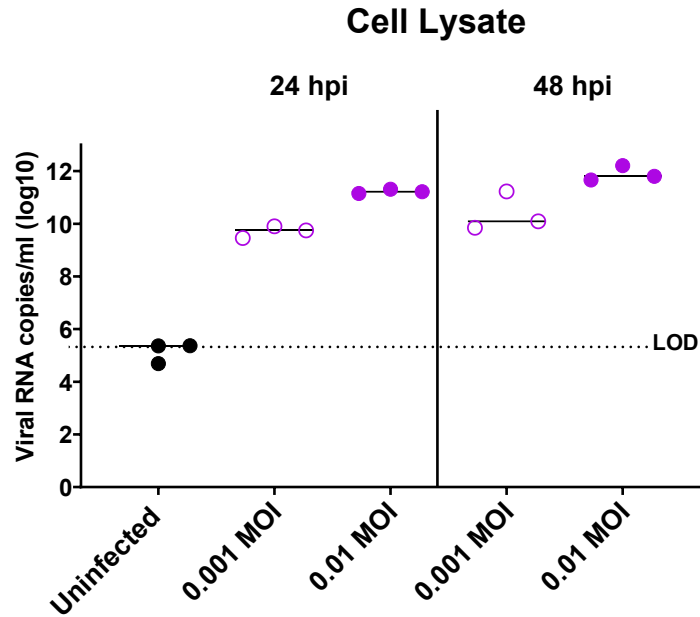


Fig. 4.10 Viral copies/ml (log10) on cell lysate of organoids MOI: 0.01 and 0.001 SARS-CoV-2 infected-purple, and non-infected-black, 24 hpi and 48 hpi (n=3). Two-way ANOVA $p < 0.05$ in every condition. LOD: Limit of detection.

4.3. 4 Lung organoids to model Asthma

Organoids derived from primary airway epithelial cells of a donor coded as BA00814, 67 years old female subject with asthma, were generated.

Firstly, the pre-established protocol discussed in Chapter 2, was used. But no organoid could be formed after 7 days of culture. Instead, cells remained rounded and dispersed within the gel as shown in Fig. 4.11A.

Given the role of fibroblasts promoting chronic inflammation in already inflammatory diseases^{158,159}, we modulated the original density of fibroblasts of 2.5×10^6 /ml to 1.6×10^6 /ml. However as shown in Fig. 4.11B, no organoid was formed.

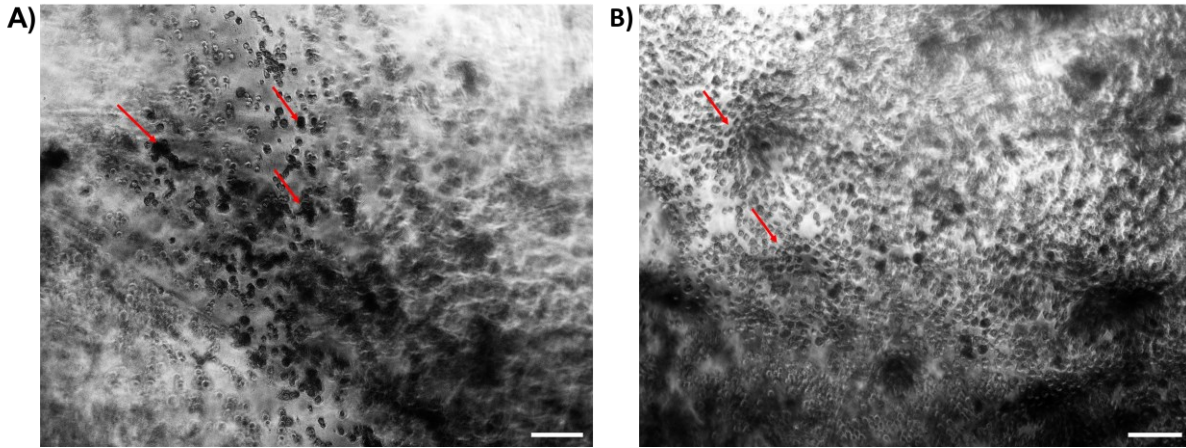


Fig. 4.11 Brightfield pictures of airway epithelium cultured along different density of fibroblasts and Geltrex at day 7. No organoid formation was achieved under these conditions. A) 1 fibroblast per 2 epithelial cells. B) 1 fibroblast per 3 epithelial cells. Red arrows pointing airway epithelium. Magnification 10X. Scale Bar 100 μm .

Therefore, additional conditions were tested. Figure 4.12 show the morphology obtained after culturing 5×10^6 per/ml of airway epithelial cells with 5×10^5 per/ml of fibroblasts, final ratio 10:1, at day 6 and day 14. Under this condition, some cells regrouped, but the typical organoid achieved with healthy cells was not formed. At day 14 the cells looked clustered together without a specific morphology, and cells shedding from the “main” structure were observed. Therefore, these conditions were not considered successful.

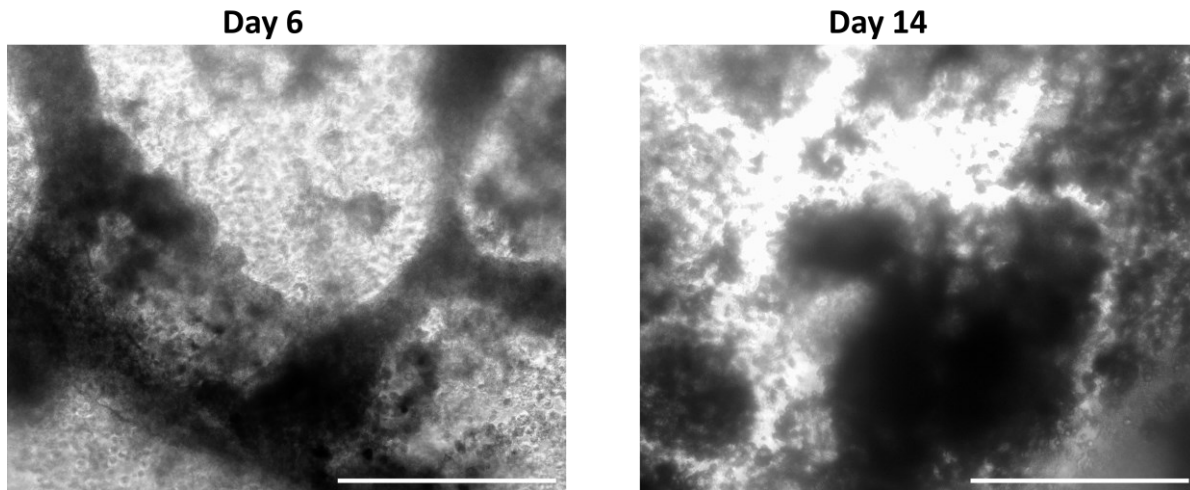


Fig. 4.12. Airway epithelial cells from an asthma donor cultured along with fibroblasts in “low” density. Final ration 10:1. Initially, some cells grouped together, but cell shedding, and abnormal morphology was observed on day 14. Magnification 10X. Scale Bar 500 μm . Images processed with ImageJ using the tool “Enhance contrast”.

Subsequently, airway epithelial cells were cultured without fibroblasts, on top of Geltrex. At day 3, it was observed cells went into a more tubular morphology with bifurcations as shown in Fig. 4.13. However, these structures started to disassociate, some at day 6, as shown in Fig. 4.14, while some only at day 11. All structures were disassociated at day 14, into more sphere like structures, as shown in Fig.4.15.

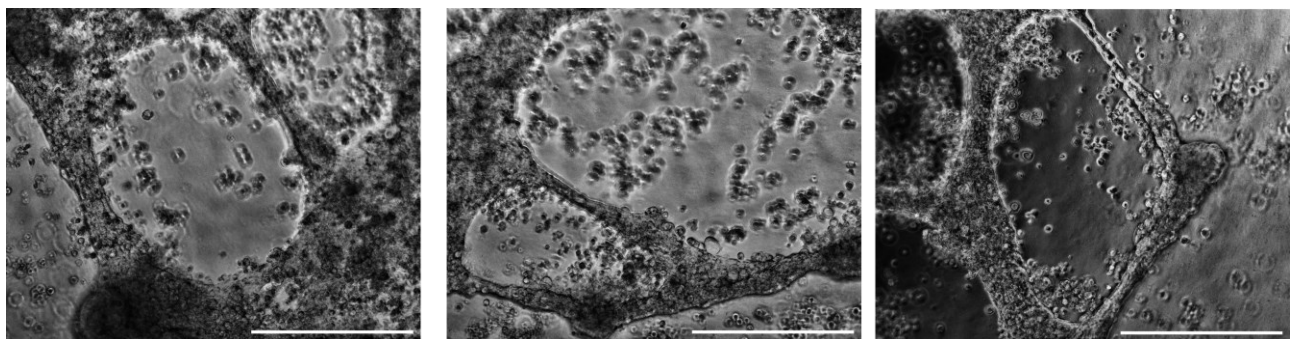


Fig. 4.13. Asthmatic airway epithelial cells cultured without fibroblasts on day 3. Elongations and bifurcations were observed. Magnification 10X. Scale Bar 500 μm . Images processed with ImageJ using the tool “Enhance contrast”.

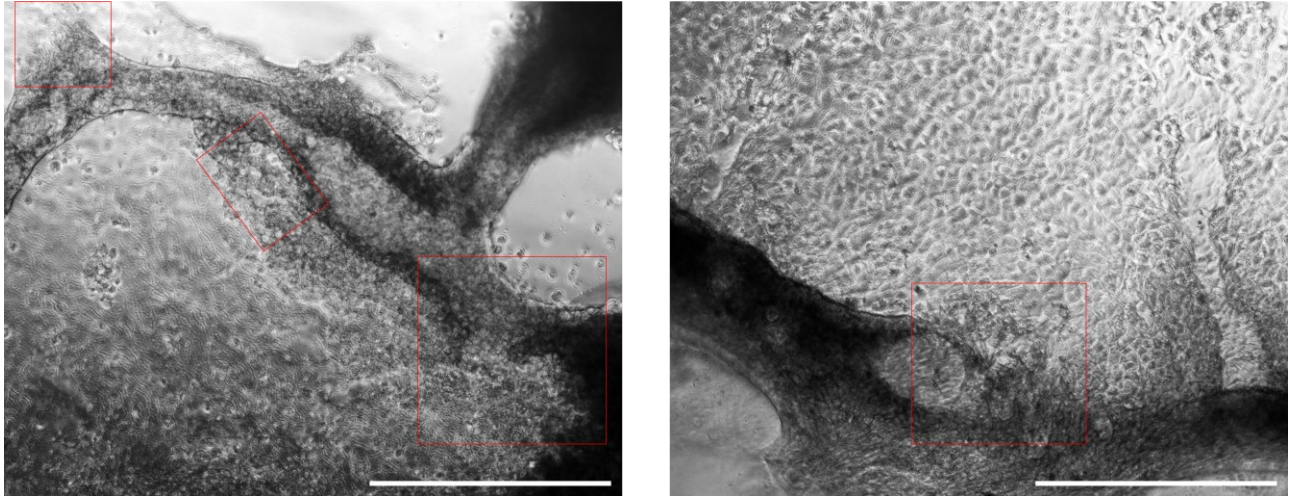


Fig. 4.14. Asthmatic airway epithelial cells cultured without fibroblasts on day 6. Cell disassociation from the main structure was observed, shown in red squares. Magnification 10X. Scale Bar 500 μm . Images processed with ImageJ using the tool “Enhance contrast”.

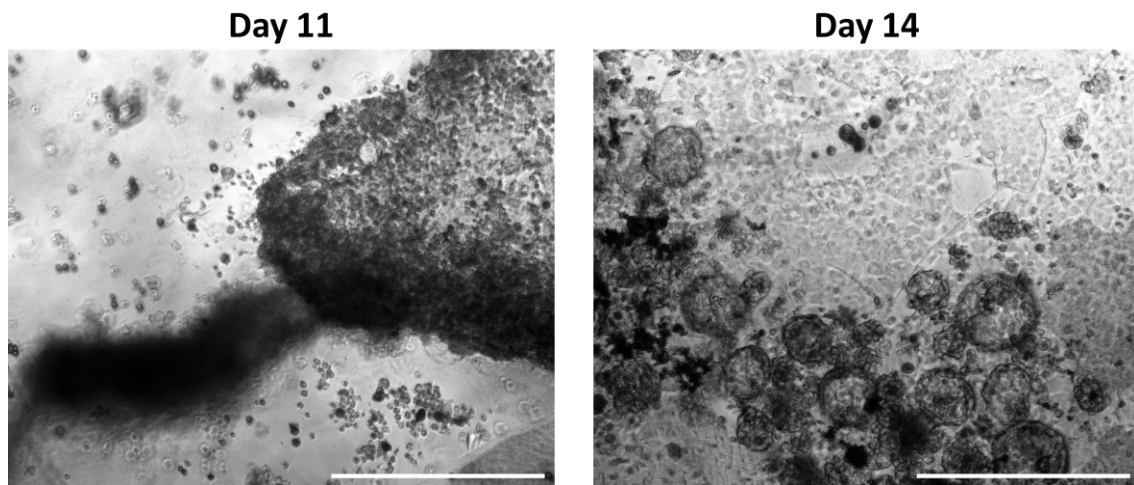


Fig. 4.15 asthmatic airway epithelial cells cultured without fibroblasts on day 11 and day 14. Structures are broken, and spheres like structures remain. Magnification 10X. Scale Bar 500 μm . Images processed with ImageJ using the tool “Enhance contrast”.

Culturing asthmatic airway epithelial cells without fibroblasts lead to better morphology but just for short term culture. It has been well documented that during asthma there is interleukin storm associated with inflammation¹⁶⁰. IL-4, IL-5, and IL-13 are highly

abundant¹⁶⁰, while low levels of IL-10 are normally found in patients with asthma¹⁶¹. Steroid treatment are commonly used for asthma increases IL-10 production¹⁶⁰. Therefore, we cultured asthmatic airway epithelial cells, without fibroblasts, in a medium with 10 ng of IL-10. This condition was found to be optimal. Organoids grew, starting to show a robust and tubular morphology at day 4, with continued growth without disruption until day 17. From day 14 to day 17, there was not notorious change of morphology. The organoids formed under this condition are shown in Fig. 4.16.

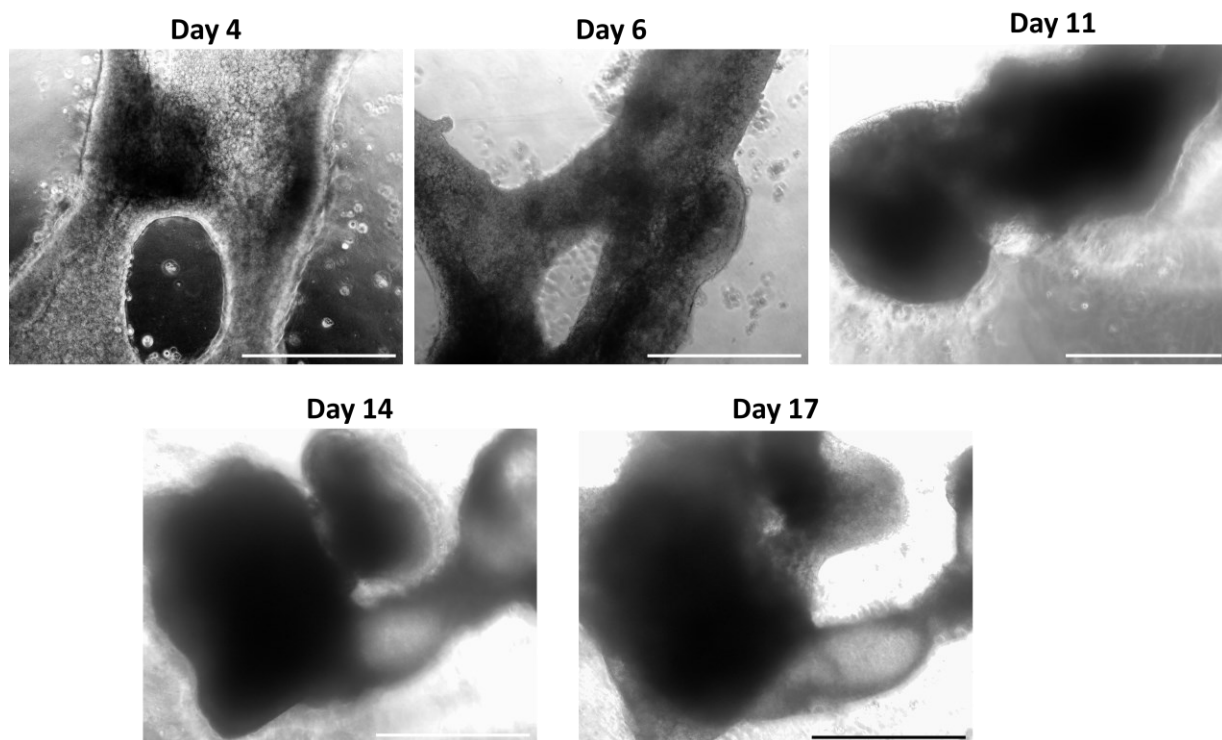


Fig. 4.16. Representative images of asthmatic organoids achieved by incorporation of IL-10 into the medium. No fibroblasts were incorporated into the culture. Magnification 10X. Scale Bar 500 μ m.

Since IL-10 shows improvement in the organoid formation using only airway epithelium, we tested their effect on their culture along with fibroblasts. However, no tubular shape was found, instead sphere-like structures were formed and maintained for 11 days of

culture (Fig. 4.17). It was observed that not all cells formed a spheroidal structure. Results for all conditions tested are summarized in Table 4.1.

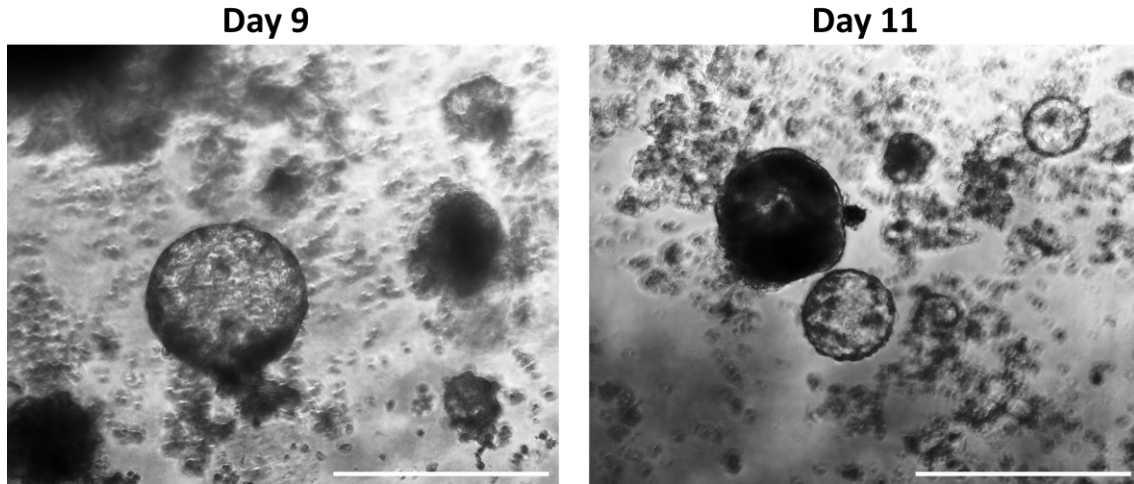


Fig. 4.17. Airway epithelial cells cultured with fibroblasts in 10:1 ratio in a medium supplemented with IL-10. Magnification 10X. Scale Bar 500 μ m.

Condition tested	Outcome
Airway epithelium with lung fibroblasts in a 2:1 ratio	No organoid formation
Airway epithelium with lung fibroblasts in a 3:1 ratio	No organoid formation
Airway epithelium with lung fibroblasts in a 10:1 ratio	Cell clustering and “tube” like structure observed at day 4 but cells dissociated by day 14
Airway epithelium with lung fibroblasts in a 10:1 ratio and IL-10	Spheres-like structures were formed, and remained steady for 11 days
Airway epithelium without fibroblasts	Tube-like structures were formed but disassociated at day 11 or 14.
Airway epithelium without fibroblasts, supplemented with IL-10	Organoids were formed with a tubular structure. The structure was found still robust at day 17.

Table 4.1 Conditions tested and their outcomes for generation of organoids derived from a patient with asthma.

4. 4 Discussion

In this chapter a few possible applications of pulmonary organoids were explored. It was shown that our organoids can be infected with influenza H1N1, H3N2 and SARS-CoV-2. Viral replication was observed in all infections and confirmed in organoid lysate in case of SARS-CoV-2 and influenza H1N1. Viral titer was found to be within the range of previous published work using organoids and cell monolayers for both influenza⁶⁵ and SARS-CoV-2^{61,75}. In contrast, to other models, infection did not require rupture⁷⁵. This may represent a conceptual advantage of the complexity of organoids compared to other types of organoids, which are typically disrupted into monolayers before being infected. The heterogeneity of the organoid, described in chapter 3, may be beneficial for the evaluation of natural viral infection¹⁴⁰. The infection took place in the entire model, including the organoid and the layer of fibroblasts embedded in Al-Ge. This offers another advantage over other lung organoids composed only of epithelial cells^{6,62,64-66}. Fibroblasts are relevant for viral infections since they provide a mechanism for host resistance, such as cytokine IL-6 and chemokine CCL2 production, as well as degradation of ECM proteins by metalloproteinases. They can also provide tolerance to the infection by synthesis of collagens and elastin, as well as production of FGF, VEGF, GM-CSF. Ultimately, the balance of secreted products by fibroblasts determines the outcome of respiratory viral infection¹⁴⁰.

Several genes associated with SARS-CoV-2 infection and severity were identified in LO. This highlights the potential of the model for therapeutic targeting and in-dept viral studies. For instance, FOXP4 was found abundantly in LOi. It is associated with the risk of having long-term effects of COVID-19¹⁴⁹. Therefore, the model can be used for the

evaluation of long-term effects of COVID-19, and possible drugs or treatments to reverse these effects. This could require an increase in the lifetime of the organoid, as discussed in Chapter 2.

Some of the genes associated with severity of SARS-CoV-2 are present in the model, while other genes restricting the entry of the virus are also highly expressed. Future work should be aimed at monitoring these genes during infection to evaluate their dynamics. They may indicate a compensatory mechanism of the organoid. OAS3, for instance, was highly upregulated in LOi. This is known to be an antiviral enzyme¹⁴⁶. DPP9 was also upregulated in the organoids, a factor associated with increased severity of COVID-19¹⁴⁸.

The utilization of primary organoids during infection needs further exploration to evaluate donor-specific characteristics, infection dynamics, and therapeutic outcomes. It is essential to compare infection dynamics between LOp and LOi, especially considering that LOp exhibits higher similarity to adult lung tissues and differentiates into distal lung regions.

Genes associated with permissibility of influenza A, were also found in the organoids. While these genes (COPI) were present in both LOp and LOi, LOp exhibited a slightly higher upregulation of these genes. Therefore, primary organoids could be preferable for future influenza infections. Both strains of influenza used in this study are adapted to mice. Results shown in this study are a proof of concept. But for more physiological relevant studies, human strains need to be used without adaptation to animals. During and after infection with influenza strains, TPCK was added into the viral solution and medium. Typically, this is done using animal models, either cells lines or full organisms,

to achieve virus cleavage and infection¹⁶². The organoid model expresses other proteases such as TMPRSS2, which theoretically is sufficient to cleavage influenza¹⁴². Given the animal adapted strains, the best condition for influenza infection was the addition of TPCK.

The original protocol for organoid formation, was adapted for using cells from a patient with asthma. The incorporation of fibroblasts in typical concentrations was not beneficial for organoid formation. A lower fibroblast concentration improved the outcome. Organoid formation could not be induced without removing the fibroblasts from the culture. This observation is interesting because it highlights the essential role of fibroblasts in supporting organoid growth under healthy conditions, whereas under unhealthy conditions, fibroblasts may contribute to microenvironmental damage, inflammation, and impaired remodeling¹⁶³. It would be interesting to sort out the fibroblasts from healthy and unhealthy models to analyze their specific phenotype and secretions.

It was also observed that the use of geltrex alone, with airway epithelial cells from an asthma donor, did not grow beyond day 6 without cell shedding. Similar behavior was observed when culturing endothelial cells on geltrex. Tubes were formed at the beginning of the culture, but their growth was disrupted by day 5. Studies of angiogenesis, for instance, in monocultures using geltrex and other substrates are only short term^{164,165}. This emphasize geltrex alone may not be sufficient to support the long-term formation of organoids or three-dimensional structures.

Even if tubes are formed with healthy epithelial cells under these conditions, these structures are temporarily and flatter than when fibroblasts are added.

It was only when the medium was enriched with IL-10, that epithelial cells were capable of self-organizing into tubular shapes and preserved until day 17. IL-10 has been reported to suppress the production of proinflammatory cytokines¹⁶⁶. This approach can be further explored to induce lung organoid formation derived from cystic fibrosis and emphysema donors, since all these diseases are characterized by chronic inflammation^{167,168}.

To incorporate fibroblasts into diseased organoids, lower cell densities should be tested such 1:1000, 1:10,000 ratios in their relationship to airway epithelial cells. This will maintain the advantage achieved with our traditional protocol.

Full characterization of asthmatic organoids developed in this chapter must be done in the future, using methods described in Chapter 3. Nevertheless, results are encouraging since no other organoid is available to model asthma.

4. 5 Methods

4. 5. 1 RNA sequencing analysis

The genes were grouped by abundance and analyzed using Z-score. This was calculated as the difference between the average of the group of interest (X) and the average of the dataset of the gene (μ), and the result divided by the standard deviation of the gene (σ), as shown in the following equation (I).

$$Z = \frac{X - \mu}{\sigma} \quad (I).$$

4.5.2 SARS-CoV-2 infection in human lung organoids

A clinical viral isolate (isolated prior to November 2020) termed SARS-CoV-2 CP13.32 passage 2 (Genbank accession no. 599736; lineage B.1.1.147) stock was obtained from the McGill University Health Center. It was propagated in VeroE6 cells five times. The latter stock (P5) was used for infecting the organoid samples.

Before infection, the organoids were washed twice with plain DMEM. Organoids were then inoculated with MOI of 0.001 and 0.01 of SARS-CoV-2 (CP13.32 strain, P5) in serum free medium for 3 h at 37°C and were rocked every 15 min. The method of infection is shown in Fig. 4.18 The virus is added directly on the organoids, using 300 µl of solution per sample. This method allows the infection of native organoids without shape disruption, nor dissociation of the organoid to be cultured as 2D cell monolayers before being infected²⁴⁻²⁶.

After inoculation, the media was switched to 1ml of DMEM 2% FBS per sample. At the indicated times, the organoids and cell culture medium were harvested for detection of viral load. The cell-free culture medium was analyzed as “supernatant.”

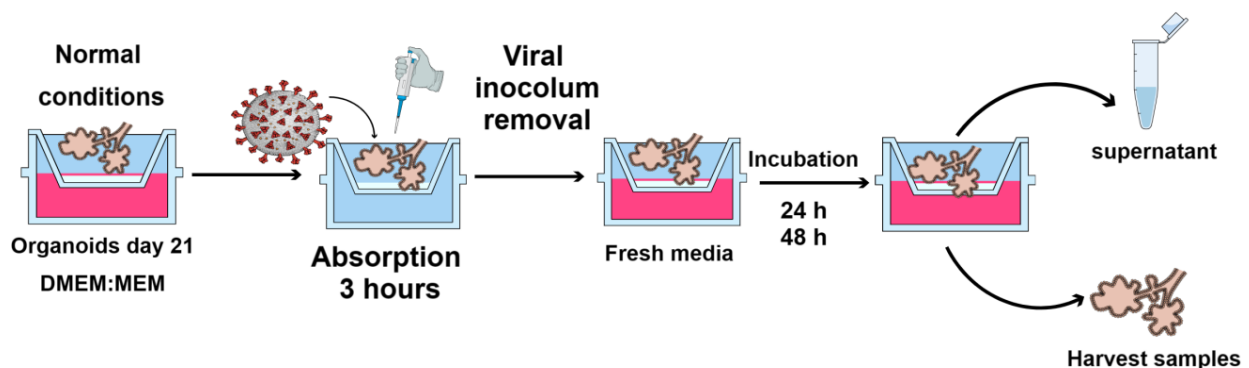


Fig. 4.18. Viral infection of organoids with SARS-CoV-2. Organoid culture medium is substituted by viral solution in serum free media, during an absorption time of 3 h. Afterwards, the viral inoculum is removed and substituted by fresh medium. Infected organoids are cultured during 24 and 48 h at 37°C. Finally, supernatant and organoids are harvested for further analysis.

4.5. 3 Influenza infection in human lung organoids

Triplicates of organoids were infected with the influenza H3N2 Strain with a MOI of 0.1 using an absorption time of 3 h. Tosyl phenylalanyl chloromethyl ketone (TPCK)-treated trypsin ('TPCK-trypsin) was added into the viral inoculum, and in the fresh media in a final concentration of 0.1%. 24 hpi and 48 hpi supernatant was retrieved for further analysis. The pipeline of infection is similar to the one shown in Fig. 4.18 with the exception of TPCK addition.

At the indicated times of infections, viral RNA was extracted from 140 μ L of supernatant using the QIAamp Viral Mini Kit. The primers used are described in the supplementary section. SARS-CoV-2 RNA was detected in a 10 μ L reaction containing 1 μ L of extracted RNA sample, 200 nM of SARS-CoV-2-specific primers, 1X RT enzyme mix in the reaction mixture containing SYBR Green (*Power SYBR™ Green RNA-to-C_T™ 1-Step Kit*). The one-step RT–qPCR comprises a 30min RT step at 38 °C and 10 min of AmpliTaq Gold DNA polymerase activation at 95 °C, followed by 40 cycles of PCR at 95 °C for 15 s and 60 °C for 1 min. The RNA copy number was calculated from a standard curve 10-fold serially diluted RNA made from in vitro transcripts consisting of SARS-CoV-2 with known copy numbers. The limit of detection (LOD) was 51 genomic copies per reaction.

4.5. 5 Quantification of SARS-CoV-2 RNA in Cell Lysates using RT–qPCR

At the indicated times of infections, viral RNA was extracted from cell lysates (organoids resuspended in 1mL of TRIzol) using the PureLink RNA Mini Kit (ThermoFisher). The primers used are described in the appendix (Table A5). SARS-CoV-2 RNA was detected in a 10 μ L reaction containing 1 μ L of extracted RNA sample, 200nM of SARS-

CoV-2-specific primers, 1X RT enzyme mix in the reaction mixture containing SYBR Green (*Power SYBR™ Green RNA-to-C_T™ 1-Step Kit*). The one-step RT-qPCR comprises a 30min RT step at 38 °C and 10 min of AmpliTaq Gold DNA polymerase activation at 95 °C, followed by 40 cycles of PCR at 95 °C for 15 s and 60 °C for 1 min. The RNA copy number was calculated from a standard curve 10-fold serially diluted RNA made from in vitro transcripts consisting of SARS-CoV-2 with known copy numbers. The limit of detection (LOD) was 48.6 genomic copies per reaction.

4.5. 6 Plaque Assay

“The plaque assays were performed using a monolayer of MDCK cells. MDCK cells were raised in T175 culture flasks. When confluent, they were washed with 10 mL of phosphate-buffered saline (PBS). Cells were then detached from flasks using 3 mL of trypsin and transferred to a 50 mL tube before spinned at 1200 rpm for 5 min and resuspended in complete DMEM. 600,000 cells were then transferred to each well of 6 well culture plates and were left to grow for 24h so they could form a monolayer. Using the thawed supernatant samples collected from the lung organoids, tenfold serial dilutions were made (from 10^{-1} to 10^{-8}) in plain DMEM. Once confluent, the MDCK monolayers were washed with PBS and 400 μ L of each viral dilution were distributed evenly in the appropriate wells. The viral inoculum was left for an absorption period of 1 h and before being aspirated replaced with 3 mL of CMC mix (98% CMC, 2% BSA and 0.001% TPCK) per well. The plates were then left to incubate for 72h after which each well was fixed with 4 mL of 10% buffered formalin and the MDCK monolayer was stained with 400 μ L of 0.2% Crystal violet to expose plaques (zones of cell lysis). The

plaques in each dilution were then counted and the titer of plaque forming units (PFUs) per milliliter in the supernatant was calculated” using the following equation (II).

$$PFU = \frac{\text{Number of plaques}}{D \times V} \quad (II).$$

Where D is the dilution factor and V the volume of diluted virus per well.

The pipeline of plaque assay is shown in Fig. 4.19.

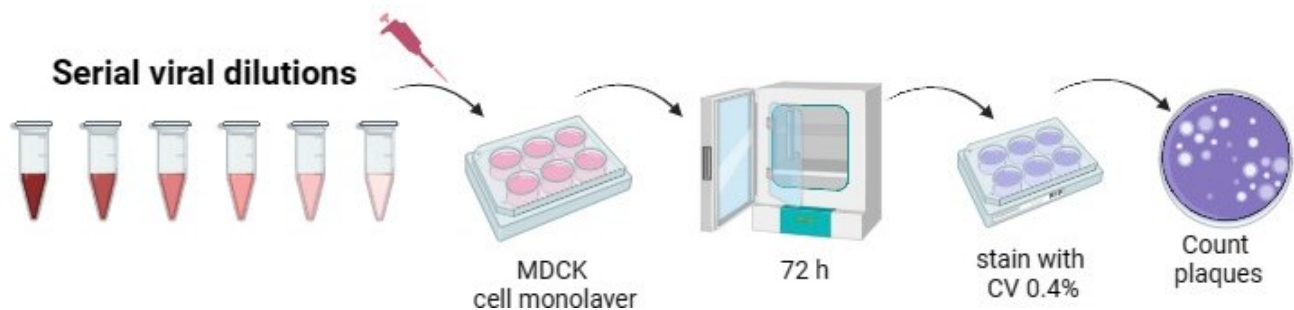


Fig. 4.19. Plaque assay pipeline. Serial viral dilutions are made with the supernatant of infected organoids. These viral dilutions are used to infect MDCK cell monolayers during an absorption time of 1 hour. Media containing TPCK is used to cover cell monolayers for 72 h. MCDK are fixed with crystal violet to expose plaques.

4.5. 7 Quantification of Nucleocapsid protein for influenza infection using RT-qPCR

RT-qPCR was performed using Applied Biosystems™ High-Capacity cDNA Reverse Transcription Kit (Catalogue number 4368814) to create a cDNA library from the extracted RNA. First, to eliminate DNA contamination, the RNA (10 µL at 40 µg / µL) was incubated with an equal volume of 15% DNase mix in 1st strand buffer for a final volume of 20 µL and incubated in the ThermoCycler programmed at 37°C for 15 min, followed by denaturant at 95°C for 10 min and maintained at 4°C. Then, 10 µL of Reverse transcription mix (20 % buffer, 20 % primers, 8% dNTP, 10 % and 42 % H₂O)

was added to each tube and they were spined and put in the ThermoCycler once more programmed at 25°C for 10 min, 37°C for 60 min, 95°C for 7 min and then maintained at 4°C. The cDNA was then be stored at -20°C until needed for qPCR.

qPCR was performed using β actin, H1N1 nucleocapsid protein and IFN β primers from Integrated DNA Technologies™(appendix Table A5). The cDNA samples were diluted in RNase free water to make a 1 in 8 dilution. A master mix was made for each primer (3.33% forward and 3.33% reverse primers, 83.33% SYBR Green and 10% water) and 4 μ L of sample and 6 μ L of mix were added to each well of a 96 well qPCR plate. The plate was covered in film, spun, and put in a Thermocyclers with the following program: 95°C for 15 seconds, 58°C for 20 seconds and 70°C for 15 seconds for 45 cycles. Results were then collected and analysed. The change in gene expression relative to housekeeping gene ($\Delta\Delta$ Ct) was calculated using the manufacturer's software package.

4.5. 8 Generation of asthmatic organoids

Human fetal lung, IMR90, cells were cultured overnight in alginate-gelatin hydrogels with different density, according to specific conditions. 250,000, 166,000, and 50,000 cells per/cm² were used using DMEM (Corning, 15-017-CV) with Penicillin-Streptomycin (Fisher Scientific, SV30010) non-essential amino acids (Fisher Scientific, LS11140050) and FBS (Sigma-Aldrich, F1051) at 37°C. The media was removed, and the hydrogels were coated using 100 μ L/cm² of Geltrex (Thermo Fisher, A1413202) for 30 min at 37°C. Afterwards, Human Bronchial Epithelial derived from an asthmatic patient were seeded on the top with a density of 500,000 cells per/cm² using Bronchial Epithelial Cell Growth Medium (BEGM) acquired from PACB and L-Glutamine (Thermo Fisher, A2916801) forming a co-culture interface. The next day the medium was substituted by a

combination of DMEM and BEGM in a ration 1:1 supplemented with 10 mM CaCl₂ (Sigma, Aldrich, C4901). Only when no fibroblasts were used, and the medium was supplemented with 10 ng/ml of IL-10 (Abcam, ab259402), did organoids form branching structures. The organoids were cultured in solution at 37°C under a humidified atmosphere with 5% CO₂ and 95% air. During culture, the medium was refreshed at most every two days.

4.5. 9 Statistical analysis

GraphPad was used for data analysis. Two-way ANOVA was performed for evaluation of SARS-CoV-2 infection P<0.05 was consider statistically significant. *p<0.05, **p<0.01, ***p<0.005. For influenza infections, since less parameters were used One-way ANOVA was used. ***p<0.005. T. test was used for the evaluation of differentially expressed genes associated with viral infection as described in section 3.5.4. It was considered significant when p. adjust was <0.05.

Chapter 5: Conclusions and Perspectives

5.1 Summary and conclusions

Animal models widely used for the study of biomedical research very often fail to indicate outcome of human clinical trials²⁶. Mouse lungs differ substantially from human lungs^{24,25}. This has created a need for using *lung-in-vitro* models with human cells. Lung-in-vitro models include *2D cell monolayers*, with variations in their culture using *air-liquid-interface* cultures in porous membranes, *lung-on-a-chip technologies* which typically add mechanical cues into the cell culture^{37,38}, and *lung organoids*. *2D cell monolayers*, including *ALI* and *lung-on-a-chip* do not represent the architecture of the lung; they consist of “flat cells” of which the behavior differ from cells in 3D^{22,51}.

One of the main limitations of the current *lung-in-vitro* models, including lung organoids, is the absence of integration between different lung regions. They can only model specifically the bronchi, or the alveoli^{21,40,41,43,45,47,48,62–65,65,75,77,78}. This hampers the replication of viral tropism as in the human body¹⁴⁰. The main advantage of lung organoids over other lung-in-vitro models is that they can better recapitulate the cellular organization and physiology of lungs, including cell communication²². However, their typical morphology remains spherical^{21,62–65,65,75,77,78} and the benefits of 3D culturing are lost when such organoids are disassociated to study LRT diseases^{63,65,75}. ASC derived lung organoids depend on harvested deep lung tissue biopsies¹⁹⁻²⁵. Given the invasive nature, and cost of lung tissue biopsy^{86,87} the cellular availability is limited, in special from healthy donors^{63,65,66,75}.

In the present study, a new *lung-organoid type* model, was created. The model resembles the tubular and arborized architecture of the lungs, while integrating some of

their proximal and distal components in one single model. To improve cell accessibility, airway epithelial cells from the proximal airways (Trachea/Bronchi) and, alternatively, immortalized bronchial epithelial cells (CFBE) were used instead of deep lung tissue biopsies. These models are fast-maturing and show an adult phenotype, two further sought-after characteristics. The value of these new lung organoid models is demonstrated by their use in modelling infections of important pathogens (COVID19, Influenza H3N2, H1N1) and the prevalent asthmatic condition.

5. 1.1 Protocol for developing lung organoids.

The building blocks of our model are natural BMZ proteins containing in Geltrex, airway epithelium (primary HBE/ immortalized CFBE), porous membrane cell culture inserts, and lung fibroblasts encapsulated in a soft substrate made with ALGe. Instead of incorporation of exogenous factors to trigger cell differentiation and organoid formation, our strategy depends on the patterning molecules, growth factors and cytokines released by the fibroblasts grown in these conditions. Minimal exogenous factors were supplemented into the cell medium, which can eventually decrease production cost.

Our rationale for using lung fibroblasts (IMR-90) instead of exogenous factors, as other protocols do¹⁹⁻²⁵, was based on the lung development process, which is triggered by airway epithelial progenitor cells and their mesenchymal interactions. The secretion of FGF10 in the mesenchyme, and its interactions with Wnt signalling¹ play a critical role for lung differentiation, patterning and branching morphogenesis^{1,19}. It is not surprising that most lung organoid protocols incorporate FGF10, FGF7, and FGF18, among others, during their culture^{65,77}. We hypothesized that the interaction of these cells in ALGe in contact with membrane zone proteins, would trigger the formation of lung

organoid with a more sophisticated morphology than the spherical morphology of the current lung organoids described in the literature^{21,62–65,65,75,77,78}. We hypothesized that, in response to these cellular interactions, airway epithelial cells from the proximal region will differentiate into cells from distal lung regions while preserving some of their initial characteristics (proximal phenotype).

When using immortalized epithelial cells (CFBE), we hypothesized that these cells would have favorable conditions to promote their differentiation within the microenvironment. These could then induce a lung organoid formation with similar characteristics from the ones derived from ASC.

To test our hypothesis, we first induced the organoid formation using HBE (primary-LOp) and CFBE (immortalized-LOi) cells. In chapter 2, we described the morphology obtained when using these two cell types. Self assembly tubular macro structures were formed with both cell types (LOi and LOp). In both cases, the organoid formation started with cell clustering in small spherical aggregates, which over time elongated and increased their size and thickness. Secondary tubular structures were observed, and typically the “end edge” of the organoids had a “saccular” shape. Organoids mature at day 21 and they can be kept on culture until day 30. We found that fibroblasts culture conditions affect the overall morphology of the organoids. The ideal fibroblast density in proportion to epithelium was found to be 1:2 to 1:3. Increasing fibroblast density or promoting their proliferation by using a non-neutral substrate (e.g. GelMa) led to the prompt disassociation of lung organoids. Cell medium also affects the morphology of the organoids. We found that organoids grow better using a mixture of DMEM: MEM/DMEM: BEGM for LOi and LOp, respectively, than using branching and Lung

Organoid Maturation medium, 3dGRO™ medium. Organoids grown in DMEM: MEM show more elongated structures and ramifications, as well as higher cell density. We also found that the source of feeder cells turned out to be a determining aspect in the generation of organoid morphology. Future work is needed to determine if the phenotype of the organoids varies according to the origin of the feeder cells.

Structural heterogeneity was observed in LOi through analysis with FIB microscopy, revealing regions with both stratified and pseudostratified epithelium. Additionally, the presence of microvilli in certain cells suggests a level of cellular differentiation and specialization within the organoids. Despite originating from cell lines typically considered homogeneous^{29,30}, the identification of microvilli, commonly associated with brush cells in the lung¹¹², underscores the organoids' ability to mimic critical features of native lung tissue.

5.1.2. Organoid phenotypes

In chapter 3, we fully characterized the proteome and transcriptome of both organoid types on 21 days of culture, using tandem mass tags and bulk RNA sequencing, respectively. We compared their gene and protein expression with the expression of 2D cell monocultures: HBE, CFBE in ALI, and IMR-90. RNA sequencing data show that the markers of the major cell types in the lung are found in the LOp. Basal cell markers remain the same in both HBE and LOp. However, there was significant downregulation of proximal lung markers in LOp, including SOX2, mucins (MUC5AC, MUC5B, MUC15) markers of goblet cells, and FOXJ1, marker of progenitors of ciliated cells. Conversely, distal markers such as PDPN and HOPX, typically found in AT1, surfactants (SFTPC) markers of AT2 were upregulated in LOp. This confirms the heterogeneity of the model

and proximal/distal patterning. By functional enrichment analysis, considering the major changes in gene expression of LOp, HBE and IMR-90, it was found that the organoids showed upregulation in pathways associated with lung development, alveolar development process, and branching morphogenesis. This suggest that the morphology of LOp it is not a random process. TMT data confirmed the similarity of this organoid type with adult lung tissue and confirmed the upregulation of surfactants and the downregulation of mucins. All together, the results shows that the use of fibroblasts as source of patterning molecules is successful in the generation of an heterogenous lung organoid. In the future, the phenotype of this model can be improved. To induce higher proliferation of goblet cells, for example, media can be enriched with Notch2, and IL17a^{62,79}. However, this process needs to be followed carefully, since increasing of one cell population type could result in the reduction of another cell type.

When utilizing immortalized cells, the LOi organoids exhibit alterations in their RNA sequencing compared to cell lines. Although the counts normalized to library size overall increased, in comparison to CFBE, and IMR-90, the changes were only significant in TP63, SCGB1A1, MUC5B, MUC2, TRPM5, and ALOX5AP, markers of basal, secretory cells type I, goblet cells, and brush cells. The upregulation of some of these genes can be an indication of inflammation, perhaps caused by fibroblasts. However, the upregulation of brush cell markers is consistent with the microvilli structures found in LOi organoids using FIB microscopy. This underscores the organoid's plasticity, even when formed with immortalized cells.

Although the morphology of LOi is similar to the morphology of LOp, there is not a linear extrapolation of the protocol between primary and immortalized cells. The major

changes, based on RNA sequencing, found among LOi, CFBE, and IMR90, were related to ECM organization, and not cell differentiation or lung development.

The proteomics analysis of LOi reveals that LOp exhibits higher specificity towards the lung and greater similarity to lung tissue in terms of protein regulation. Quantitatively, LOi and tissues share a high number of proteins, with the tissue having only four exclusive proteins not found in the organoid. The proteomic analysis revealed the superiority of LOi over CFBE and IMR-90, providing a better lung-in-vitro model than traditional monolayers. The biological functions of certain proteins, upregulated in LOi in comparison to CFBE and IMR90, were associated with response to stress, tissue development, oral mucosa, bronchus, and respiratory epithelium, as well as AT2 cells and lung macrophages. It appears that the immortalized cell lines through the use of environmental cues may have been able to recuperate some, albeit not all, their differentiation potential. There is evidence of changes in the phenotype and proteins secreted by the cells once the organoids are formed. This highlights the relevance of the microenvironment and cell culture conditions. Careful tuning led to the growth of organoids at least partly representative of the lung, directly from common immortalized cell lines. To improve this model further, it could be valuable to add exogenous factors in their culture.

Future work is needed to gain insights into the structure of the organoid using complementary qualitative methods. It is necessary to elucidate if the patterning of proximal and distal of LOp is random or if it follows somewhat its tubular morphology. Single-cell sequencing can provide depth characterization to assess specific cellular composition and track their response to modifications of the protocol.

5.1.3. Lung organoid as model of respiratory diseases

5.1.3.1 Lung organoids for modelling respiratory viral infections.

Some of the genes associated with the severity of SARS-CoV-2 are present in the models, while other genes restricting the entry of the virus are also highly expressed. This interesting duality may be a compensatory mechanism from the organoids. In any case, their presence supports the use of the organoids as model systems for in vitro infection.

TMPRSS2, ACE2, and FURIN were found in LOp and LOi, which highlights the potential of LOp and LOi to be infected with coronaviruses. In the case of influenza A, genes associated with various pathways (such as COPI vesicles, IP3-PCK pathway, and endosomal uptake and maturation) facilitating infection were identified in both LOp and LOi. This information was used as a basis for further infection of these organoids in the laboratory.

Due to their availability, LOi were used instead LOp for viral infections with influenza H1N1, H3N2 and SARS-CoV-2. Viral replication was clearly observed in all infections, and further confirmed in organoid lysate. In contrast to all previous infections, described in the literature⁷⁵, infection did not require organoid rupture.

5.1.3.2 Organoids for modelling asthma

The initial protocol to induce lung organoid was modified to induce lung organoid formation with primary airway epithelial cells from patients with asthma. The incorporation of fibroblasts using asthmatic cells was not beneficial to the organoid formation. This highlights the role of fibroblasts to contribute to health or disease, according to their environment¹⁶³.

The final protocol to develop robust organoids from asthmatic cells excluded fibroblasts, but required BMZ of Geltrex, and IL-10. The phenotype and characterization of these organoids needs to be expanded in the future, but their use holds potential for modeling asthma, and drug testing. The use of IL-10 as exogenous factor, can be beneficial to induce lung organoid formation from cystic fibrosis and emphysema donors, since all these diseases are characterized by chronic inflammation^{167,168}.

5. 2 Perspectives and Future work

Given the approval of the legislation *FDA modernization Act 2.0* in 2022, the use of alternative non-animal methods including cell-based assays is being promoted²⁸. Human organoid market is increasing as its value as models has been demonstrated. This market was established at 1.1 billion USD in 2021. It is estimated to reach USD 3.7 billion by year 2027¹⁶⁹. Accounting for 9.5% of the global organoids market the lung segment is expected to increase from 129.6 million USD in 2022 to 350 million USD revenues in 2027¹⁶⁹. To date, most commercially available lung in-vitro models are iPSC or HBE cultured in ALI conditions to represent proximal regions of the lung. The main advantage of these models is their scalability and ease to use, making them a valuable tool for scientific research. However, they have several limitations. They consist of 2D cellular culture, instead of mimicking the 3D cellular interactions as in the human lung. They lack integration with different regions of the lung, as such the holistic effect of cell-to-cell communication from proximal and distal region, and their contribution to health and disease is limited^{29,29-31}. For instance, viral tropisms cannot be accurately represented in this type of model¹⁴⁰. Additionally, there is evidence of parainfluenza virus mutation when infecting 2D cell monolayers⁷⁸.

Several lung organoid models^{6,21,61–66,75}, are still not commercially available, perhaps because of their need for primary cells retrieved from deep lung tissue biopsies¹⁹⁻²⁵. Nevertheless, biobanks of organoids are being established around the world. For instance, in The Netherlands, the foundation Hubrecht Organoid biobank has available several lung organoids from patients with cystic fibrosis, COPD, and lung cancer¹⁷⁰. There is still a need for healthy organoids to test toxicology of drugs, substances, and vaccines. Most lung organoids, see table 1.2, are epithelial based cell model¹⁹⁻²⁵. Because of their 3D cellular structure, the incorporation of other cell type is difficult. Conversely, the lung model generated in this work has stromal support. Fibroblasts play a key role in the progression of the disease^{88,163}. After damage, they produce ECM-remodelling enzymes, and pro-inflammatory cytokines such as TGF- β and interleukins, which can lead to fibrotic tissue^{34,163}. Therefore, their integration into lung-models is necessary to evaluate cellular cross-talk in healthy and diseased tissues. In our model, fibroblasts do not form part of the main organoid structure.

Other non-epithelial cell types could be incorporated in lung organoid models, for instance, macrophages. Lung macrophages are distributed in proximal and distal airways of the lung. They are part of the innate immunity of the lung. They are critical to maintain lung homeostasis, and clear pathogens^{171,172}. Their incorporation could be beneficial and yield a better understanding of the pathophysiology of respiratory infections.

We explored the integration of monocytes (THP-1) into our model, as shown in Fig. 5.1. We used a cell density of 1:1000, and 1:10,000 in relationship to airway epithelial cells. The preliminary study showed a potential strategy for the integration of different cell

types into organoids. Monocytes were cultured on top of an 8 μm porous membrane for 24 or 72 h on day 4 of organoid formation. Increasing time and cell density caused partial breakdown of the organoid (red arrows). Further studies are needed to confirm the integration and the phenotype of monocytes into the culture, and to determine the best conditions cell concentration and culture period for their development.

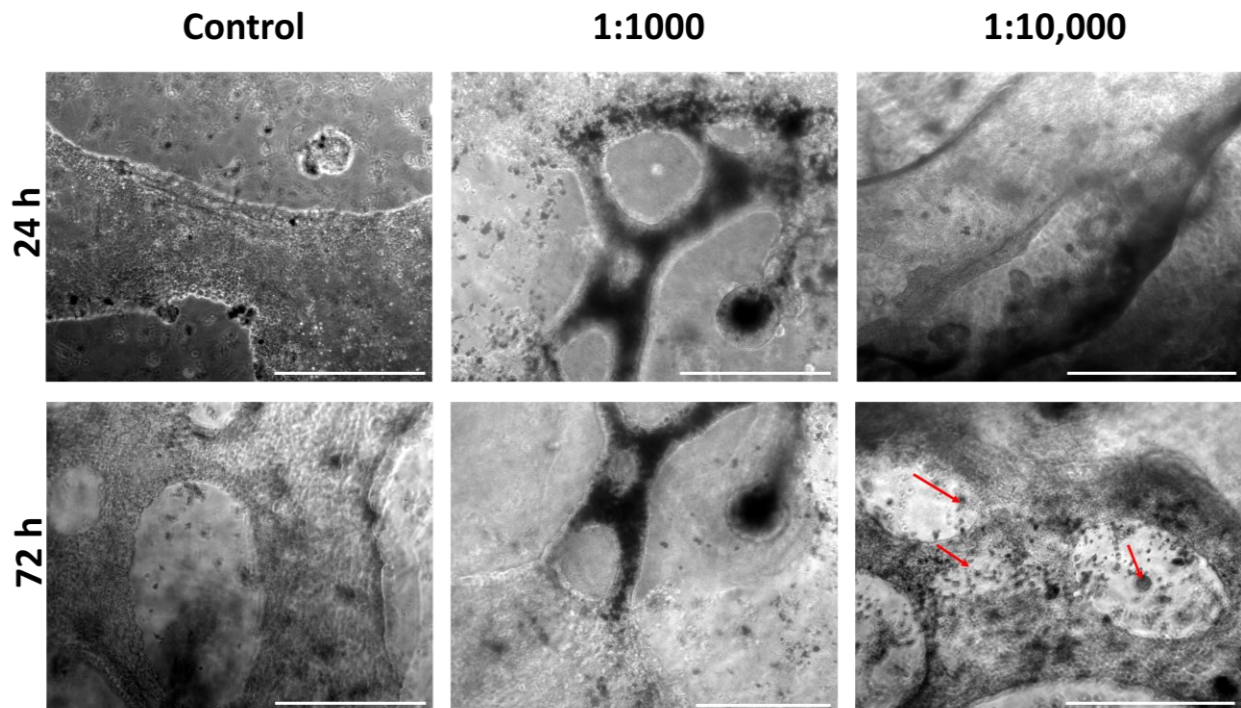


Fig. 5.1 Potential strategy to increase complexity of lung organoids. Monocytes (THP-1) were cultured on top of 8 μm porous membranes using two different cell densities: 1:1000, and 1:10000, in relationship to airway epithelial cells (CFBE) during 24 h or 72 h after 4 days post organoid formation. Red arrows show cell debris from the main structure. Magnification 10X. Scale Bar 500 μm .

Endothelial cells could also be integrated in lung organoids. This could enrich the model by providing an interface with pneumocytes, where gases exchange occurs¹. A potential strategy to integrate endothelial cells into lung organoids would be to mix the different cell types before organoid formation. This has been done with brain organoids¹⁷³.

One key aspect of the integration of non-epithelial cell types into organoids is the maintenance of physiologically relevant cell number, as in the human lung. Typically, cell co-cultures ratios do not necessarily reflect the ratio in the tissue. For instance, co-cultures of AT2 with monocytes are typically in a ratio 2:1¹⁷⁴, which seems to exceed the natural number of macrophages per AT2 in the human lung¹⁷⁵.

There is a new strategy to increase the complexity of organoids, called “assembloids”. Assembloids are fused region-specific organoids. In this technique, two different organoids are embedded together causing cell migration and ultimately organoid fusion^{176,177}. This can be possibly attempted for lung spheroids representing either proximal, or distal lung region. For iPSC-derived lung organoids and the model generated in this study, this could be a problematic approach, given the morphological complexity and heterogeneity of the organoids.

Despite their physiological mimicry and relevance, organoids still face challenges with their viability¹¹⁹. To improve this, bioreactors can be used to culture organoids for long periods of time. Spinning bioreactors promote the diffusion of Oxygen and nutrients, preserving the organoids for longer period of time^{71,72}. We demonstrated the feasibility of using bioprinting, to create easily manageable 'organoids' that can be cultured in a spinning bioreactor without rupture. The impact of this culture method remains to be determined.

The implementation of other automated manufacturing technologies is needed to help scale up the production of organoids. This has been done successfully with kidney organoids¹²⁰. This method has generated faster and more reproducible organoids¹²⁰.

To commercialize lung organoids, freezing techniques for organoid cryopreservation, need to be explored. There are available protocols for cryopreservation of intestinal organoids by StemCell Technologies. In these protocols, the substrate needs to be broken, and the organoids fragmented prior to the addition of freezing medium¹⁷⁸. The incorporation of Rho kinase inhibitors is typically added into the thawing medium to improve the cryopreservation. These inhibitors have shown to reduce organoid dissociation due to apoptosis by strengthening organoid adhesive properties^{179,180}. However, these inhibitors are added after the disassociation of the organoids on small fragments^{178,179}. Therefore, this is not the most appropriate methodology to cryopreserve the LO generated in this study, since these organoids are 1.2 cm length and show elongated and complex morphology. Vitrification is a freezing technique used to preserve large objects such as embryos, whole organs, and tissue fragments^{180,181}. This technique seems more appropriate to preserve complex organoids. During this process, high concentrations of cryopreserving agents in the vitrification solution (Me₂SO, ethylene glycol and sucrose, raffinose, and dextran) promote the rapid penetration and saturation of central areas of the organoid¹⁸⁰. In situ, vitrification has been applied to cryopreserve lung cancer organoids. Vitrification solution was applied directly on the organoid culture well, and it was placed in liquid nitrogen for long term storage¹⁸². This method could be potentially applied to the organoids generated in this study.

As we progress in the realm of lung organoid technologies, it is crucial to contextualize their capabilities within the broader landscape of in vitro lung models. Comparing and contrasting these innovations with other methodologies, including lung-on-a-chip

systems, ALI cultures (as demonstrated in this study), and, critically, human clinical data, becomes imperative, particularly when simulating disease conditions.

5. 3 Final contributions

In this work, we have pioneered a methodology for the development of lung organoids derived from ASC originating from more accessible regions of the proximal airways, namely the trachea and bronchi. Leveraging fibroblasts, our approach has facilitated the formation of tubular structures on a macro-scale, exhibiting markers associated with both proximal and distal lung regions. Notably, our model has demonstrated superiority when compared to traditional human bronchial epithelial (HBE) grown in air-liquid-interface.

Furthermore, our adaptability extends to the formation of organoids from patients with asthma, underscoring the potential clinical relevance of our methodology. While we have successfully generated organoids with similar morphologies using immortalized epithelial cells, it is noteworthy that, although complete cell differentiation was not attained, our initial findings reveal distinct phenotypic characteristics compared to the cells prior to their incorporation into our microenvironment.

These organoids hold promise for the evaluation of influenza and coronavirus infections. This work establishes a foundational framework for future research in the field. Looking ahead, it is essential to focus on enhancing the accessibility of our model to researchers from diverse backgrounds, enabling them to explore its nuances from various perspectives. We anticipate that our model will serve as a valuable resource of inspiration and guidance for future studies, potentially leading to significant advancements in respiratory research and therapeutics.

Bibliography

1. Zepp, J. A. & Morrisey, E. E. Cellular crosstalk in the development and regeneration of the respiratory system. *Nat Rev Mol Cell Biol* **20**, 551–566 (2019).
2. Cupello, C. *et al.* Lung evolution in vertebrates and the water-to-land transition. *eLife* **11**, e77156 (2022).
3. Iber, D. The control of lung branching morphogenesis. in *Current Topics in Developmental Biology* vol. 143 205–237 (Elsevier, 2021).
4. Mintz, M. L. *Disorders of the Respiratory Tract: Common Challenges in Primary Care*. (Humana Press, Totowa, N.J, 2006).
5. Chu, X. *et al.* Evidence for lung repair and regeneration in humans: key stem cells and therapeutic functions of fibroblast growth factors. *Front. Med.* **14**, 262–272 (2020).
6. Cunniff, B., Druso, J. E. & van der Velden, J. L. Lung organoids: advances in generation and 3D-visualization. *Histochem Cell Biol* **155**, 301–308 (2021).
7. Travaglini, K. J. *et al.* A molecular cell atlas of the human lung from single-cell RNA sequencing. *Nature* **587**, 619–625 (2020).
8. Barkauskas, C. E. *et al.* Lung organoids: current uses and future promise. *Development* **144**, 986–997 (2017).
9. Whitsett, J. A. & Alenghat, T. Respiratory epithelial cells orchestrate pulmonary innate immunity. *Nat Immunol* **16**, 27–35 (2015).
10. Reyes Valenzuela Alicia, Mark Turner, Nathan Markarian, Christophe Lachance-Brais, Charlotte Fouquet, John Haranhan, Silvia Vidal, Luc Mongeau. Fabrication and analysis of heterogenous lung organoids derived from adult bronchial cells and fetal fibroblasts for SARS-CoV-2 infection.
11. Noguchi, M., Furukawa, K. T. & Morimoto, M. Pulmonary neuroendocrine cells: physiology, tissue homeostasis and disease. *Disease Models & Mechanisms* **13**, dmm046920 (2020).
12. Schneider, C., O’Leary, C. E. & Locksley, R. M. Regulation of immune responses by tuft cells. *Nat Rev Immunol* **19**, 584–593 (2019).
13. Lei, L. *et al.* CFTR-rich ionocytes mediate chloride absorption across airway epithelia. *Journal of Clinical Investigation* **133**, e171268 (2023).
14. Wu, A. & Song, H. Regulation of alveolar type 2 stem/progenitor cells in lung injury and regeneration. *Acta Biochim Biophys Sin (Shanghai)* **52**, 716–722 (2020).
15. Chua, F. & Laurent, G. J. FIBROBLASTS. in *Encyclopedia of Respiratory Medicine* (eds. Laurent, G. J. & Shapiro, S. D.) 213–219 (Academic Press, Oxford, 2006). doi:10.1016/B0-12-370879-6/00156-3.

16. Warburton, D. *et al.* The molecular basis of lung morphogenesis. *Mechanisms of Development* **92**, 55–81 (2000).
17. Dettmar, P. W. Immune: A Journey into the Mysterious System That Keeps You Alive. in (2021).
18. Marko Z. Nikolić,^{1,2,*} Dawei Sun,¹ and Emma L. Rawlins¹. Human lung development: recent progress and new challenges. *Development*.
19. Aros, C. J., Pantoja, C. J. & Gomperts, B. N. Wnt signaling in lung development, regeneration, and disease progression. *Commun Biol* **4**, 601 (2021).
20. Frank, D. B. *et al.* Emergence of a Wave of Wnt Signaling that Regulates Lung Alveologenesis by Controlling Epithelial Self-Renewal and Differentiation. *Cell Reports* **17**, 2312–2325 (2016).
21. Miller, A. J. *et al.* Generation of lung organoids from human pluripotent stem cells in vitro. *Nat Protoc* **14**, 518–540 (2019).
22. Kim, J., Koo, B.-K. & Knoblich, J. A. Human organoids: model systems for human biology and medicine. *Nat Rev Mol Cell Biol* **21**, 571–584 (2020).
23. Si, L. *et al.* Human Organ Chip-Enabled Pipeline to Rapidly Repurpose Therapeutics during Viral Pandemics. <http://biorxiv.org/lookup/doi/10.1101/2020.04.13.039917> (2020).
24. Basil, M. C. *et al.* Human distal airways contain a multipotent secretory cell that can regenerate alveoli. *Nature* **604**, 120–126 (2022).
25. Wu, H. & Tang, N. Stem cells in pulmonary alveolar regeneration. *Development* **148**, dev193458 (2021).
26. Akhtar, A. The Flaws and Human Harms of Animal Experimentation. *Camb Q Healthc Ethics* **24**, 407–419 (2015).
27. Del Pace, L., Viviani, L. & Straccia, M. Researchers and Their Experimental Models: A Pilot Survey in the Context of the European Union Health and Life Science Research. *Animals* **12**, 2778 (2022).
28. Science. A new path to new drugs: Finding alternatives to animal testing.
29. Agraval, H., Sharma, J. R., Dholia, N. & Yadav, U. C. S. Air–Liquid Interface Culture Model to Study Lung Cancer-Associated Cellular and Molecular Changes. in *Cancer Biomarkers* (ed. Deep, G.) vol. 2413 133–144 (Springer US, New York, NY, 2022).
30. Leach, T. *et al.* Development of a novel air–liquid interface airway tissue equivalent model for in vitro respiratory modeling studies. *Sci Rep* **13**, 10137 (2023).
31. Rui-Wen He ^{1 2}, Hedwig M Braakhuis ¹, Rob J Vandebriel ¹, Yvonne C M Staal ¹, Eric R Gremmer ¹, Paul H B Fokkens ¹, Claudia Kemp ¹, Jolanda Vermeulen ¹, Remco H S Westerink ², Flemming R Cassee ^{1 2}. Optimization of an air-liquid interface in vitro cell co-culture model to estimate the hazard of aerosol exposures. *J Aerosol Sci.* doi:10.1016/j.jaerosci.2020.105703.
32. Wong, A. P. *et al.* Directed differentiation of human pluripotent stem cells into mature airway epithelia expressing functional CFTR protein. *Nat Biotechnol* **30**, 876–882 (2012).

33. Dave A. Lagowala, Arabelis Wally, Kai Wilmsen, Byunggik Kim, Bonnie Yeung-Luk, Jeongseob Choi, Carter Swaby, Matthew Luk, Laine Feller, Baishakhi Ghosh, Austin Niedrkofler, Ethan Tieng, Ethan Sherman, Daniel Chen, Nisha Upadya, Rachel Zhang, Deok-Ho Kim,* and Venkataramana Sidhaye. Microphysiological Models of Lung Epithelium-Alveolar Macrophage Co-Cultures to Study Chronic Lung Disease.
34. Barron, S. L. *et al.* Modelling bronchial epithelial-fibroblast cross-talk in idiopathic pulmonary fibrosis (IPF) using a human-derived in vitro air liquid interface (ALI) culture. *Sci Rep* **14**, 240 (2024).
35. HiLung. Human iPSC-derived Airway plates (cells in ALI formats). <https://www.hilung.com/en/products-services/#cellproducts>.
36. Bhatia, S. N. & Ingber, D. E. Microfluidic organs-on-chips. *Nature Biotechnology* **32**, 760–772 (2014).
37. Huh, D. *et al.* Reconstituting Organ-Level Lung Functions on a Chip. *Science* **328**, 1662–1668 (2010).
38. Huh, D. *et al.* Microfabrication of human organs-on-chips. *Nature Protocols* **8**, 2135–2157 (2013).
39. Zhang, Y. S. *et al.* Bioprinted thrombosis-on-a-chip. *Lab on a Chip* **16**, 4097–4105 (2016).
40. Zamprogno, P. *et al.* Second-generation lung-on-a-chip with an array of stretchable alveoli made with a biological membrane. *Commun Biol* **4**, 168 (2021).
41. Si, L. *et al.* A human-airway-on-a-chip for the rapid identification of candidate antiviral therapeutics and prophylactics. *Nat Biomed Eng* **5**, 815–829 (2021).
42. Huh, D. *et al.* A Human Disease Model of Drug Toxicity–Induced Pulmonary Edema in a Lung-on-a-Chip Microdevice. *Sci. Transl. Med.* **4**, (2012).
43. Yang, X. *et al.* Nanofiber membrane supported lung-on-a-chip microdevice for anti-cancer drug testing. *Lab Chip* **18**, 486–495 (2018).
44. Muhammad Asad Ullah Khalida *et al.* A lung cancer-on-chip platform with integrated biosensors for physiological monitoring and toxicity assessment. (2019).
45. A Jain^{1,2,3,7*}, R Barrile^{1,8*}, AD van der Meer^{1,9}, A Mammoto², T Mammoto², K De Ceunynck³, O Aisiku³, MA Otieno⁴, CS Louden⁴, GA Hamilton⁵, R Flaumenhaft³ and DE Ingber^{1,2,6}. Primary Human Lung Alveolus-on-a-chip Model of Intravascular Thrombosis for Assessment of Therapeutics. *Clinical pharmacology & Therapeutics* (2018).
46. Nawroth, J. C. *et al.* A Microengineered Airway Lung Chip Models Key Features of Viral-induced Exacerbation of Asthma. *Am J Respir Cell Mol Biol* **63**, 591–600 (2020).
47. Zhang, M., Xu, C., Jiang, L. & Qin, J. A 3D human lung-on-a-chip model for nanotoxicity testing. *Toxicol. Res.* **7**, 1048–1060 (2018).
48. Angana De a *et al.* Lung-on-chip: Its current and future perspective on pharmaceutical and biomedical applications. *Journal of Drug Delivery Science and Technology* **78**, (2022).

49. Emulate. *Organ-on-a-chip. Lung-on-a-chip*.
50. CN Bio. organ-on-a-chip model. <https://cn-bio.com/organ-models/>.
51. Rossi, G., Manfrin, A. & Lutolf, M. P. Progress and potential in organoid research. *Nat Rev Genet* **19**, 671–687 (2018).
52. Seghir, R. & Arscott, S. Extended PDMS stiffness range for flexible systems. *Sensors and Actuators A: Physical* **230**, 33–39 (2015).
53. Guimarães, C. F., Gasperini, L., Marques, A. P. & Reis, R. L. The stiffness of living tissues and its implications for tissue engineering. *Nat Rev Mater* **5**, 351–370 (2020).
54. Bayir, E., Sendemir, A. & Missirlis, Y. F. Mechanobiology of cells and cell systems, such as organoids. *Biophys Rev* **11**, 721–728 (2019).
55. Pawluchin, A. & Galic, M. Moving through a changing world: Single cell migration in 2D vs. 3D. *Front. Cell Dev. Biol.* **10**, 1080995 (2022).
56. Hou, Y. J. *et al.* SARS-CoV-2 Reverse Genetics Reveals a Variable Infection Gradient in the Respiratory Tract. *Cell* **182**, 429-446.e14 (2020).
57. Chen, D. *et al.* Human Organoids as a Promising Platform for Fighting COVID-19. *Int. J. Biol. Sci.* **18**, 901–910 (2022).
58. Ramezankhani, R., Solhi, R., Chai, Y. C., Vosough, M. & Verfaillie, C. Organoid and microfluidics-based platforms for drug screening in COVID-19. *Drug Discovery Today* **27**, 1062–1076 (2022).
59. Sasai, Y. Cytosystems dynamics in self-organization of tissue architecture. *Nature* **493**, 318–326 (2013).
60. Aisenbrey, E. A. & Murphy, W. L. Synthetic alternatives to Matrigel. *Nat Rev Mater* **5**, 539–551 (2020).
61. Mulay, A. *et al.* SARS-CoV-2 infection of primary human lung epithelium for COVID-19 modeling and drug discovery. *Cell reports* **35**, 109055 (2021).
62. Sprott, R. F. *et al.* Flagellin shifts 3D bronchospheres towards mucus hyperproduction. *Respir Res* **21**, 222 (2020).
63. Tindle, C. *et al.* Adult stem cell-derived complete lung organoid models emulate lung disease in COVID-19. *eLife* **10**, e66417 (2021).
64. Rock, J. R. *et al.* Basal cells as stem cells of the mouse trachea and human airway epithelium. *Proc Natl Acad Sci USA* **106**, 12771 (2009).
65. Zhou, J. *et al.* Differentiated human airway organoids to assess infectivity of emerging influenza virus. *Proc. Natl. Acad. Sci. U.S.A.* **115**, 6822–6827 (2018).
66. Sachs, N. *et al.* Long-term expanding human airway organoids for disease modeling. *The EMBO Journal* **38**, e100300 (2019).

67. Sachs, N., Tsukamoto, Y., Kujala, P., Peters, P. J. & Clevers, H. Intestinal epithelial organoids fuse to form self-organizing tubes in floating collagen gels. *Development* **144**, 1107–1112 (2017).
68. Gjorevski, N. *et al.* Designer matrices for intestinal stem cell and organoid culture. *Nature* **539**, 560–564 (2016).
69. Lindborg, B. A. *et al.* Rapid Induction of Cerebral Organoids From Human Induced Pluripotent Stem Cells Using a Chemically Defined Hydrogel and Defined Cell Culture Medium. *Stem Cells Translational Medicine* **5**, 970–979 (2016).
70. Lancaster, M. A. Cerebral organoids model human brain development and microcephaly.
71. Qian, X. *et al.* Generation of human brain region-specific organoids using a miniaturized spinning bioreactor. *Nat Protoc* **13**, 565–580 (2018).
72. Klöckner, W., Diederichs, S. & Büchs, J. Orbitally Shaken Single-Use Bioreactors. in *Disposable Bioreactors II* (eds. Eibl, D. & Eibl, R.) vol. 138 45–60 (Springer Berlin Heidelberg, Berlin, Heidelberg, 2013).
73. Takasato, M. *et al.* Directing human embryonic stem cell differentiation towards a renal lineage generates a self-organizing kidney. *Nat Cell Biol* **16**, 118–126 (2014).
74. Eiraku, M. *et al.* Self-organizing optic-cup morphogenesis in three-dimensional culture. *Nature* **472**, 51–56 (2011).
75. Chiu, M. C. *et al.* A bipotential organoid model of respiratory epithelium recapitulates high infectivity of SARS-CoV-2 Omicron variant. *Cell Discov* **8**, 57 (2022).
76. Takebe, T. *et al.* Vascularized and functional human liver from an iPSC-derived organ bud transplant. *Nature* **499**, 481–484 (2013).
77. Chen, Y.-W. *et al.* A three-dimensional model of human lung development and disease from pluripotent stem cells. *Nat Cell Biol* **19**, 542–549 (2017).
78. Porotto, M. *et al.* Authentic Modeling of Human Respiratory Virus Infection in Human Pluripotent Stem Cell-Derived Lung Organoids. *mBio* **10**, e00723-19, /mbio/10/3/mBio.00723-19.atom (2019).
79. Danahay, H. *et al.* Notch2 Is Required for Inflammatory Cytokine-Driven Goblet Cell Metaplasia in the Lung. *Cell Reports* **10**, 239–252 (2015).
80. Tan, Q., Choi, K. M., Sicard, D. & Tschumperlin, D. J. Human airway organoid engineering as a step toward lung regeneration and disease modeling. *Biomaterials* **113**, 118–132 (2017).
81. *Epithelial Cell Culture Protocols: Second Edition*. vol. 945 (Humana Press, Totowa, NJ, 2013).
82. Millipore Sigma. 3dGRO™ Human Lung Organoids (PDXO.149). <https://www.sigmaaldrich.com/CA/en/product/mm/scc607#product-documentation>.
83. McCauley, K. B. *et al.* Efficient Derivation of Functional Human Airway Epithelium from Pluripotent Stem Cells via Temporal Regulation of Wnt Signaling. *Cell Stem Cell* **20**, 844–857.e6 (2017).

84. Konishi, S. *et al.* Directed Induction of Functional Multi-ciliated Cells in Proximal Airway Epithelial Spheroids from Human Pluripotent Stem Cells. *Stem Cell Reports* **6**, 18–25 (2016).
85. Dye, B. R. *et al.* In vitro generation of human pluripotent stem cell derived lung organoids. *eLife* **4**, e05098 (2015).
86. Chiu, Y.-W. *et al.* Costs of Biopsy and Complications in Patients with Lung Cancer. *CEOR Volume* **13**, 191–200 (2021).
87. Hutchinson, J. P., Fogarty, A. W., McKeever, T. M. & Hubbard, R. B. In-Hospital Mortality after Surgical Lung Biopsy for Interstitial Lung Disease in the United States. 2000 to 2011. *Am J Respir Crit Care Med* **193**, 1161–1167 (2016).
88. Gomes, R. N., Manuel, F. & Nascimento, D. S. The bright side of fibroblasts: molecular signature and regenerative cues in major organs. *npj Regen Med* **6**, 43 (2021).
89. Wang, Y., Chen, S., Yan, Z. & Pei, M. A prospect of cell immortalization combined with matrix microenvironmental optimization strategy for tissue engineering and regeneration. *Cell Biosci* **9**, 7 (2019).
90. Maddaly Ravi. Enhancing the Utility of Cancer Cell Lines by culturing them as 3D Aggregates and 3D Reverts – My experiences thus far. (2018) doi:10.13140/RG.2.2.33998.51521.
91. Obinata, M. The immortalized cell lines with differentiation potentials: Their establishment and possible application. *Cancer Science* **98**, 275–283 (2007).
92. Soleimani, M. & Ghasemi, N. Lithium Chloride can Induce Differentiation of Human Immortalized RenVm Cells into Dopaminergic Neurons. **9**, (2017).
93. Okamoto, T. *et al.* Clonal heterogeneity in differentiation potential of immortalized human mesenchymal stem cells. *Biochemical and Biophysical Research Communications* **295**, 354–361 (2002).
94. Gotoh Noriko. Control of Stemness by Fibroblast Growth Factor Signaling in Stem Cells and Cancer Stem Cells. *Current Stem Cell Research & Therapy* (2009).
95. Ghabrial, A. S. & Krasnow, M. A. Social interactions among epithelial cells during tracheal branching morphogenesis. *Nature* **441**, 746–749 (2006).
96. Kina, Y. P., Khadim, A., Seeger, W. & El Agha, E. The Lung Vasculature: A Driver or Passenger in Lung Branching Morphogenesis? *Front. Cell Dev. Biol.* **8**, 623868 (2021).
97. Goodwin, K. & Nelson, C. M. Branching morphogenesis. *Development* **147**, dev184499 (2020).
98. Kim, H. Y., Varner, V. D. & Nelson, C. M. Apical constriction initiates new bud formation during monopodial branching of the embryonic chicken lung. *Development* **140**, 3146–3155 (2013).
99. *Alginates and Their Biomedical Applications*. vol. 11 (Springer Singapore, Singapore, 2018).
100. Szekalska, M., Puciłowska, A., Szymańska, E., Ciosek, P. & Winnicka, K. Alginate: Current Use and Future Perspectives in Pharmaceutical and Biomedical Applications. *International Journal of Polymer Science* **2016**, 1–17 (2016).

101. Reyes, A. *In Vitro Analysis of Polymeric Microspheres Containing Human Vocal Fold Fibroblasts for Regeneration of Vocal Fold Lamina Propria*. (McGill University Libraries, 2019).
102. Chan, L. W., Lee, H. Y. & Heng, P. W. S. Mechanisms of external and internal gelation and their impact on the functions of alginate as a coat and delivery system. *Carbohydrate Polymers* **63**, 176–187 (2006).
103. *Nanotechnology for the Regeneration of Hard and Soft Tissues*. (World Scientific, Singapore ; Hackensack, N.J, 2007).
104. Tibbitt, M. W. & Anseth, K. S. Hydrogels as extracellular matrix mimics for 3D cell culture. *Biotechnology and Bioengineering* **103**, 655–663 (2009).
105. Jiang, T. *et al.* Engineering bioprintable alginate/gelatin composite hydrogels with tunable mechanical and cell adhesive properties to modulate tumor spheroid growth kinetics. *Biofabrication* **12**, 015024 (2019).
106. Futaki, S. *et al.* Molecular Basis of Constitutive Production of Basement Membrane Components. *Journal of Biological Chemistry* **278**, 50691–50701 (2003).
107. Benedetto, R. *et al.* Epithelial Chloride Transport by CFTR Requires TMEM16A. *Sci Rep* **7**, 12397 (2017).
108. Bebok, Z. *et al.* Failure of cAMP agonists to activate rescued $\Delta F508$ CFTR in CFBE41o⁻ airway epithelial monolayers: $\Delta F508$ CFTR activity in CFBE41o⁻ cells. *The Journal of Physiology* **569**, 601–615 (2005).
109. Loessner, D. *et al.* Functionalization, preparation and use of cell-laden gelatin methacryloyl-based hydrogels as modular tissue culture platforms. *Nat Protoc* **11**, 727–746 (2016).
110. Lange, K. Fundamental role of microvilli in the main functions of differentiated cells: Outline of an universal regulating and signaling system at the cell periphery. *Journal Cellular Physiology* **226**, 896–927 (2011).
111. Orbach, R. & Su, X. Surfing on Membrane Waves: Microvilli, Curved Membranes, and Immune Signaling. *Front. Immunol.* **11**, 2187 (2020).
112. Yusuf S. Khan. David T. Lynch. *Histology, Lung*. (StatPearls, 2023).
113. Mizushima, N. Autophagy: process and function. *Genes Dev.* **21**, 2861–2873 (2007).
114. Li, X. *et al.* The Role of Autophagy in Lamellar Body Formation and Surfactant Production in Type 2 Alveolar Epithelial Cells. *Int. J. Biol. Sci.* **18**, 1107–1119 (2022).
115. Sun, N. *et al.* Applications of brain organoids in neurodevelopment and neurological diseases. *J Biomed Sci* **28**, 30 (2021).
116. Hazell, G., Khazova, M. & O’Mahoney, P. Low-dose daylight exposure induces nitric oxide release and maintains cell viability in vitro. *Sci Rep* **13**, 16306 (2023).

117. Millipore Sigma. 3dGRO Lung Organoid Medium. <https://www.sigmaaldrich.com/CA/en/product/mm/scm308> (2024).
118. Cozens, A. L. *et al.* CFTR expression and chloride secretion in polarized immortal human bronchial epithelial cells. *Am J Respir Cell Mol Biol* **10**, 38–47 (1994).
119. Zhao, X. *et al.* Review on the Vascularization of Organoids and Organoids-on-a-Chip. *Front. Bioeng. Biotechnol.* **9**, 637048 (2021).
120. Lawlor, K. T. *et al.* Cellular extrusion bioprinting improves kidney organoid reproducibility and conformation. *Nat. Mater.* **20**, 260–271 (2021).
121. Hermanson, G. T. Chapter 2 - The Chemistry of Reactive Groups. in *Bioconjugate Techniques (Second Edition)* (ed. Hermanson, G. T.) 169–212 (Academic Press, New York, 2008). doi:10.1016/B978-0-12-370501-3.00002-3.
122. Shu, X. Z. *et al.* Attachment and spreading of fibroblasts on an RGD peptide–modified injectable hyaluronan hydrogel. *Journal of biomedical materials research Part A* **68**, 365–375 (2004).
123. McDonagh, B. H. Optimised Carbodiimide Chemistry for RGD-coupled Alginate. (Institut for bioteknologi, 2012).
124. Rowley, J. A., Madlambayan, G. & Mooney, D. J. Alginate hydrogels as synthetic extracellular matrix materials. *Biomaterials* **20**, 45–53 (1999).
125. Brodland, G. W. How computational models can help unlock biological systems. in *Seminars in cell & developmental biology* vol. 47 62–73 (Elsevier, 2015).
126. Gontan, C. *et al.* Sox2 is important for two crucial processes in lung development: Branching morphogenesis and epithelial cell differentiation. *Developmental Biology* **317**, 296–309 (2008).
127. Raudvere, U. *et al.* g:Profiler: a web server for functional enrichment analysis and conversions of gene lists (2019 update). *Nucleic Acids Research* **47**, W191–W198 (2019).
128. Laurenzi MA, Arcuri C, Rossi R, Marconi P, Bocchini V. Effects of microenvironment on morphology and function of the microglial cell line BV-2. *Neurochem Res.* (2001).
129. Bell, S. M. *et al.* R-spondin 2 is required for normal laryngeal-tracheal, lung and limb morphogenesis. *Development* **135**, 1049–1058 (2008).
130. Walker, D. J. & Land, S. C. Regulation of vascular signalling by nuclear Sprout2 in fetal lung epithelial cells: Implications for co-ordinated airway and vascular branching in lung development. *Comparative Biochemistry and Physiology Part B: Biochemistry and Molecular Biology* **224**, 105–114 (2018).
131. Szklarczyk, D. *et al.* The STRING database in 2021: customizable protein–protein networks, and functional characterization of user-uploaded gene/measurement sets. *Nucleic Acids Research* **49**, D605–D612 (2021).
132. Wright, J. R. Immunoregulatory functions of surfactant proteins. *Nat Rev Immunol* **5**, 58–68 (2005).

133. Uhlén, M. *et al.* Tissue-based map of the human proteome. *Science* **347**, 1260419 (2015).
134. Nassiri, I. & McCall, M. N. Systematic exploration of cell morphological phenotypes associated with a transcriptomic query. *Nucleic Acids Research* **46**, e116–e116 (2018).
135. Elbez, R. *et al.* Cell-morphodynamic phenotype classification with application to cancer metastasis using cell magnetorotation and machine-learning. *PLoS ONE* **16**, e0259462 (2021).
136. World Health Organization. *Tuberculosis*. <https://www.who.int/news-room/fact-sheets/detail/tuberculosis> (2023).
137. Terrier, O. *et al.* Influenza viruses and coronaviruses: Knowns, unknowns, and common research challenges. *PLoS Pathog* **17**, e1010106 (2021).
138. Manzanares-Meza, L. D. & Medina-Contreras, O. SARS-CoV-2 and influenza: a comparative overview and treatment implications. *BMJIM* **77**, 4621 (2020).
139. World Health Organization. Coronavirus disease (COVID-19). (2023).
140. Flerlage, T., Boyd, D. F., Meliopoulos, V., Thomas, P. G. & Schultz-Cherry, S. Influenza virus and SARS-CoV-2: pathogenesis and host responses in the respiratory tract. *Nat Rev Microbiol* **19**, 425–441 (2021).
141. Hu, B., Guo, H., Zhou, P. & Shi, Z.-L. Characteristics of SARS-CoV-2 and COVID-19. *Nat Rev Microbiol* **19**, 141–154 (2021).
142. Limburg, H. *et al.* TMPRSS2 Is the Major Activating Protease of Influenza A Virus in Primary Human Airway Cells and Influenza B Virus in Human Type II Pneumocytes. *J Virol* **93**, e00649-19 (2019).
143. Momtazmanesh, S. *et al.* Global burden of chronic respiratory diseases and risk factors, 1990–2019: an update from the Global Burden of Disease Study 2019. *eClinicalMedicine* **59**, 101936 (2023).
144. Holgate, S. T. *et al.* Asthma. *Nat Rev Dis Primers* **1**, 15025 (2015).
145. The GenOMICC Investigators *et al.* Genetic mechanisms of critical illness in COVID-19. *Nature* **591**, 92–98 (2021).
146. Choi, U. Y., Kang, J.-S., Hwang, Y. S. & Kim, Y.-J. Oligoadenylate synthase-like (OASL) proteins: dual functions and associations with diseases. *Exp Mol Med* **47**, e144–e144 (2015).
147. Yao, Y. *et al.* Genome and epigenome editing identify CCR9 and SLC6A20 as target genes at the 3p21.31 locus associated with severe COVID-19. *Sig Transduct Target Ther* **6**, 85 (2021).
148. Sharif-zak, M. *et al.* CCR2 and DPP9 expression in the peripheral blood of COVID-19 patients: Influences of the disease severity and gender. *Immunobiology* **227**, 152184 (2022).
149. Wu, P. *et al.* Trans-ethnic genome-wide association study of severe COVID-19. *Commun Biol* **4**, 1034 (2021).
150. Zani, A. *et al.* Interferon-induced transmembrane proteins inhibit cell fusion mediated by trophoblast syncytins. *Journal of Biological Chemistry* **294**, 19844–19851 (2019).

151. Sun, E., He, J. & Zhuang, X. Dissecting the Role of COPI Complexes in Influenza Virus Infection. *J Virol* **87**, 2673–2685 (2013).
152. König, R. *et al.* Human host factors required for influenza virus replication. *Nature* **463**, 813–817 (2010).
153. Hoffmann, M. *et al.* SARS-CoV-2 Cell Entry Depends on ACE2 and TMPRSS2 and Is Blocked by a Clinically Proven Protease Inhibitor. *Cell* **181**, 271-280.e8 (2020).
154. Shen, L. W., Mao, H. J., Wu, Y. L., Tanaka, Y. & Zhang, W. TMPRSS2: A potential target for treatment of influenza virus and coronavirus infections. *Biochimie* **142**, 1–10 (2017).
155. Essalmani, R. *et al.* Distinctive Roles of Furin and TMPRSS2 in SARS-CoV-2 Infectivity. *J Virol* **96**, e00128-22 (2022).
156. Johnson, B. A. *et al.* *Furin Cleavage Site Is Key to SARS-CoV-2 Pathogenesis*. <http://biorxiv.org/lookup/doi/10.1101/2020.08.26.268854> (2020) doi:10.1101/2020.08.26.268854.
157. Xia, S. *et al.* The role of furin cleavage site in SARS-CoV-2 spike protein-mediated membrane fusion in the presence or absence of trypsin. *Sig Transduct Target Ther* **5**, 92 (2020).
158. Zeng, F. *et al.* Role and mechanism of CD90+ fibroblasts in inflammatory diseases and malignant tumors. *Mol Med* **29**, 20 (2023).
159. *Stromal Immunology*. vol. 1060 (Springer International Publishing, Cham, 2018).
160. Lambrecht, B. N. & Hammad, H. The airway epithelium in asthma. *Nature medicine* **18**, 684 (2012).
161. Kawano, H. *et al.* IL-10-producing lung interstitial macrophages prevent neutrophilic asthma. *INTIMM* **28**, 489–501 (2016).
162. Hoang, P. T. *et al.* Enhancing neutralizing activity against influenza H1N1/PR8 by engineering a single-domain VL-M2 specific into a bivalent form. *PLoS ONE* **17**, e0273934 (2022).
163. Davidson, S. *et al.* Fibroblasts as immune regulators in infection, inflammation and cancer. *Nat Rev Immunol* **21**, 704–717 (2021).
164. ThermoFisher. *Endothelial Tube Formation Assay Protocol Using Geltrex™ Reduced Growth Factor Basement Membrane Matrix*. Available from: https://www.thermofisher.com/content/dam/life_tech/documents/pdfs/cell_culture/endothelial-tube-formation-assay-protocol-using-geltrex.pdf [Accessed 13 Dec. 2023].
165. Faulkner, A. *et al.* A thin layer angiogenesis assay: a modified basement matrix assay for assessment of endothelial cell differentiation. *BMC Cell Biol* **15**, 41 (2014).
166. Ogawa, Y., Duru, E. & Ameredes, B. Role of IL-10 in the Resolution of Airway Inflammation. *CMM* **8**, 437–445 (2008).
167. Petrocheilou, A., Moudaki, A. & Kaditis, A. G. Inflammation and Infection in Cystic Fibrosis: Update for the Clinician. *Children* **9**, 1898 (2022).

168. Chung, K. F. Cytokines in chronic obstructive pulmonary disease. *European Respiratory Journal* **18**, 50–59 (2001).
169. BCC Research. Laboratory Animal Models, 3D Cultures and Organoids: Global Markets,. (2022).
170. Foundation Hubrecht. Adult stem cell derived organoids. <https://www.hubrechtorganoidbiobank.org/technology/>.
171. Bain, C. C. & MacDonald, A. S. The impact of the lung environment on macrophage development, activation and function: diversity in the face of adversity. *Mucosal Immunology* **15**, 223–234 (2022).
172. Aegerter, H., Lambrecht, B. N. & Jakubzick, C. V. Biology of lung macrophages in health and disease. *Immunity* **55**, 1564–1580 (2022).
173. Cakir, B. *et al.* Engineering of human brain organoids with a functional vascular-like system. *Nat Methods* **16**, 1169–1175 (2019).
174. Alfaro-Moreno, E. *et al.* Co-cultures of multiple cell types mimic pulmonary cell communication in response to urban PM10. *European Respiratory Journal* **32**, 1184–1194 (2008).
175. Hou, F., Xiao, K., Tang, L. & Xie, L. Diversity of Macrophages in Lung Homeostasis and Diseases. *Front. Immunol.* **12**, 753940 (2021).
176. Bagley, J. A., Reumann, D., Bian, S., Lévi-Strauss, J. & Knoblich, J. A. Fused cerebral organoids model interactions between brain regions. *Nat Methods* **14**, 743–751 (2017).
177. Marton, R. M. & Paşca, S. P. Organoid and Assembloid Technologies for Investigating Cellular Crosstalk in Human Brain Development and Disease. *Trends in Cell Biology* **30**, 133–143 (2020).
178. StemCell Technologies. How to Cryopreserve Intestinal Organoids. <https://www.stemcell.com/how-to-cryopreserve-intestinal-organoids.html> (2024).
179. Jacob, F., Ming, G. & Song, H. Generation and biobanking of patient-derived glioblastoma organoids and their application in CAR T cell testing. *Nat Protoc* **15**, 4000–4033 (2020).
180. Rogulska, O., Havelkova, J. & Petrenko, Y. Cryopreservation of Organoids. *cryo letters* **44**, 65–75 (2023).
181. Nagy, Z. P., Shapiro, D. & Chang, C.-C. Vitrification of the human embryo: a more efficient and safer in vitro fertilization treatment. *Fertility and Sterility* **113**, 241–247 (2020).
182. Liu, Q. *et al.* In Situ Vitrification of Lung Cancer Organoids on a Microwell Array. *Micromachines* **12**, 624 (2021).

Appendix

Lung Region	Cell type	Genes	p.adjust LOp and HBE	p.adjust LOp and IMR-90	
	Basal	p63	0.980	0.000 ↑	
		C14	0.130	0.000 ↑	
		Krt5	0.540	0.000 ↑	
		BNC1	0.150	0.000 ↑	
	Secretory type I	SCGB1A1	0.170	0.000 ↑	
	Ciliated cells	FOXJ1	0.000 ↓	0.000 ↑	
	Multipotency	SOX2	0.016 ↓	0.000 ↑	
	Goblet cells	MUC5AC	0.000 ↓	0.000 ↑	
		MUC5B	0.000 ↓	0.000 ↑	
		MUC2	0.100	0.000 ↑	
		MUC15	0.044 ↑	0.000 ↑	
	Proximal	Brush	POU2F3	0.021	0.000 ↑
			TRPM5	0.000 ↑	0.000 ↑
			IL-25	0.130	0.018
ALOX5AP			0.000 ↑	0.000 ↑	
PNEC		ASCL1	0.001 ↑	0.004 ↑	
		CALCA	0.022	0.003 ↑	
Secretory type II		SCGB3A2	0.000 ↑	0.001 ↑	
Multipotency		SOX9	0.825	0.264	
AT2		SFTPC	0.000 ↑	0.008 ↑	
		SFTPB			
	SFTPA1	0.177	0.004 ↑		
	SFTPD	0.028 ↑	0.000 ↑		
Distal	AT1	HOPX	0.003 ↑	0.000 ↑	
		PDPN	0.010 ↑	0.000 ↑	

Table A.1 P. adjust value from multiple t-test comparisons between RNA sequencing of LOp vs cell monolayers: HBE, and IMR-90 ↑ means upregulation in LOp (p.adjust<0.05). ↓ means downregulation in LOp (p. adjust <0.05). Lower the p value, more significant the up or downregulation.

Lung Region	Cell type	Genes	p-adj LOi and CFBE	p adj LOi and IMR90
Proximal	Basal	p63	0.017 ↑	0.000 ↑
		C14	0.417	0.189
		Krt5	0.931	0.000 ↑
		BNC1	0.349	0.000 ↑
	Secretory type I	SCGB1A1	0.007 ↑	0.005 ↑
	Multipotency	SOX2	0.061	0.001 ↑
	Ciliated cells	FOXJ1	0.063	0.000 ↑
	Goblet cells	MUC5AC	0.018 ↑	0.000 ↑
		MUC5B	0.000 ↑	0.000 ↑
		MUC2	0.000 ↑	0.000 ↑
		MUC15	0.827	0.031 ↑
	Brush	POU2F3	0.054	0.000 ↑
		TRPM5	0.006 ↑	0.000 ↑
		IL-25	0.041 ↑	0.031 ↑
		ALOX5AP	0.000 ↑	0.259
	PNEC	ASCL1	0.022 ↑	0.011 ↑
		CALCA	0.212	0.036 ↑
Distal	Multipotency	SOX9	0.007 ↑	0.308
	Secretory type II	SCGB3A2	0.018 ↑	0.009 ↑
	AT2	SFTPC	0.285	0.060
		SFTPB		
		SFTPA1	0.227	0.010 ↑
		SFTPD	0.849	0.000 ↑
	AT1	HOPX	0.159	0.654
		PDPN	0.643	0.143
		AKAP5	0.089	0.000 ↑
SCNN1G		0.000 ↑	0.000 ↑	

Table A.2 P. adjust value from multiple t-test comparisons between RNA sequencing of LOi vs cell monolayers: CFBE, and IMR-90. ↑ means upregulated in LOi (p.adjust<0.05).

Reagent or Resource	Source	Identifier
Antibodies		
SFTPB	Santa Cruz	SC-133143
SFTPC	Santa Cruz	SC-518029
Hoechst dye	Thermo Fisher	H3569
Biological samples		
Human Fetal Lung Fibroblasts, IMR-90	Cederlane	CCL-186
Human Bronchial CF Epithelial cells, CFBE	Cystic Fibrosis Translational Research Centre (CFTRc) McGill	NA
Human Primary Bronchial Tracheal Epithelial cells (male)	Cystic Fibrosis Translational Research Centre (CFTRc) McGill	BD649
Human Primary Bronchial Tracheal Epithelial cells (female)	Cystic Fibrosis Translational Research Centre (CFTRc) McGill	BD999
Human Tissue Superior Bronchi (male 51 years old)	Cystic Fibrosis Translational Research Centre (CFTRc) McGill	BD649
Human Tissue Inferior Bronchi (male 51 years old)	Cystic Fibrosis Translational Research Centre (CFTRc) McGill	BD649
Human Tissue Superior Bronchi (male 42 years old)	Cystic Fibrosis Translational Research Centre (CFTRc) McGill	BD342
Human Tissue Inferior Bronchi (male 42 years old)	Cystic Fibrosis Translational Research Centre (CFTRc) McGill	BD342
Human Tissue Superior Bronchi (male 66 years old)	Cystic Fibrosis Translational Research Centre (CFTRc) McGill	BD888
Human Tissue Inferior Bronchi (male 66 years old)	Cystic Fibrosis Translational Research Centre (CFTRc) McGill	BD888
Human Tissue Superior Bronchi (male 56 years old)	Cystic Fibrosis Translational Research Centre (CFTRc) McGill	BD743
Human Tissue Inferior Bronchi (male 56 years old)	Cystic Fibrosis Translational Research Centre (CFTRc) McGill	BD743
Human Tissue Superior Bronchi (male 62 years old)	Cystic Fibrosis Translational Research Centre (CFTRc) McGill	BD458
Human Tissue Inferior Bronchi (male 62 years old)	Cystic Fibrosis Translational Research Centre (CFTRc) McGill	BD458
Human Tissue Superior Bronchi (male 59 years old)	Cystic Fibrosis Translational Research Centre (CFTRc) McGill	BD843
Human Tissue Inferior Bronchi (male 59 years old)	Cystic Fibrosis Translational Research Centre (CFTRc) McGill	BD843
Chemicals		
Geltrex	ThermoFisher	A1413202

L-Glutamine	ThermoFisher	A2916801
Fetal Bovine Serum	Sigma Aldrich	F1051
Dulbecco's Modified Eagle's Medium (DMEM)	Corning	15-017-CV
MEM Non-essential aminoacids	Fisher Scientific	LS11140
Penicillin-Streptomycin	Fisher Scientific	SV30010
Minimum Essential Medium (EMEM)	Corning	10-010-CMR
PBS	Fisher Scientific	10-010-049
Goat Serum 10%	ThermoFisher	50062Z
RIPA buffer	Sigma Aldrich	R0278
Trizol	ThermoFisher	15596026
Qubit Protein Assay	ThermoFisher	Q33211
Compensation beads	ThermoFisher	01-2222-42
eBioscience Flow cytometry Staining Buffer	ThermoFisher	00-4222-57
Bovine Serum Albumin	Sigma Aldrich	A9647
Alginate	Sigma Aldrich	A0682
Gelatin-type A	Sigma Aldrich	G2500
CaCl ₂	ACP	C-0360
5X RT Master Mix	Diamed	ABMG486
RNA Spin Mini kit	Ge Healthcare	GE25-0500-71
Trypsin	Fisher Scientific	MT25053CI
5X RT Master Mix	Diamed	ABMG486
SYBR Green	ThermoFisher	A46109
Fibronectin	Promo cell	C-43060
2-Mercaptoethanol	Sigma Aldrich	35600

Table A.3 Key resources table for methods described in Chapter 3.

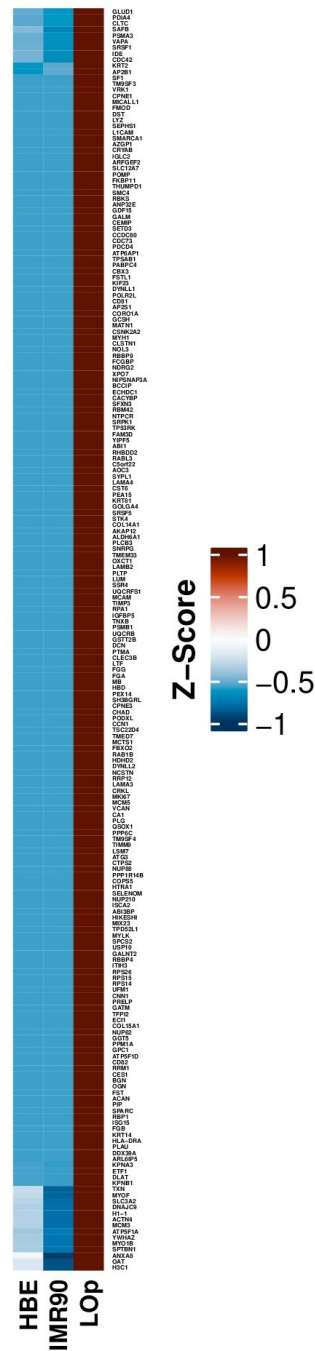
Primers	Forward	Reverse	Company
HPRT	5'-GCGATGTCAATAGGACTCCAG-3'	5'-TTGTTGTAGGATATGCCCTTGA-3'	IDT

Table A.4 Key resources table. Primer sequence used in chapter 3 as housekeeping gene.

Primers	Forward	Reverse	Company
TMPRSS-2	5'CTTTGAACTCAGGGTCACCA-3'	5- 'TAGTACTGAGCCGGATGCAC-3'	IDT
ACE2	5'-CATTGGAGCAAGTGTGGATCTT-3'	5'- GAGCTAATGCATGCCATTCTCA- 3'	IDT
SARS-CoV-2- Nucleocapsid (N)	5'- TAATACGACTCACTATAGGGAAATTTGGGGACCAGGAAC -3'	5'- TGGCAGCTGTGTAGGTCAAC-3'	IDT
H1N1 PR8 NP	5' GGG TGA GAA TGG ACG AAA AA -3'	5-' TCC ATC ATT GCT TTT TGT GC -3'	IDT
B actin	5'- AAG GAG AAG CTG TGC TAG GTC GTC GC -3'	5'- AGA CAG CAC TGT GTT GGC GTA CA -3'	IDT
IFN-B	5'- CAT TAC CTG AAG CCC AAG GA -3'	5'- CAA TTG TCC AGT CCC AGA GG -3'	IDT

Table A.5 Key resources table. Primer sequences used in chapter 4 to evaluate infectability of SARS-CoV-2 and Influenza in the organoids.

Proteins upregulated in LOp – cluster 2



Proteins upregulated in LOp

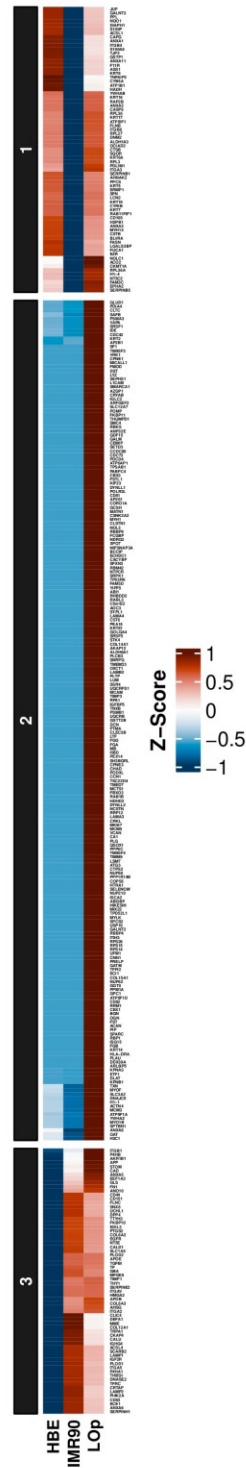


Figure A.2 Complete heatmap of proteins in cell monolayers HBE, IMR-90 and LOp organoids. Cluster 2 corresponds to the proteins upregulated in the organoid. Abundances grouped, linked by average. Red show upregulation and blue downregulation. N=3.

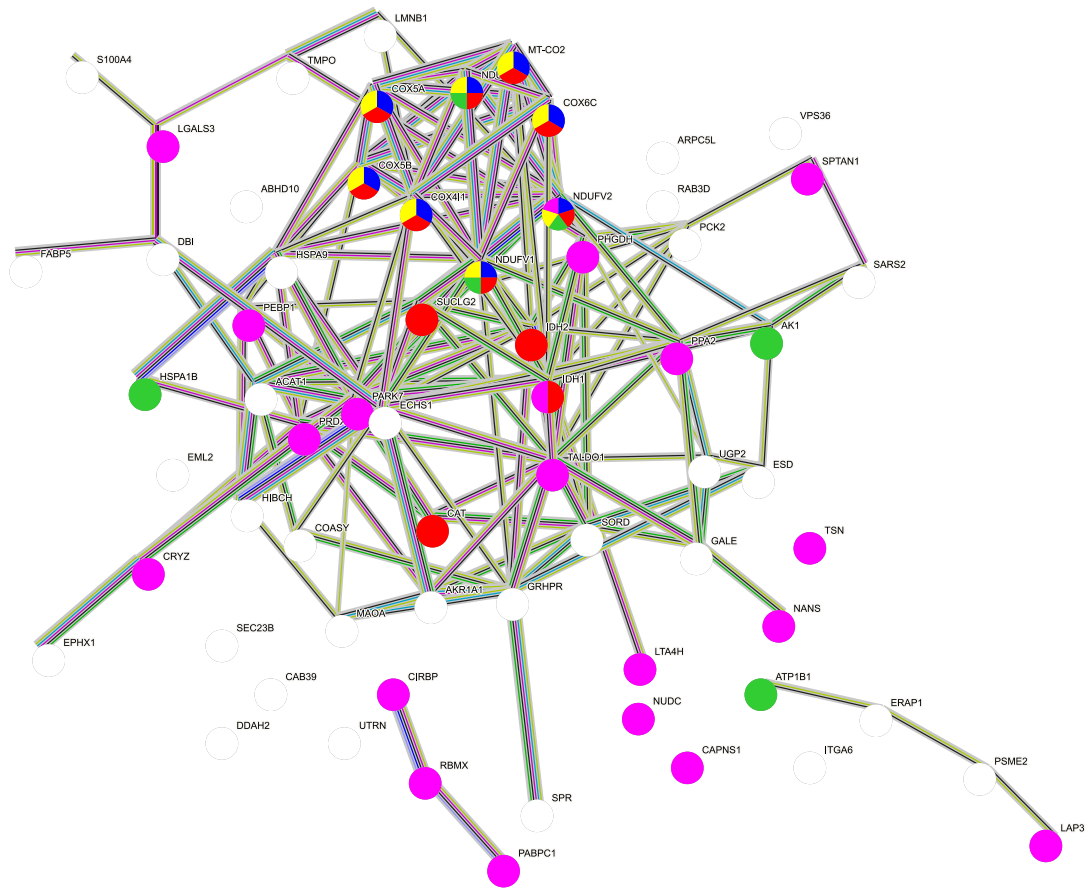


Figure A.3. Proteins downregulated in LOP in comparison to HBE. Color code: **Pink-Lung**. **Yellow-Respiratory chain complex**. **Green-ATP**. Generated by STRING. Pathways colors: Blue-from curated database, Pink-experimentally determined. Green-Gene neighborhood. Red-Gene fusions. Blue-Gene co-occurrence. Yellow-Textmining. Black co-expression. Dark blue: protein homology.

Proteins upregulated in LOi – cluster 3

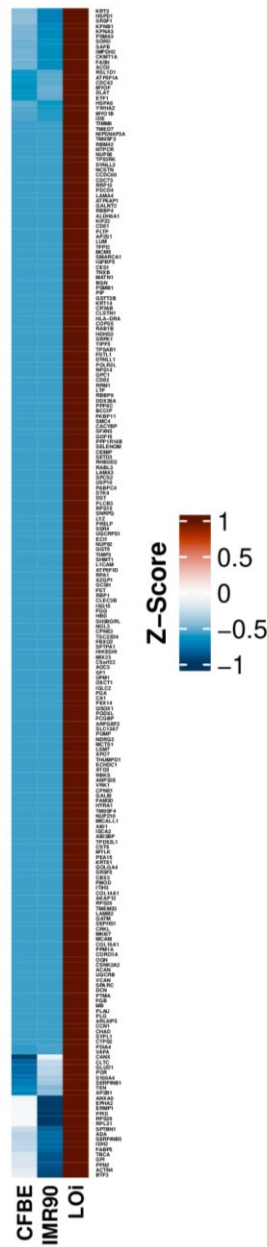


Figure A.4 Complete heatmap of proteins upregulated in LOi (cluster 3) in respect to cell monolayers CFBE, IMR-90. Abundances grouped, linked by average. Red show upregulation and blue downregulation. N=3.

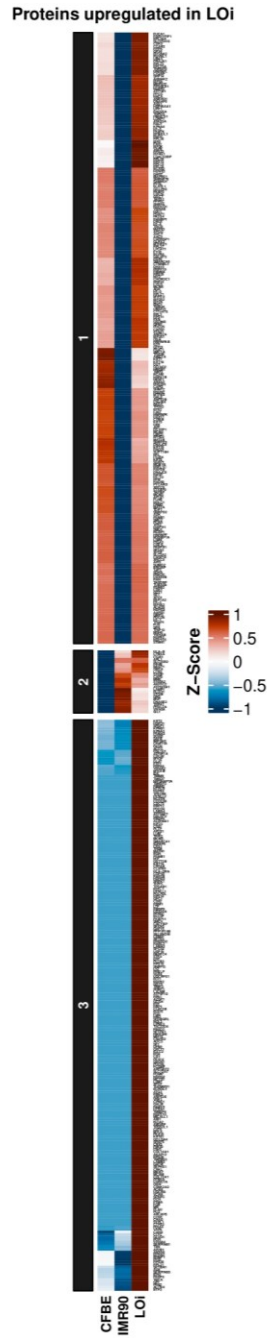


Figure A.5 Complete heatmap of proteins in cell monolayers CFBE, IMR-90 and LOi organoids. Cluster 3, correspond to the proteins upregulated in the organoid. Abundances grouped, linked by average. Red show upregulation and blue downregulation. N=3.

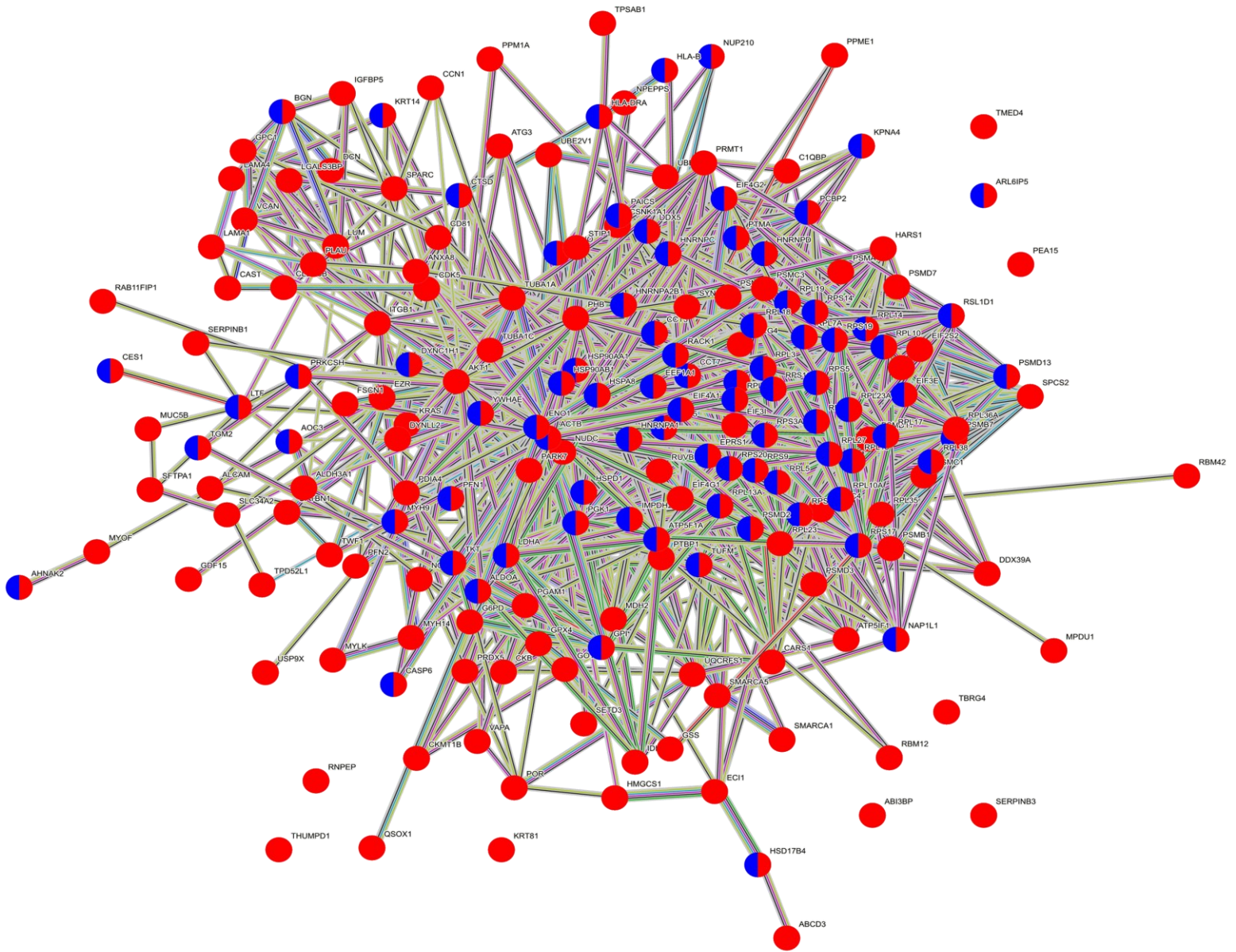


Fig. A6 Proteins upregulated in LOi in comparison to cell monolayers with specificity to the lung-red, and immune system-purple. Generated by STRING. Pathways colors: Blue-from curated database, Pink-experimentally determined. Green-Gene neighborhood. Red-Gene fusions. Blue-Gene co-occurrence. Yellow-Text mining. Black co-expression. Dark blue: protein homology.

